Pontifícia Universidade Católica
do Rio de Janeiro

Natália Victoria dos Santos

Development of Additively Manufactured bio-based components with the use of continuous natural fibers as reinforcement in Fused Filament Fabrication (FFF)

Tese de Doutorado

Thesis presented to the Programa de Pós-Graduação em Engenharia Civil of PUC-Rio in partial fullfilments of the requirements for the degree of Doutor em Engenharia Civil.

Advisor: Prof. Daniel Carlos Taissum Cardoso
Coadvisor: Prof. Doina Mariana Banea
Coadvisor: Prof. Paolo Minetola

Rio de Janeiro
February 2025

Pontifícia Universidade Católica
do Rio de Janeiro

Natália Victoria dos Santos

Development of Additively Manufactured bio-based components with the use of continuous natural fibers as reinforcement in Fused Filament Fabrication (FFF)

Thesis presented to the Programa de Pós-Graduação em Engenharia Civil of PUC-Rio in partial fulfillments of the requirements for the degree of Doutor em Engenharia Civil. Approved by the Examination Committee.

Prof. Daniel Carlos Taissum Cardoso
Advisor
Departamento de Engenharia Civil e Ambiental – PUC-Rio

Prof. Doina Mariana Banea
Co-Advisor
CEFET/RJ

Prof. Paolo Minetola
Co-Advisor
Polito

Prof. Sandro Campos Amico
UFRGS

Prof. Thiago de Carvalho Rodrigues Doca
UnB

Prof. Giovanni Filippone
UNINA

Prof. Flavio Andrade da Silva
Departamento de Engenharia Civil e Ambiental - PUC-Rio

Rio de Janeiro, February 25th, 2025

Natália Victoria dos Santos

Graduou-se em Engenharia Civil pela Universidade do Estado do Rio de Janeiro em 2019 e obteve o título de Mestre em Engenharia Civil pela Pontifícia Universidade Católica do Rio de Janeiro em 2021.

Bibliographic data

Santos, Natália Victoria dos

Development of additively manufactured bio-based components with the use of continuous natural fibers as reinforcement in fused filament fabrication (FFF) / Natália Victoria dos Santos ; advisor: Daniel Carlos Taissum Cardoso ; coadvisors: Doina Mariana Banea, Paolo Minetola. – 2025.

269 f. : il. color. ; 30 cm

Tese (doutorado)–Pontifícia Universidade Católica do Rio de Janeiro, Departamento de Engenharia Civil e Ambiental, 2025.

Inclui bibliografia

1. Engenharia Civil e Ambiental - Teses. 2. Impressão 3D. 3. Fabricação por filamento fundido. 4. Biocompósitos. 5. Fibras naturais. 6. Impressão em larga escala. I. Cardoso, Daniel Carlos Taissum. II. Banea, Doina Mariana. III. Minetola, Paolo. IV. Pontifícia Universidade Católica do Rio de Janeiro. Departamento de Engenharia Civil e Ambiental. V. Título.

CDD:624

Acknowledgments

This work was made possible thanks to the support and collaboration of various individuals and institutions, to whom I am deeply grateful.

To my parents, for their unconditional love, encouragement, and continuous support throughout this academic journey.

My special thanks go to my advisor, Professor Daniel Carlos Taissum Cardoso, for his tireless guidance, continuous support, and dedication throughout the entire process, from my master's degree to these six years of research.

To the Pontifical Catholic University of Rio de Janeiro (PUC-Rio) and the Department of Civil and Environmental Engineering for the opportunity to pursue my master’s and now my doctoral degree. I also extend my gratitude to my research colleagues Vitor Botton, Júlia Costa, Thais Rocha, Jésse Beserra, Marina Saad, Felipe Rodrigues, Victor Justen, Vitor Morales, and to the technical staff Euclides, José Marques, Rogério, and Jansen for their partnership and friendship, which made this journey even more enriching.

To the Federal Center for Technological Education Celso Suckow da Fonseca (CEFET-Rio), especially to my co-advisor, Professor Doina Mariana Banea, for her support and friendship, and to the research group that welcomed me as one of their own: Daniel Kawasaki, Jorge Neto, Henrique Queiroz, and Rogério Junior, for their technical support, friendship, and collaboration.

To the Politecnico di Torino (POLITO), where I conducted part of this research through the CAPES-Print program for six months. I am particularly grateful to my co-supervisor, Professor Paolo Minetola, and to Professor Alberto Giubilini for all their support during this significant challenge. I also thank my colleagues Adriano Pilagatti, Federica Valenza, and Mankirat Khandpur, who welcomed me and provided academic assistance during my stay in Italy. Additionally, I acknowledge the technical staff of the department, particularly Mateo, for their great help during these six months.

To the University of Brasília (UnB), with special thanks to my friend Karoline Gusmão and Professor Thiago Doca for their cooperation and knowledge exchange.

This study was financed in part by the Coordenação de Aperfeiçoamento de Pessoal de Nível Superior - Brasil (CAPES) - Finance Code 001, as well as the Brazilian agencies FAPERJ, through the Faperj Nota 10 scholarship, and CNPq. This project also received support from the State Institute of Engineering and Architecture (IEEA), linked to the Secretariat of Infrastructure of the State of Rio de Janeiro, through Contract 001/2021, with resources from the Government of the State of Rio de Janeiro.

Abstract

Santos, Natália Victoria; Cardoso, Daniel Carlos Taissum (Advisor); Banea, Doina Mariana (Co-advisor). Minetola, Paolo (Co-advisor). **Development of Additively Manufactured bio-based components with the use of continuous natural fibers as reinforcement in Fused Filament Fabrication (FFF).** Rio de Janeiro, 2023. 269 p. Tese de Doutorado – Departamento de Engenharia Civil e Ambiental. Pontifícia Universidade Católica do Rio de Janeiro.

Additive manufacturing (3D printing) has evolved from prototyping to producing complex structures with advanced materials, enabling creative designs and reducing resource waste. However, the use of polymers in structural components is limited by their mechanical properties and long printing times. In response to the construction industry’s growing demand for sustainable materials, this thesis focuses on developing biocomposites reinforced with continuous natural yarns (jute, ramie, sisal, and flax) and polylactic acid (PLA) polymer. The research covers the development of printing techniques for continuous natural yarns, thermomechanical analysis of these printed biocomposites, printed bonded joints, and large-scale production of biocomposite components. This study demonstrated the feasibility of using a large-diameter nozzle for printing biocomposites reinforced with vegetable yarns, leading to energy savings and replacing up to 48.2% of polymer content, thereby reducing the composite’s carbon footprint. Thermal analysis confirmed that natural fibers remain intact at PLA's processing temperature, while the addition of fibers increased the composite’s glass transition temperature. The primary challenge in printing continuous natural fibers was fiber impregnation, which directly impacted fiber-matrix adhesion and mechanical performance. The semi-finished filament (SF) method improved fiber bonding, resulting in superior tensile strength and elastic modulus (up to 18.4% higher than in-nozzle impregnation) and allowing faster printing speeds. Additionally, natural fiber reinforcement enhanced the mechanical behavior of single-lap bonded joints, particularly in bi-material applications. JFRP-wood joints exhibited the highest failure loads, demonstrating their potential for mixed sustainable structures. Furthermore, optimizing layer orientation significantly improved mechanical performance, with stiffness and strength gains of up to 35.2% and 80.0%, respectively. The findings highlight the viability of continuous natural fiber reinforcement in AM, paving the way for scalable and sustainable structural applications. Future work should focus on improving fiber-matrix interaction through pre-treatments and optimizing printing parameters to enhance composite performance.

Keywords

3D Printing; Fused Filament Fabrication; Biocomposites; Natural Fiber; Large Scale Printing.

Resumo

Santos, Natália Victoria; Cardoso, Daniel Carlos Taissum (Orientador); Banea, Doina Mariana (Coorientadora). Minetola, Paolo (Coorientador). **Desenvolvimento de biocompósitos fabricados por manufatura aditiva com o uso de fibras naturais contínuas como reforço por Fabricação De Filamentos Fundidos (FFF).** Rio de Janeiro, 2023. 269 p. Tese de Doutorado – Departamento de Engenharia Civil e Ambiental. Pontifícia Universidade Católica do Rio de Janeiro.

Manufatura aditiva (impressão 3D) evoluiu da prototipagem para a produção de estruturas complexas com materiais avançados, possibilitando designs inovadores e reduzindo o desperdício de recursos. No entanto, o uso de polímeros em componentes estruturais é limitado por suas propriedades mecânicas e longos tempos de impressão. Em resposta à crescente demanda da indústria da construção por materiais sustentáveis, esta tese se concentra no desenvolvimento de biocompósitos reforçados com fios contínuos de fibras naturais (juta, rami, sisal e linho) e um polímero de ácido polilático (PLA). A pesquisa abrange o desenvolvimento de técnicas de impressão para fios naturais contínuos, análise termomecânica desses biocompósitos impressos, juntas adesivas impressas e a produção em larga escala de componentes de biocompósitos. Este estudo demonstrou a viabilidade do uso de um bico de grande diâmetro para a impressão de biocompósitos reforçados com fios vegetais, resultando em economia de energia e substituição de até 48,2% do conteúdo polimérico, reduzindo assim a pegada de carbono do compósito. A análise térmica confirmou que as fibras naturais permanecem intactas na temperatura de processamento do PLA, enquanto a adição de fibras aumentou a temperatura de transição vítrea do compósito. O principal desafio na impressão de fibras naturais contínuas foi a impregnação da fibra, que impactou diretamente a adesão fibra-matriz e o desempenho mecânico. O método de filamento semiacabado (SF) melhorou a ligação da fibra, resultando em maior resistência à tração e módulo de elasticidade (até 18,4% superior à impregnação no bico) e permitindo velocidades de impressão mais altas. Além disso, o reforço com fibras naturais aprimorou o comportamento mecânico de juntas adesivas sobrepostas simples, especialmente em aplicações bi-materiais. As juntas JFRP-madeira apresentaram as maiores cargas de falha, demonstrando seu potencial para estruturas mistas sustentáveis. Além disso, a otimização da orientação das camadas melhorou significativamente o desempenho mecânico, com ganhos de rigidez e resistência de até 35,2% e 80,0%, respectivamente. Os resultados destacam a viabilidade do reforço com fibras naturais contínuas na manufatura aditiva, abrindo caminho para aplicações estruturais escaláveis e sustentáveis. Trabalhos futuros devem se concentrar na melhoria da interação fibra-matriz por meio de pré-tratamentos e na otimização dos parâmetros de impressão para aprimorar o desempenho dos compósitos.

Palavras-Chave

Impressão 3D; Fabricação por Filamento Fundido; Biocompósitos; Fibras Naturais;
Impressão em Larga Escala.

Table of Contents

List of Figures

List of tables

The only thing that's left is the manuscript
One last souvenir from my trip to your shores
Now and then I re-read the manuscript
But the story isn't mine anymore
Taylor Swift, The manuscript

Chapter 1 - INTRODUCTION

1.1 Motivation

Additive manufacturing (AM) has advanced significantly, transitioning from basic prototyping to the fabrication of intricate objects and structures using innovative materials. Commonly referred to as 3D printing, this process offers substantial design flexibility while minimizing material waste. It is widely applied across various industries, including aerospace, mechanical engineering, medical, and construction. In construction, 3D printing is used to create architectural elements and even entire buildings. However, while polymers are frequently used for small-scale applications, their limited mechanical strength and the slow printing process restrict their use for large structural components. To address these challenges, fiber reinforcements—both continuous and discontinuous—are being incorporated to enhance the mechanical properties of printed materials, expanding their potential for more demanding engineering applications. As the technology continues to evolve, AM is pushing the boundaries of what is possible in the production of advanced structural components for large-scale production.

Aligned with the pursuit of sustainability, incorporating natural fibers as filler and reinforcement agents in the 3D printing process has been gaining attention. Due to their lightweight nature, biodegradability, and mechanical resistance , these fibers have become increasingly popular in many sectors. Utilizing natural fibers not only aligns with eco-conscious practices but also enhances the overall performance and environmental footprint of the 3D-printed objects. As a result, this approach holds promise for fostering a more sustainable trajectory in AM processes. Natural fiber reinforcement can be incorporated in either discontinuous or continuous forms. Discontinuous fibers are generally used for manufacturing composite filaments, wherein a weight percentage of fibers is blended with the pellet matrix and extruded into filaments with dimensions compatible with market-available 3D printers [20]. The potential applications of Discontinuous Fiber-Reinforced Thermoplastic Composites (DFRTPCs) include various sectors [21], including biomedical [22–24], design [25–

28], and non-structural construction [29], due to their capacity for material recycling and ability to reuse waste materials [30]. Nevertheless, from a mechanical behavior perspective, the inclusion of discontinuous natural fibers often reduces the composite's mechanical characteristics. However, using 3D printing methods with Continuous Fiber Reinforced Thermoplastic Composites (CFRTPCs) presents a highly effective approach to enhancing the mechanical properties of components produced through Fused Filament Fabrication (FFF). Unlike DFRTPCs, CFRTPCs offer superior load transfer along the entire length of the material, resulting in significantly higher strength and stiffness [31–33]. This continuous reinforcement minimizes weak points, reduces void formation, and ensures uniform mechanical performance across the printed structure. As a result, CFRTPCs are particularly advantageous for structural applications, where high mechanical reliability and consistency are essential, making them a more efficient solution than DFRTPCs.

Therefore, it is essential to investigate the effects of larger-diameter natural fiber yarns (i.e. jute, ramie, sisal and flax) on the production of 3D-printed biocomposites for structural applications. This research aims to develop and optimize bio-based components reinforced with continuous natural fibers through Fused Filament Fabrication (FFF), focusing on effective fiber integration, mechanical performance, sustainability, and printability.

1.2 Objectives

This research aims to develop and optimize bio-based components reinforced with continuous natural fibers of jute, ramie, sisal, and flax through Fused Filament Fabrication (FFF). . These general objectives will be met by following the steps:

- To develop bio-based composite materials using continuous vegetable fibers as reinforcement in PLA matrix by Fused Filament Fabrication (FFF).
- To investigate the 3D printing process of polymer components reinforced with vegetable yarns, focusing on the effective integration of natural fibers into the FFF process and evaluating the mechanical performance in terms of strength and stiffness of the resulting composites.
- To analyse the interfacial, thermal, and void formation properties of additively manufactured biocomposites reinforced with continuous natural fibers,

determining the factors that influence the quality and structural performance of these materials.

- To compare different 3D printing methods for the fabrication of thermoplastic biocomposites reinforced with continuous natural fibers, assessing the advantages, limitations, and impact of each method on the mechanical and structural properties of the components.
- To study the performance of mono and bi-material adhesive joints using additively manufactured biocomposite adherends reinforced with continuous natural fibers, focusing on bonding strength, durability, and structural applicability.
- To explore and validate the application component joints additively manufactured and reinforced with natural fibers, investigating their load-bearing capacity and structural integrity in various application scenarios.

1.3 Thesis Organization

This thesis is composed of an introduction, and a literature review, followed by five chapters structured as individual full papers, and concludes with general conclusions organized as follows (Figure 1.1):

Chapter 1: Introduction

This chapter provides an overview of the research context, motivation, objectives, and structure of the study. It introduces the development of 3D-printed bio-based components using continuous vegetable fibers as reinforcement in Fused Filament Fabrication (FFF) for structural applications.

Chapter 2: Literature Review

The literature review presents a comprehensive examination of existing research on 3D printing technologies, particularly FFF, and their application in creating bio-based composites. It explores the properties and applications of natural fibers in polymer matrices and reviews current advancements in the use of continuous vegetable fibers for reinforcing thermoplastic materials.

Chapter 3: 3D Printing of Vegetable Yarn-Reinforced Polymer Components

This chapter investigates the fabrication process of 3D-printed components reinforced with continuous vegetable yarns. It discusses the challenges and methodologies associated with integrating natural fibers into the FFF process and evaluates the mechanical performance of the resulting composites.

Chapter 4: Analysis of Voids, Interfacial, and Thermal Properties of Additively Manufactured Continuous Natural Fiber-Reinforced Biocomposites

In this chapter, the void content, interfacial adhesion, and thermal properties of 3D-printed biocomposites reinforced with continuous natural fibers are analyzed. The study provides insights into the factors affecting the quality and performance of these materials in structural applications.

Chapter 5: Exploring Printing Methods for Continuous Natural Fiber-Reinforced Thermoplastic Biocomposites: A Comparative Study

This chapter presents a comparative analysis of different 3D printing methods used for fabricating continuous natural fiber-reinforced thermoplastic biocomposites. It assesses the advantages and limitations of each method, focusing on their impact on the mechanical and structural properties of the final components and the effects in the fiber-matrix interface.

Chapter 6: Mono and Bi-Material Adhesive Joints with Additively Manufactured Continuous Natural Fiber-Reinforced Biocomposite Adherends

This chapter examines the performance of mono and bi-material adhesive joints using additively manufactured biocomposite adherends reinforced with continuous natural fibers. The study evaluates the bonding strength, durability, and potential applications of these joints in structural contexts.

Chapter 7: Enhancing Structural Printed Component Joint Performance with Optimization Paths and Continuous Natural Yarn Reinforcement in Additive Manufacturing

In this chapter, the design and fabrication of printed joints reinforced with natural fibers are explored for their potential in structural applications. The study assesses these joints' load-bearing capacity and structural integrity when subjected to various stresses.

Chapter 8: General Conclusions

The final chapter summarizes the key findings from the previous chapters, highlighting the contributions of this research to the field of 3D-printed bio-based composites. It also provides recommendations for future research and potential advancements in the use of natural fibers in additive manufacturing.

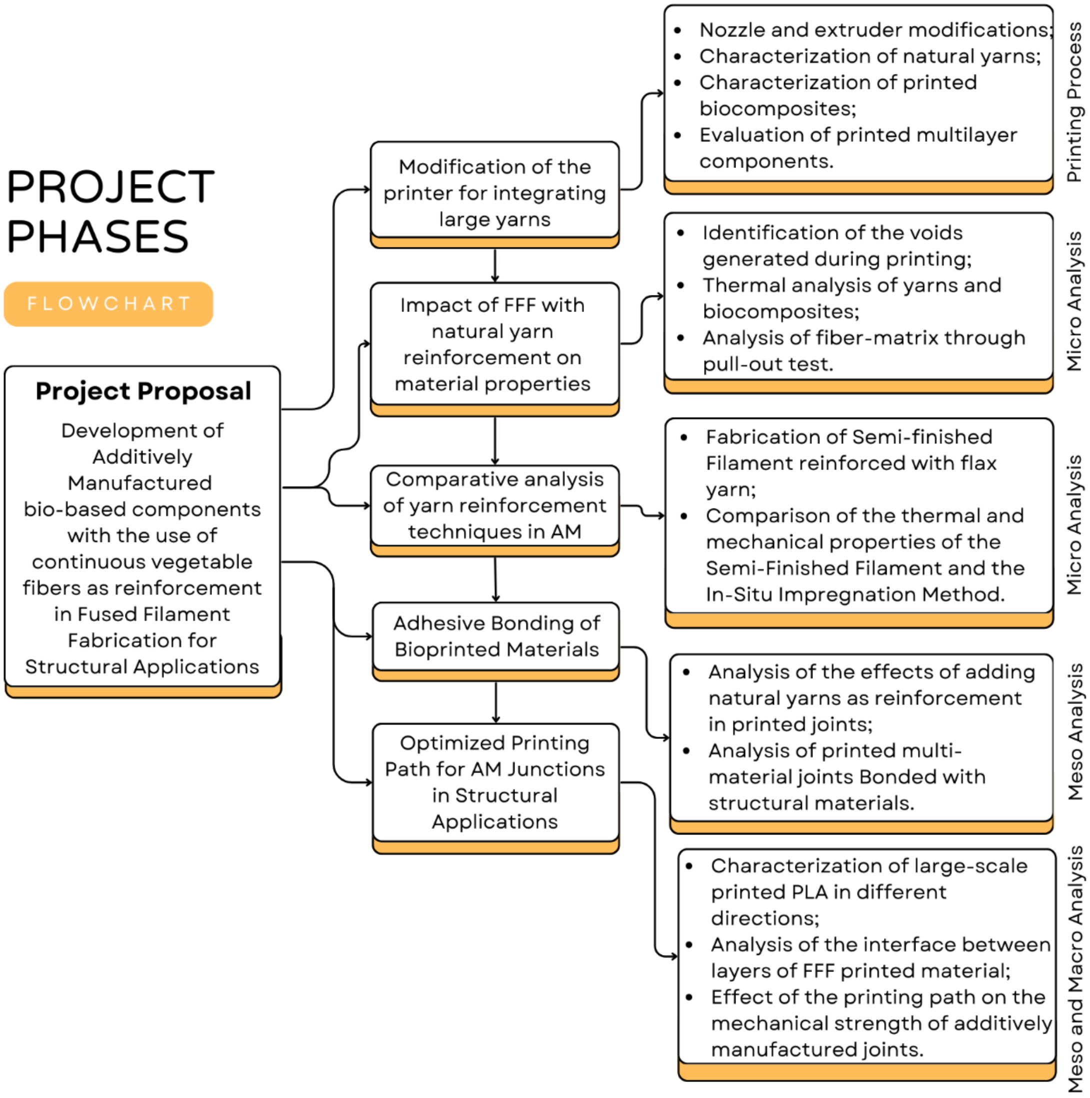

Figure 1.1 - Organization of the experimental program.

1.4 Publications

- Natália V. Santos, Daniel C.T. Cardoso, 3D printing of vegetable yarn-reinforced polymer components, Journal of Cleaner Production, Volume 415, 2023, https://doi.org/10.1016/j.jclepro.2023.137870

- dos Santos, N.V., Cavalcanti, D.K.K., Neto, J.S.S. *et al.* Analysis of voids, interfacial and thermal properties of additively manufactured continuous natural fiber-reinforced biocomposites. *Prog Addit Manuf* (2024). https://doi.org/10.1007/s40964-024-00913-5

- Natália V. dos Santos, Alberto Giubilini, Daniel Carlos T. Cardoso, Paolo Minetola, Exploring printing methods for continuous natural fiber-reinforced thermoplastic biocomposites: A comparative study, Sustainable Materials and Technologies, Volume 43, 2025, https://doi.org/10.1016/j.susmat.2025.e01253.

- dos Santos NV, Cavalcanti DKK, de Queiroz HFM, Neto JSS, Banea MD, Cardoso DCT. Mono and bi-material adhesive joints with additively manufactured continuous natural fiber-reinforced biocomposite adherends. Polym Compos. 2025;1-16. doi:10.1002/ pc.29674

References

[1] Atkins C, Betters E, Boulger A, Chesser P, Heineman J, Hun D, et al. Construction-scale concrete additive manufacturing and its Application in infrastructure energy storage. n.d.

[2] Lim S, Buswell RA, Le TT, Austin SA, Gibb AGF, Thorpe T. Developments in construction-scale additive manufacturing processes. Autom Constr 2012;21:262–8. https://doi.org/10.1016/j.autcon.2011.06.010.

[3] Winsun 3D. 2015 Global Highest 3D Printing Building n.d. http://www.winsun3d.com/ (accessed March 25, 2024).

[4] WASP. 3D Printed House TECLA: Eco-Housing n.d. https://www.3dwasp.com/en/3d-printed-house-tecla/ (accessed March 25, 2024).

[5] BAM Infra. Two world's first 3D printed reinforced concrete bridges 2017:1. https://materialdistrict.com/article/3d-printed-reinforced-concrete-bridges/ (accessed September 2, 2020).

[6] Eindhoven University of Technology. The world's first 3D printed reinforced concrete bridge starts to take shape. Eindhoven University of Technology 2017:1–3. https://www.tue.nl/en/university/news-and-press/news/16-06-2017-the-worlds-first-3d-printed-reinforced-concrete-bridge-starts-to-take-shape/ (accessed September 2, 2020).

[7] Kokkinis D, Schaffner M, Studart AR. Multimaterial magnetically assisted 3D printing of composite materials. Nat Commun 2015;6. https://doi.org/10.1038/ncomms9643.

[8] Els Zijlstra. The 3D Printed Bridge of Amsterdam 2020:1–2. https://iaac.net/project/3d-printed-bridge/.

[9] New Story Company. Introducing the world's first community of 3D-printed homes 2021. https://www.newstoryhomes.org/ (accessed October 24, 2024).

[10] Caron JF, Demont L, Ducoulombier N, Mesnil R. 3D printing of mortar with continuous fibres: Principle, properties and potential for application. Autom Constr 2021;129. https://doi.org/10.1016/j.autcon.2021.103806.

[11] Sobolev K, Lin Z, Cao Y, Sun H, Flores-Vivian I, Rushing T, et al. The influence of mechanical activation by vibro-milling on the early-age hydration and strength development of cement. Cem Concr Compos 2016;71:53–62. https://doi.org/10.1016/j.cemconcomp.2016.04.010.

[12] Sharanova A V., Panfilova AD, Plahtiy AA, Dmitrieva MA. Investigation of viscosity of construction mixtures applied for 3D printing. IOP Conf Ser Mater Sci Eng 2019;525. https://doi.org/10.1088/1757-899X/525/1/012055.

[13] Plymill A, Minneci R, Alexander Greeley D, Gritton J, Greeley D, Minneci R, et al. Graphene and Carbon Nanotube PLA Composite Feedstock Development for Fused Deposition Modeling 2016.

[14] Namsone E, Korjakins A, Sahmenko G, Sinka M. The environmental impacts of foamed concrete production and exploitation. IOP Conf Ser Mater Sci Eng, vol.

251, Institute of Physics Publishing; 2017. https://doi.org/10.1088/1757-899X/251/1/012029.

[15] Dsilva J, Zarmukhambetova S, Locke J. Assessment of building materials in the construction sector: A case study using life cycle assessment approach to achieve the circular economy. Heliyon 2023;9:e20404. https://doi.org/10.1016/j.heliyon.2023.e20404.

[16] International Energy Agency., Global Alliance for Buildings and Construction. 2019 Global Status Report for Buildings and Construction. International Energy Agency; 2019.

[17] Monteiro PJM, Miller SA, Horvath A. Towards sustainable concrete. Cem Concr Res 2018;114:40–8. https://doi.org/10.1016/j.cemconres.2017.02.009.

[18] International Energy Agency., Global Alliance for Buildings and Construction. 2023 Global Status Report for Buildings and Construction. United Nations Environment Programme; 2024. https://doi.org/10.59117/20.500.11822/45095.

[19] European Commission of Energy C change and E. Construction and demolition waste n.d. https://environment.ec.europa.eu/topics/waste-and-recycling/construction-and-demolition-waste_en (accessed March 22, 2024).

[20] Ahmad MN, Ishak MR, Mohammad Taha M, Mustapha F, Leman Z. A Review of Natural Fiber-Based Filaments for 3D Printing: Filament Fabrication and Characterization. Materials 2023;16. https://doi.org/10.3390/ma16114052.

[21] Romani A, Suriano R, Levi M. Biomass waste materials through extrusion-based additive manufacturing: A systematic literature review. J Clean Prod 2023;386. https://doi.org/10.1016/j.jclepro.2022.135779.

[22] Shahar FS, Hameed Sultan MT, Safri SNA, Jawaid M, Abu Talib AR, Basri AA, et al. Physical, thermal and tensile behaviour of 3D printed kenaf/PLA to suggest its usability for ankle–foot orthosis – a preliminary study. Rapid Prototyp J 2022;28:1573–88. https://doi.org/10.1108/RPJ-08-2021-0207.

[23] Tao Y, Li P, Zhang J, Wang S, Shi SQ, Kong F. A review of fused filament fabrication of continuous natural fiber reinforced thermoplastic composites: Techniques and materials. Polym Compos 2023;44:8200–22. https://doi.org/10.1002/pc.27477.

[24] Durfee WK, Iaizzo PA. Medical applications of 3D printing. Engineering in Medicine: Advances and Challenges, Elsevier; 2018, p. 527–43. https://doi.org/10.1016/B978-0-12-813068-1.00021-X.

[25] Pringle AM, Rudnicki M, Pearce JM. Wood furniture waste-based recycled 3-D printing filament. For Prod J 2018;68:86–95. https://doi.org/10.13073/FPJ-D-17-00042.

[26] Yang F, Zeng J, Long H, Xiao J, Luo Y, Gu J, et al. Micrometer copper-zinc alloy particles-reinforced wood plastic composites with high gloss and antibacterial properties for 3d printing. Polymers (Basel) 2020;12. https://doi.org/10.3390/polym12030621.

[27] Sanandiya ND, Ottenheim C, Phua JW, Caligiani A, Dritsas S, Fernandez JG. Circular manufacturing of chitinous bio-composites via bioconversion of urban refuse. Sci Rep 2020;10. https://doi.org/10.1038/s41598-020-61664-1.

[28] Sauerwein M, Zlopasa J, Doubrovski Z, Bakker C, Balkenende R. Reprintable paste-based materials for additive manufacturing in a circular economy. Sustainability (Switzerland) 2020;12:1–15. https://doi.org/10.3390/su12198032.

[29] Cislaghi A, Sala P, Borgonovo G, Gandolfi C, Bischetti GB. Towards more sustainable materials for geo-environmental engineering: The case of geogrids. Sustainability (Switzerland) 2021;13:1–21. https://doi.org/10.3390/su13052585.

[30] Romani A, Rognoli V, Levi M. Design, materials, and extrusion-based additive manufacturing in circular economy contexts: From waste to new products. Sustainability (Switzerland) 2021;13. https://doi.org/10.3390/su13137269.

[31] Le Duigou A, Barbé A, Guillou E, Castro M. 3D printing of continuous flax fibre reinforced biocomposites for structural applications. Mater Des 2019;180:107884. https://doi.org/10.1016/j.matdes.2019.107884.

[32] Le Duigou A, Correa D, Ueda M, Matsuzaki R, Castro M. A review of 3D and 4D printing of natural fibre biocomposites. Mater Des 2020;194:108911. https://doi.org/10.1016/j.matdes.2020.108911.

[33] Cheng P, Peng Y, Wang K, Le Duigou A, Yao S, Chen C. Quasi-static penetration property of 3D printed woven-like ramie fiber reinforced biocomposites. Compos Struct 2023;303:116313. https://doi.org/10.1016/j.compstruct.2022.116313.

[34] Santos N V., Cardoso DCT. 3D printing of vegetable yarn-reinforced polymer components. J Clean Prod 2023;415. https://doi.org/10.1016/j.jclepro.2023.137870.

Chapter 2 - TOWARDS SUSTAINABLE ADDITIVE MANUFACTURING OF CONTINUOUS NATURAL YARN-REINFORCED THERMOPLASTIC BIOCOMPOSITES: A REVIEW

Natália V. Santos, Alberto Giubilini, Paolo Minetola, Mariana D. Banea, Daniel C.T Cardoso. *Accepted for publication in the journal Cellulose.*

This chapter presents a comprehensive literature review on the 3D printing of continuous natural fiber-reinforced thermoplastic biocomposites, structured in the format of a scientific article. The review encompasses all relevant studies published up to the date of the thesis defense, providing an in-depth analysis of advancements in this emerging field. As part of this review, some of the articles developed during this doctoral research are also included, highlighting their contribution to the broader scientific discussion.

The application of 3D printing with natural materials emerges as a promising strategy for achieving more sustainable production practices. Natural fibers offer an eco-friendly alternative for reinforcing composite materials due to their biodegradability, reusability, and low environmental impact. This review provided an in-depth analysis of Continuous Natural Fiber Reinforced Thermoplastic Composites (CNFRTCs) produced through Fused Filament Fabrication (FFF), focusing on incorporating Continuous Natural Yarn Reinforcement (CNYR) in a polymer matrix. The study examined the effects of continuous natural yarn insertion in FFF printing, specifically analyzing parameters such as insertion method, nozzle characteristics, printing speed, and curvature. These factors significantly impacted key printing properties, including fiber-matrix adhesion and porosity, which were also examined. The review further explored how the insertion of natural yarns impacts the material's overall performance, particularly in terms of mechanical strength and printability, emphasizing their potential in large-scale applications, and reducing reliance on synthetic fibers while enhancing the eco-friendliness of 3D-printed composites.

2.1 Introduction

CFRTPCs are advanced materials with continuous fibers embedded in a thermoplastic matrix. The continuous fibers provide high strength and stiffness, while the thermoplastic matrix offers toughness, processability, and improved resistance to environmental factors. This synergy between reinforcement and matrix enhances mechanical properties, making CFRTPCs ideal for lightweight applications. Additionally, their thermoplastic nature allows for recycling and reshaping, contributing to sustainable production cycles.

The application of Additive Manufacturing (AM) with natural materials opens a promising pathway toward more sustainable production practices [1]. Traditional manufacturing processes can generate significant waste and require high energy inputs. However, AM offers advantages such as material efficiency, customization, and on-demand production [2], promoting advances in the automotive [3], construction [4], aerospace [5], and medicine industries [6]. When reinforced with natural materials, AM can further reduce environmental impact using bio-based and/or biodegradable feedstock [1,7].

Recent studies have highlighted the progress in using natural materials specifically tailored for AM, along with efforts to optimize geometries and refine printing techniques to create products that maximize material efficiency and minimize ecological footprint. In this context, biocomposites with plant-based matrices and reinforcements represent a sustainable and high-performance option for 3D printing [8]. Due to their low density, renewability, and biodegradability, these composites can substantially lower carbon dioxide emissions [9,10]. Moreover, their ability to decompose at the end of their service life contributes to waste reduction, fostering a more sustainable and eco-friendly production cycle [11].

This review provides an analysis of the use of natural fibers in yarn format for CNFRTPCs produced by FFF. It examines the influence of critical factors such as fiber insertion methods, nozzle design, printing parameters (e.g., speed and temperature), and part geometry on key properties, including fiber-matrix adhesion, porosity, and print quality. Additionally, it explores the complex interactions between natural fibers and the thermoplastic matrix during the printing process, which are essential for enhancing mechanical strength, stiffness, and dimensional stability.

The structural benefits of CNFRTPCs include their ability to improve printability and produce components with consistent and reliable mechanical properties. Beyond performance advantages, the use of natural fibers highlights their sustainability as renewable, biodegradable, and low-density materials, offering an eco-friendly alternative to synthetic reinforcements. Their use aligns with the shift toward greener manufacturing practices, reducing the ecological footprint of composite production and supporting the development of high-performance materials for various applications. Although numerous review articles have been published on the additive manufacturing of biocomposites, a comprehensive evaluation of this field remains essential. The authors believe that a review article focusing on the use of continuous natural fibers in filament-based 3D printing holds significant value for the composite community, benefiting both academic researchers and industry engineers by identifying knowledge gaps and outlining potential research directions.

2.2 Process and Materials for FFF Printing with CNYR

2.2.1 FFF Process

Additive Manufacturing (AM), commonly known as 3D printing, refers to a process where objects are created layer by layer from a digital model [12]. AM processes can be categorized according to ISO/ASTM 52900 standard [13] into seven classifications: binder jetting, directed energy deposition, material extrusion, material jetting, powder bed fusion, sheet lamination, and vat photopolymerization.

Considering polymer 3D printing, material extrusion is the most common method, which consists of heating up the material and then extruding it through a nozzle to form consecutive layers [14]. This process can be divided into three main steps: modeling, slicing, and printing. Modeling involves creating a 3D digital model using CAD software. This model is normally saved in STL (Standard Triangle Language) format, which, as the name says, converts the outer shell of the object into a triangular mesh. Slicing is a crucial part of the AM process, since here all main parameters are defined, including nozzle and platform temperatures, printing speeds, and layer thickness, along with printer specifications, nozzle size, and printing area limits. Once the printing parameters are defined, the slicing software divides the STL file into thin layers, each containing vector data in G-code format. During the printing process, the 3D printer follows the instructions from the sliced file, fabricating the object layer by layer through coordinated movements along the XY axes, continuing until the entire structure is completed [15].

AM provides numerous advantages over traditional methods, including increased automation, enhanced productivity, and minimized material waste, and greater design flexibility [12]. The process allows the production of complex geometries that would be difficult or impossible to achieve with conventional methods [16]. Furthermore, since the material is deposited exclusively where required, waste generation is minimized, enhancing the sustainability of the process. Despite these advantages, 3D printing also has inherent limitations, such as the limited dimensions of objects that can be produced in a single job, constraining their application to fabricate large-scale components. Additionally, due to production rates, AM is generally reserved for middle to low volumes productions, and, in any case, far from a mass-production method.

AM was initially used only for Rapid Prototyping (RP), where the final component was not meant to be an end-usable part and did not require high mechanical properties [12]. However, advancements in materials development and processing technologies have extended their application to functional and complex components. The range of materials used in AM has significantly increased and diversified. Initially, confined to polymers, currently, AM includes ceramics, concrete, metals, glass, and biomaterials.

Among all cited classes of materials, polymers encountered a wide range of application fields, such as biomedical, electronics, construction, and aerospace, mostly due to their low weight, minimal wear, recyclability, and reusability [17]. Compared to thermoset polymers, thermoplastic ones are even more widespread in 3D printing because of their capacity to be remelted and reshaped into specified geometries [18].

However, their application in structural components requiring high mechanical performance necessitates the incorporation of reinforcements to enhance their properties. These reinforcements can take various forms, such as discontinuous or continuous fibers, which may be configured as strands, ropes, mats, or fabrics [19].

2.3 Materials for FFF Printing with CNYR

2.3.1 Thermoplastic matrix

The most common materials used in extrusion-based 3D printing are thermoplastic polymers [20], among which acrylonitrile butadiene styrene (ABS), polylactic acid (PLA), and nylon are the most used (Table 2.1). These polymers are favored due to their advantageous processing characteristics and mechanical properties. In AM, a variety of polymer matrices are employed, each exhibiting distinct physical properties that attend to specific applications across diverse industrial sectors. The selection of these matrices is crucial, as it directly influences the performance, durability, and suitability of the printed components for their intended use. Pervaiz et al. [21] highlight several materials used as matrices, such as polyester sulfone for flame resistance in the automotive sector, polyphenylene sulfide for chemical and high-temperature resistance in the electric industry, and polysulfone for low moisture absorption in Navy applications. Polyethylene (PE) is known for its corrosion resistance in pipe construction, while polypropylene (PP) is favored for packaging due to its chemical resistance, and PLA's biodegradable nature suits biomedical applications.

Table 2.1 - Properties of FFF printed most common thermoplastics [22–24].

Properties	**PLA**	**ABS**	**Nylon**
Density (g/cm^3)	1.3	1.1	1.1
Melting temperature (°C)	160-235	210-250	235-280
Decomposition temperature (°C)	300-400	380-430	390-450
Tensile strength (MPa)	24.4-44.8	43.3-43.4	49.6-75
Strain at break (%)	4.0-23.1	6.5-24.8	14.3-50
Young modulus (GPa)	0.8-3.8	1.3-2.3	1.4-2.8

Biodegradable polymers are materials that undergo photodegradation, oxidation, and hydrolysis due to microbial action, leading to chain scission and the breakdown of the material. The significance of biodegradability lies in its potential to substantially reduce environmental waste, as these polymers can decompose naturally at the end of their useful life [11]. This intrinsic property minimizes landfill accumulation and mitigates the long-term ecological impact associated with traditional, non-biodegradable plastics, which can persist in the environment for centuries. By replacing conventional plastics with biodegradable alternatives, industries can contribute to a circular economy, where materials are continuously reused and reintroduced into the environment without contributing to pollution. Furthermore, the development and implementation of biodegradable polymers represent a vital step toward a more sustainable future, addressing the pressing challenges of plastic waste and promoting ecological balance.

2.3.2 Natural fibers

2.3.2.1 Natural Fibers Characteristics

Natural fibers represent a valuable and greener alternative to synthetic reinforcing fibers, due to their biodegradability, low abrasion, excellent stiffness to weight ratio, reusability, and low environmental impact [25]. The addition of fibers in polymeric materials allows the improvement of the mechanical properties of the set since the matrices alone present brittle behavior and low mechanical properties. Moreover, these fibers may be derived from plant, animal, or mineral sources, and they generally require minimal processing after extraction [26]. Historically, these fibers have been used in non-structural applications like carpets, ropes, and paper production [27]. More recently, they have been widely adopted for reinforcing polymers in the production of biocomposites, enabling the development of structural elements across various industries (Figure 2.1). This progression demonstrates their versatility and ability to withstand diverse types of loading conditions, supporting applications in both non-structural and structural contexts.

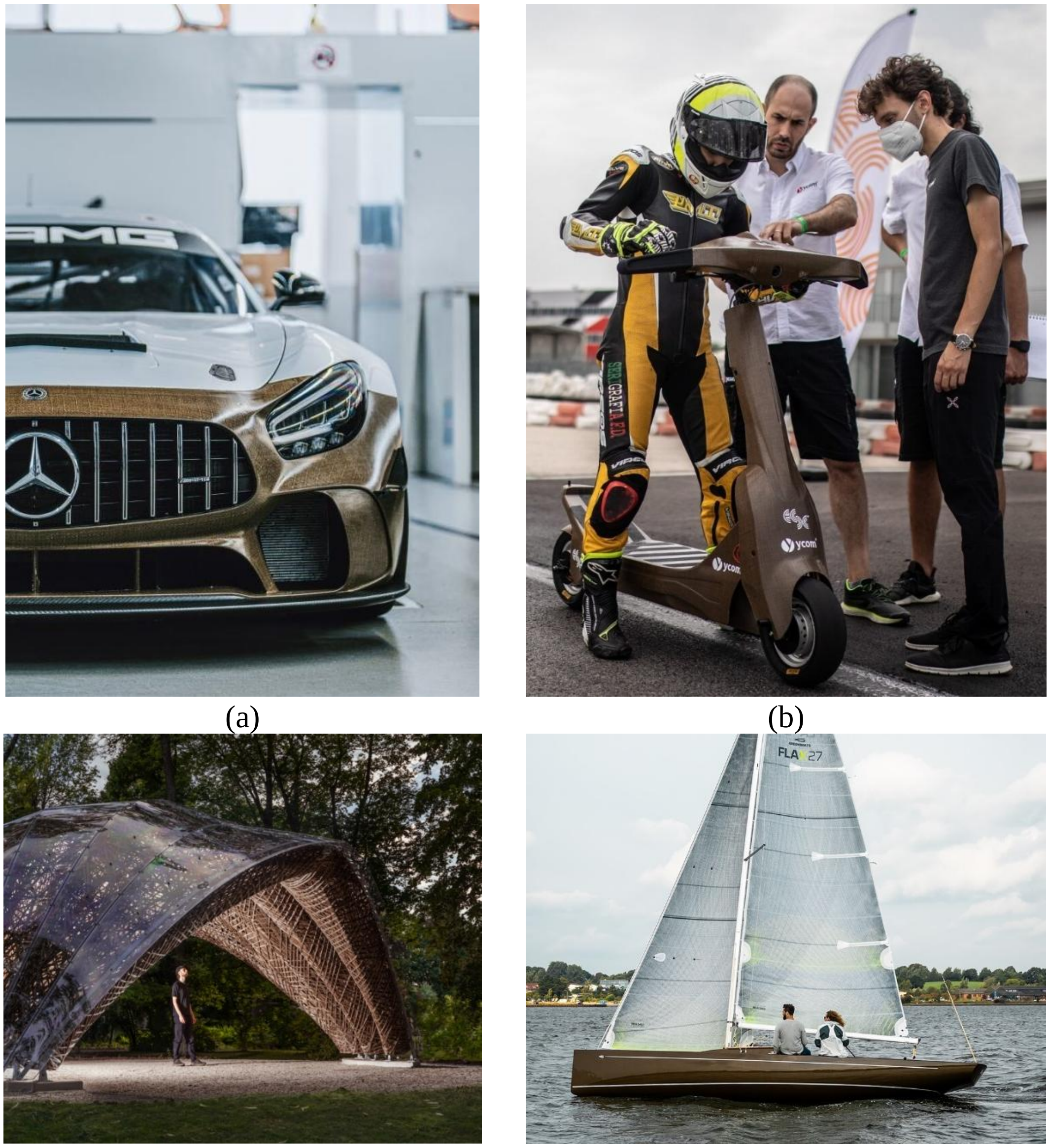
(a) (b)
(c) (d)

Figure 2.1 - Biocomposite structural application: (a) Mercedes-AMG GT4 race car [28], (b) YCOM S1-X eSkootr [29], (c) livMatS Pavilion [30], (d) Greenbolts Flax 27 [31].

The extraction of lignocellulosic fibers entails separating them from various plant parts, including the bast, fruit, grass, leaf, seed, stalk, and wood (Figure 2.2) [27]. These fibers are commercially available in several forms, such as tow, chopped, yarn, nonwoven, woven, and prepregs [27]. Structurally, lignocellulosic fibers are composed of a cellular structure made of different proportions of cellulose, hemicellulose, and lignin; each constituent contributes to the overall properties of the fiber [32]. While lignin demonstrates thermal stability and is susceptible to degradation from UV radiation, hemicellulose is primarily responsible for the biodegradation, moisture absorption, and thermal degradation of the fiber, owing to its comparatively lower resistance [16,33]. The incorporation of these vegetable fibers with a biodegradable polymer matrix in biocomposites can significantly reduce the carbon dioxide footprint, thanks to their low density, biodegradability, and renewability [9,10].

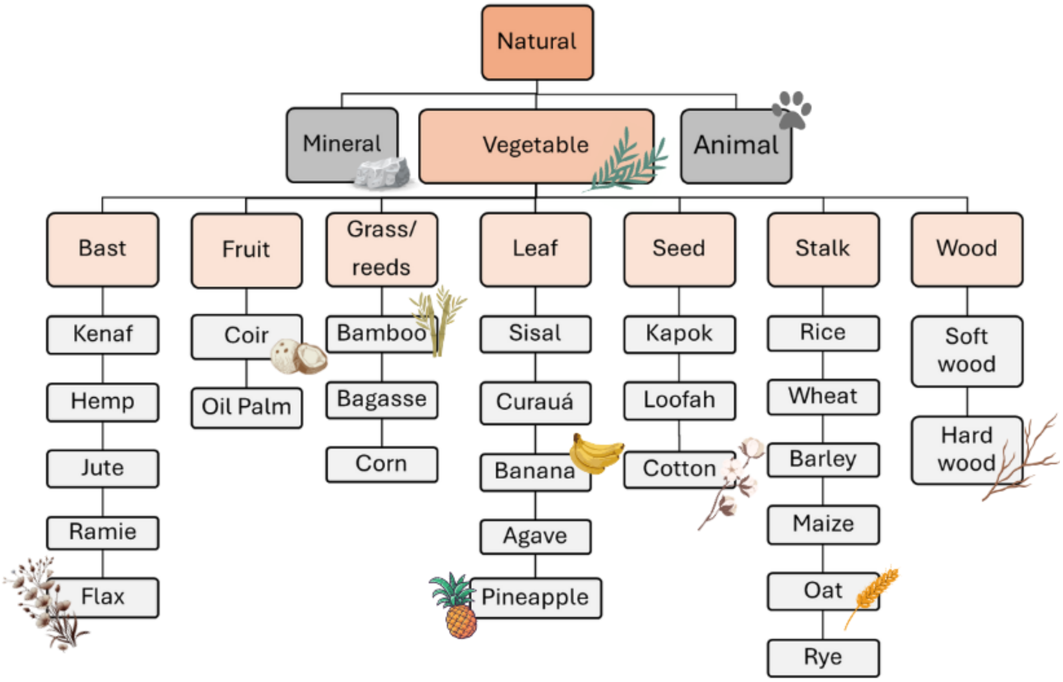

Figure 2.2 - Natural fiber's classification with examples based on their source of extraction.

In terms of mechanical properties, vegetable fibers typically have lower tensile strength and Young's modulus values than synthetic fibers. However, it is noteworthy that their lower density results in specific strength and modulus values comparable to those of glass fibers [8].

Since the length of vegetable fibers is finite and species-dependent, a continuous bundle can be created by twisting multiple long fibers together. Consequently, the choice of vegetable fiber for continuous 3D printing also depends on the feasibility of manufacturing them into yarn. Consequently, the selection of vegetable fibers for such purposes is significantly influenced by the feasibility of manufacturing high-quality yarns. Table 2.2 presents a summary of the mechanical and physical properties of several vegetable fibers commonly available in yarn format. These properties are crucial as they determine the fibers' performance as continuous reinforcement in 3D printing applications.

Table 2.2 - Properties of vegetable fibers [34–40].

Properties	**Flax**	**Hemp**	**Jute**	**Ramie**	**Sisal**
Density (g/cm^3)	1.5	1.5	1.3-1.5	1.5	1.3-1.4
Tensile strength (MPa)	500-1500	900	400-800	400-968	500-1150
Young modulus (GPa)	27.6	34	10-30	44-128	11-15
Cellulose content (%)	65-80	57-77	58-63	76	58.8
Hemicellulose content (%)	12-16	14-22	12	17	23.8
Lignin content (%)	2-5	4-13	12-14	1	14.7
Onset degradation temperature (°C)	274	260	242	247	222

2.3.2.2 Natural yarn production

According to the American Society for Testing and Materials [41], textile fibers or textile filaments are characterized by their unique physical properties that make them suitable for fabric production. According to widely accepted standards, textile fibers are defined by a high aspect ratio, with a length typically at least 100 times greater than their width, allowing them to be spun into yarn or woven into fabric. These fibers are filamentous structures in the form of a bundle, which have a much higher strength than the same material in its bulk form since the fiber has fewer defects [42]. These fibers can be sourced from various natural origins, including plant-based materials like cotton or flax, animal-derived fibers like wool or silk, and mineral fibers like asbestos. Additionally, they may be produced through artificial processes, including synthetic polymers like polyester and nylon, designed to meet specific performance requirements for diverse textile applications. Due to its length, this material is classified into two groups: discontinuous fibers and continuous yarns. Discontinuous fibers represent the raw form of the material and are categorized based on length as short or long fibers, which is determined by the plant's growth characteristics. In contrast, continuous yarns have an indefinite length and are typically measured in kilometers. The fiber length and arrangement are directly linked to the final mechanical behavior of the composite. It may be arranged and oriented in one or more directions or dispersed [43].

The production of natural yarns involves multiple stages, beginning with agricultural processes such as planting, maintenance, and harvesting. Fibers are then extracted through methods specific to their type—retting for phloem fibers, decortication for leaf fibers, and ginning for cotton—followed by defibration using mechanical, chemical, or enzymatic techniques to separate them from pulp or mucilage. After cleaning and drying, the fibers are carded to align them before being spun into yarn through drawing, roving, and twisting. Depending on the desired properties, the yarn may undergo plying for added strength, as well as dyeing and chemical treatments to enhance durability, before being wound onto spools or cones for packaging (Santos et al. 2013). Each stage plays a crucial role in determining the quality, strength, and application of the final yarn product and Figure 2.3 illustrates all stages of this process.

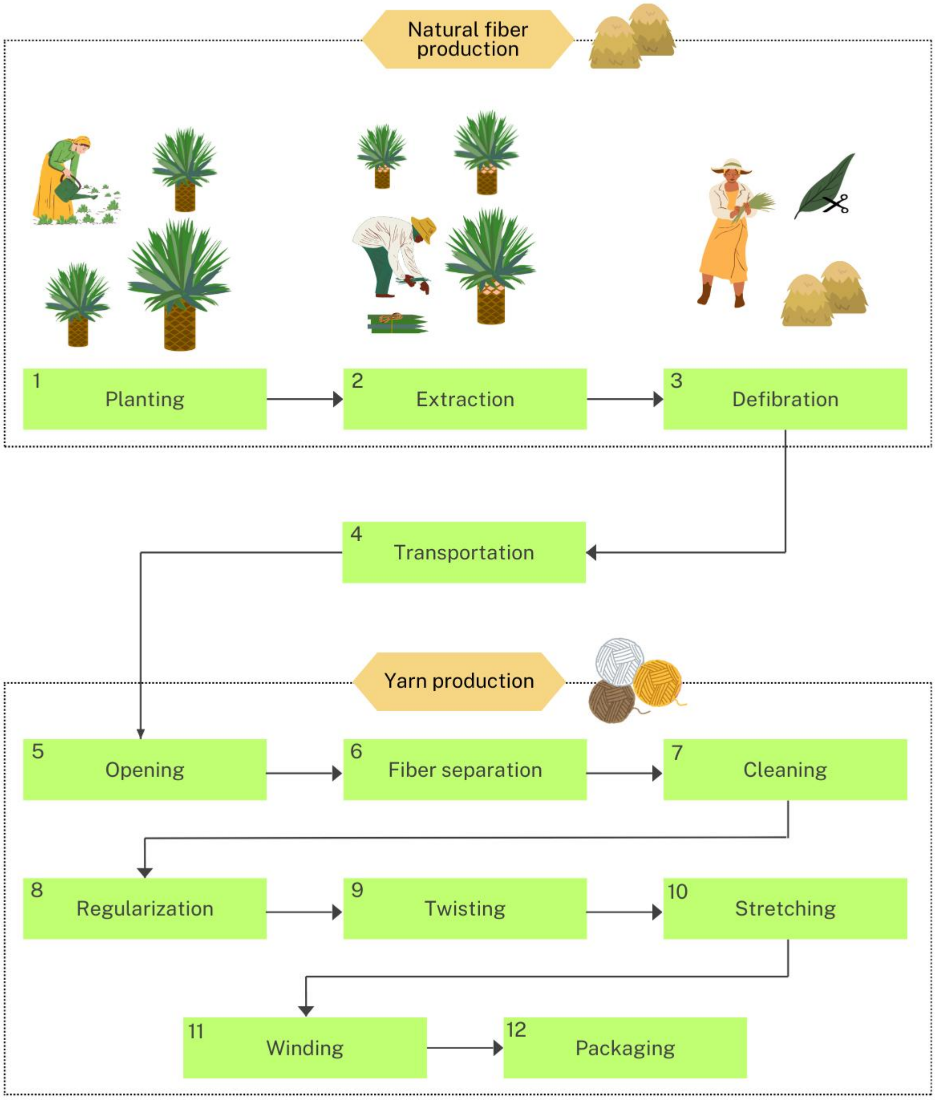

Figure 2.3 - Stages of natural yarn production.

The textile yarn is the final product of an extensive spinning process, where its identifying parameter is the yarn count, which represents its diameter or thickness. Textile yarn production involves several stages, beginning with opening and fiber separation, where bales are divided into smaller portions using a bale opener. Next is cleaning, where a beater removes impurities, followed by parallelization using a carder and combing machine. The carder produces fiber slivers, known as carding ribbons, and performs mechanical cleaning. The combing machine eliminates short fibers remaining in the material, ensuring uniform fiber length. Regularization with a roving machine standardizes the weight per unit length, homogenizing the material, while thinning using a roving frame stretches, parallelizes, and applies an initial twist to improve yarn strength. Finally, twisting and further stretching are carried out in a ring-spinning machine, and winding machines coil the finished yarn onto spools, ready for packaging [45].

One of the main challenges in using natural yarns is that their finite length, combined with the manufacturing processes, which typically involve cutting and twisting the fibers, often significantly reduces tensile strength compared to individual fibers. Unlike continuous synthetic fibers, yarns become discontinuous during processing, which impacts their load-bearing capacity.

2.4 Natural-Yarn Reinforced Thermoplastic Composites

2.4.1 Polymer extrusion printing

In FFF, the filament feedstock is driven into the printer by a stepper motor through the cold end, which controls heat dissipation from the hot end [16]. This separation enables the thermoplastic material to reach and maintain its melting temperature only at the desired location, preventing premature softening or melting along the filament path. By contrast, Fused Granulate Fabrication (FGF) shares a similar operational principle but relies on thermoplastic polymers in pellet form rather than filament. In FGF, pellets are fed into a heating chamber where they are heated and compressed by a rotating vertical extrusion screw. This action transforms the pellets into a molten, homogeneous thermoplastic mass, ensuring consistent flow and fusion during deposition [46]. Figure 2.4 provides a comparison of these two processes, highlighting their key operational differences.

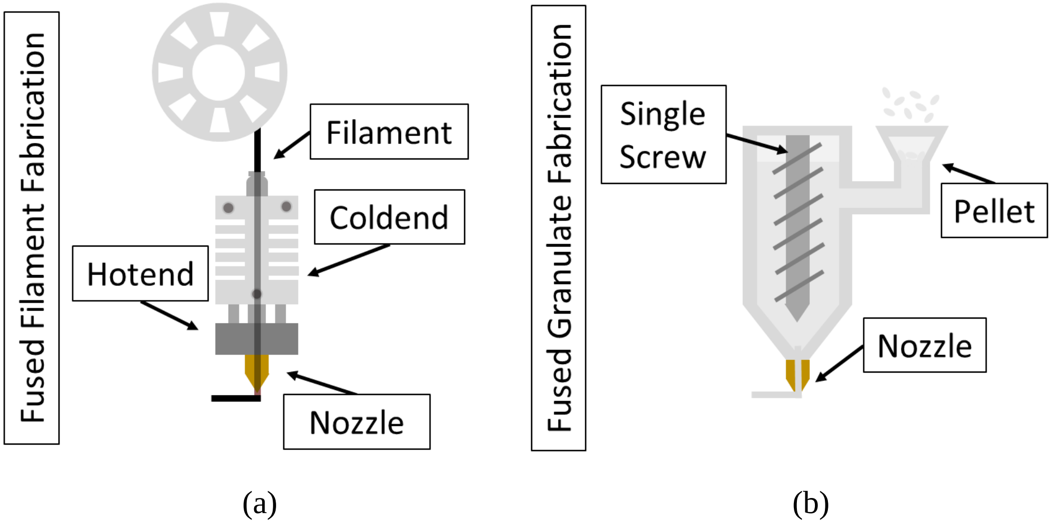

Figure 2.4 - Types of polymer extrusion: (a) FFF process, and (b) FGF process.

2.4.2 Discontinuous Natural Yarn-Reinforcement

Biocomposite filaments reinforced with natural fibers are commonly produced using discontinuous fibers, where fibers are mixed in specific weight ratios with a pellet-based matrix, and then extruded into filaments suited for standard 3D printers [47]. Discontinuous Fiber-Reinforced Thermoplastic Composites (DFRTPCs) hold promise for diverse fields [1], such as biomedicine [48–50], and design [51–53], owing to their recyclability and capacity to incorporate waste materials [54,55].

The fabrication process of filaments for FFF reinforced with biofillers and natural discontinuous fibers involves a series of critical steps. Initially, the thermoplastic material is processed in granule form to be extruded into a wire filament compatible with FFF [56]. This preparation requires several key stages, including screening to remove impurities, crushing to achieve a uniform particle size, and thorough mixing to ensure homogeneity of the fiber distribution. Compounding then blends the biofillers and thermoplastic matrix, followed by grinding to refine the granules further before extrusion, where the material is shaped into the final FFF filament wire form [47].

However, regarding mechanical performance, the addition of discontinuous natural fibers often reduces the composite's mechanical properties, as reported in the literature [48,57–60]. This decrease is mainly due to challenges in fiber impregnation, void formation, and non-uniform fiber distribution within the matrix. Table 2.3 summarizes the effects of discontinuous fiber addition on tensile strength, demonstrating that, unlike traditional processing methods, 3D printing with discontinuous fibers presents significant challenges in fiber impregnation and void formation. These factors negatively impact mechanical performance, often resulting in lower tensile strength than neat PLA composites. Without proper fiber surface treatment or optimization of printing parameters, the mechanical benefits of discontinuous fibers in reinforcing biocomposites may be limited.

Table 2.3 - Mechanical properties of DFRTPCs using natural fibers.

Material	**Fiber content (wt%)**	**Tensile strength (MPa)**	**Reference**
PLA-Agave	0-10	51.0 (0 wt%) to 28.0 (10 wt%)	[57]
PLA-Kenaf	0-7	56.3 (0 wt%) to 11.8 (7 wt%)	[48]
PLA-Kenaf	0-2.5	49.9 (0 wt%) to 39.8 (2.5wt%)	[58]
PLA-Sugarcane	0-15	64.2 (0 wt%) to 45.3 (15wt%)	[61]
PLA-Rubber	0-20	56.4 (0 wt%) to 34.3 (20 wt%)	[59]
PLA-Soybean	0-10	36.4 (0 wt%) to 21.5 (10 wt%)	[60]

2.4.3 Continuous Natural Yarn-Reinforcement

CNFRTPCs are advanced materials in which continuous natural fibers in yarn format are embedded within a thermoplastic matrix to create composite structures via FFF. These materials utilize the mechanical properties of natural fibers, providing effective strength, stiffness, and enhanced load transfer due to the alignment of the yarn along the composite's length, allowing fiber distribution in optimal load-bearing directions.

The primary CNFRTPCs incorporate continuous natural yarns from fibers such as flax, ramie, sisal, jute, pineapple, and hemp. These fibers provide a strong, sustainable reinforcement, with each type offering distinct mechanical advantages suited to specific performance requirements. For example, Flax/PLA has demonstrated notable effects, achieving an Elastic Modulus of 23.3 GPa and tensile strengths reaching 253.7 MPa, as documented by Le Duigou et al. [62]. These value improvements provide CNFRTPCs as competitive alternatives to traditional synthetic composites in fields requiring lightweight, durable, and sustainable materials. From a production perspective, CNFRTPCs, with fiber volume fractions approaching 50% and yarn diameters up to 3 mm, show considerable potential for large-scale manufacturing. The use of continuous natural fibers enables high throughput and substantial mechanical performance, making these composites viable for industrial applications with high flow rates. Table 2.4 summarizes the main properties of biocomposites with continuous natural yarns found in the literature.

Table 2.4 - Mechanical properties of 3D printed biocomposites.

Composite (type of yarn and matrix)	**CNFRTPCs Method**	**Yarn**	**Fiber Volumetric Fraction, Vf (%)**	**Mechanical properties (longitudinal of unidirectional printing)**			**References**
				Young’s modulus (GPa)	**Ultimate tensile strength (MPa)**	**Strain at break (%)**	
Flax/PLA	SF	68 tex	30.4	23.3	253.7	1.67	[62]
Ramie/PLA	IN	Φ = 0.35 mm	N.D.	N.D.	86.4	N.D.	[63,64]
Pineapple leaf/PLA	IN	Φ = 0.1 mm	N.D.	N.D.	96.8	0.21	[65]
Jute/PLA	IN	250 tex	6.1	N.D.	57.1	0.25	[66]
Sisal/PLA	IN	Φ = 1.4-2.0mm 1800 tex	34.8-48.2	4.0	71.6	N.D.	[16]
Ramie/PLA		Φ = 0.7-1.3mm 330 tex	10.8-18.3	3.8	57.2	N.D.	
Jute/PLA		Φ = 0.5-1.2mm 310 tex	12.5-21.8	4.3	62.8	N.D.	
Flax/PA 6	IN	Φ = 1.4-1.8mm 26 tex	15.0-22.0	5.7	82	N.D.	[67]
Flax/PLA	ON	Φ = 0.50mm 68 tex	10.6-36.7	2.9	89	N.D.	[68,69]
Hemp/PLA	ON	557 tex	33.3	15.2	137.2	1.4	[70]

Flax/PLA	ON	Φ = 0.35mm 105 tex	22.0	9.2	123	1.7	[71]

SF - Semi-finished filament; IN - In-situ impregnation; ON - Out-of-nozzle printing; Φ – Diameter; N.D - Not declared

According to Pervaiz et al. [72], there are three main types of fiber incorporation techniques: Semi-finished filament (SF), In-situ impregnation (IN), and out-of-nozzle printing (ON) (Figure 2.5). Each method offers distinct advantages in terms of adhesion, distribution, and production within the printed structure, which ultimately affects the overall performance characteristics of the final composite.

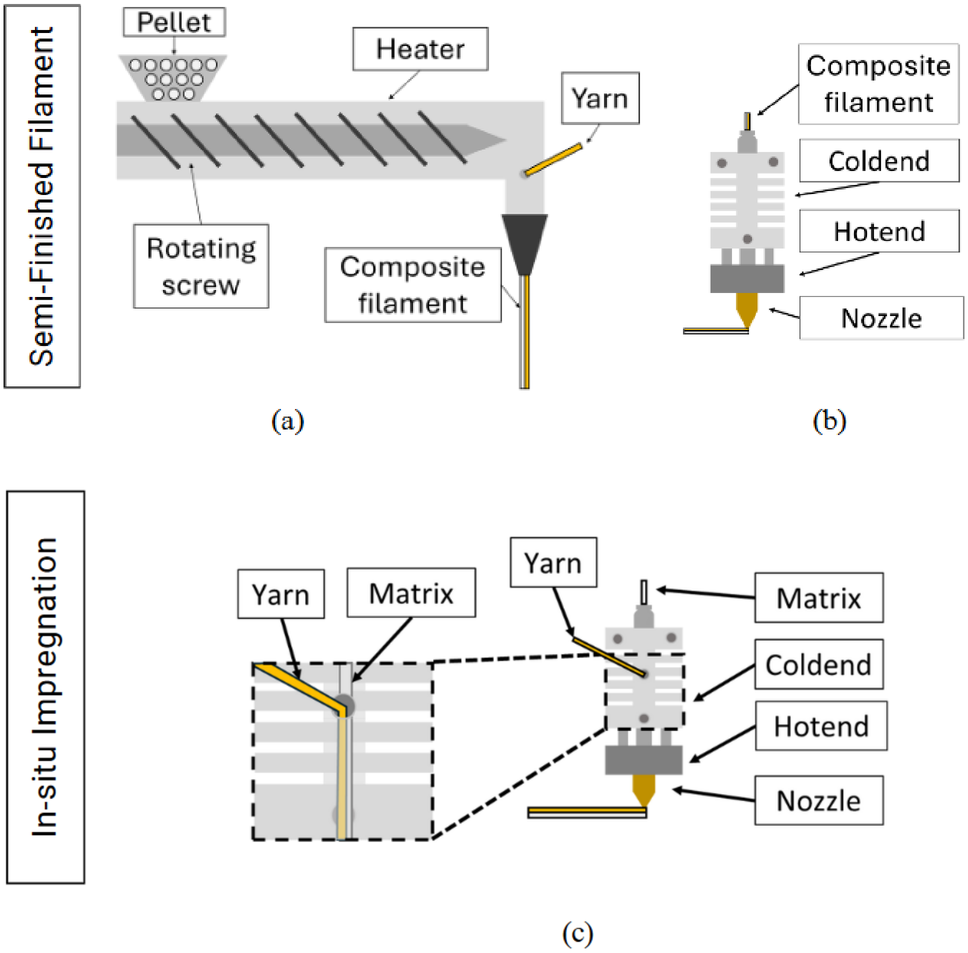

(a) (b)

(c)

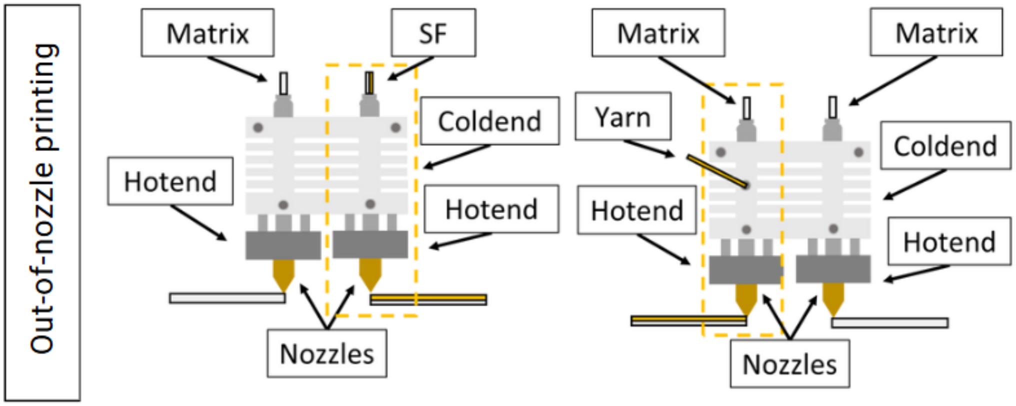

(d)

Figure 2.5 - CNFRTPCs process: (a) SF Filament fabrication's schematic process, (b) SF printing's schematic process, (c) In-situ impregnation process, (d) Out-of-nozzle schematic drawing possibilities.

2.4.3.1 Semi-finished filament (SF)

A SF is a composite filament made by combining fibers and a matrix, where the fiber is pre-embedded in the matrix, resulting in a ready-to-use composite filament compatible with conventional printers, as it requires no modifications [72]. However, this method is limited in terms of material variety and fiber volume content. Moreover, adding fiber to the filament increases its stiffness, making storage challenging, especially when stiff fibers are used [73].

The production of the SF filaments starts with a screw extruder, which heats polymer pellets until they melt. The extruder consists of a single or twin rotating screw within a stationary barrel, divided into three distinct zones: feed, compression, and metering [47]. As the polymer transitions through these zones, it melts and is subsequently pushed through a specially designed nozzle that incorporates a continuous yarn feed, resulting in a composite filament [68]. Table 2.5a and 2.5b schematize the SF filament fabrication process.

Le Duigou et al. [62] and Fruleux et al. [74,75] reported on SF filaments using 68 tex flax yarn and PLA matrix to fabricate composite filaments, later 3D printed with a 0.6 mm nozzle. Le Duigou et al. [62] investigated this innovative method to enhance the mechanical properties of biocomposites in 3D printing. With a fiber mass fraction of 34.5%, the authors achieved a modulus of elasticity of 23.3 GPa along the main fiber axis and a maximum tensile strength of 253.7 MPa.

On the other hand, Fruleux et al. [74] explored the effect of matrix stiffness on the swelling of 3D-printed continuous flax fiber-reinforced biocomposites, a factor often considered a drawback for structural applications. However, the study revealed that this hydroexpansion mechanism could be leveraged for the development of Hygromorph BioComposites (HBC), which respond to water absorption by changing shape. The findings showed that increased matrix stiffness reduces water absorption, hydroexpansion, and the evolution of elastic properties due to the constraining effect it has on the fibers. Conversely, lower matrix stiffness leads to greater hydroexpansion.

2.4.3.2 In-situ impregnation (IN)

In the IN method, fiber is directly compounded into the polymer matrix during 3D printing (Table 2.5c). This integration occurs within the printhead, where the fiber is drawn by friction through an inlet hole or an auxiliary entrance in the coldend, leading into the deposition nozzle [72,73]. This approach allows for adjusting the fiber volume ratio and enables 3D printing of both pure polymer and fiber-reinforced parts. However, IN requires special print head modifications and is more likely to clogging [16,72]. This method is the most documented in the literature, and has been adapted for various natural fibers, including flax [67,76], pineapple [65], sisal [16,32], ramie [16,32,63], and jute [16,32,66].

To the best of the authors' knowledge, the first reported study using CNFRTPCs was conducted by Matsuzaki et al. [66]. They adapted a 3D printing nozzle to allow direct fiber insertion into the internal nozzle, where the thermoplastic matrix impregnated the fiber. Synthetic carbon fiber, consisting of 24,000 filaments, and 250 Tex jute fiber were used, with a 1.4 mm diameter nozzle enabling thicker carbon fiber integration. While the carbon fiber significantly increased tensile strength to 185.2 MPa, the jute fiber showed no notable strength improvement (σmax = 57.1 MPa), likely due to its low fiber volume fraction (Vf = 6.1%) and relatively low stiffness.

Focusing on further improving the mechanical properties of 3D-printed polymers with natural CNFRTPCs, Cheng et al. [63,64,77] conducted a series of studies investigating the behavior of 3D-printed biocomposites reinforced with continuous ramie yarns with a diameter of 0.35 mm, using an IN method. In their initial work, dry twisted ramie fibers served as reinforcement for a PLA matrix, revealing that the interfacial properties between deposited layers and between ramie yarn and PLA significantly influenced the mechanical performance. The biocomposites achieved an optimal tensile strength of 86.4 MPa with low porosity and strong interlayer bonding [63]. In a subsequent study, they examined the penetration behaviour of biocomposites with woven-like and non-woven-like architectures, showing that woven-like structures increased energy absorption by 31.2% and maximum penetration force by 18% compared to non-woven configurations [64]. Finally, Cheng et al. [77] explored the quasi-static compression behaviour and shape memory effect of continuous ramie fiber-reinforced biocomposite corrugated structures (CFCSs). They found improvements in compressive strength and energy absorption with decreased fiber volume fraction and continuous ramie yarn. Additionally, they introduced shape memory capabilities for these structures, highlighting their potential in lightweight, programmable smart systems.

Moreover, Terekhina et al. [67] combined 3D printing continuous bleached textile flax yarn/polyamide 6 (PA6) composites using FFF with IN method. The study evaluated the effect on Young's modulus and tensile strength of three fiber orientation strategies (0°, 90°, and ±45°). The results demonstrated significant mechanical improvements, with tensile modulus and strength (σmax=82 MPa) increasing by 9 times and 2.4 times, respectively, compared to neat PA6.

Santos et al. [16] focused on enhancing additive manufacturing by developing a larger-diameter nozzle head and modifying the FFF hotend to enable IN of various natural fibers, including jute, ramie, and sisal, into a PLA matrix. This modification facilitated the production of bio-based filaments with diameters up to 3 mm. The incorporation of continuous yarn reinforcements led to significant improvements in both the strength and stiffness of the 3D-printed composites, with increases up to 28.6%

and 28.9%, respectively compared to the neat PLA matrix. The fiber content reached up to 48.2%, contributing to a substantial reduction in polymer consumption. Additionally, Suteja et al. [65] investigated the mechanical properties of 3D-printed composites reinforced with continuous pineapple leaf fiber (0.1 mm yarn diameter) in a PLA matrix. The study demonstrated that including continuous pineapple leaf fiber significantly enhanced the tensile strength of the composite, without increasing the printing time compared to pure PLA. However, the authors noted that the composite exhibited lower elongation than the pure PLA.

2.4.3.3 Out-of-nozzle printing

The ON method (Table 2.5d) uses two nozzles: one to extrude the main polymer and the other to deposit the reinforcement material, which can be introduced through either the SF method [68,69] or the IN method [70]. This approach is highly versatile, allowing various fiber types and matrix materials to be used [72], thus enabling enhanced customization and performance in FFF-manufactured composites.

Zhang et al. [68,69] proposed a hybrid 3D printing method combining pure polymer (PLA) with CNFRTPCs using flax fiber pre-impregnated filaments (i.e. SF method). To overcome FFF limitations, such as poor interlayer adhesion and limited mechanical properties, Zhang et al. [68] developed a path-planning algorithm to position CNFRTPC filaments along both axial and radial directions in polymer-based parts. Applied to pipe components, this method significantly improved mechanical performance, with improvements of 250 N in compression, 500 N in tensile strength, and 190 N in bending for a 0.5 mm yarn diameter. The feasibility of this approach was demonstrated using a five-axis, dual-nozzle 3D printer. In a related study, Zhang et al. [69] addressed additional challenges of FFF, such as the need for support structures and unfavorable surface quality. By manufacturing continuous natural fiber prepreg filaments and employing curved path planning, the five-axis printing process improved surface quality and mechanical properties. Compared to PLA, the tensile strength and modulus of CFFRP parts increased by 89% and 73%, while flexural strength and modulus rose by 211% and 224%. Additionally, the curved slicing method enhanced the maximum bending force and stiffness by 39% and 115%, respectively, demonstrating the potential of these methods for high-performance applications.

Ginoux et al. [70] investigated the ON method, combining a PLA matrix with CNFRTPCs using hemp yarn as the reinforcement material, introduced through one of the nozzles via the IN method. They compared hemp yarn-reinforced biocomposites with a hemp/PLA hybrid yarn prepared through commingling, which demonstrated a higher impregnation rate, reduced void content, better fiber alignment, and a more homogeneous constituent distribution, resulting in significantly improved mechanical properties and a more brittle behavior compared to the pure hemp yarn biocomposite. The hybrid yarn also showed superior performance with a lower fiber fraction, highlighting the importance of fiber impregnation and volume fraction. Similarly, Wu et al. [71] explored damage and fracture mechanisms in biobased composites reinforced with continuous flax fibers, also manufactured via the ON method. This study focused on the impact of different fiber orientations on mechanical behavior, revealing that the primary damage mechanism was fiber rupture, accompanied by transverse cracks in the polymer. In contrast, composites with fibers oriented at 45° and 90° exhibited premature fiber/matrix interface debonding. These findings emphasize the relationship between damage mechanisms, deposition strategies, and defects in printed composites, contributing to a deeper understanding of their mechanical properties and supporting optimization for high-performance applications.

2.5 Effects of printing parameters on the properties of CNFRTPCs

2.5.1 Printing parameters

The printing parameters of CNFRTPCs in the FFF process are crucial in determining the quality and structural integrity of the final 3D-printed components. Structural integrity is verified through the assessment of void size, surface roughness (Ra), dimensional accuracy, and the precise deposition of the fiber within the matrix without or with minimal delamination. The FFF process is primarily governed by three key printer parameters: nozzle temperature, flow rate, and printing speed. The nozzle temperature directly affects the processability of the thermoplastic matrix, ensuring that it reaches an optimal viscosity for proper extrusion without degrading the material [16].

Bed temperature, on the other hand, plays a critical role in enhancing the adhesion of the composite to the printing surface and reducing shrinkage caused by uneven cooling. Printing speed affects the total print time and final material quality, as faster speeds may hinder fiber impregnation and compromise the composite's structural performance [78].

Recent studies, such as that conducted by Cheng et al. [63], have shown that variations in printing parameters - such as increased matrix flowability, higher forming pressure, and longer impregnation times for fibers like ramie - can significantly alter the microstructure of biocomposites. These findings underscore the need for further investigation into the printing properties of CNFRTPCs, particularly to optimize fiber impregnation and reduce issues such as porosity and fiber misalignment.

Additionally, the properties of the 3D printed composite are influenced by various factors, including the type of thermoplastic filament, the natural fiber reinforcement, yarn diameter, fiber length, and fiber content. Factors inherent to the printing process, such as material adhesion, layer geometry, printing speed, and layer geometry, are also critical in determining the mechanical performance and reliability of the 3D-printed part [79]. These complexities highlight the necessity for a more comprehensive understanding of how the interactions between natural fibers and thermoplastic matrices affect the structural performance and scalability of CNFRTPCs for applications in industries like construction, automotive, and aerospace. Table 2.5 shows the main printing properties of CNFRTPC studies.

Table 2.5 - Printing properties of CNFRTPCs.

Biocomposite	**Yarn**	**Volumetric fraction, V_f (%)**	**Nozzle diameter (mm)**	**Nozzle temperature (°C)**	**Porosity (%)**	**Layer width (mm)**	**Layer height (mm)**	**Speed (mm/min)**	**References**
Flax/PLA	68 tex	30.4	0.60	195	3.2	0.25	-	360	[62]
Flax/PLA	68 tex	32.6	0.60	190	2.1	-	0.2	420	[74]
Flax/PBS		29.1		135	4.1		0.15		
Flax/PBSA		29.2		145	3.7		0.15		
Flax/PBAT		33.0		145	3.7		0.15		
Ramie/PLA	0.35 mm 36 Nm/2R	-	1.30	190-220	1.8-7.1	0.30-0.60	-	100-500	[63,64]
Pineapple leaf/PLA	Φ = 0.1 mm	-	0.40	200-210	-	0.40	0.50	900-1500	[65]
Jute/PLA	250 tex	6.1	1.40	210	-	-	-	60	[66]

Flax/PLA	67 tex	25	0.80	200	1.1	0.80	0.25	240	[76]
Sisal/PLA	Φ = 1.4-2.0mm 1800 tex	34.8-48.2	2.1	200	11.7	3.0	1.5	600	[16]
Ramie/PLA	Φ = 0.7-1.3mm 330 tex	10.8-18.3							
Jute/PLA	Φ = 0.5-1.2mm 310 tex	12.5-21.8							
Ramie/PLA	24Nm/2R	-	1.3	205	-	0.3-0.5	0.3-1.2	300	[80]
Flax/PA 6	Φ = 1.4-1.8mm 26 tex	15.0-22.0	0.6	225	8-14	0.55	0.3	600	[67]
Banana/PLA	Φ = 0.19mm	-	1.0	193-205	0.6-9.5	2.4	1.0	180-321	[81]
Flax/PLA	Φ = 0.50mm 68 tex	10.6-36.7	0.8-1.2	200	-	0.5	0.35	100	[68,69]
Hemp/PLA	557 tex	33.3	0.8	230	14.1-25.7	0.8	0.4	900	[70]

Flax/PLA	Φ = 0.35mm 105 tex	21	0.8	205	8	-	0.35		[71]

2.5.1.1 Nozzle characteristics

The nozzle plays a crucial role in AM, as it directly influences the final properties of the 3D printed material. In FFF, the nozzle is heated to the melting temperature of the thermoplastic matrix, which is extruded and deposited onto the print bed. For CNFRTPCs and large-scale applications, factors such as printing temperature, nozzle size, and geometry are especially influential.

The nozzle geometry defines the capabilities and limitations of the 3D printing process. Narrow nozzles (below 0.6 mm) offer better resolution but are prone to sieving and clogging, as the restricted size can lead to uneven material flow and defects in the printed sample. Moreover, narrow nozzles may struggle or fail to accommodate fiber-reinforced filaments, particularly those in rope or thread form, increasing the likelihood of clogging during extrusion [82]. In contrast, wider nozzles tend to deposit excessive molten material, making precise detail challenging and often resulting in deformed and irregular final shapes. These nozzles also increase the risk of void formation and bubble generation, which can compromise the mechanical integrity of the 3D printed parts. Chen et al. [83] further demonstrated that increasing nozzle width reduces surface flatness, negatively affecting the printed material's overall quality. Additionally, Balderrama-Armendariz et al. [84] observed that nozzles with square extrusion geometry can enhance the bonding between 3D printed rasters by generating larger contact areas, reducing air gaps, and minimizing corner shrinkage at the layer level, ultimately improving surface quality.

Regarding temperature, the nozzle plays a critical role in directing the heated material from the hotend to the deposition bed, affecting the printing quality. The filament should be free of voids and defects, and its composition must be thoroughly examined for AM, focusing on its quantity, morphology, and distribution. Effective methods for this assessment include scanning electron microscopy imaging and dissolving the biocomposite in a solvent to isolate the natural fillers through filtration [85]. Additionally, selecting the appropriate filament is critical, as its characteristics directly impact reinforcement capabilities. Whether the filament is pre-embedded as a composite or introduced into the print head, the continuous fiber is exposed to the melting temperature of the thermoplastic polymer (Table 2.1). This exposure is particularly significant for vegetable fibers, which typically have lower degradation temperatures (Table 2.2). Therefore, it is essential to assess whether the polymer's melting temperature will compromise the integrity of the natural materials involved.

The working temperature of PLA influences fiber performance, as vegetable fibers degrade at high temperatures [33], while low temperatures reduce the mechanical properties of PLA [86]. Santos et al. [16] noted that, at lower temperatures, fiber impregnation by the matrix is limited due to the higher viscosity of PLA, which restricts its penetration into natural yarns. Conversely, elevated printing temperatures enhanced the fluidity of the thermoplastic matrix, promoting greater matrix penetration into the interlayer regions. This increased interfacial interaction, thereby reducing porosity [63]. However, if the temperature exceeds a certain threshold, the fiber may degrade, potentially leading to the formation of bubbles expelled from within larger yarns [16]. Figure 2.6 summarizes the main findings about the effects of the nozzle in the CNFRTPCs printing.

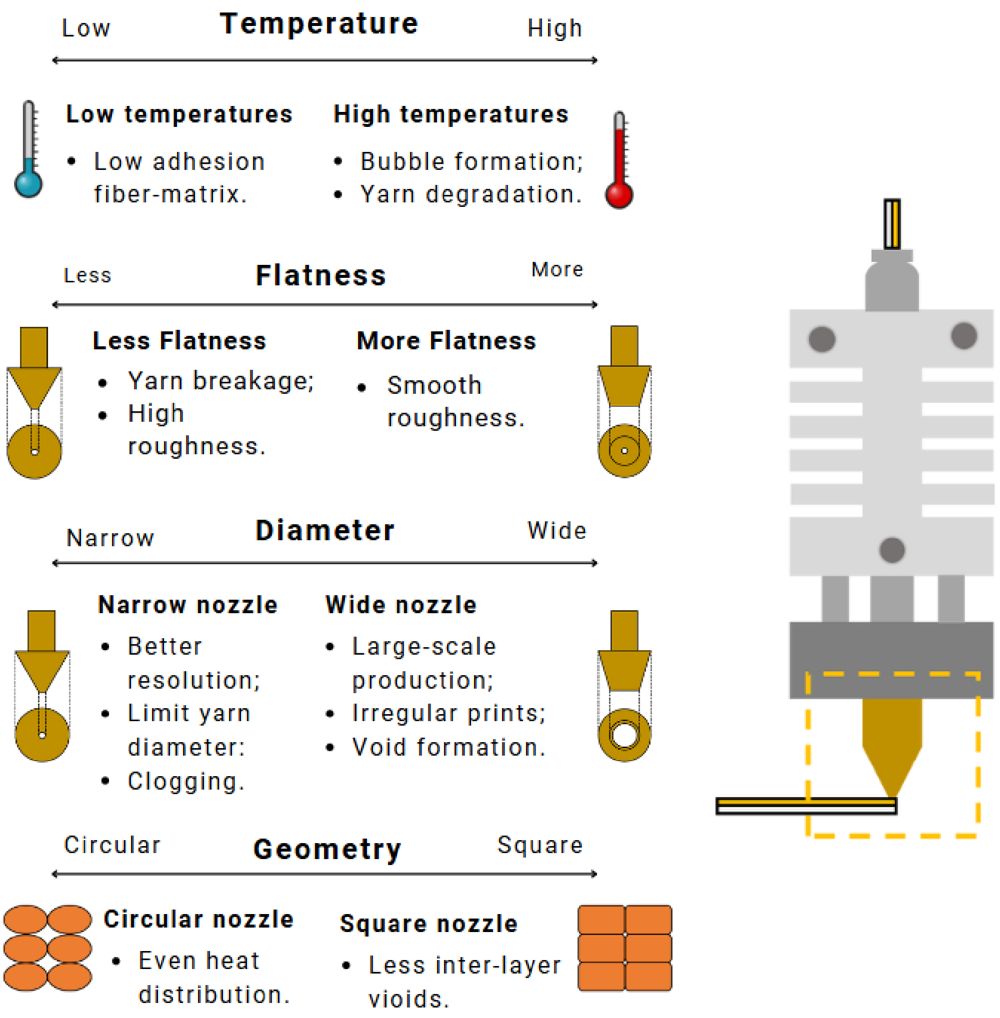

Figure 2.6 - Nozzle effects in the printing.

2.5.1.2 Printing speed, flow, and curvature

The printing speed is essential when dealing with CNFRTPCs, as it influences the adhesion of the deposited filament to the platform or structure. This speed is constrained by the maximum velocity required for the deposited filament to adhere effectively to the build plataform or structure. Proper adhesion is essential to ensure that each layer maintains its intended position during the printing process. If the speed exceeds this limit, the filament may not have sufficient time to bond with the surface, potentially leading to misalignment or detachment.

In the case of vegetable fibers, Cheng et al. [87] observed that an increase in printing speed resulted in a significant reduction in the tensile strength of ramie-reinforced composites. Similarly, Long et al. [88] optimized the printing conditions for flax-reinforced PLA composites and found that a print speed of 540 mm/min, with a volumetric fraction of 38% ± 7%, provided the best results. However, as demonstrated by Suteja et al. [65], exceeding a feed rate of 25 mm/s for pineapple leaf fibers led to fiber breakage due to excessive tension caused by nozzle movement. These findings underscore the importance of adjusting printing speed and feed rate to maintain the mechanical integrity and performance of fiber-reinforced composites.

When analyzing 3D printing path and geometry, Fruleux et al. [75] tried to determine the 3D printability and design constraints of various cellular lattice structures by analyzing the differences between the programmed and actual printing trajectories of pure PLA, short flax fiber biocomposite (FF/PLA), and continuous flax fiber/PLA biocomposites (cFF/PLA). Using a specific set of 3D printing and slicing parameters within the IN method, the authors found that curvatures below 20 mm exhibited poor adhesion, due to insufficient solidification time for the matrix between layers and increased tangential stresses relative to the bonded area Similarly, Santos et al. [16] identified adhesion issues in curved geometries using the IN method, applied to a truss structure reinforced with large-diameter yarns. The yarns tended to deviate from the intended path when subjected to multiple consecutive curves, likely due to the stiffness of the fibers and the extended cooling time required for the matrix material to solidify and gain strength. Consequently, for complex geometries, it is necessary to reduce the printing speed in curved sections and reshape curvature diameters to ensure adhesion and alignment with the designated path.

For the case of large-scale printing, speed setting is also an issue. The increase in printing speed generated a reduction in the flexural strength of composites reinforced by continuous fiber according to a study by Hu et al. [89]. In addition, Tian et al. [90] found that, for a speed increase from 100 to 600mm/min, the CNFRTPCs had a slight drop in flexural strength. They attributed this reduction to the shorter melting time of the polymer at higher speeds, which generates poor impregnation of the resin in the fiber yarns and, thus, causes high levels of voids within the composites. Figure 2.7 summarizes the main findings about the effects of printing speed, flow and curvature in the CNFRTPC printing.

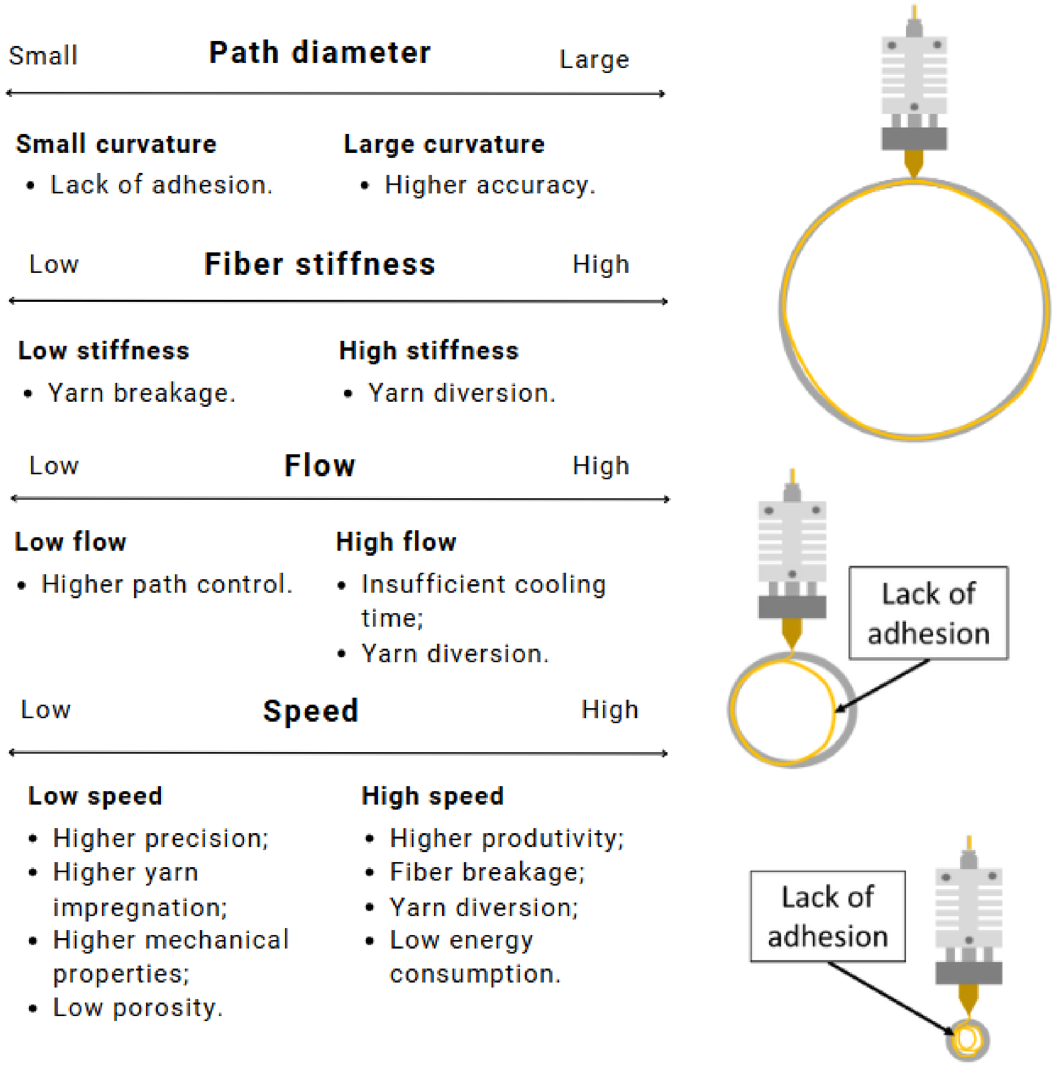

Figure 2.7 - Effects of printing speed, flow, and curvature in the CNFRTPCs printing.

25.2 Key challenges in the CNFRTPCs

2.5.2.1 Porosity

In AM, porosity is a critical issue, particularly with composite materials. Voids in these materials can be classified into three main categories: inter-filament voids, pores/bubbles, and fiber-matrix interfacial voids (Figure 2.8) [32].

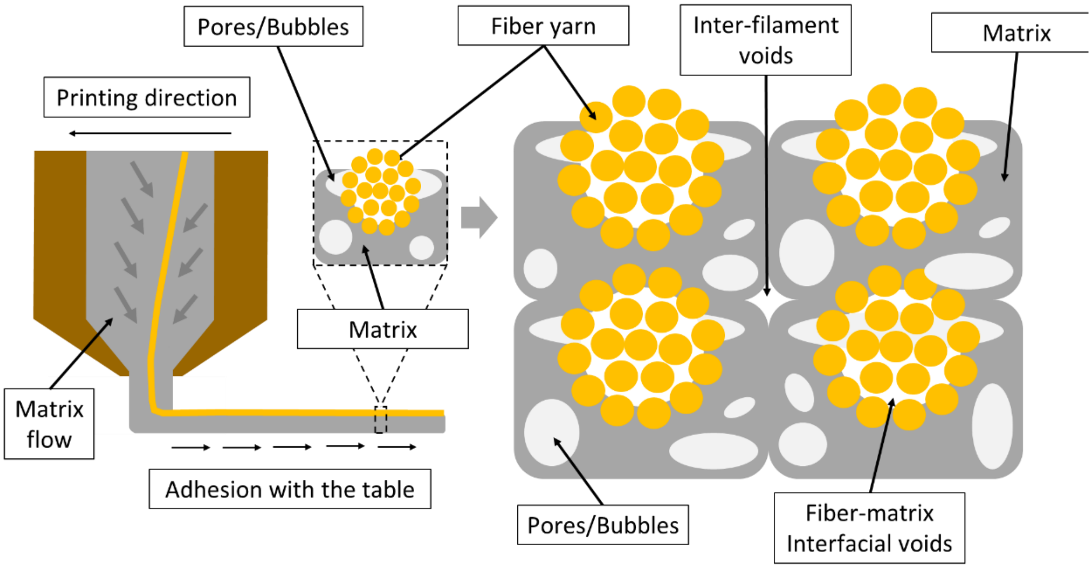

Figure 2.8 - Types of voids and effects of eccentricity in CNFRTPCs.

Bubbles arise primarily due to fluctuations in deposition speed and printing temperature. As noted by Santos and Cardoso [15], inconsistencies in these parameters can lead to uneven flow and cooling of the material, causing air entrapment within layers. Additionally, high polymer melting temperatures and larger yarn diameters contribute to increased bubble formation. In the case of thicker yarns, part of the air trapped inside the yarn is forced outward during 3D printing, leading to trapped surface bubbles as the material cools down, contributing to the overall void content. Managing the deposition parameters, including temperature control and yarn selection, is crucial to reduce the presence of bubbles, which otherwise weakens layer bonding and reduces the overall strength of the 3D printed structure.

Flow inconsistencies during the IN process also create fiber misalignment, as observed by Rivero-Romero et al. [81] and Cheng et al. [63]. The flow of the molten composite material exerts a drag force on the fibers, partially displacing them from the deposited line, leading to misalignment. This can cause adhesion issues between the yarn and the thermoplastic matrix, resulting in small interfacial gaps, often manifesting as bubbles. Furthermore, when the composite material is deposited, the wettability of the yarn is influenced by the slip velocity between the moving yarn and the molten material flow.

Inter-filament voids are primarily associated with the geometric characteristics of the printed layers, often exhibiting an ellipsoidal morphology. This shape is influenced by various factors, including the geometry of the nozzle, as previously discussed. These voids arise from incomplete interlayer adhesion during the deposition process, leading to the formation of air pockets or gaps between adjacent filaments [91]. Terekhina et al. [67] and Badouard et al. [10] highlighted that these voids typically form in triangular shapes between filaments due to the nature of the layer-by-layer deposition. Such voids are considered the primary site for porosity, negatively impacting the mechanical properties of the final printed part.

Additionally, Cai et al. [80] found that void size increases with the layer thickness and hatch spacing, with larger voids forming when thicker layers are 3D printed or with more spacing between paths, reducing overall density and mechanical performance. Therefore, controlling layer thickness and hatch spacing is another important factor in reducing the formation of voids in 3D-printed composites. Moreover, Cheng et al. [63] demonstrated that increasing the printing thickness from 0.3 mm to 0.6 mm led to a rise in porosity from 2.2% to 7.1%, while raising the printing speed from 100 mm/min to 500 mm/min raised porosity from 1.8% to 3.4%. This suggests that optimizing printing parameters is essential for minimizing void formation and ensuring high-quality 3D printing.

Fiber-matrix interfacial voids arise due to inefficient impregnation of the matrix into the fiber yarn. This phenomenon is closely linked to the geometry of the layers and the ability of the matrix material to fully penetrate the fibers during 3D printing. Le Duigou et al. [62,92] observed that porosities tend to form within the flax fiber yarn itself, rather than between the printed layers, primarily due to the inadequate compression during the printing process. Proper compression and material flow are essential for achieving good fiber-matrix adhesion, which in turn reduces the formation of voids at the interface and enhances the mechanical performance of the composite. Additionally, Cheng et al. [63] demonstrated that increasing the printing temperature from 190 °C to 220 °C reduced the average porosity from 5.6% to 1.8% due to enhanced matrix fluidity, which allowed better impregnation of the yarn. Furthermore, Matsuzaki et al. [66] reported that using a polymer filament with a diameter larger than the nozzle facilitates material flow, as the melted resin inside the nozzle generates pressure that aids in impregnating the fiber bundles. However, it is important to remember that increasing nozzle size is inversely proportional to printing resolution.

Fiber pre-treatments can also help address high void content in 3D-printed continuous fiber-reinforced composites. Long et al. [76] demonstrated that a pre-treatment for Continuous Flax Fiber Reinforced Composites (CFFRCs) significantly improved compatibility between flax fibers and thermoplastic matrix, reducing void content to below 1.1% and improving mechanical performance. This improvement was attributed to enhanced interfacial bonding between the flax yarns and the resin matrix. The mechanical properties of the 3D-printed CFFRCs were comparable to those of composites produced by traditional compression molding methods.

2.5.2.2 Fiber-matrix interface

In composites, the interface is defined as a reaction or diffusion zone where the two elements are chemically, physically, and/or mechanically integrated [93]. This interface plays a crucial role in determining the overall properties and performance of the composite material, as it influences factors such as adhesion, load transfer, and stress between materials and significantly impacts composite properties.

Continuous plant fiber reinforcements in AM often face challenges related to poor impregnation quality, primarily due to the chemical composition, surface morphology, and internal structure of natural fibers and their associated yarns [66,70,94]. Natural fibers contain hydrophilic components such as cellulose, hemicellulose, and lignin, which are incompatible with most hydrophobic polymer matrices, leading to weak interfacial bonding [95–97].

Additionally, the structural complexity within yarns, such as fiber twisting and voids, further complicates polymer matrix infiltration, reducing interface quality. According to Le Duigou et al. [62], the twisted structure of the yarns impedes complete matrix impregnation, resulting in reduced transverse cohesion within the yarn. This lack of cohesion diminishes the fiber-fiber interface area, weakening the internal bonding and ultimately compromising the mechanical performance of the composite. Therefore, treatments that reduce fiber sensitivity to moisture help limit fiber swelling, which can otherwise compromise interface integrity and lead to delamination [98].

The mechanical performance of these fiber-reinforced composites heavily depends on effective interfacial adhesion between the fibers and polymer matrix [99]. Weak bonding at the interface may cause stress concentrations, fiber pull-out, and delamination under mechanical loads, reducing the overall strength and durability of the bio-composite. Consequently, achieving optimal matrix impregnation and enhancing fiber-matrix adhesion through chemical treatments like silanization and alkalinization [100,101] or process optimization is essential to improve the structural integrity of AM-produced plant fiber composites.

2.6 Research Needs and Perspectives for the Development of CNFRTPCs

Although significant advances have been made in CNFRTPCs, key challenges remain to be addressed to enhance the practicality and efficiency of this technology, enabling its adoption in large-scale structural applications. Large-Scale Additive Manufacturing (LSAM) printing has allowed the production of more complex structures with less labor force [102]. This process made it possible to significantly reduce production time, material consumption, and labor and machinery costs. Furthermore, there is virtually no waste, as only the necessary material is used, leading to more economical, optimized, and more sustainable models [103,104]. These challenges can be outlined as follows:

2.6.1 Adhesion

The primary challenge in CNFRTPCs lies in the impregnation of natural fiber yarns and the adhesion interlayers, particularly due to the high viscosity of thermoplastics and the low chemical compatibility between natural fibers and matrices [105,106]. Consequently, potential areas of study include:

- Development of strategies for impregnating large-diameter yarns to achieve uniform fiber infiltration within the matrix material, thereby maximizing mechanical performance and structural cohesion.

- Chemical or physical treatments can enhance interfacial adhesion and improve compatibility between continuous natural yarns and the thermoplastic matrix.

- Developing techniques to improve interlayer interfaces, as fibers primarily reinforce within individual layers, necessitating strategies to enhance the bonding and mechanical integrity between adjacent layers.

2.6.2 Optimization and Production

The optimization of AM processes for CNFRTPCs involves addressing critical challenges related to production efficiency and structural performance. Achieving high printing speeds without sacrificing precision and adhesion, minimizing material waste, and enabling the fabrication of complex geometries are key areas requiring further research and development. Consequently, potential areas of focus include:

- Develop technological solutions to enhance printing speed without compromising precision and resolution in the printed components.

- Formulate strategies to optimize structural performance while minimizing material waste.

- Facilitate the production of intricate geometries by enabling complex path printing, ensuring fiber continuity and structural integrity.

2.6.3 Sustainability and end-of-life considerations

Ensuring the sustainability of CNFRTPCs involves addressing challenges related to material recycling, environmental resistance, and disposal strategies. Evaluating the long-term performance and environmental impact of these materials is critical for their adoption in sustainable applications. Consequently, potential areas of focus include:

- Analysis of the recyclability of continuous natural fibers for reuse, including the effects of multiple thermal cycles on the material's mechanical properties.

- Long-term performance evaluation of printed biocomposites under conditions such as moisture, temperature variations, and cyclic loading.

- Investigation of environmental effects on materials exposed to UV radiation, alkaline environments, and organic degradation.

- Life cycle analysis and end-of-life strategies for sustainable disposal and material recovery.

2.6.4 Large-scale production

Large-scale additive manufacturing of structural elements is an emerging research trend with the potential to revolutionize sustainable construction and industrial practices. While large-scale 3D printing with thermoplastic composites is already being implemented, it predominantly relies on systems reinforced with synthetic [107,108] or discontinuous natural fibers [109,110]. Scaling up AM processes for CNFRTPCs requires addressing challenges related to material throughput, equipment design, and fiber integration. Enhancing production capabilities while maintaining material quality and mechanical performance is critical for enabling the widespread application of this technology. Consequently, potential areas of focus include:

- Develop advancements in printing processes to enable higher fiber content while maintaining processability and mechanical performance.

- Implement high-throughput extruders capable of achieving increased material deposition rates with uniform thermoplastic heating throughout the volume.

- Design nozzles to accommodate larger diameters and multiple yarns simultaneously.

This approach aims to guide the development of research and technologies, positioning CNFRTPCs as a viable alternative for industrial-scale and high-performance applications. By combining advanced mechanical properties with a low environmental impact, these materials present a promising solution for both structural and functional applications, aligning innovation with sustainability.

2.7 Conclusions

Despite promising advancements in the quality and strength of CNFRTPCs, driven by extensive research efforts from the scientific community exploring a wide range of natural continuous fibers, such as jute, ramie, flax, sisal, hemp, and pineapple leaf, to produce environmentally friendly bio-composites, several challenges remain. The primary obstacles to improving the structural performance of CNFRTPCs are related to low adhesion between natural yarns and the matrix and issues such as high porosity, curvature defects during 3D printing, and yarn misalignment. Key factors influencing the 3D print quality of continuous natural fiber-reinforced biocomposites include matrix melting time, yarn diameter, printing speed, and nozzle temperature.

At the large-scale production level, achieving higher flow rates with larger yarn diameters remains in its early stages, as these larger flows and diameters tend to exacerbate fiber-matrix interface issues, ultimately affecting the mechanical properties and reliability of the 3D printed structures. Nevertheless, with appropriate surface treatments to enhance impregnation, the application of CNFRTPCs for large-scale use—particularly in the construction, automotive, and aerospace industries—is highly promising. The adoption of these materials is expected to significantly increase due to their potential for optimized, more sustainable structures with low ecological footprint, recyclability, and cost efficiency.

Reference

[1] Romani A, Suriano R, Levi M. Biomass waste materials through extrusion-based additive manufacturing: A systematic literature review. J Clean Prod 2023;386. https://doi.org/10.1016/j.jclepro.2022.135779.

[2] Calignano F, Mercurio V. An overview of the impact of additive manufacturing on supply chain, reshoring, and sustainability. Cleaner Logistics and Supply Chain 2023;7:100103. https://doi.org/10.1016/j.clscn.2023.100103.

[3] Holbery J, Houston D. Natural-fiber-reinforced polymer composites in automotive applications. Jom 2006;58:80–6. https://doi.org/10.1007/s11837-006-0234-2.

[4] Beserra JHN, de Melo JVA de MC, Cardoso DCT. Development of a novel 3D-printed moment connection for pultruded profiles joints. Structures 2024;60. https://doi.org/10.1016/j.istruc.2024.105850.

[5] Pilagatti AN, Atzeni E, Salmi A. Exploiting the generative design potential to select the best conceptual design of an aerospace component to be produced by additive manufacturing 2022. https://doi.org/10.21203/rs.3.rs-2330572/v1.

[6] Vecchi G, Atzeni E, Salmi A, Iuliano L. Prosthesis customization in maxillofacial surgery by means of Additive Manufacturing. Procedia CIRP 2023;118:781–6. https://doi.org/10.1016/j.procir.2023.06.134.

[7] Romani A, Levi M. Large-Format Material Extrusion Additive Manufacturing for Circular Economy Practices: A Focus on Product Applications with Materials from Recycled Plastics and Biomass Waste. Sustainability 2024;16:7966. https://doi.org/10.3390/su16187966.

[8] Mohanty AK, Misra M, Hinrichsen G. Biofibres, biodegradable polymers and biocomposites: An overview. Macromol Mater Eng 2000;276–277:1–24. https://doi.org/10.1002/(SICI)1439-2054(20000301)276:1<1::AID-MAME1>3.0.CO;2-W.

[9] Wang K, Addiego F, Laachachi A, Kaouache B, Bahlouli N, Toniazzo V, et al. Dynamic behavior and flame retardancy of HDPE/hemp short fiber composites: Effect of coupling agent and fiber loading. Compos Struct 2014;113:74–82. https://doi.org/10.1016/j.compstruct.2014.03.009.

[10] Badouard C, Traon F, Denoual C, Mayer-Laigle C, Paës G, Bourmaud A. Exploring mechanical properties of fully compostable flax reinforced composite filaments for 3D printing applications. Ind Crops Prod 2019;135:246–50. https://doi.org/10.1016/j.indcrop.2019.04.049.

[11] Mohanty AK, Misra M, Drzal LT. Natural fibers, biopolymers, and biocomposites. Taylor & Francis; 2005.

[12] Tekinalp HL, Kunc V, Velez-Garcia GM, Duty CE, Love LJ, Naskar AK, et al. Highly oriented carbon fiber-polymer composites via additive manufacturing. Compos Sci Technol 2014;105:144–50. https://doi.org/10.1016/j.compscitech.2014.10.009.

[13] ASTM. ASTM 52900 Additive manufacturing - General principles - Terminology 2021.

[14] ASTM. ASTM International. ISO/ASTM52900 — 15 Standard Terminology for Additive Manufacturing — General Principles — Terminology. 2015.

[15] Santos N V., Cardoso DCT, Rodrigues GJO. Characterization of Green Composites for Social Housing. Dissertation (Master in Civil Engineering). Pontifical Catholic University of Rio de Janeiro - PUC-Rio, 2021.

[16] Santos N V., Cardoso DCT. 3D printing of vegetable yarn-reinforced polymer components. J Clean Prod 2023;415. https://doi.org/10.1016/j.jclepro.2023.137870.

[17] Sing SL, Yeong WY. Process–Structure–Properties in Polymer Additive Manufacturing. Polymers (Basel) 2021:13–4.

[18] Ngo TD, Kashani A, Imbalzano G, Nguyen KTQ, Hui D. Additive manufacturing (3D printing): A review of materials, methods, applications and challenges. Compos B Eng 2018;143:172–96. https://doi.org/10.1016/j.compositesb.2018.02.012.

[19] Mechtcherine V, Buswell R, Kloft H, Bos FP, Hack N, Wolfs R, et al. Integrating reinforcement in digital fabrication with concrete: A review and classification framework. Cem Concr Compos 2021;119. https://doi.org/10.1016/j.cemconcomp.2021.103964.

[20] Turner BN, Strong R, Gold SA. A review of melt extrusion additive manufacturing processes: I. Process design and modeling. Rapid Prototyp J 2014;20:192–204. https://doi.org/10.1108/RPJ-01-2013-0012.

[21] Pervaiz S, Qureshi TA, Kashwani G, Kannan S. 3D Printing of Fiber-Reinforced Plastic Composites Using Fused Deposition Modeling: A Status Review. Materials 2021;14:4520. https://doi.org/10.3390/ma14164520.

[22] Wojtyła S, Klama P, Baran T. Is 3D printing safe? Analysis of the thermal treatment of thermoplastics: ABS, PLA, PET, and nylon. J Occup Environ Hyg 2017;14:D80–5. https://doi.org/10.1080/15459624.2017.1285489.

[23] Lay M, Thajudin NLN, Hamid ZAA, Rusli A, Abdullah MK, Shuib RK. Comparison of physical and mechanical properties of PLA, ABS and nylon 6 fabricated using fused deposition modeling and injection molding. Compos B Eng 2019;176. https://doi.org/10.1016/j.compositesb.2019.107341.

[24] Johnson GA, French JJ. Evaluation of Infill Effect on Mechanical Properties of Consumer 3D Printing Materials. vol. 3. 2018.

[25] Zhao X, Copenhaver K, Wang L, Korey M, Gardner DJ, Li K, et al. Recycling of natural fiber composites: Challenges and opportunities. Resour Conserv Recycl 2022;177. https://doi.org/10.1016/j.resconrec.2021.105962.

[26] Nunna S, Chandra PR, Shrivastava S, Jalan AK. A review on mechanical behavior of natural fiber based hybrid composites. Journal of Reinforced Plastics and Composites 2012;31:759–69. https://doi.org/10.1177/0731684412444325.

[27] Castoldi RS, Silva FA, Souza LMS. Influence of surface modifications on sisal fiber durability and interface bond towards cement-based matrices. Pontifical Catholic University of Rio de Janeiro, 2023.

[28] Bcomp. Mercedes-AMG GT4 race cars with natural fibre composite bumpers 2022. https://www.bcomp.com/news/mercedes-amg-gt4-race-cars-with-natural-fibre-composite-bumpers/ (accessed September 4, 2024).

[29] JECcomposites. High-performance YCOM S1-X eSkootr n.d. https://www.jeccomposites.com/news/spotted-by-jec/high-performance-ycom-s1-x-eskootr/ (accessed September 4, 2024).

[30] Pérez MG, Bodea S, Dambrosio N, Rogen B, Zechmeister C, Rinderspacher K, et al. livMatS Pavilion. 2021 n.d.

[31] Bcomp. Greenboats Flax 27. Bcomp 2020. https://www.bcomp.com/news/greenboats-flax27/ (accessed September 4, 2024).

[32] dos Santos N V., Cavalcanti DKK, Neto JSS, de Queiroz HFM, Banea MD, Cardoso DCT. Analysis of voids, interfacial and thermal properties of additively manufactured continuous natural fiber-reinforced biocomposites. Progress in Additive Manufacturing 2024. https://doi.org/10.1007/s40964-024-00913-5.

[33] Neto JSS, Lima RAA, Cavalcanti DKK, Souza JPB, Aguiar RAA, Banea MD. Effect of chemical treatment on the thermal properties of hybrid natural fiber-reinforced composites. J Appl Polym Sci 2019;136:1–13. https://doi.org/10.1002/app.47154.

[34] Neto JSS, Lima RAA, Cavalcanti DKK, Souza JPB, Aguiar RAA, Banea MD. Effect of chemical treatment on the thermal properties of hybrid natural fiber-reinforced composites. J Appl Polym Sci 2019;136:1–13. https://doi.org/10.1002/app.47154.

[35] Wambua P, Ivens J, Verpoest I. Natural fibres: Can they replace glass in fibre reinforced plastics? Compos Sci Technol 2003;63:1259–64. https://doi.org/10.1016/S0266-3538(03)00096-4.

[36] Mohanty AK, Misra M, Drzal LT. Natural fibers, biopolymers, and biocomposites. Taylor & Francis; 2005.

[37] Morrison WH, Archibald DD, Sharma HSS, Akin DE. Chemical and physical characterization of water- and dew-retted flax fibers. Ind Crops Prod 2000;12:39–46. https://doi.org/10.1016/S0926-6690(99)00044-8.

[38] Martin AR, Martins MA, Da Silva ORRF, Mattoso LHC. Studies on the thermal properties of sisal fiber and its constituents. Thermochim Acta 2010;506:14–9. https://doi.org/10.1016/j.tca.2010.04.008.

[39] Xia X, Shi X, Liu W, Zhao H, Li H, Zhang Y. Effect of flax fiber content on polylactic acid (PLA) crystallization in PLA/flax fiber composites. Iranian Polymer Journal (English Edition) 2017;26:693–702. https://doi.org/10.1007/s13726-017-0554-9.

[40] Dong Z e., Ding RY, Zheng L, Zhang X, Yu CW. Thermal properties of flax fiber scoured by different methods. Thermal Science 2015;19:939–45. https://doi.org/10.2298/TSCI130329005Z.

[41] American society for testing and materials. Journal of Synthetic Lubrication 1985;2:166–74. https://doi.org/10.1002/jsl.3000020206.

[42] Jones RM. Mechanics Of Composite Materials 1999:519.

[43] Bentur A, Mindess S. Fibre Reinforced Cementitious Composites (Routledge, Ed.). (2nd ed.). CRC Press; 1990. https://doi.org/https://doi.org/10.1201/9781482267747.

[44] Khoshnevis B. Automated construction by contour crafting - Related robotics and information technologies. Autom Constr 2004;13:5–19. https://doi.org/10.1016/j.autcon.2003.08.012.

[45] Santos RD dos, Neves ALA, Pereira LGR, de Araujo GGL, Voltolini TV, Costa CTF, et al. Sisal Defibration Co-Products as an Alternative in Ruminant Feeding. 2013.

[46] Fontana L, Giubilini A, Arrigo R, Malucelli G, Minetola P. Characterization of 3D Printed Polylactic Acid by Fused Granular Fabrication through Printing Accuracy, Porosity, Thermal and Mechanical Analyses. Polymers (Basel) 2022;14. https://doi.org/10.3390/polym14173530.

[47] Ahmad MN, Ishak MR, Mohammad Taha M, Mustapha F, Leman Z. A Review of Natural Fiber-Based Filaments for 3D Printing: Filament Fabrication and Characterization. Materials 2023;16. https://doi.org/10.3390/ma16114052.

[48] Shahar FS, Hameed Sultan MT, Safri SNA, Jawaid M, Abu Talib AR, Basri AA, et al. Physical, thermal and tensile behaviour of 3D printed kenaf/PLA to suggest its usability for ankle–foot orthosis – a preliminary study. Rapid Prototyp J 2022;28:1573–88. https://doi.org/10.1108/RPJ-08-2021-0207.

[49] Tao Y, Li P, Zhang J, Wang S, Shi SQ, Kong F. A review of fused filament fabrication of continuous natural fiber reinforced thermoplastic composites:

Techniques and materials. Polym Compos 2023;44:8200–22. https://doi.org/10.1002/pc.27477.

[50] Durfee WK, Iaizzo PA. Medical applications of 3D printing. Engineering in Medicine: Advances and Challenges, Elsevier; 2018, p. 527–43. https://doi.org/10.1016/B978-0-12-813068-1.00021-X.

[51] Pringle AM, Rudnicki M, Pearce JM. Wood furniture waste-based recycled 3-D printing filament. For Prod J 2018;68:86–95. https://doi.org/10.13073/FPJ-D-17-00042.

[52] Yang F, Zeng J, Long H, Xiao J, Luo Y, Gu J, et al. Micrometer copper-zinc alloy particles-reinforced wood plastic composites with high gloss and antibacterial properties for 3d printing. Polymers (Basel) 2020;12. https://doi.org/10.3390/polym12030621.

[53] Sanandiya ND, Ottenheim C, Phua JW, Caligiani A, Dritsas S, Fernandez JG. Circular manufacturing of chitinous bio-composites via bioconversion of urban refuse. Sci Rep 2020;10. https://doi.org/10.1038/s41598-020-61664-1.

[54] Romani A, Rognoli V, Levi M. Design, materials, and extrusion-based additive manufacturing in circular economy contexts: From waste to new products. Sustainability (Switzerland) 2021;13. https://doi.org/10.3390/su13137269.

[55] Biagi F, Giubilini A, Veronesi P, Nigro G, Messori M. Valorization of Winery By-Products as Bio-Fillers for Biopolymer-Based Composites. Polymers (Basel) 2024;16. https://doi.org/10.3390/polym16101344.

[56] Ahmed W, Alnajjar F, Zaneldin E, Al-Marzouqi AH, Gochoo M, Khalid S. Implementing FDM 3D printing strategies using natural fibers to produce biomass composite. Materials 2020;13. https://doi.org/10.3390/ma13184065.

[57] Figueroa-Velarde V, Diaz-Vidal T, Cisneros-López EO, Robledo-Ortiz JR, López-Naranjo EJ, Ortega-Gudiño P, et al. Mechanical and physicochemical properties of 3d-printed agave fibers/poly(Lactic) acid biocomposites. Materials 2021;14. https://doi.org/10.3390/ma14113111.

[58] Haryati A, Razali N, Petrů M, Taha M, Muhammad N, Ilyas RA. Effect of chemically treated kenaf fibre on mechanical and thermal properties of PLA composites prepared through fused deposition modeling (FDM). Polymers (Basel) 2021;13. https://doi.org/10.3390/polym13193299.

[59] Fekete I, Ronkay F, Lendvai L. Highly toughened blends of poly(lactic acid) (PLA) and natural rubber (NR) for FDM-based 3D printing applications: The effect of composition and infill pattern. Polym Test 2021;99. https://doi.org/10.1016/j.polymertesting.2021.107205.

[60] Dey A, Rahman MM, Yodo N, Grewell D. Development of biocomposite filament for fused filament fabrication from soy hulls and soy protein isolate. Mater Today Commun 2023;34. https://doi.org/10.1016/j.mtcomm.2023.105316.

[61] Liu H, He H, Peng X, Huang B, Li J. Three-dimensional printing of poly(lactic acid) bio-based composites with sugarcane bagasse fiber: Effect of printing orientation on tensile performance. Polym Adv Technol 2019;30:910–22. https://doi.org/10.1002/pat.4524.

[62] Le Duigou A, Barbé A, Guillou E, Castro M. 3D printing of continuous flax fibre reinforced biocomposites for structural applications. Mater Des 2019;180:107884. https://doi.org/10.1016/j.matdes.2019.107884.

[63] Cheng P, Wang K, Chen X, Wang J, Peng Y, Ahzi S, et al. Interfacial and mechanical properties of continuous ramie fiber reinforced biocomposites fabricated by in-situ impregnated 3D printing. Ind Crops Prod 2021;170:113760. https://doi.org/10.1016/j.indcrop.2021.113760.

[64] Cheng P, Peng Y, Wang K, Le Duigou A, Yao S, Chen C. Quasi-static penetration property of 3D printed woven-like ramie fiber reinforced biocomposites. Compos Struct 2023;303:116313. https://doi.org/10.1016/j.compstruct.2022.116313.

[65] Suteja J, Firmanto H, Soesanti A, Christian C. Properties investigation of 3D printed continuous pineapple leaf fiber-reinforced PLA composite. Journal of Thermoplastic Composite Materials 2022;35:2052–61. https://doi.org/10.1177/0892705720945371.

[66] Ryosuke Matsuzaki, Masahito Ueda, Masaki Namiki, Tae-Kun Jeong H, Keisuke Horiguchi, Taishi Nakamura A& YH. Three-dimensional printing of continuous-fiber composites by in-nozzle impregnation 2016.

[67] Terekhina S, Egorov S, Tarasova T, Skornyakov I, Guillaumat L, Hattali ML. In-nozzle impregnation of continuous textile flax fiber/polyamide 6 composite during FFF process. Compos Part A Appl Sci Manuf 2022;153. https://doi.org/10.1016/j.compositesa.2021.106725.

[68] Zhang H, Lei X, Hu Q, Wu S, Aburaia M, Gonzalez-Gutierrez J, et al. Hybrid Printing Method of Polymer and Continuous Fiber-Reinforced Thermoplastic Composites (CFRTPCs) for Pipes through Double-Nozzle Five-Axis Printer. Polymers (Basel) 2022;14. https://doi.org/10.3390/polym14040819.

[69] Zhang H, Liu D, Huang T, Hu Q, Lammer H. Three-dimensional printing of continuous flax fiber-reinforced thermoplastic composites by five-axis machine. Materials 2020;13. https://doi.org/10.3390/ma13071678.

[70] Ginoux G, Wu X, Laqraa C, Soulat D, Paux J, Ferreira M, et al. Continuous additive manufacturing of hemp yarn-reinforced biocomposites with improved impregnation method. Compos Sci Technol 2024;251:110561. https://doi.org/10.1016/j.compscitech.2024.110561.

[71] Wu X, Ginoux G, Paux J, Allaoui S. Damage and fracture studies of continuous flax fiber-reinforced composites 3D printed by in-nozzle impregnation additive manufacturing. International Journal of Damage Mechanics 2024. https://doi.org/10.1177/10567895241279845.

[72] Pervaiz S, Qureshi TA, Kashwani G, Kannan S. 3D Printing of Fiber-Reinforced Plastic Composites Using Fused Deposition Modeling: A Status Review. Materials 2021;14:4520. https://doi.org/10.3390/ma14164520.

[73] Wang T, Li N, Link G, Jelonnek J, Fleischer J, Dittus J, et al. Load-dependent path planning method for 3D printing of continuous fiber reinforced plastics. Compos Part A Appl Sci Manuf 2021;140. https://doi.org/10.1016/j.compositesa.2020.106181.

[74] Fruleux T, Castro M, Sauleau P, Matsuzaki R, Le Duigou A. Matrix stiffness: A key parameter to control hydro-elasticity and morphing of 3D printed biocomposite. Compos Part A Appl Sci Manuf 2022;156. https://doi.org/10.1016/j.compositesa.2022.106882.

[75] Fruleux T, Castro M, Correa D, Wang K, Matsuzaki R, Duigou A Le. Geometric limitations of 3D printed continuous flax-fiber reinforced biocomposites cellular lattice structures. Composites Part C: Open Access 2022;9. https://doi.org/10.1016/j.jcomc.2022.100313.

[76] Long Y, Zhang Z, Fu K, Li Y. Efficient plant fibre yarn pre-treatment for 3D printed continuous flax fibre/poly(lactic) acid composites. Compos B Eng 2021;227. https://doi.org/10.1016/j.compositesb.2021.109389.

[77] Cheng P, Wang K, Chen X, Le Duigou A, Peng Y, Wen W. Compressive property and shape memory effect of 3D printed continuous ramie fiber reinforced biocomposite corrugated structures. Smart Mater Struct 2022;31:124003. https://doi.org/10.1088/1361-665x/ac95e4.

[78] Krajangsawasdi N, Longana ML, Hamerton I, Woods BKS, Ivanov DS. Batch production and fused filament fabrication of highly aligned discontinuous fibre thermoplastic filaments. Addit Manuf 2021;48:102359. https://doi.org/10.1016/j.addma.2021.102359.

[79] Sun Q, Rizvi GM, Bellehumeur CT, Gu P. Effect of processing conditions on the bonding quality of FDM polymer filaments. Rapid Prototyp J 2008;14:72–80. https://doi.org/10.1108/13552540810862028.

[80] Cai R, Lin H, Cheng P, Zhang Z, Wang K, Peng Y, et al. Investigation on dynamic strength of 3D-printed continuous ramie fiber reinforced biocomposites at various strain rates using machine learning methods. Polym Compos 2022;43:5235–49. https://doi.org/10.1002/pc.26816.

[81] Rivero-Romero O, Barrera-Fajardo I, Unfried-Silgado J. Effects of printing parameters on fiber eccentricity and porosity level in a thermoplastic matrix composite reinforced with continuous banana fiber fabricated by FFF with in situ impregnation.

International Journal of Advanced Manufacturing Technology 2023;125:1893–901. https://doi.org/10.1007/s00170-022-10799-8.

[82] Ahmed W, Alnajjar F, Zaneldin E, Al-Marzouqi AH, Gochoo M, Khalid S. Implementing FDM 3D printing strategies using natural fibers to produce biomass composite. Materials 2020;13. https://doi.org/10.3390/ma13184065.

[83] Chen K, Yu L, Cui Y, Jia M, Pan K. Optimization of printing parameters of 3D-printed continuous glass fiber reinforced polylactic acid composites. Thin-Walled Structures 2021;164:107717. https://doi.org/10.1016/j.tws.2021.107717.

[84] Omar Balderrama-Armendariz C, Aracely Maldonado-Macias A, MacDonald E, Aguilar-Duque JI, Garcia-Pereyra R. Square nozzle to improve mechanical performance and density in fused filament Fabrication additive manufacturing. Manuf Lett 2024;40:179–84. https://doi.org/10.1016/j.mfglet.2024.05.004.

[85] Mazzanti V, Malagutti L, Mollica F. FDM 3D printing of polymers containing natural fillers: A review of their mechanical properties. Polymers (Basel) 2019;11. https://doi.org/10.3390/polym11071094.

[86] Hsueh MH, Lai CJ, Wang SH, Zeng YS, Hsieh CH, Pan CY, et al. Effect of printing parameters on the thermal and mechanical properties of 3d-printed pla and petg, using fused deposition modeling. Polymers (Basel) 2021;13. https://doi.org/10.3390/polym13111758.

[87] Cheng P, Wang K, Chen X, Wang J, Peng Y, Ahzi S, et al. Interfacial and mechanical properties of continuous ramie fiber reinforced biocomposites fabricated by in-situ impregnated 3D printing. Ind Crops Prod 2021;170:113760. https://doi.org/10.1016/j.indcrop.2021.113760.

[88] Long Y, Zhang Z, Yan C, Huang Z, Fu K, Li Y. Multi-objective optimization for improving printing efficiency and mechanical properties of 3D-printed continuous plant fibre composites. Composites Communications 2022;35:101283. https://doi.org/10.1016/j.coco.2022.101283.

[89] Hu Q, Duan Y, Zhang H, Liu D, Yan B, Peng F. Manufacturing and 3D printing of continuous carbon fiber prepreg filament. J Mater Sci 2018;53:1887–98. https://doi.org/10.1007/s10853-017-1624-2.

[90] Tian X, Liu T, Yang C, Wang Q, Li D. Interface and performance of 3D printed continuous carbon fiber reinforced PLA composites. Compos Part A Appl Sci Manuf 2016;88:198–205. https://doi.org/10.1016/j.compositesa.2016.05.032.

[91] Cavalcanti DKK, Banea MD, de Queiroz HFM. Effect of material on the mechanical properties of additive manufactured thermoplastic parts. Annals of "Dunarea de Jos" University of Galati, Fascicle XII, Welding Equipment and Technology 2020;31:5–12. https://doi.org/10.35219/awet.2020.01.

[92] Le Duigou A, Davies P, Baley C. Exploring durability of interfaces in flax fibre/epoxy micro-composites. Compos Part A Appl Sci Manuf 2013;48:121–8. https://doi.org/10.1016/j.compositesa.2013.01.010.

[93] Kabir MM, Wang H, Lau KT, Cardona F. Chemical treatments on plant-based natural fibre reinforced polymer composites: An overview. Compos B Eng 2012;43:2883–92. https://doi.org/10.1016/j.compositesb.2012.04.053.

[94] Le Duigou A, Correa D, Ueda M, Matsuzaki R, Castro M. A review of 3D and 4D printing of natural fibre biocomposites. Mater Des 2020;194:108911. https://doi.org/10.1016/j.matdes.2020.108911.

[95] Célino A, Fréour S, Jacquemin F, Casari P. The hygroscopic behavior of plant fibers: A review. Front Chem 2014;1:1–12. https://doi.org/10.3389/fchem.2013.00043.

[96] El-Nemr KF, Khalil AM. Gamma irradiation of treated waste rubber powder and its composites with waste polyethylene. Journal of Vinyl and Additive Technology 2011;17:58–63. https://doi.org/10.1002/vnl.20245.

[97] Bisanda ETN. Effect of alkali treatment on the adhesion characteristics of sisal fibres. Applied Composite Materials 2000;7:331–9. https://doi.org/10.1023/A:1026586023129.

[98] Zhou Y, Fan M, Chen L. Interface and bonding mechanisms of plant fibre composites: An overview. Compos B Eng 2016;101:31–45. https://doi.org/10.1016/j.compositesb.2016.06.055.

[99] Bisanda ETN. Effect of alkali treatment on the adhesion characteristics of sisal fibres. Applied Composite Materials 2000;7:331–9. https://doi.org/10.1023/A:1026586023129.

[100] Beg MDH, Pickering KL, Gauss C. The effects of alkaline digestion, bleaching and ultrasonication treatment of fibre on 3D printed harakeke fibre reinforced polylactic acid composites. Compos Part A Appl Sci Manuf 2023;166. https://doi.org/10.1016/j.compositesa.2022.107384.

[101] Gauss C, Pickering KL. A new method for producing polylactic acid biocomposites for 3D printing with improved tensile and thermo-mechanical performance using grafted nanofibrillated cellulose. Addit Manuf 2023;61. https://doi.org/10.1016/j.addma.2022.103346.

[102] Caron JF, Demont L, Ducoulombier N, Mesnil R. 3D printing of mortar with continuous fibres: Principle, properties and potential for application. Autom Constr 2021;129. https://doi.org/10.1016/j.autcon.2021.103806.

[103] Sobolev K, Lin Z, Cao Y, Sun H, Flores-Vivian I, Rushing T, et al. The influence of mechanical activation by vibro-milling on the early-age hydration and strength development of cement. Cem Concr Compos 2016;71:53–62. https://doi.org/10.1016/j.cemconcomp.2016.04.010.

[104] Plymill A, Minneci R, Alexander Greeley D, Gritton J, Greeley D, Minneci R, et al. Graphene and Carbon Nanotube PLA Composite Feedstock Development for Fused Deposition Modeling 2016.

[105] Georgopoulos ST, Tarantili PA, Avgerinos E, Andreopoulos AG, Koukios EG. Thermoplastic polymers reinforced with fibrous agricultural residues. Polym Degrad Stab 2005;90:303–12. https://doi.org/10.1016/j.polymdegradstab.2005.02.020.

[106] Chand N, Hashmi SAR. Mechanical properties of sisal fibre at elevated temperatures. J Mater Sci 1993;28:6676–82. https://doi.org/10.1007/BF00356422.

[107] Pappas JM, Thakur AR, Leu MC, Dong X. A parametric study and characterization of additively manufactured continuous carbon fiber reinforced composites for high-speed 3D printing. Int J Adv Manuf Technol 2021;113:2137–51. https://doi.org/https://doi.org/10.1007/s00170-021-06723-1.

[108] Wang B, Ming Y, Zhu Y, Yao X, Ziegmann G, Xiao H, et al. Fabrication of continuous carbon fiber mesh for lightning protection of large-scale wind-turbine blade by electron beam cured printing. Addit Manuf 2020;31:100967. https://doi.org/10.1016/j.addma.2019.100967.

[109] Sanandiya ND, Vijay Y, Dimopoulou M, Dritsas S, Fernandez JG. Large-scale additive manufacturing with bioinspired cellulosic materials. Sci Rep 2018;8. https://doi.org/10.1038/s41598-018-26985-2.

[110] Zhao X, Tekinalp H, Meng X, Ker D, Benson B, Pu Y, et al. Poplar as Biofiber Reinforcement in Composites for Large-Scale 3D Printing. ACS Appl Bio Mater 2019;2:4557–70. https://doi.org/10.1021/acsabm.9b00675.

Chapter 3 - 3D PRINTING OF VEGETABLE YARN-REINFORCED POLYMER COMPONENTS

This chapter was published under the reference:
Natália V. Santos, Daniel C.T Cardoso, 3d printing of vegetable yarn-reinforced polymer components, Journal of Cleaner Production 415 (2023).
https://doi.org/10.1016/j.jclepro.2023.137870

Additive manufacturing has rapidly transformed over the years, moving from simply prototyping to producing objects and structures with advanced materials. The process, also known as 3D printing, enables complex shapes to be generated with great freedom of creation and low waste of resources. Although polymers have been widely used for the manufacture of small objects, the poorer mechanical properties and time required for 3D printing make the technique impractical for the production of real size structural components. This chapter presents the development of a larger-diameter head nozzle for the manufacturing of a polymer-based material reinforced with continuous yarns. To address this issue, a continuous yarn reinforcing method was developed, utilizing a modified Fused Filament Fabrication (FFF) hotend adapted to the in-nozzle impregnation of vegetable fibers (i.e., a process by which the yarn and matrix are joined in a single nozzle), such as jute, ramie, and sisal, combined with polylactic acid (PLA) to produce bio-based printed filaments with diameters up to 3mm. The combination of these materials aims to create printed composites with better mechanical properties and, above all, to meet the environmental need for low-energy biodegradable materials from natural sources that ultimately contribute to reduce the sector's ecological footprint. It was observed that the reinforced samples achieved gains of 28.6% in strength and 28.9% in stiffness in comparison to the unreinforced matrix, using fiber contents up to 48.2% that reduce the polymer utilization per printed volume. The feasibility of the production of multilayer components using the developed method was also confirmed for different types of reinforcement and printing paths.

3.1 Introduction

Human development is directly related to the evolution of engineering materials and manufacturing processes to meet mechanical, environmental and design performance criteria. Indeed, technological development has been directly linked to environment and, in the last few decades, the concerns have arisen worldwide have about impact of production and consumption on future generations' access to resources [1].

Additive manufacturing (AM), popularly called 3D printing, is a rapid prototyping process for the production of three-dimensional objects [2]. It enables the fabrication of complex designs, thus meeting users' geometry needs and significantly reducing the amount of raw material towards an efficient production [3]. From an environmental perspective, recent investigations in the field have focused on topics such as the use of natural materials, geometry optimization and printing process improvement that may lead to sustainable products with material savings and reduced energy consumption. In this context, biocomposites with plant-origin matrix and reinforcement consist in an mechanical-efficient and sustainable solution for 3D printing [4]. These composites can significantly contribute to reduce the carbon dioxide footprint due to their low density, renewability and biodegradability [5,6]. The latter may ultimately lead to a reduction of waste on the planet, as material decomposes at the end of its design life [7].

Kechagias and Chaidas [8] analyzed the effect of printing parameters to create good practices that enable the production of low-cost sustainable printed components. The authors concluded that the primary parameters governing the energy expenditure during printing are the volumetric dimensions of the component, the thickness of individual layers, the material composition and the printing speed. Fountas *et al.* [9] evaluated PLA/Wood composites using the Taguchi methods to search for optimal solutions for the layer thickness, nozzle temperature, raster deposition angle and printing speed. They observed that discrete regions can be found where parameter settings are advantageous for maximizing ultimate tensile strength. Bianchi *et al.* [10] analyzed the influence of printing parameters to minimize energy consumption and CO_2 emissions. For a given printing velocity, the authors observed that the energy consumption decreases when the thickness of individual layers increases. This phenomenon is particularly pronounced when operating at lower printing speeds. Also, Long *et al.* [11] proposed an optimization method to determine the optimal 3D printing parameters for continuous vegetable fiber composites. The authors verified that the parameters could be optimized without compromising the mechanical strength, achieving an efficiency increase of up to 40%, i.e. produced in less time and with less energy expenditure.

Recently, several studies using fibers as reinforcement on 3D printing have been conducted. The use of fibers can be done in three different ways: as fillers, discontinuous or continuous fibers. The use as fillers does not improve substantially the mechanical properties and can eventually reduce them when higher volume fractions are used [12,13]. Interlayer cohesion issues have also been reported in literature [14]. Furthermore, if viscosity increases with the addition of reinforcement, an increase in temperature will be necessary [15], which may lead to fiber degradation and higher energy consumption. In most cases, authors have adopted vegetable fibers in the discontinuous form in extrusion-based filaments for 3D printing [16]. This technique allows the production of composites with improved strength-to-weight ratio, as well as with renewable and biodegradable characteristics [17], although an increased porosity has been also reported due to their dispersive characteristics [15]. Moreover, its implementation concurrently reduces the ecological impact of composites that would conventionally be fabricated utilizing synthetic fibers. Jauhari *et al.* [18] stated that synthetic carbon fibers need 355,000 MJ/t of manufacturing energy, whereas vegetable fibers entail a considerably lower consumption, as an example of sisal with 2488 MJ/t. Table 3.1 shows the mechanical and physical properties of the vegetable fibers used in the present study.

Table 3.1 - Mechanical and physical properties of vegetable fibers.

Properties	**Jute**	**Ramie**	**Sisal**	**Reference**
Diameter (μm)	25-200	20-35	50-300	[7,19–21]
Density (g/cm³)	1.3-1.5	1.5-1.6	1.3-1.5	[7,22,23]
Tensile strength (MPa)	400-800	400-968	500-1150	[7,19,22,23]
Young modulus (GPa)	10-30	44-128	11-15	[7,19,22,23]

Cellulose (%)	58-63	76	59	[19,20]
Hemicellulose (%)	12	17	24	[19]
Lignin content (%)	12-14	1	15	[19,20]

The literature on continuous fibers is scarce and applications with vegetable fiber are even more limited, especially in the yarn form [15]. Most of the works have focused on the use of commercial printers already set up for that condition [24–27]. Since such printers are usually applicable for small-diameter synthetic fibers such as carbon and glass, vegetable fiber yarns, which have larger dimensions due to their manufacturing process, cannot be used in a standard way. Fused filament fabrication (FFF) has been mainly adopted for the production of printed components with continuous fibers [28]. Pervaiz *et al.* [29] pointed out the three main types of printing with continuous fibers, namely pre-embedment of the fiber as a composite filament (semi-finished filament printing), embedment in the printhead (in-nozzle impregnation) and embedment in the component (out-of-nozzle impregnation).

Regarding continuous synthetic fibers, Mohammadizadeh *et al.* [24] used carbon, glass, and aramid fibers. Among the failure mechanisms observed by the authors one may cite fiber pull-out, fiber breakage and delamination. Mohammadizadeh *et al.* [25] studied the behavior of nylon composites reinforced with carbon fiber, glass and aramid at different temperatures for creep and fatigue analyses. Melenka *et al.* [26] evaluated the tensile properties of nylon composites reinforced with aramid continuous fibers obtaining an elastic modulus of up to 9.0 GPa for the largest volume fraction. Furthermore, Khosravani *et al.* [30] evaluated the fracture process in composites reinforced with continuous glass fiber. By incorporating a volumetric fraction of up to 75% of glass fiber, the authors observed that the fracture strength increased up to approximately 193%, indicating that the specimens with the highest volumetric fraction exhibited superior mechanical properties. Despite the utilization of fibers inhibiting crack propagation in 3D-printed components, Khosravani *et al.* [31] indicated that an elevation in fiber content can lead to increase porosity and reduce strength and stiffness in the reinforced structures.

With respect to the use of natural fibers, Le Duigou *et al.* [27] used flax as PLA (polylactic acid) reinforcement and obtained a modulus of elasticity of 23.3 GPa and a maximum tensile strength of 253.7 MPa in the direction parallel to fibers for a 34.5% fiber mass fraction. Cheng *et al.* [32–34] printed PLA reinforced with ramie yarn and evaluated the influence of temperature on the printed material strength and characteristics, as well as the effects of the yarn reinforcement on compression property, energy absorption capacity, penetration, and memory effects for different cell shapes.

On the other hand, research on the adaptation of traditional printers for a continuous fiber insertion have been studied by Yang *et al.* [35]. The authors used an adapted printer of 0.8mm nozzle diameter for incorporation into the printhead of carbon fiber as an ABS reinforcement in the fiber weight fraction of 10%, reaching tensile and flexural strength values of 147 MPa and 127 MPa, respectively. Moreover, Krajangsawasdi *et al.* [36,37] modified the extrusion nozzle to 1.4mm diameter with a 1.25mm fillet in their study on discontinuous fiber to allow for material deposition with no fiber breakage during the print flow increase.

The examination of nozzle type is a crucial factor in the printing process as seen by Ahmed *et al.* [15]; the authors show that the nozzle size and shape have a direct impact on the final result of printing quality (i.e., cloggings, voids, bubbles and dimension accuracy). Li *et al.* [38] modified the printhead so that fibers were incorporated near the nozzle entrance reducing clogging inside the extruder. Matsuzaki *et al.* [39] also adopted a printing nozzle for fiber insertion into the internal nozzle, but a nozzle with 1.4mm of diameter was used, allowing the incorporation of a larger diameter carbon fiber.

The mechanical properties of composites reinforced with continuous fibers, as reported in the literature, are summarized in Table 3.2, where constituents and reinforcement fractions used are also reported obtained. It is worth highlighting that Mohammadizadeh *et al.* [24] and Le Duigou *et al.* [27] used printers designed for fiber insertion and obtained higher fractions, hence, higher mechanical strength.

Table 3.2 - Tensile strength of printed composites with continuous fiber of collected studies.

Fiber	**Matrix**	**Fiber mass fraction (%)**	**Fiber volume fraction (%)**	**Tensile strength (MPa)**	**Reference**
Carbon	ABS	10.0	-	147.0	[35]
Carbon	Nylon	58.0	-	404.3	[24]
Glass	Nylon	28.0	-	372.1	
Aramid	Nylon	43.0	-	309.1	
Flax	PLA	34.5	-	253.7	[27]
Carbon	PLA	-	34.0	91.0	[38]
Carbon	PLA	-	6.6	185.2	[39]
Jute	PLA	-	6.1	57.1	
Ramie	PLA	-	-	86.4	[32]

This work presents the development of a novel methodology for reinforcing a polylactic acid (PLA) matrix with vegetable yarns. The study differentiates itself from prior literature in two main ways: firstly, instead of the out-of-nozzle impregnation technique mainly used in traditional continuous fiber reinforcement printers, an in-nozzle impregnation through a modified extruder is adopted. This technique allows for fiber impregnation in the matrix prior to deposition, which is not possible with the out-of-nozzle impregnation method, where fibers are deposited onto already cooled polymer layers. Secondly, the study makes the use of vegetable fibers, which offer an interesting alternative to commonly used synthetic counterparts such as carbon and glass. Additionally, the study demonstrates the potential for manufacturing larger structural parts by using high flow nozzles and larger diameter vegetable fiber yarns such as sisal. The use of both modifications should provide increased mechanical strength while maintaining desirable characteristics such as sustainability and biodegradability and thus, expanding the potential applications for 3D printed continuous yarns reinforced biocomposites.

3.2 Experimental program

3.2.1 Materials and printing parameters

A 1.75mm diameter polylactic acid filament (PLA) supplied by 3DLAB Corp. (Brazil) was used as a matrix for the printed samples. The material works with nozzle temperatures ranging between 190°C and 220°C; ideally at 200°C, for which the best viscosity with lowest porosity can be anticipated.

Ramie, jute, and sisal fiber yarns provided by SISAL SUL Corp. (Brazil) were used as reinforcement with diameters ranging from 0.5 to 2.0mm (Figure 3.1). Ramie yarns were supplied only as three-ply twisted ropes and were untwisted to achieve a smaller diameter suitable for printing.. No surface treatment was adopted.

Figure 3.1 - Vegetable fibers used as reinforcement in 3D printing (Nikon SMZ800N optical microscope).

Print settings were established for suitable fiber insertion. The layer height was set as 1.5 mm, with a 2.0 mm width and 10 mm/s filament deposition speed. The nozzle temperature was set as 200°C, while the table temperature was set as 60°C. Despite the good properties achieved for printing speeds up to 22mm/s, a lower speed was chosen to ensure a lower void fraction and a better print quality.

3.2.2 Printing head development and biocomposite printing

A new print head adapted for the insertion of continuous fibers was developed by modifying a standard Zmorph VX brand press. The system was designed so that yarns with diameters up to 2.0 mm could be joined with the PLA filament. According to the in-nozzle impregnation method, both reinforcement and matrix are jointly printed – the matrix enters as a filament in the upper entrance of the coldend made of polyether ether ketone (PEEK), whereas the yarn is inserted through a polytetrafluoroethylene (PTFE) tube on the side opening of the coldend. This methodology allows the use of low-cost printers with simple modifications and the use of a wide range of fibers with different diameters. Figure 3.2 shows the printhead developed.

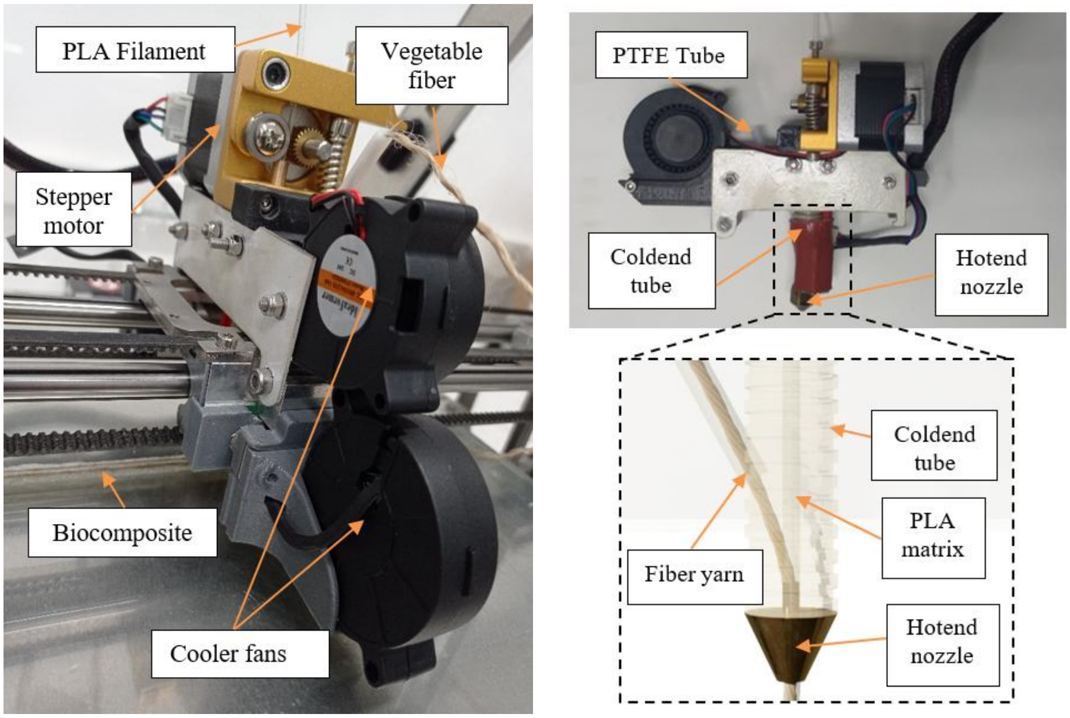

Figure 3.2 - Printhead adapted for the 3D printing of biocomposites with continuous fiber.

Regarding the printing of the composite reinforced with continuous fiber, the fiber is inserted into the extruder – while it is still off – by a flexible guide and passes the PTFE tube and through the coldend to reach the hotend nozzle. Once turned on, the printer starts depositing the biocomposite filament onto the heated table, to which it adheres. As the extruder moves along the Cartesian axes, the reinforcing fibers are pulled through the printing nozzle along with the polymeric matrix. The high temperature and confinement at the hotend nozzle are expected to promote an appropriate fiber impregnation.

Printed samples made of PLA reinforced with vegetable fiber in yarn format were fabricated throughout printhead development to assess the material properties. Printing characteristics of the biocomposite were analyzed regarding the effect of yarn on geometry and printing quality, from a micro scale (e.g., evaluation of the appearance of bubbles) to the study of the effects in multilayer components. Optical microscopy technique using a Nikon SMZ800N equipment and scanning electron microscopy (detail in Section 2.3.3) were used for this purpose. The quality of the printed samples was assessed through SEM by evaluating the fiber-matrix interface, and the presence of voids.

3.3. Testing and characterization

3.3.1 Raw material characterization

Fiber yarn tensile tests were conducted in a model 23-30, EMiC Series 23 universal testing machine with a 5kN load cell (Figure 3.3). A digital camera with a resolution of 624 pixels and taking 15 frames per second was used for measuring the elongation. The tests were performed at room temperature 23°C, and 50% relative humidity, at a displacement control of 5mm/min rate up to failure. The test setup, developed by Castoldi [40], consists of two 17.1 cm pulleys to which the fiber is attached (two turns).

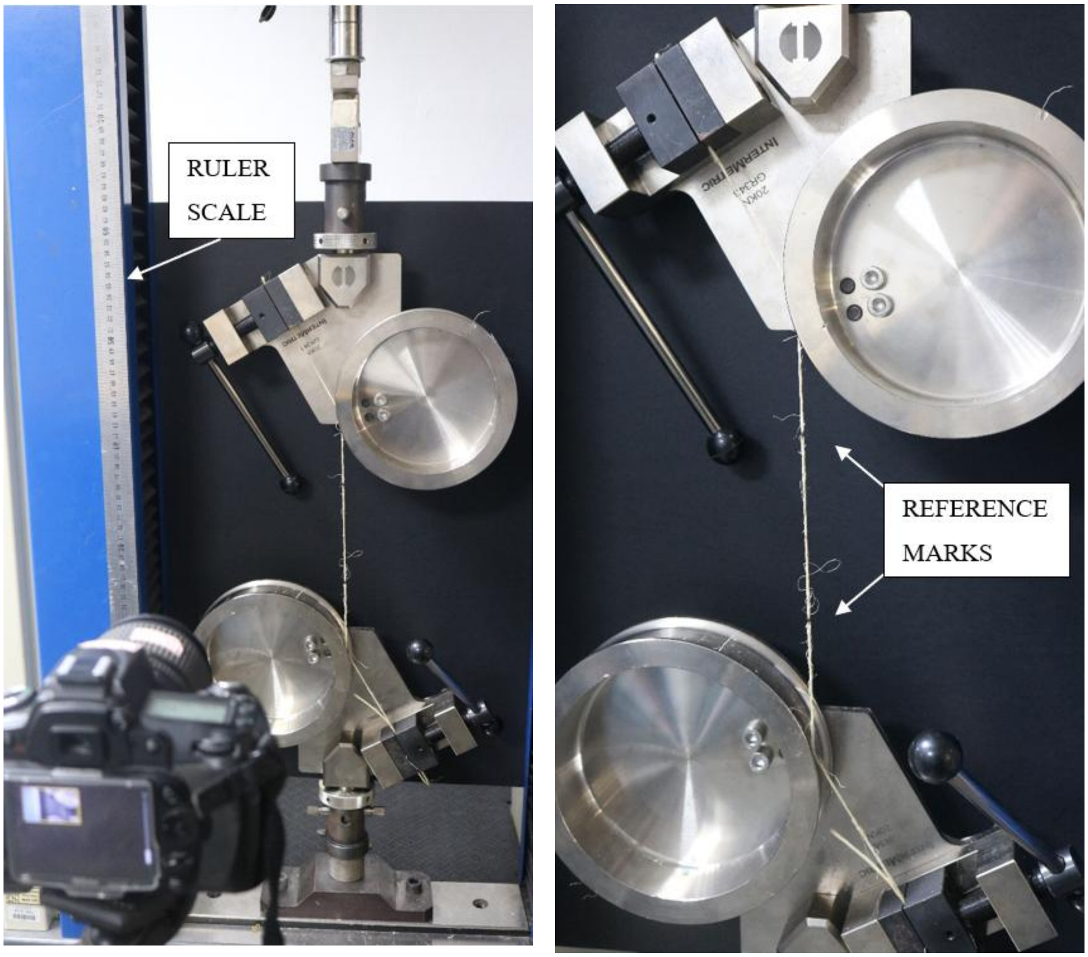

(a) (b)

Figure 3.3 - Layout of vegetable fibers tensile test.

Reference marks 100 mm from each other were introduced for strain measurement and Fiji software [41] measured the relative distances at desired times. The strains were determined as the ratio between relative displacement and gage length (initial distance between reference marks) and Catman® software synchronized the recorded force and time with video. The modulus of elasticity was obtained as the slope of a secant line corresponding to a force equivalent to 30% of the breaking load.

The test was performed on 5 samples for each type of vegetable fiber (sisal, ramie, and jute). The cross-sectional area of each yarn was measured by Fiji's plugin *Trainable Weka Segmentation* [41] with images acquired through optical microscope technique (Nikon SMZ800N).

3.3.2 Biocomposite tensile test

Biocomposite tensile tests were used to determine the properties of fiber reinforced PLA. Five specimens for each type and five additional specimens for the unreinforced condition were tested at room temperature (23°C) and 50% relative humidity. The testing protocol followed the recommendations of ASTM D3039 [42]. Figure 3.4 displays the 200x10x1.5 mm printed specimens, which were prepared with a single layer containing four continuous filaments with fibers oriented in the loading direction. The prismatic shape was chosen due to the facilitated printing path and following the methodology used in previous works with vegetable fiber reinforcement [27,32]. Parameters were chosen in an attempt to achieve the highest volume fraction for the biocomposites, thus generating a 2.0x1.5mm layer.

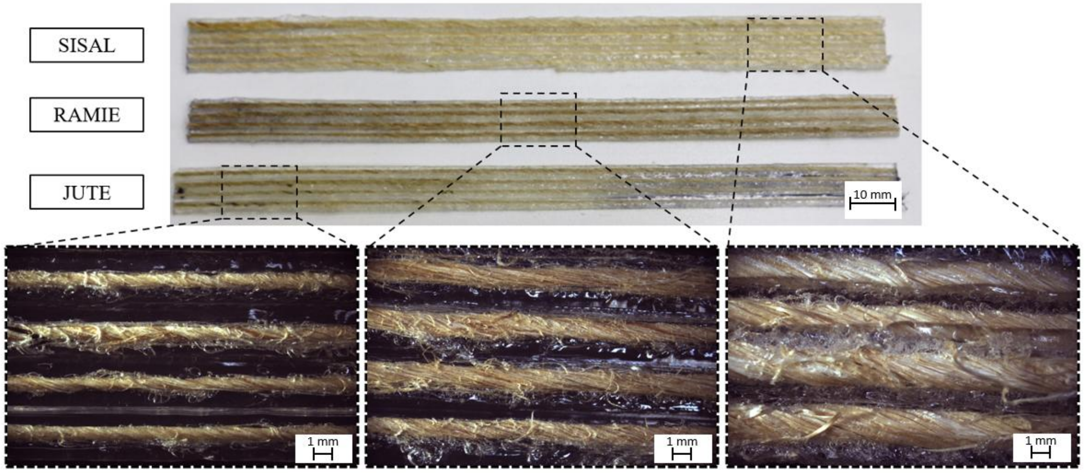

Figure 3.4 - Printed specimens for tensile tests.

The tests were conducted under displacement control at 1.00 mm/min loading rate until failure (i.e. loss of structural integrity due to damage such as cracking, delamination, or fiber breakage.) in a model 23-30 EMiC Series 23 universal testing machine equipped with a 5 kN external load cell. A clip-gage extensometer was attached to the specimen at the central portion for strain measurement with loading.

3.3.3 Scanning Electron Microscopy (SEM) Analysis

The cross-sections of the specimens were analyzed using a TESCAN CLARA Scanning Electron Microscope equipment operating at 2 keV. The samples were dried in an oven at 60 °C for 24 hours and kept in a desiccator for the removal of as much moisture as possible. The metallization process was conducted by covering the samples with a layer of gold towards improving their conductivity.

3.4 Results and discussion

3.4.1 Printhead development

Initial attempts to manufacture a fiber-reinforced printhead were made with the aid of a PTFE tube that enabled the fiber to pass to the filament feed tube where it adhered to the heated PLA filament and was pulled to the hotend of a 2.1 mm nozzle. Like any developing technology, the procedure showed several problems at the beginning (e.g., tube clogging due to fiber winding, difficulty in the matrix's passing as a consequence of fiber diameter, and fiber breakage because of friction between fiber and nozzle during material deposition).

Another consequence of material extrusion printing with fibers is their stretching during deposition. Therefore, during the printing of the composite at the table, the yarns ended up on the top of the layer, i.e. not centered in the deposited filament, causing the yarn not to be completely impregnated by the polymeric matrix. Therefore, during a layer-on-layer deposition, part of the fiber-matrix interface occurred in the so-called cold joints, thus apparently generating less interfacial bonding in the area [35]. Figure 3.5 shows images of a printed layer.

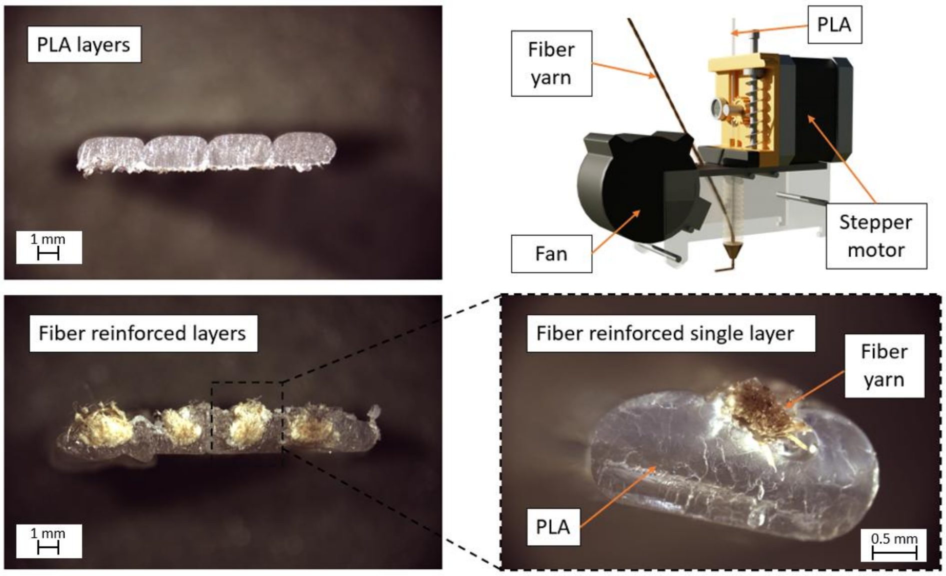

Figure 3.5 - Printing process showing yarn decentralization in layers.

The larger the yarn diameter, presumably the more difficult the impregnation of the inner filament will be, further compromising the final mechanical performance [38]. Figure 3.6, produced by Scanning Electron Microscope (SEM), shows the fiber detachment after a tensile test, with a fragile fiber-matrix interaction probably due to the low penetration of the matrix in the fiber yarn. In this case, modifying the polymer with additives and fiber pre-treatments could be an alternative for an improved fiber impregnation.

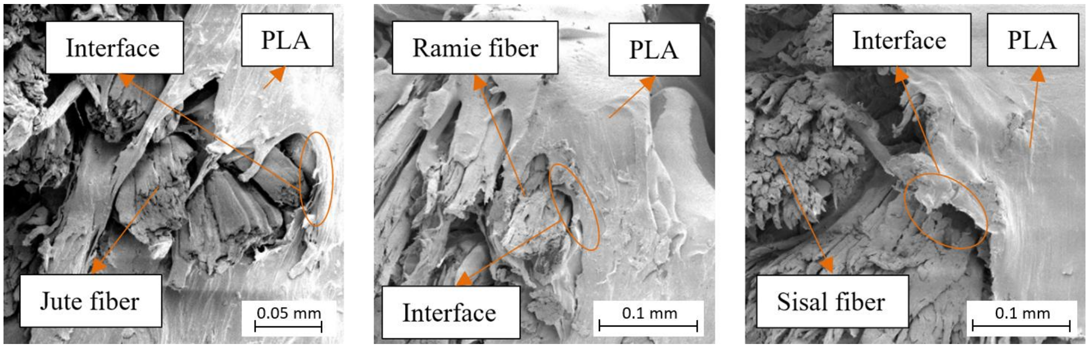

(a) (b) (c)

Figure 3.6 - Layers interface showing fiber detachment from matrix by SEM: (a) Jute, (b) Ramie, and (c) Sisal.

Different from a single layer component, the yarn becomes fully surrounded by the matrix when many stacked layers are adopted, thus partially mitigating the aforementioned problem. As shown in Figure 3.7, the fibers are aligned in a multilayer model, whereas the matrix creates a shield around them, showing compaction, since the top layer improves the material interface, generating a smaller fiber-matrix detachment. However, the impregnation is not complete, occurring mainly at the yarn perimeter, while the inner regions remain less permeated by the matrix.

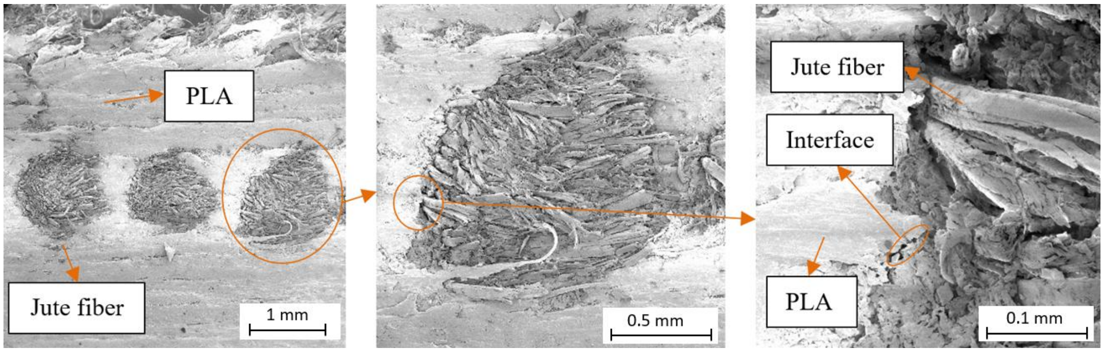

(a) (b) (c)

Figure 3.7 - SEM images from multiplayer biocomposite reinforced with jute fiber.

In addition, analyses using optical microscopy were conducted to assess the effect of different temperatures on the impregnation and quality of the layer, starting with temperatures near in the melting temperature of PLA, which is between 170-180°C [43]. Kandemir *et al.* [44] highlighted that a greater homogenization occurs and an improved adhesion between layers can be obtained for working temperatures higher than the melting point. The temperature upper limit is characterized by the formation of bubbles that might compromise the mechanical properties of the matrix, harming the composite. Figure 3.8 shows the variation in layer production quality according to the temperature.

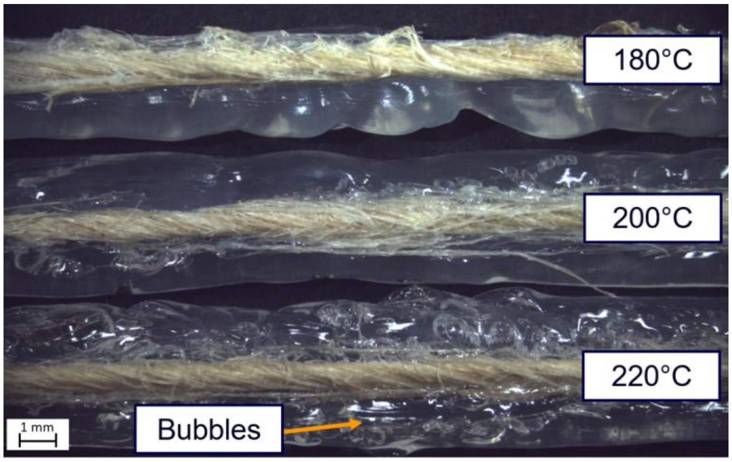

Figure 3.8 - Variation in layer production quality according to the temperature.

Since vegetable fibers are natural and made mostly of cellulose, problems such as strand breakage (Figure 3.9a), carbonized parts of fibers during printing (Figure 3.9b) and formation of matrix bubbles (Figure 3.9c) can be faced during printing due to either the characteristics of the fiber nature, the vegetable fiber-matrix interaction, or the 3D printed process.

(a) (b) (c)

Figure 3.9 - Problems during reinforced continuous vegetable fiber during 3d printing a) Fiber breakage, b) Carbonized fibers, and c) Matrix bubbles generation.

An important effect observed was the increase in porosity with the yarn diameter, as depicted in Figure 3.10. This is apparently due to the formation of air bubbles between the fibers of the yarn – when passing the printing nozzle, it undergoes diametral compression, thus releasing the air trapped between the fiber and the matrix.

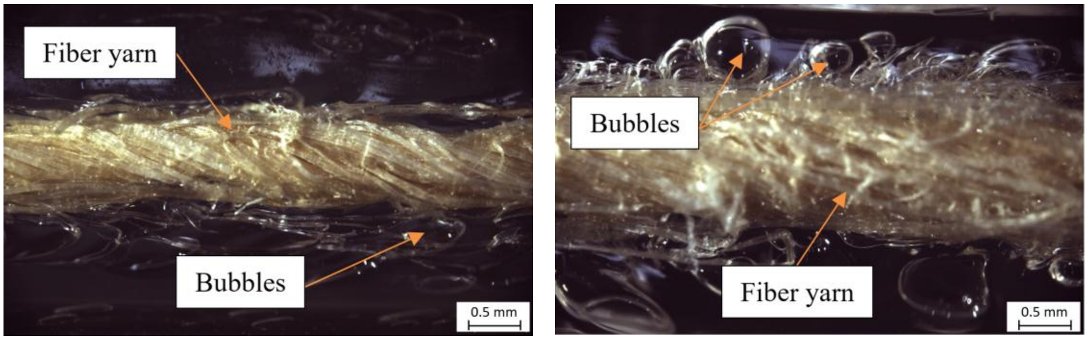

(a) (b)

Figure 3.10 - Variation in bubble formation according to yarn diameter: (a) 0.79mm (b) 1.35mm.

The working temperature of PLA can affect the performance of the fibers since vegetable fibers are degraded at high temperatures [19] and low temperature reduces PLA mechanical properties [45]. To avoid the degradation of the fiber during printing due to exposure to higher temperatures at the hotend, a higher speed can be adopted. However, the increase in speed hampers composite adhesion to the printable table and printing in curves, causing fiber breakage from friction on the nozzle printer during printing [15].

Such problems observed during printhead development were corrected or minimized over time. Clogging was minimized by positioning the fiber inlet tube near the nozzle printer, thus reducing the length of fiber passage in the extruder. The die passage was facilitated by either decreasing the fiber diameter, or increasing nozzle size, which also reduced air bubbles. The probability of fiber carbonization was reduced by increasing the printing speed, while the fiber breakage due to friction was resolved by sanding the edges of the nozzle for a smoother surface.

Table 3.3 summarizes the printing characteristics of materials reported in literature. It can be seen that, in most cases, the fiber diameter was restricted to 0.20 to 0.60 mm, with extrusion temperatures ranging between 190 and 270°C, depending on the matrix. The developed printhead allows fibers with diameters significantly greater (0.50 to 2.00mm), evidencing a real change of scale. The 2.1mm fiber-entry nozzle extruder was developed as a basis for a scale-up in polymer printing, enabling the production of up to 3mm wide fiber-reinforced layers, which is a large increase compared to previous studies. Consequently, a significant increase in productivity is expected. Since a standard printer with a 0.4mm nozzle and 40-60mm/s average print speed (limited by polymer's characteristics) [46] generates an up to 7.5mm^3/s print flow, the adaptation of the 2.1mm nozzle to 22mm/s print speed generates a 76.2mm^3/s flow rate, (i.e. ten times the usual production). Indeed, from an environmental perspective, an increase in productivity is favorable, as highlighted by Kechagias and Chaidas [8], since the energy cost for 3D printing manufacturing is affected by the total printing time. Therefore, higher throughput results in faster production and, consequently, in more energy-efficient processes.

Table 3.3 - Printing properties for composites with continuous fibers reported by previous studies.

Reference	**Fiber**	**Matrix**	**Yarn diameter (mm)**	**Nozzle diameter (mm)**	**Extrusion temperature (°C)**
Yang *et al.* [35]	Carbon	ABS	0.60	0.80	230
	Carbon	Nylon	0.35	0.12	265-270

Mohammadizadeh *et al.* [24]	Glass	Nylon	0.30	0.10	265-270
	Aramid	Nylon	0.30	0.10	265-270
Matsuzaki *et al.* [39]	Carbon	PLA	0.20	1.40	210
	Jute	PLA	0.20	1.40	210
Le Duigou *et al.* [27]	Flax	PLA	0.40	0.60	190
Li *et al.* [38]	Carbon	PLA	0.60	-	180
Cheng *et al.* [32]	Ramie	PLA	0.35	1.30	220
Present research	Jute	PLA	0.50-1.20	2.10	200
	Ramie	PLA	0.70-1.30	2.10	200
	Sisal	PLA	1.40-2.00	2.10	200

3.4.2 Assessment of printed multilayer components

Analyses of geometry of printed multilayer composites reinforced with vegetable fibers require the definition of the printing path and the evaluation of its influence on the result. Print path, infill type and other factors can be defined through slicing software such as Cura, Slic3r, Simplify3D and others [8]. Different from a traditional printing process, the fabrication of structural components reinforced with continuous yarns requires the development of a printing path code to make the extruder to follow a single path from the beginning to the end of the component.

The definition of printing paths considers the geometry of the component, the required fiber alignment, and the need to maintain continuous deposition without interruptions. The paths are programmed to minimize sharp turns, ensuring smooth transitions that prevent excessive fiber bending or detachment from the substrate. Additionally, the deposition sequence is optimized to maximize fiber-matrix contact and avoid overlapping inconsistencies that could compromise the mechanical performance of the final part.

The first analysis performed was focused on the effects of different fibers such as yarns on the printing of a multilayer component (Figure 3.11), revealing that the maintenance of the same flow, temperature and printing speed led the smallest fiber diameters to generate components with higher precision and little resistance to change in direction. This characteristic is of great importance to avoid loss of contact with adjacent and top layers; in the latter case, the base becomes irregular and propagates errors to subsequent top layers.

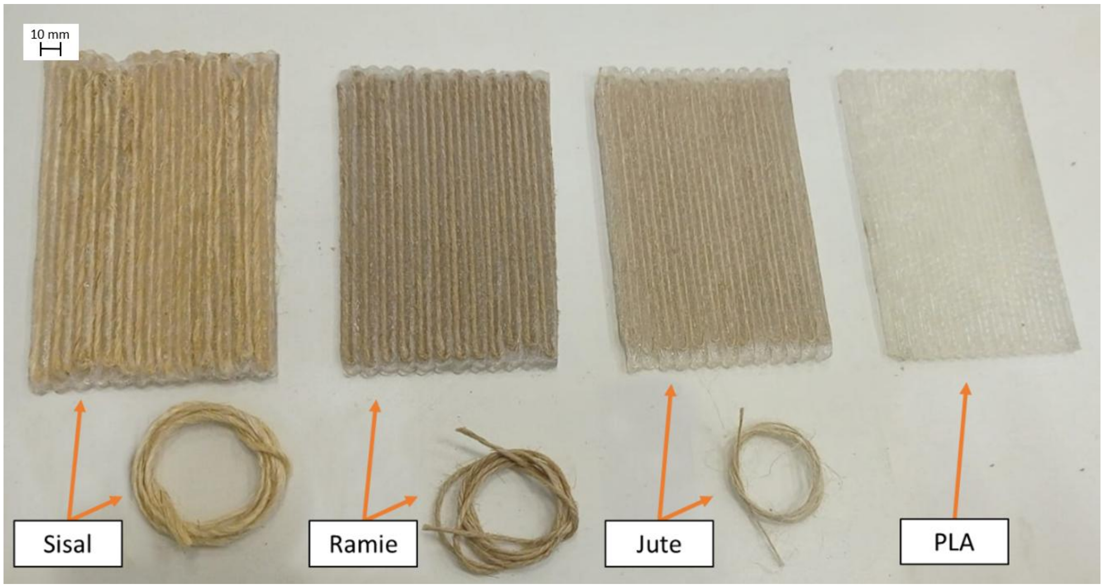

Figure 3.11 - Printing of multilayer composites reinforced with yarn from different vegetable fibers.

Models with different printing paths were then tested towards forming a laminate with continuous fibers in different directions (Figure 3.12). When the printing process involves layers with different paths, the end of the bottom layer must coincide with the beginning of the top layer and the upper layers must always have a support so that they can be printed — unlike traditional printing, printing is not performed on a removable support.

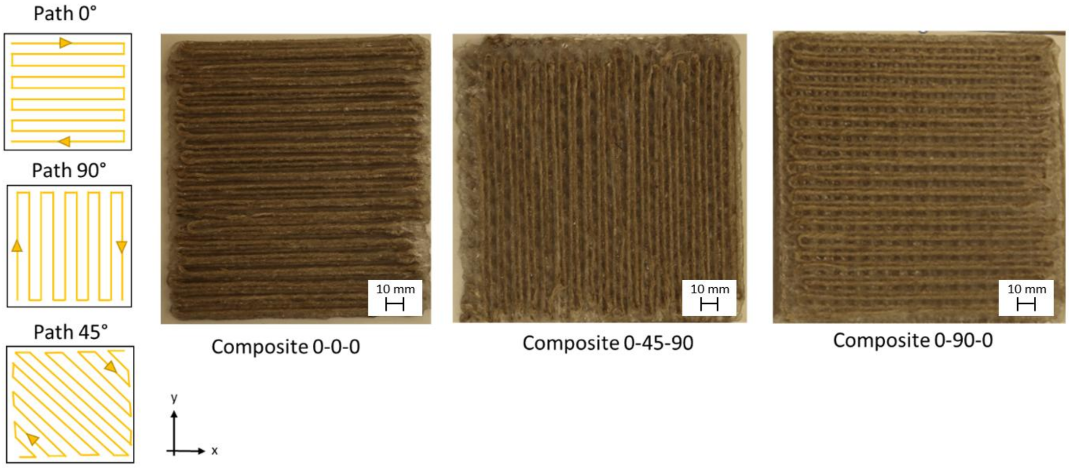

Figure 3.12 - Printing paths of multilayer composites.

To assess the code efficiency and printing results for the production of multilayer components with curved parts, a fifteen-layer structural truss element was produced (Figure 3.13). The printing settings were the same as those used in the biocomposite tensile test, resulting in a fifteen-layer truss of 307x72x15mm overall dimensions. Figure 3.14 displays the truss during and after printing.

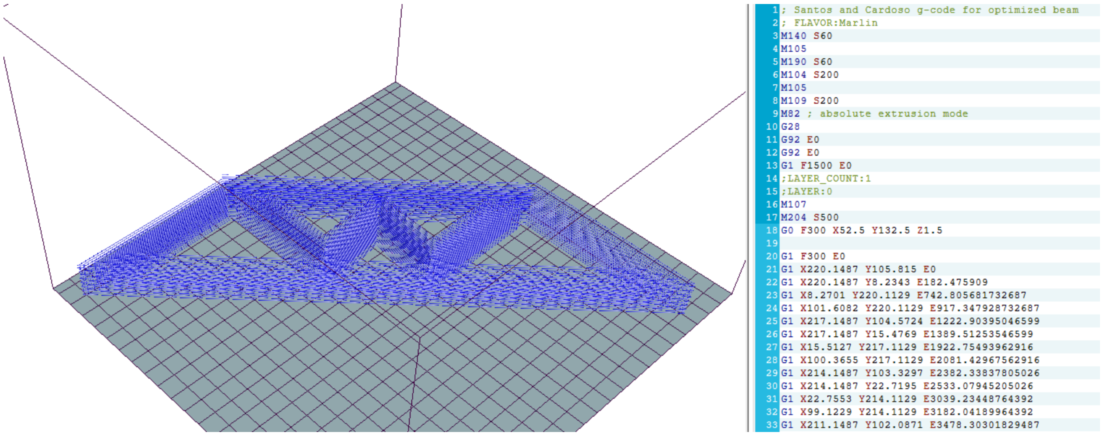

```
; Santos and Cardoso g-code for optimized beam
; FLAVOR:Marlin
M140 S60
M105
M190 S60
M104 S200
M105
M109 S200
M82 ; absolute extrusion mode
G28
G92 E0
G92 E0
G1 F1500 E0
;LAYER_COUNT:1
;LAYER:0
M107
M204 S500
G0 F300 X52.5 Y132.5 Z1.5

G1 F300 E0
G1 X220.1487 Y105.815 E0
G1 X220.1487 Y8.2343 E182.475909
G1 X8.2701 Y220.1129 E742.805681732687
G1 X101.6082 Y220.1129 E917.347928732687
G1 X217.1487 Y104.5724 E1222.90395046599
G1 X217.1487 Y15.4769 E1389.51253546599
G1 X15.5127 Y217.1129 E1922.75493962916
G1 X100.3655 Y217.1129 E2081.42967562916
G1 X214.1487 Y103.3297 E2382.33837805026
G1 X214.1487 Y22.7195 E2533.07945205026
G1 X22.7553 Y214.1129 E3039.23448764392
G1 X99.1229 Y214.1129 E3182.04189964392
G1 X211.1487 Y102.0871 E3478.30301829487
```

Figure 3.13 - G-Code printing path for truss.

(a) (b)

Figure 3.14 - 3D printing of the truss: (a) printing process (b) printed truss.

Figure 3.15 shows the final configuration of the truss. Despite the excellent result, the yarns tended to move from the path defined in the model when it is exposed to several curves in a row seemingly due to fiber stiffness and because the matrix material takes longer to cool and to acquire strength. Therefore, in complex elements, the curves must be printed at a lower speed to prevent the fiber from being drawn out of position. Although the printing process may eventually result in yarn breakage, it seems not to compromise the process, since the friction between the matrix and yarn inside the nozzle is strong enough to pull the cut fiber and continue the process without interruption. On the other hand, this may lead to loss of mechanical properties in the broken region.

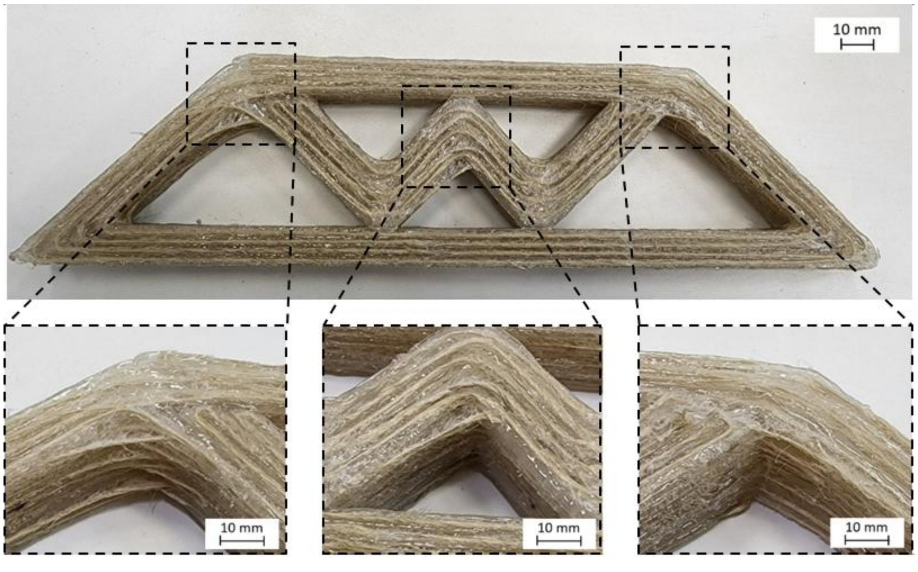

Figure 3.15 - Defects present in the current methodology.

3.4.3 Vegetable fiber yarn mechanical properties

Results for strength and elastic modulus of fiber yarns are summarized in Table 3.4 and reveal that the lowest strength was achieved for ramie, despite its higher Young's modulus. On the other hand, sisal yarns showed the highest tensile strength and the lowest modulus of elasticity. A comparison of such results with those expected for isolated fibers (Table 3.1) shows a significant variation.

Table 3.4 - Tensile properties of vegetal fiber yarns.

Type of vegetable fiber yarns	Tensile strength [MPa]	Young's Modulus [GPa]
Ramie	57.2±12.9	8.4±1.3
Jute	71.0±8.9	5.7±1.2
Sisal	112.8±9.2	5.4±0.3

Since vegetable fibers have a finite length that depends on the species [47], they form a continuous yarn by twisting several long fibers into a single one. Moreover, these yarns are normally intended for handicrafts and ropes and, therefore, are not subject to a high-quality control. A significant variability in the number of fibers that compromise its diameter also directly influences the results of mechanical properties, as shown in Table 3.3. For jute yarns, for instance, diameters ranging from 0.5 to 1.2 mm can be seen. The yarns tend to exhibit lower tensile strength and Young's modulus in comparison to a single isolated fiber, due to the presence of defects such as discontinuity and waviness of fibers.

3.4.4 Biocomposite mechanical properties

Regarding the effect of the vegetable fibers as 3D printing reinforcement, Table 3.5 shows the results of tensile strength and modulus of elasticity for each type of 3D printed biocomposite studied. It should be noted that, differently from synthetic fibers, vegetable fibers undergo changes in mechanical and physical properties due to climatic conditions, soil, and age [48]. Furthermore, these fibers are provided by a low-developed industry worldwide and variations in diameter, for example, are expected. On the other hand, the effective diameter of the deposited composite filament is similar in all cases and each sample was constituted by four parallel filaments, which contribute to minimizing variability issues. However, another crucial factor influencing the results is the non-perfect alignment of the fibers in the in situ impregnated samples. In inherently brittle matrices such as PLA, this misalignment can prevent efficient load transfer, as the matrix may fail prematurely before transferring stress to the fibers. This phenomenon likely contributes to the discrepancies observed in Table 3.5, where the tensile properties of the fibers and their volume fractions do not always correlate with the composite performance as expected. Nonetheless, some reasonable trends emerge, particularly in tensile strength, which is generally less sensitive to fiber misalignment than Young's modulus.

Although no one-to-one comparison in volume fraction was performed, other parameters were set and controlled. PLA flow is controlled according to the number of revolutions of the stepper motor during the deposition of the material in the hotend at constant speed. Therefore, the fixed parameters in all composites are: flow, displacement speed on Cartesian axes, table and extruder temperature, and printing path.

Table 3.5 - Tensile test result for 3D printed biocomposites.

Type of reinforcement	**Linear density [g/m]**	**Fiber volume fraction [%]**	**Tensile strength [MPa]**	**Young's Modulus [GPa]**
Unreinforced matrix	-	-	55.7±4.6	3.4±0.2
Ramie	0.31±0.05 (310 tex)	10.8 -18.3	57.2±2.5	3.8±0.1
Jute	0.33±0.03 (330 tex)	12.5 - 21.8	62.8±3.6	4.3±0.3
Sisal	1.80±0.05 (1800 tex)	34.3 - 48.2	71.6±2.6	4.0±0.5

The specimens reinforced with sisal fibers showed the highest strength, reaching an 28.6% improvement compared to an unreinforced specimen. The low resistance gains can be explained by the low volume fraction used and the low adhesion – the former was limited by the conditions of the printing process addressed in the printhead development section. The best results were obtained by sisal, used with the highest volume fraction (34.3 - 48.2%) among the three types of fiber.

Despite the aforementioned comparison, the objective of this study is not to compare the behavior of the different composites, but to show the feasibility of applying vegetable yarns of different types supplied by local companies to larger diameter nozzles for the production of printed multilayer components, emphasizing the positive and negative aspects of the process. Although composites of sisal showed the best mechanical responses, largely due to its higher volume fraction and large diameter, it faces obstacles, since its larger diameter hampers printing on complex paths, as mentioned in Section 3.2.

The economic benefit of replacing PLA with natural fibers in 3D-printed biocomposites is an important consideration. Natural fibers are generally lower in cost compared to PLA, as they are derived from renewable resources and often sourced as agricultural byproducts. This cost reduction can be significant, especially when fibers partially replace PLA in the composite formulation. Additionally, even if the increase in mechanical properties is marginal, it may still lead to material savings, as a lower amount of composite could achieve the same performance as a pure PLA structure. This potential for material reduction, combined with the lower cost of fibers, enhances the overall economic viability of fiber-reinforced PLA biocomposites, making them a more sustainable and cost-effective alternative in specific applications.

However, an increase only in the reinforcement yarn diameter is not a good solution for printing on larger scales, since the internal fibers of the yarn are not impregnated by the matrix. Consequently, an insufficient wetting is obtained, resulting in a reduced load transfer capacity and affecting the composite performance [49]. An option would be the use of more than one yarn per print, as done by Caron *et al.* [50], who used in flow-based pultrusion process.

Another important result was the higher Young's modulus in jute fiber composites. Despite the smaller diameter and consequent smaller fiber volume fraction, the yarns presented a higher percentage of fibers at their interface compared to ramie and sisal, whose fibers of the yarns were unbonded and presumably did not contribute effectively.

Sisal modulus was the lowest among the yarns tested despite its highest volume fraction for sisal specimens; other characteristics such as waviness may also affect the composite behavior during the elastic range. Moreover, the composite strength is mostly governed by the matrix and the presence of defects in it and along the interface between jute/PLA and ramie/PLA may lead to a premature failure.

The use of continuous vegetable fibers in 3D printing, even in low volumes, has shown potential for reinforcement. Figure 3.16 compares the results from this study with those reported in literature. As mentioned previously, the highest tensile results were obtained with the use of synthetic fibers such as carbon, glass, and aramid. Moreover, several authors used 3D printers already prepared for fiber insertion with nozzles and pre-defined parameters that enabled the use of a high-volume fraction of fiber. On the other hand, the increase in fiber diameter is inversely proportional to the tensile strength of the composite.

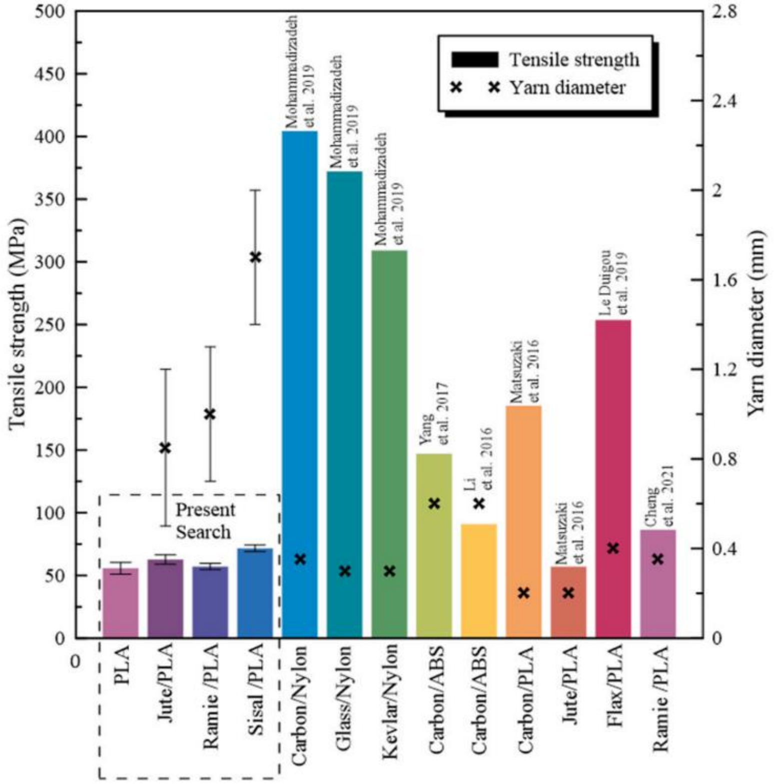

Figure 3.16 - Comparison of tensile strength for different continuous yarn printed composites [24,27,32,35,38,39].

Regarding vegetable reinforced specimens, Le Duigou *et al.* [27] and Cheng *et al.* [32] used low diameters of 0.40 and 0.35mm for a better fiber-matrix interaction; however, the large-scale printing production was compromised. Cheng *et al.* [32] performed a pre-treatment of the fiber decreasing porosity, thus resulting in a better interfacial behavior. The ramie used in the present study was obtained by untwisting a commercial string, thus this may result in weaker yarns.

Figure 3.17 shows a mean yarn stress-strain curve; the grey band corresponds to the envelope (i.e. scatter dispersion). Brittle failure with fiber slippage was observed as the typical failure mode, evidencing the low interfacial adhesion between the fiber and the matrix. Such a low adhesion combined with a low volume fraction, especially in cases of reinforcement with jute and ramie, shows the small difference between the mechanical properties of the composite and the matrix. Moreover, all samples failed at the free length, showing that the adoption for prismatic-sampled specimen did not influence the results. Although incipient, such an improvement demonstrated adequate treatments to the process for increasing the fiber fraction can generate a composite of even better properties.

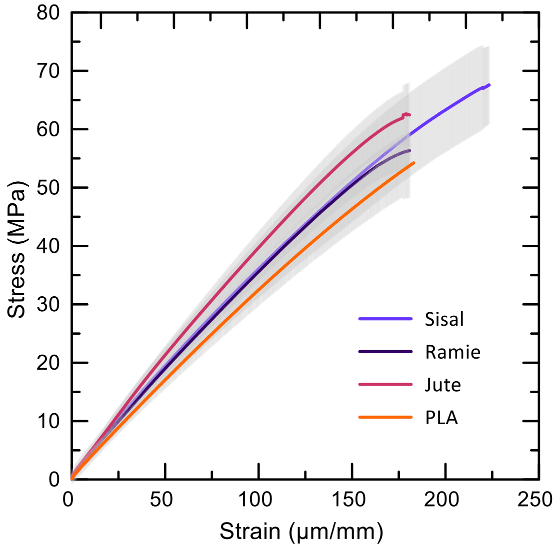

Figure 3.17 - Stress- Strain behavior for each composite.

Regarding composites reinforced with sisal fiber, which showed the highest volume fraction tested, some of the specimens exhibited a pseudo-ductile behavior. In fact, after the matrix failure, fibers were able to bridge the crack and sustain a certain load, showing an increase in toughness. Figure 3.18 displays a comparative force x displacement test of each vegetable fiber printed specimen and the sisal's ability to sustain a certain load after matrix rupture.

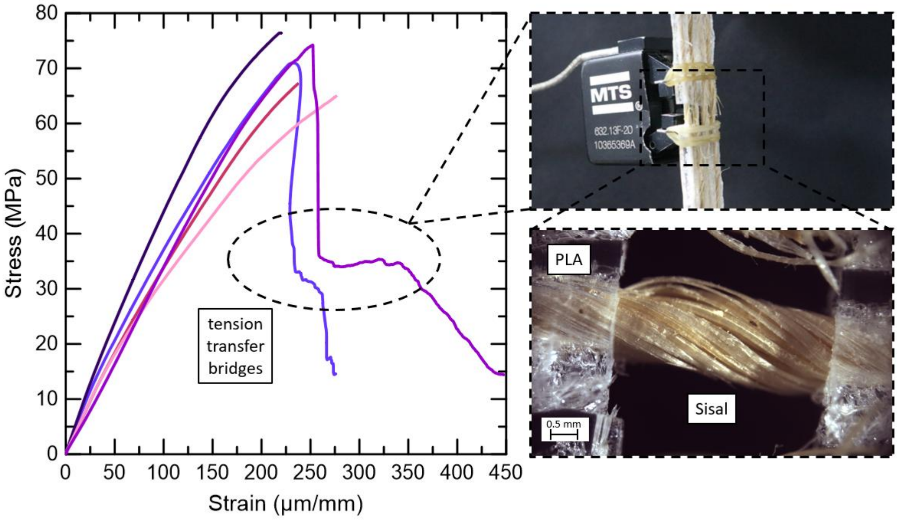

Figure 3.18 - Stress x Strain curves for specimens produced with sisal yarns.

3.5 Conclusions

This study assessed the possibilities of using vegetable fibers in the form of yarns as reinforcement for 3D printing complex biocomposite-based components. Analysis of the method was conducted through by using printed composites reinforced with yarns of jute, ramie and sisal fibers subjected to fiber mechanical tests. The following conclusions have been drawn:

- The study demonstrated the feasibility of using a large diameter printing nozzle for printing biocomposites reinforced with larger vegetable yarns. Furthermore, it was found that a larger diameter is correlated with a reduction in energy consumption per unit volume. In addition, the use of vegetable fiber yarns also contributes to the reduction of the total volume of polymer to be heated (up to 48.2% of polymer replaced by fiber in printing), reducing the overall carbon footprint of the composite.

- The printing parameters such as speed, temperature and flow were kept constant for a better qualitative analysis of the prints with the different fibers tested. It was observed that the load transfer capacity, fiber-matrix adhesion, and the composite performance are strongly dependent on the impregnation of the fiber by the matrix, which are related to the aforementioned parameters, as well as on the yarn diameter and characteristics.
- Despite their lower strength in comparison to the single fiber, vegetable yarns reinforcement potential for 3D printing was confirmed. Increases of 12.76% and 28.61% were observed for composites reinforced with jute and sisal, respectively. The highest modulus was reported for jute-reinforced PLA, with 4.32±0.34 GPa.
- Lastly, the investigation highlighted the feasibility of incorporating plant-based continuous fibers as reinforcement in the 3D printing of multilayer components. The occurrence of fiber slippage during the deposition of angled layers emphasized the necessity of setting the printing parameters (such as speed, temperature, and flow) specifically for these regions to prevent this phenomenon and enable the utilization of such fibers in the fabrication of structural elements. Substituting the prevalent synthetic fibers employed in the large-scale printing industry will result in a noteworthy reduction in emissions within the sector.

References

[1] Saxena P, Stavropoulos P, Kechagias J, Salonitis K. Sustainability assessment for manufacturing operations. Energies 2020;13. https://doi.org/10.3390/en13112730.

[2] Tekinalp HL, Kunc V, Velez-Garcia GM, Duty CE, Love LJ, Naskar AK, et al. Highly oriented carbon fiber-polymer composites via additive manufacturing. Composites Science and Technology 2014;105:144–50. https://doi.org/10.1016/j.compscitech.2014.10.009.

[3] Plymill A, Minneci R, Alexander Greeley D, Gritton J, Greeley D, Minneci R, et al. Graphene and Carbon Nanotube PLA Composite Feedstock Development for Fused Deposition Modeling 2016.

[4] Mohanty AK, Misra M, Hinrichsen G. Biofibres, biodegradable polymers and biocomposites: An overview. Macromolecular Materials and Engineering 2000;276–277:1–24. https://doi.org/10.1002/(SICI)1439-2054(20000301)276:1<1::AID-MAME1>3.0.CO;2-W.

[5] Wang K, Addiego F, Laachachi A, Kaouache B, Bahlouli N, Toniazzo V, et al. Dynamic behavior and flame retardancy of HDPE/hemp short fiber composites: Effect of coupling agent and fiber loading. Composite Structures 2014;113:74–82. https://doi.org/10.1016/j.compstruct.2014.03.009.

[6] Badouard C, Traon F, Denoual C, Mayer-Laigle C, Paës G, Bourmaud A. Exploring mechanical properties of fully compostable flax reinforced composite filaments for 3D printing applications. Industrial Crops and Products 2019;135:246–50. https://doi.org/10.1016/j.indcrop.2019.04.049.

[7] Mohanty AK, Misra M, Drzal LT. Natural Fibers, Biopolymers, And Biocomposites. 2005.

[8] Kechagias J, Chaidas D. Fused filament fabrication parameter adjustments for sustainable 3D printing. Materials and Manufacturing Processes 2023;38:933–40. https://doi.org/10.1080/10426914.2023.2176872.

[9] Fountas NA, Kechagias JD, Zaoutsos SP, Vaxevanidis NM. Experimental and statistical study on the effects of fused filament fabrication parameters on the tensile strength of hybrid PLA/Wood fabricated parts. Procedia Structural Integrity 2022;41:638–45. https://doi.org/10.1016/j.prostr.2022.05.072.

[10] Bianchi I, Forcellese A, Mancia T, Simoncini M, Vita A. Process parameters effect on environmental sustainability of composites FFF technology. Materials and Manufacturing Processes 2022;37:591–601. https://doi.org/10.1080/10426914.2022.2049300.

[11] Long Y, Zhang Z, Yan C, Huang Z, Fu K, Li Y. Multi-objective optimization for improving printing efficiency and mechanical properties of 3D-printed continuous plant fibre composites. Composites Communications 2022;35:101283. https://doi.org/10.1016/j.coco.2022.101283.

[12] Osman MA, Atia MRA. Investigation of ABS-rice straw composite feedstock filament for FDM. Rapid Prototyping Journal 2018;24:1067–75. https://doi.org/10.1108/RPJ-11-2017-0242.

[13] Girdis J, Gaudion L, Proust G, Löschke S, Dong A. Rethinking Timber: Investigation into the Use of Waste Macadamia Nut Shells for Additive Manufacturing. Jom 2017;69:575–9. https://doi.org/10.1007/s11837-016-2213-6.

[14] Le Guen MJ, Hill S, Smith D, Theobald B, Gaugler E, Barakat A, et al. Influence of Rice Husk and Wood Biomass Properties on the Manufacture of Filaments for Fused Deposition Modeling. Frontiers in Chemistry 2019;7:15–20. https://doi.org/10.3389/fchem.2019.00735.

[15] Ahmed W, Alnajjar F, Zaneldin E, Al-Marzouqi AH, Gochoo M, Khalid S. Implementing FDM 3D printing strategies using natural fibers to produce biomass composite. Materials 2020;13. https://doi.org/10.3390/ma13184065.

[16] Wang X, Jiang M, Zhou Z, Gou J, Hui D. 3D printing of polymer matrix composites: A review and prospective. Composites Part B: Engineering 2017;110:442–58. https://doi.org/10.1016/j.compositesb.2016.11.034.

[17] Kandemir A, Pozegic TR, Hamerton I, Eichhorn SJ, Longana ML. Characterisation of natural fibres for sustainable discontinuous fibre composite materials. Materials 2020;13. https://doi.org/10.3390/ma13092129.

[18] Jauhari N, Mishra R, Thakur H. Natural Fibre Reinforced Composite Laminates - A Review. Materials Today: Proceedings 2015;2:2868–77. https://doi.org/10.1016/j.matpr.2015.07.304.

[19] Neto JSS, Lima RAA, Cavalcanti DKK, Souza JPB, Aguiar RAA, Banea MD. Effect of chemical treatment on the thermal properties of hybrid natural fiber-reinforced composites. Journal of Applied Polymer Science 2019;136:1–13. https://doi.org/10.1002/app.47154.

[20] Mukherjee PS, Satyanarayana KG. Structure and properties of some vegetable fibres - Part 1 Sisal fibre. Journal of Materials Science 1984;19:3925–34. https://doi.org/10.1007/BF00980755.

[21] Sambandamoorthy S, Narayanan V, Chinnapandi LBM, Aziz A. Impact of fiber length and surface modification on the acoustic behaviour of jute fiber. Applied Acoustics 2021;173:107677. https://doi.org/10.1016/j.apacoust.2020.107677.

[22] Arsène, M-A Savastano Jr, H. Allameh, S. M. Ghavami K, Soboyejo WO. Cementitious composites reinforced with vegetable fibers. Proceedings of the 1st Interamerican Conference on Non-Conventional Materials and Technologies in the Eco-Construction and Infrastructure (IAC-NOCMAT) 2003:13–6.

[23] Wambua P, Ivens J, Verpoest I. Natural fibres: Can they replace glass in fibre reinforced plastics? Composites Science and Technology 2003;63:1259–64. https://doi.org/10.1016/S0266-3538(03)00096-4.

[24] Mohammadizadeh M, Imeri A, Fidan I, Elkelany M. 3D printed fiber reinforced polymer composites - Structural analysis. Composites Part B: Engineering 2019;175:107112. https://doi.org/10.1016/j.compositesb.2019.107112.

[25] Mohammadizadeh M, Fidan I, Allen M, Imeri A. Creep behavior analysis of additively manufactured fiber-reinforced components. International Journal of Advanced Manufacturing Technology 2018;99:1225–34. https://doi.org/10.1007/s00170-018-2539-z.

[26] Garrett W. Melenkaa, Benjamin K.O. Cheunga, Jonathon S. Schofielda, Michael R. Dawsonb JPC. Evaluation and Prediction of the Tensile Properties of Continuous Fiber-Reinforced 3D Printed Structures Authors: Garrett W. Melenka 2016.

[27] Le Duigou A, Barbé A, Guillou E, Castro M. 3D printing of continuous flax fibre reinforced biocomposites for structural applications. Materials and Design 2019;180:107884. https://doi.org/10.1016/j.matdes.2019.107884.

[28] Abreu S. Low cost 3D printing versus high cost equipment printing 2015:235. https://doi.org/10.1002/jmri.21433.

[29] Pervaiz S, Qureshi TA, Kashwani G, Kannan S. 3D Printing of Fiber-Reinforced Plastic Composites Using Fused Deposition Modeling: A Status Review. Materials 2021;14:4520. https://doi.org/10.3390/ma14164520.

[30] Khosravani MR, Frohn-Sörensen P, Reuter J, Engel B, Reinicke T. Fracture studies of 3D-printed continuous glass fiber reinforced composites. Theoretical and

Applied Fracture Mechanics 2022;119:103317. https://doi.org/10.1016/j.tafmec.2022.103317.

[31] Khosravani MR, Reinicke T. Effects of fiber on the fracture behavior of 3D-printed fiber reinforced nylon. Procedia Structural Integrity 2021;35:59–65. https://doi.org/10.1016/j.prostr.2021.12.048.

[32] Cheng P, Wang K, Chen X, Wang J, Peng Y, Ahzi S, et al. Interfacial and mechanical properties of continuous ramie fiber reinforced biocomposites fabricated by in-situ impregnated 3D printing. Industrial Crops and Products 2021;170:113760. https://doi.org/10.1016/j.indcrop.2021.113760.

[33] Cheng P, Wang K, Chen X, Le Duigou A, Peng Y, Wen W. Compressive property and shape memory effect of 3D printed continuous ramie fiber reinforced biocomposite corrugated structures. Smart Materials and Structures 2022;31:124003. https://doi.org/10.1088/1361-665x/ac95e4.

[34] Cheng P, Peng Y, Wang K, Le Duigou A, Yao S, Chen C. Quasi-static penetration property of 3D printed woven-like ramie fiber reinforced biocomposites. Composite Structures 2023;303:116313. https://doi.org/10.1016/j.compstruct.2022.116313.

[35] Yang C, Tian X, Liu T, Cao Y, Li D. 3D printing for continuous fiber reinforced thermoplastic composites: Mechanism and performance. Rapid Prototyping Journal 2017;23:209–15. https://doi.org/10.1108/RPJ-08-2015-0098.

[36] Krajangsawasdi N, Longana ML, Hamerton I, Woods BKS, Ivanov DS. Batch production and fused filament fabrication of highly aligned discontinuous fibre thermoplastic filaments. Additive Manufacturing 2021;48:102359. https://doi.org/10.1016/j.addma.2021.102359.

[37] Krajangsawasdi N, Hamerton I, Woods BKS, Ivanov DS, Longana ML. Open Hole Tension of 3d Printed Aligned Discontinuous Composites. SSRN Electronic Journal 2022. https://doi.org/10.2139/ssrn.4204558.

[38] Li N, Li Y, Liu S. Rapid prototyping of continuous carbon fiber reinforced polylactic acid composites by 3D printing. Journal of Materials Processing Technology 2016;238:218–25. https://doi.org/10.1016/j.jmatprotec.2016.07.025.

[39] Ryosuke Matsuzaki, Masahito Ueda, Masaki Namiki, Tae-Kun Jeong H, Keisuke Horiguchi, Taishi Nakamura A& YH. Three-dimensional printing of continuous-fiber composites by in-nozzle impregnation 2016.

[40] Castoldi R. Mechanical properties and durability of concretes reinforced with polypropylene and sisal fibers. Pontifical Catholic University of Rio de Janeiro, 2018.

[41] Schindelin J, Arganda-Carreras I, Frise E, Kaynig V, Longair M, Pietzsch T, et al. Fiji: an open-source platform for biological-image analysis. 2012. https://doi.org/10.1038/nmeth.2019.

[42] ASTM INTERNATIONAL. ASTM D3039 / D3039M - Standard Test Method for Tensile Properties of Polymer Matrix Composite Materials. Annual Book of ASTM Standards n.d.;15.03. https://doi.org/10.1520/D3039_D3039M-17.

[43] Mochizuki M. Structural Effects on Biodegradation of Aliphatic Polyesters. Sen'i Gakkaishi 1996;52:203–9. https://doi.org/10.2115/fiber.52.5_P200.

[44] Kandemir A, Longana ML, Panzera TH, del Pino GG, Hamerton I, Eichhorn SJ. Natural fibres as a sustainable reinforcement constituent in aligned discontinuous polymer composites produced by the HiPerDiF method. Materials 2021;14. https://doi.org/10.3390/ma14081885.

[45] Hsueh MH, Lai CJ, Wang SH, Zeng YS, Hsieh CH, Pan CY, et al. Effect of printing parameters on the thermal and mechanical properties of 3d-printed pla and petg, using fused deposition modeling. Polymers 2021;13. https://doi.org/10.3390/polym13111758.

[46] 3dprinterly. What is the Best Print Speed for 3D Printing? Perfect Settings 2021. https://3dprinterly.com/best-print-speed-settings-for-3d-printing/#:~:text=A good print speed for 3D printing ranges from 40mm,of different speeds on quality. (accessed August 11, 2022).

[47] Joseph K, Tolêdo Filho RD, James B, Thomas S, Carvalho LH de. Review on Sisal Fiber Reinforced Polymer Composites. Brazilian Journal of Agricultural and Environmental Engineering 1999;3:367–79. https://doi.org/10.1590/1807-1929/agriambi.v3n3p367-379.

[48] Satyanarayana KG, Guimarães JL, Wypych F. Studies on lignocellulosic fibers of Brazil. Part I: Source, production, morphology, properties and applications.

Composites Part A: Applied Science and Manufacturing 2007;38:1694–709. https://doi.org/10.1016/j.compositesa.2007.02.006.

[49] Umer R, Bickerton S, Fernyhough A. The effect of yarn length and diameter on permeability and compaction response of flax fibre mats. Composites Part A: Applied Science and Manufacturing 2011;42:723–32. https://doi.org/10.1016/j.compositesa.2011.02.010.

[50] Caron JF, Demont L, Ducoulombier N, Mesnil R. 3D printing of mortar with continuous fibres: Principle, properties and potential for application. Automation in Construction 2021;129. https://doi.org/10.1016/j.autcon.2021.103806.

Chapter 4 - ANALYSIS OF VOIDS, INTERFACIAL, AND THERMAL PROPERTIES OF ADDITIVELY MANUFACTURED CONTINUOUS NATURAL FIBER-REINFORCED BIOCOMPOSITES

This chapter was published under the reference:
Natália V. Santos, Daniel K. K. Cavalcanti, Jorge S. S. Neto, Henrique F. M. de Queiroz, Mariana D. Banea, Daniel C.T Cardoso, Analysis of voids, interfacial and thermal properties of additively manufactured continuous natural fiber-reinforced biocomposites. Progress in Additive Manufacturing (2024).
https://doi.org/10.1007/s40964-024-00913-5

The incorporation of continuous natural fibers as reinforcement in Fused Filament Fabrication (FFF) is influenced by the intrinsic characteristics of the printing process. Analyzing the effects of this type of reinforcement is essential for achieving high-performance biocomposites. This study evaluates the impact of heating temperature on fiber and biocomposite properties, the types of voids generated during printing, and the quality of the fiber-matrix interface. Thermal and image analyses were conducted to investigate the fibers' thermal behavior and the presence of voids. Additionally, a novel methodology was developed to fabricate thermoplastic printed samples reinforced with natural large-diameter yarns for pull-out tests. The results indicate that the natural fibers exhibit suitable thermal stability for FFF applications, with the lignin degradation peak occurring between 294.6°C and 366.1°C, which is above the FFF printing temperature range for PLA (160°C to 220°C). However, image analysis revealed that larger yarn diameters compromise the interfacial bonding with the matrix material, despite partial impregnation along the perimeter of the yarn. Void content was observed to reach up to 57.0% of the total volume, emphasizing the inadequate material impregnation within the yarn structure. Overall, the findings confirm the potential of utilizing continuous natural fibers as reinforcements in FFF-based composites.

4.1. Introduction

Additive manufacturing (AM), also known as 3D printing, has become a go-to technology across various industry sectors, thanks to its numerous advantages over traditional manufacturing techniques. Traditionally, the complexity and the overall efficiency of a part to be manufactured are dependent on the specific printing parameters [1] and materials used. With the assistance of AM, these two factors are functionally decoupled, allowing highly complex parts to be fabricated at essentially the same cost as much simpler ones. However, despite the ease of fabrication, the polymer properties are usually insufficient to meet structural application requirements and modifications to the traditional polymer-printing approach may be necessary.

The 3D printing extrusion process called FFF stands out as one of the most attractive options in AM in terms of simplicity, making it the most widespread technique. This method is characterized by the deposition of material layer by layer in a computer-aided design fashion. Among the possible techniques for enhancing the mechanical properties of the most used polymers in FFF, the fiber reinforcement of the filament itself has proven to be one of the most promising [2]. The reinforcements can be of three main categories: fillers, discontinuous and continuous fibers. 3D printing of continuous natural fiber-polymer printing has become a suitable alternative to produce a material with good mechanical properties while accounting for the use of renewable resources [3].

The choice of which filament to use is very important because its characteristics directly influence the possibilities of reinforcement once the continuous fiber is subjected to the melting temperature of the thermoplastic polymer material [4]. Therefore, particularly in the scenario of natural fibers exhibiting diminished thermal stability, the investigation of the potential correlation between the polymer's melting temperature, where the main printing polymers have their melting point ranging from 160 to 240°C [5,6], and the degradation of the natural material becomes imperative. Some recent works reported a concern with the integrity of the fibers used as reinforcement in the printing process. Thermal studies to verify the integrity of the reinforcement of synthetic fibers in printing by FFF were carried out by analyzing the peak crystallization of the copolymer Nylon/micro carbon fibers (Onyx) and the degradation temperature of the carbon fiber, verifying that the working temperature of the printer did not lead to degradation or weight loss, i.e., not compromising the material properties [7]. Additionally, the thermal analysis of filaments reinforced with short glass fibers showed that there was an increase in the glass transition temperature (Tg) with the addition of the reinforcement, suggesting that this composition restricted the mobility of the polymeric chains of the composite [8]. Conversely, the thermal integrity analysis of short curauá fibers used as polylactic acid (PLA) reinforcement showed that the increase in fiber concentration reduced the thermal stability of the composites [9].

Another factor of great influence on the composite materials is the adhesion between fiber and matrix at the interface [10]. The influence of the fiber length and the efficiency of the adhesion between the fiber and the matrix are of prime importance to guarantee the highest strength and stiffness values for the composite [11]. In composites, the interface is defined as a reaction or diffusion zone in which these two elements are chemically, physically, and/or mechanically combined [12]. Composites made by a combination of fibers and polymers have their mechanical properties controlled largely by the efficiency of bonding at the interfacial boundary [13]. Poor adhesion is reflected in the inefficient use of the potential of the composite, which can also increase the porosity of the material, making it vulnerable to environmental attacks that can reduce its service life [14]. From a chemical point of view, this poor interfacial adhesion between the fiber and the matrix is due to natural fibers having a hydrophilic nature while most polymeric matrices are hydrophobic [15,16]. This is due to the presence of polar elements in natural fibers, i.e., water-soluble, leading to high moisture absorption [17]. The high moisture absorption of natural fibers, their poor wettability, and the insufficient adhesion between untreated fibers and the polymer matrix lead to sagging with age [18]. The presence of water also leads to the occurrence of swelling, hydrolysis, and matrix plasticization [17], which have deleterious effects on the mechanical properties.

Santos et al. [19] developed a continuous yarn reinforcing method employing a modified FFF hotend adapted for the in-situ impregnation of natural fibers with a biopolymer matrix. In this work, jute, ramie, and sisal fibers were combined with PLA to produce bio-based printed filaments with diameters up to 3 mm for large-scale printing. The results demonstrated that this technique is a viable alternative, significantly enhancing the material properties compared to the neat polymer. However, the study revealed issues related to the fiber-matrix interface and the thermal stability of the biocomposites. Current literature predominantly utilizes smaller-diameter yarns [20–22], which present challenges in producing larger-scale structural elements, and primarily focuses on flax fibers as the main natural reinforcement. This research advances the field by evaluating alternative natural fibers as potential reinforcements and assessing the feasibility of using larger-diameter natural fiber yarns in FFF-printed composites. This approach explores their potential for reinforcing eco-efficient biocomposite structures, particularly for structural applications. The study aims to investigate thermal and adhesion properties, which are crucial for achieving higher performance and broadening the scope of these materials' applications.

4.2. Materials and Methods

4.2.1 Materials

The reinforcing materials used in this work consisted of jute, ramie, and sisal yarns provided by SISALSUL (São Paulo, Brazil). A polylactic acid filament (PLA) with a diameter of 1.75 mm provided by 3DLAB (Minas Gerais, Brazil) was used for the matrix. Table 4.1 and Table 4.2 presents the main properties of the materials used. The cross-sectional area of each yarn was measured by Fiji’s plugin Trainable Weka Segmentation [23], with images acquired through the optical microscope technique (Nikon SMZ800N).

Table 4.1 - Properties of the natural yarns used

Properties	Jute	Ramie	Sisal
Yarn diameter (mm)	0.86±0.22	0.96±0.16	1.72±0.17
Fiber length (mm)	13.19±1.30	14.99±3.19	83.24±9.34
Linear density (TEX)	310±50	330±30	1800±50

Table 4.2 - Properties of the natural materials according to the literature [24,25]

Properties	**Jute**	**Ramie**	**Sisal**	**PLA**
Fiber diameter (μm)	25-200	20-35	50-300	-
Density (g/cm^3)	1.3-1.5	1.5-1.6	1.3-1.5	1.21-1.25
Tensile strength (MPa)	393-800	400-968	468-1150	21-60
Young modulus (GPa)	10-30	44-128	9-22	0.35-3.5
Cellulose (%)	58-71	76	59-73	-
Hemicellulose (%)	12	17	13-24	-
Lignin content (%)	12-14	1	11-15	-
Moisture absorption (%)	12	12-17	11	-
Melting temperature (°C)	-	-	-	160-220°C

4.2.2 Composite manufacture

4.2.2.1 Thermal tests and Image analysis samples

For the thermal tests (i.e. TGA, DSC, and FTIR) and image analysis, (i.e. SEM and μCT) PLA-jute, PLA-ramie, and PLA-sisal composites were manufactured by FFF using a Zmorph VX printer adapted for the simultaneous printing of polymer and continuous natural fiber yarns through In-situ impregnation method [4,19]. The choice for larger-diameter yarns is due to the need to manufacture larger-scale structural elements that require a greater flow for their production to be viable. Figure 4.1a presents a schematic drawing of the extruder configuration whereas the entry of the larger-diameter yarn into the extruder can be observed in Figure 4.1a, which presents a schematic drawing of the extruder configuration, while Figure 4.1b shows the printer's extruder. Table 4.3 summarizes the main printing parameters used for the biocomposite fabrication, based on Santos et al. [19]. The mechanical properties of printed biocomposites were obtained in previous works and are summarized in Table 4.4.

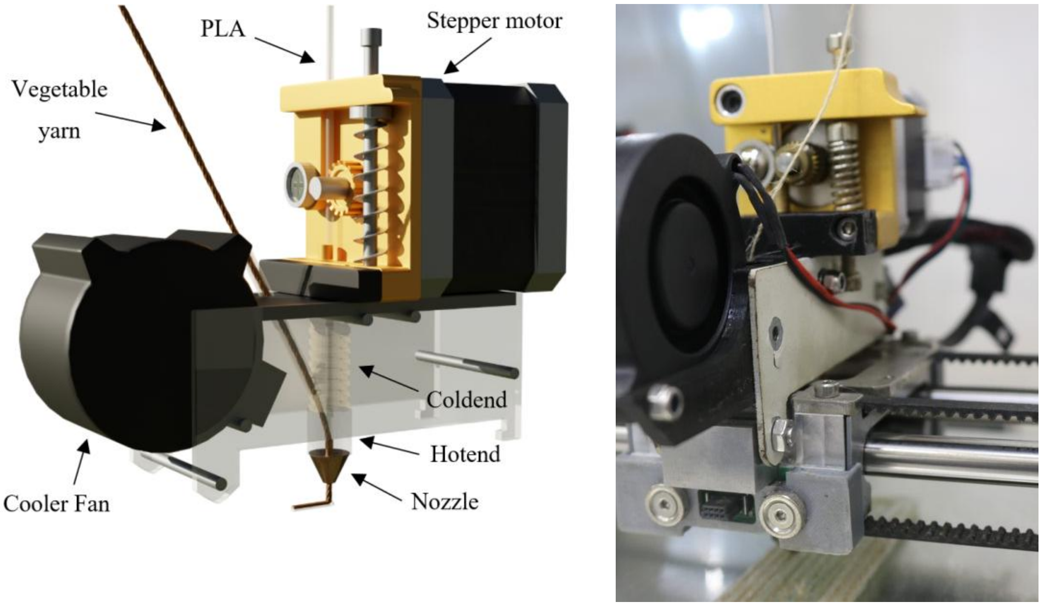

(a) (b)

Figure 4.1 - Extruder printer of the composite (a) schematic drawing and (b) printing extruder.

Table 4.3 - Printing parameters.

Parameter	**Value**
Nozzle diameter	2.1 mm
Printing speed	10 mm/s
Extruder temperature	200 °C
Bed temperature	60 °C
Layer height	1.5 mm
Layer width	3.0 mm

Table 4.4 - Mechanical properties for 3D printed biocomposites [19].

Properties	**Neat PLA**	**PLA-Ramie**	**PLA-Jute**	**PLA-Sisal**
Fiber volume fraction	-	10.8-18.3	12.5-21.8	34.3-48.2
Tensile strength (MPa)	55.7±4.6	57.2±2.5	62.8±3.6	71.6±2.6
Young's Modulus (GPa)	3.4±0.2	3.8±0.1	4.3±0.3	4.0±0.5

4.2.2.2 Pull-out test

The printed specimens for the pull-out tests were prepared with four polylactic acid (PLA) layers using an Ender V3 machine available at the Laboratory of Structures and Materials (LEM-DEC) (PUC-Rio, Rio de Janeiro, Brazil). The test methodology developed in this study is novel and was designed to replicate, with fidelity, the phenomena intrinsic to the printing process through in-situ impregnation. During this procedure, the matrix layers undergo fusion, ensuring complete encapsulation of the yarn within the interlayer joint. The layer dimensions must possess sufficient width to obviate the formation of inter-filament voids. This methodology is innovative because it simulates the pull-out behavior of natural yarns in thermoplastic composites produced via FFF, a technique that has not been previously applied in literature. The approach replicates the effect of PLA impregnation observed during printing, where the deposition of molten material over the fiber promotes its partial infiltration into the yarn structure. It is important to note that this methodology was specifically developed to simulate the impregnation behavior caused by the layer-by-layer deposition of PLA over the fiber, rather than the pressure effects occurring inside the nozzle during in-situ impregnation. Unlike the modified printer-head, where the fiber experiences pressure within the nozzle, the pull-out test specimens were designed to replicate the interaction between molten PLA and the fiber as it is deposited. The process involves producing half of the layers (Figure 4.2a), pausing the process to position the fibers (Figure 4.2b), and printing the final layers (Figure 4.2c). Table 4.5 summarizes the main printing parameters.

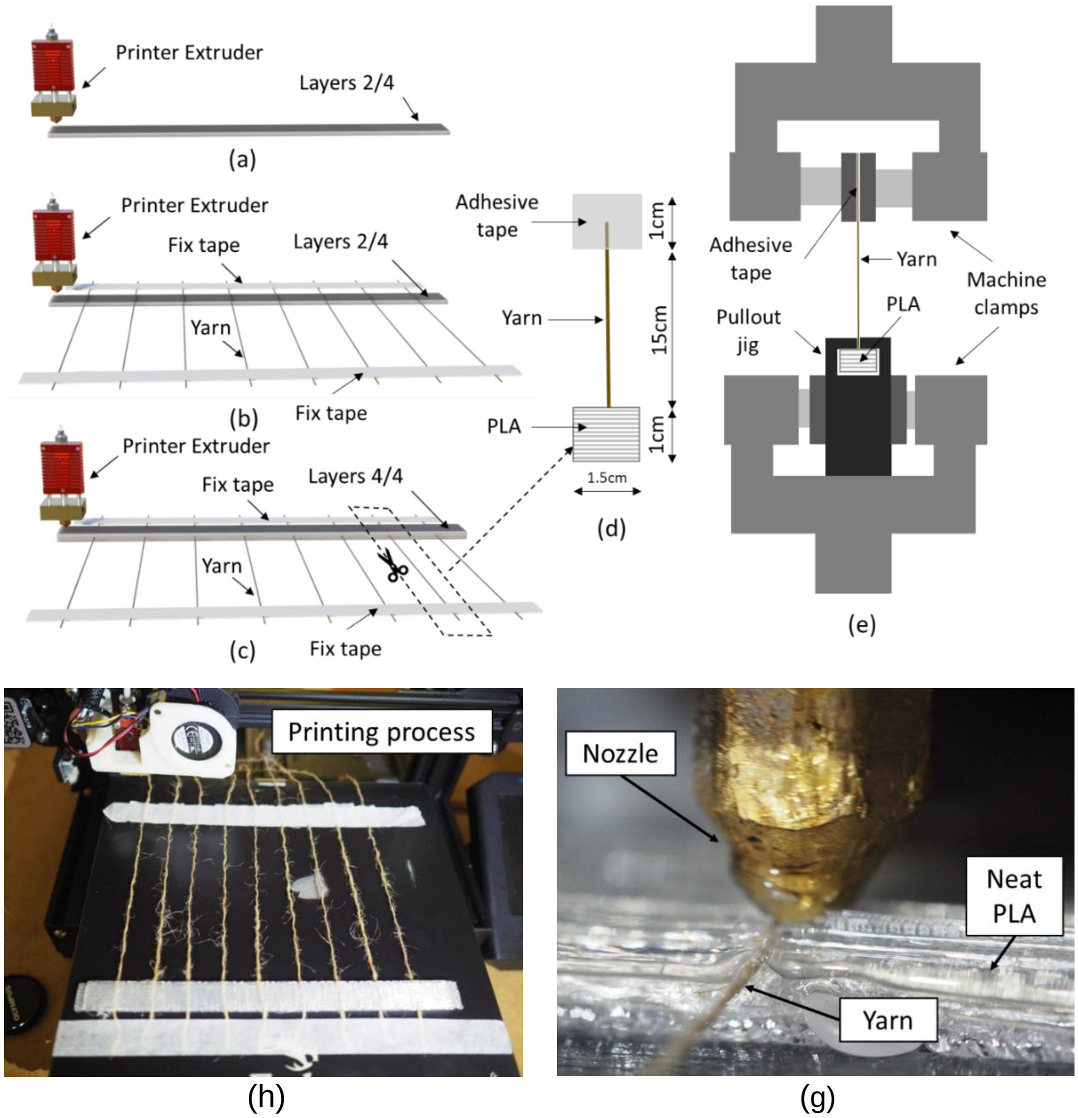

Figure 4.2 - Pull-out test process: (a) printing of half of the layers, (b) positioning the yarns, (c) printing the final layers, (d) pull-out sample, (e) pull-out test setup, (f) printing process, and (g) deposition detail.

Table 4.5 - Pull-out test printing parameters.

Parameter	**Value**
Nozzle diameter	1.0 mm
Printing speed	2.5 mm/s
Extruder temperature	200 °C
Bed temperature	60 °C
Layer height	1.0 mm
Layer width	1.0 mm

4.2.3 Testing Methods

4.2.3.1 Microstructural analyses

4.2.3.1.1 Scanning Electron Microscopy (SEM)

The cross-sections of the specimens were analyzed using a Tescan Clara Scanning Electron Microscope equipment operating at 2 keV. The samples were dried in an oven at 60°C for 24 hours and kept in a desiccator to remove moisture. The metallization process was conducted by covering the samples with a layer of gold to improve their conductivity. The SEM provides insights into fiber-matrix interactions, as well as the structure, yarn impregnation, and fiber positioning within the PLA matrix, offering a detailed understanding of the composite's internal configuration.

4.2.3.1.2 X-ray microtomography (μCT)

A XRANDIA 510 Versa microtomography microscope equipment available in Image Analysis and Digital Microscopy Group (MicDigi) in the Chemical and Materials Engineering Department (PUC-Rio, Rio de Janeiro, Brazil) was used. The fiber distribution in the matrix and the presence of defects in the sample such as porosity were evaluated. It is a non-destructive qualitative technique based on the principle of radiography that allows for obtaining 2D and 3D images of bulk material. The images were processed using the Dragonfly© software [26]. Reduced computational demands were achieved by delineating smaller regions of interest around the sample's image to eliminate the background. The tomography scan consists of the sample (multilayer jute-reinforced polymer) and an empty background. The segmentation sample image used was a prism with dimensions of 5.48×6.80×8.09mm. The technique allowed analyzing void sizes and types that cannot be assessed with other techniques.

4.2.3.2 Thermogravimetric Analysis (TGA)

The TGA analysis was carried out via NETZSCH TG 209F3 Tarsus equipment available in the LADES (CEFET/RJ, Rio de Janeiro, Brazil). Each sample was tested in the temperature range of 20-550°C at a constant rate of 10 °C min^{-1} under nitrogen (N2) atmosphere, with the temperature range selected based on studies from the literature on natural fiber-reinforced biocomposites [27] and AM [9]. Approximately 20 mg of each composite sample was used for each measurement and the testing procedure followed the recommendations of the ASTM E1131 [28]. The objective of this test was to assess the degradation characteristics of the material by analyzing moisture content, degradation temperature, the presence of volatile components, and ash content. In the context of this research, it was used to analyze the degradation behavior of natural fibers and biocomposites, evaluating the effects of heating the fibers during 3D printing and verifying their possible effects.

4.2.3.3 Differential Scanning Calorimetry (DSC)

The temperature-dependent transformations of the composite samples were carried out in a NETZSCH DSC 200F3 Maia equipment, available in the LADES (CEFET/RJ, Rio de Janeiro, Brazil). The experiment was conducted with a heating rate of 20 C° min^{-1}, in the temperature range of 20-550°C with a nitrogen (N2 flux of 50 mL min^{-1}). About 20 mg of each sample were used and the procedures of the ASTM D3418 [29] were followed. The test aims to identify the glass transition temperature (Tg) and crystalline melting temperature (Tm) as well as factors such as degree of crystallinity, crosslinking, and thermal, and oxidative stability. In the context of this research, it was used to analyze the matrix, natural fibers, and the biocomposite. The addition of fibers within the thermoplastic matrix can affect the thermal properties of the composites [24].

Although the polymer matrix used in this study has a printing temperature of 200 °C, testing up to 500 °C was necessary to capture the complete degradation profile of the natural fibers. A broader temperature range ensures the identification of all critical decomposition points. Moreover, it provides relevant data for future studies exploring high-performance polymers that operate at higher extrusion temperatures beyond 300 °C.

4.2.3.4 Fourier-transform infrared spectrometry (FTIR)

FTIR of fiber samples was carried out in FTIR-ART Spectra-Two equipment from Perkin-Elmer available in the Synthesis and Characterization Laboratory

(NanoLaserLab) (PUC-Rio, Rio de Janeiro, Brazil). The resolution for all the spectra was 4 cm^{-1}, and the average number of co-added scans was 32. The ASTM E1252 international standard was used [30]. The chemical interactions between the reinforcement and matrix are an integral part of the makeup of the composite and its overall properties, therefore, their study is necessary. FTIR tests permit the identification of the chemical groups of the samples and the evaluation of the main differences between the chemical composition of each fiber studied.

4.2.3.5 Pull-out

The pull-out tests were performed using an Instron® 5966 universal testing machine equipped with a 1kN load cell (Norwood, MA, USA) available in the Laboratory of Adhesives and Composites Materials (LADES) (CEFET/RJ, Rio de Janeiro, Brazil). The tests were carried out at room temperature (23°C) and 50% relative humidity, at a displacement rate of 0.2 mm/min up to failure. The final specimen had a free length of 125 mm and an embedded length of 11±1 mm. Five samples of each yarn were tested. A jig was used to ensure that no other forces (clamp pressure) interfered with the pull-out test. Figure 4.3 shows the pullout test sample and setup. The execution of this test was based on the work of Lima et al. [31].

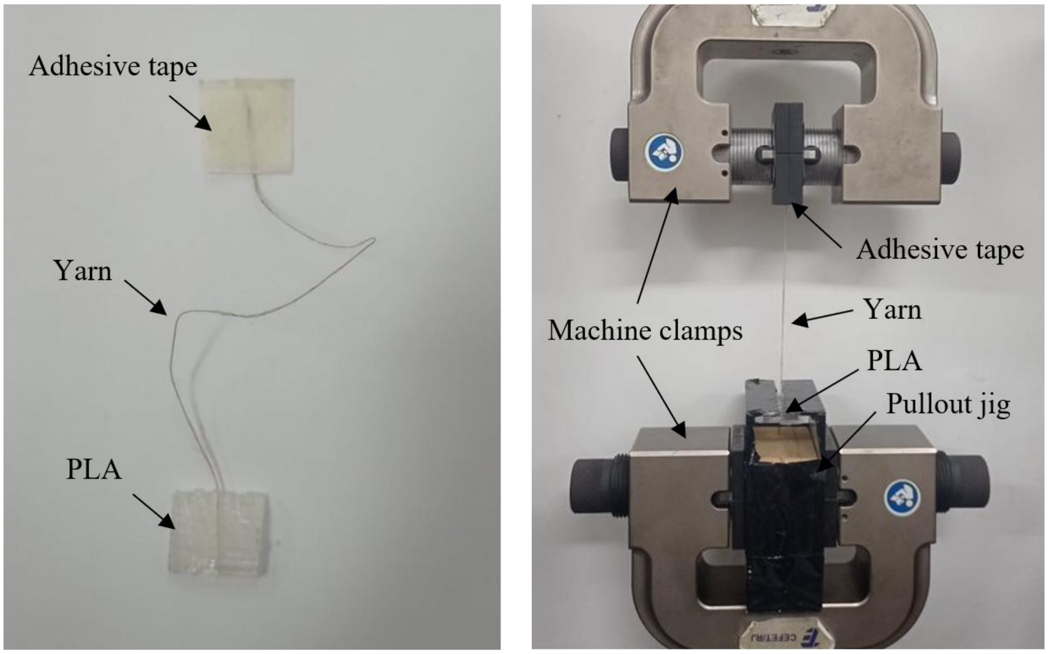

(a) (b)

Figure 4.3 - Pull-out test specimen production: (a) printed sample (b) pull-out test setup.

4.2.3.5.1 Pull-out data analysis

The Interfacial Shear Stress (IFSS) was calculated using equation (1) by Kelly et al. [32], where P is the applied load (N), r is the equivalent radius, and l corresponds to the embedded length of the yarn. The diameters of the yarns were obtained through a Nikon SMZ800N optical microscope and measured using FIJI [23] Software.

$$\tau_{ISS} = \frac{P}{2\pi r l_e} \quad (1)$$

4.3. Results and Discussion

4.3.1 Types and effects of voids on printing quality

The generation of voids during the extrusion of the fiber and matrix from the nozzle may affect the overall mechanical performance of the biocomposites. Santos et al. [19] highlight that the formation of voids results from a combination of factors including printing speed, filament diameter, and printing temperature. Figure 4.4a and 4.4b show representative SEM images of a single layer of the reinforced printed material. The 3D printing process using the in-situ impregnation of continuous fibers results in the eccentricity of the yarn in the layer, as shown in Figure 4.4c [4]. Furthermore, due to the misalignment of the natural yarn, its upper part remains exposed and is only covered by PLA when a new printed layer is deposited on top of the previous one (Figure 4.4d). Upon deposition, the upper layer experiences a temperature disparity compared to the lower layer, resulting in what is commonly called a cold joint (i.e. imperfect fusion between the upper and lower layer) [33]. Moreover, this type of interaction can result in lower interlaminar shear strength between deposited layers. The images show an apparent good yarn-matrix interaction, evidenced by the absence of voids throughout the interface. However, it appears that polymer permeation into the yarn core is minimal. As a result, the adhesion predominantly occurs at the surface of the yarn, leaving the inner fibers largely unaffected. This superficial bonding limits the ability of the polymer to effectively engage the inner fibers, reducing their contribution to the overall mechanical performance of the composite material.

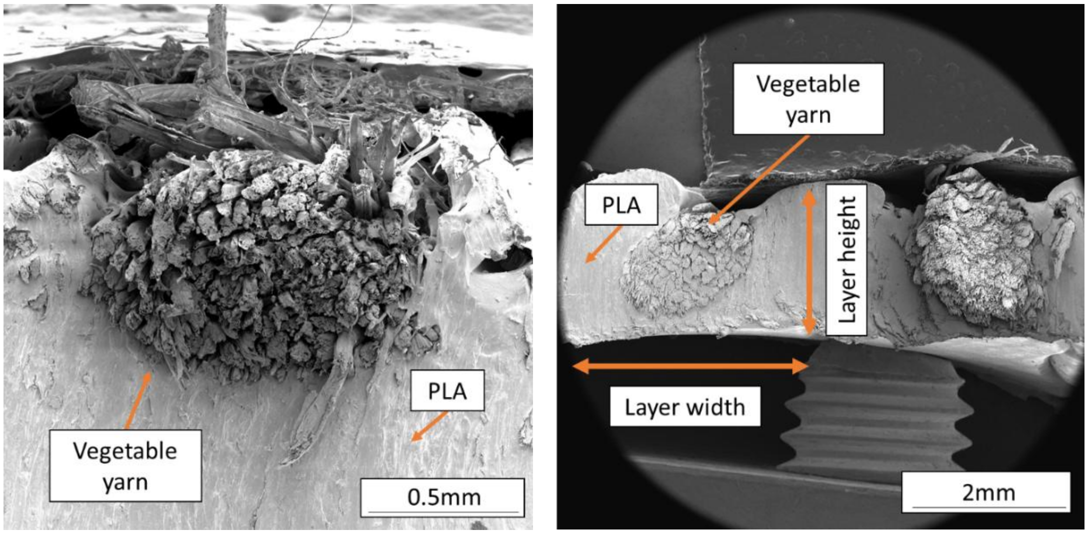

(a) (b)

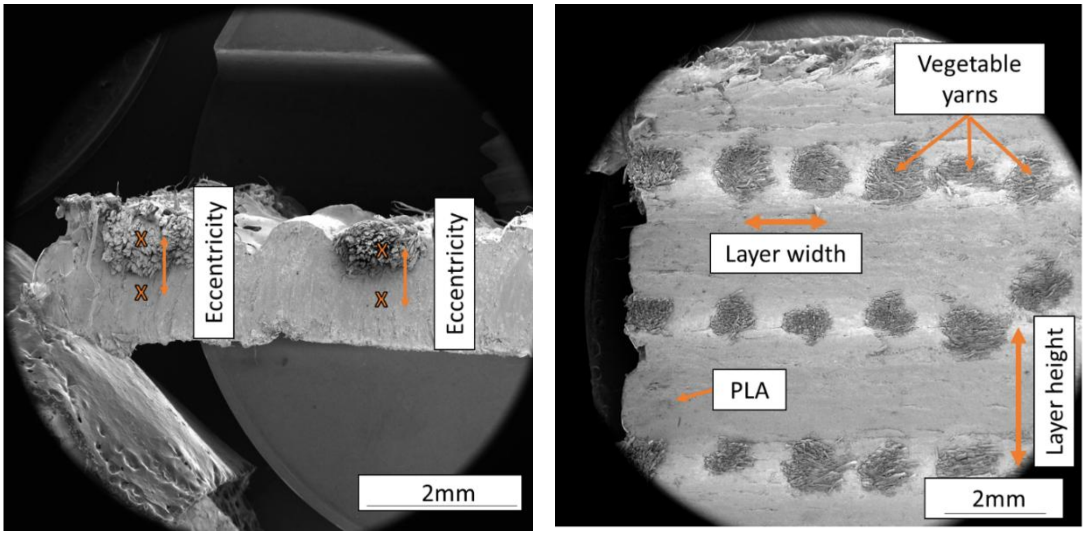

(c) (d)

Figure 4.4 - SEM of a printed layer reinforced: (a) closeup of a jute yarn within the PLA matrix, (b) single layer sisal reinforced specimen, (c) Eccentricity of single layer ramie fiber, and (d) multilayered jute reinforced specimen.

Through the examination of a tomographic specimen of the printed composite material reinforced with continuous jute fibers, it is possible to highlight the presence of three distinct categories of voids that contribute to the porosity of the biocomposite specimen, as illustrated in Figure 4.5. These voids can be categorized as inter-filament voids, bubbles, and fiber-matrix interfacial voids. Inter-filament voids are attributed to the geometric characteristics of the printed layers, exhibiting an ellipsoidal morphology resulting from imperfect interlayer adhesion during deposition [34]. On the other hand, bubbles, as explained by Santos and Cardoso [19], originate from variations in the deposition speed and printing temperature. Finally, fiber-matrix interfacial voids are related to the large-yarn diameter and the insufficient impregnation time during the printing process, which limits the complete penetration of the thermoplastic into the yarn, leading to voids.

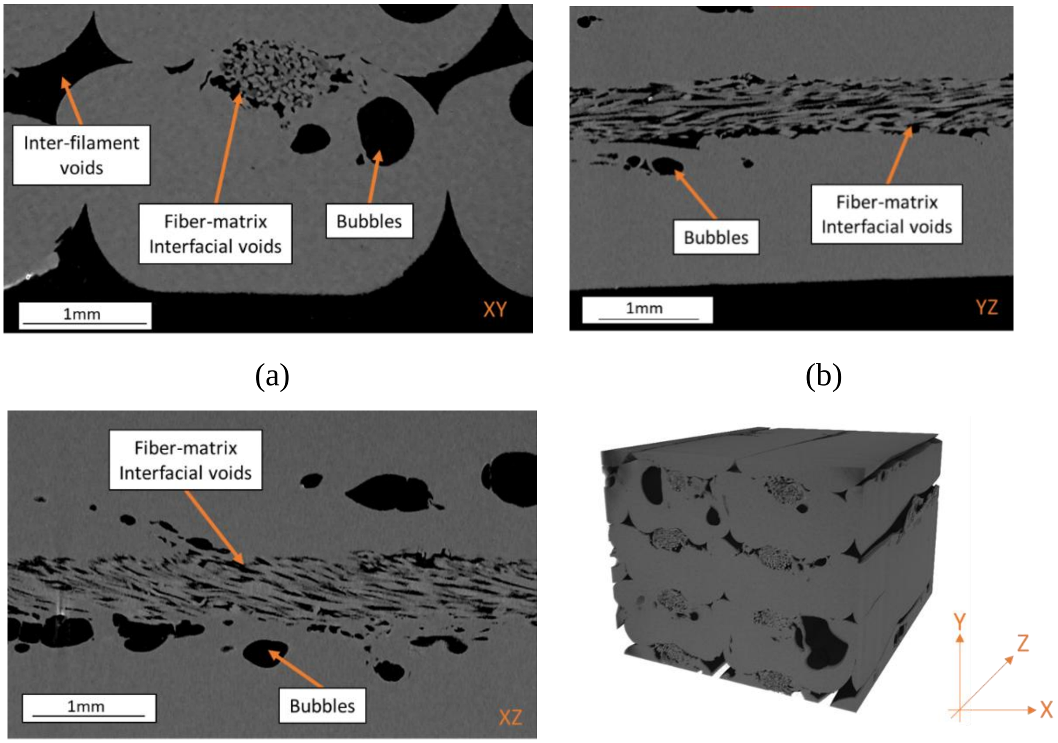

(a) (b)

(c) (d)

Figure 4.5 - MicroCT analyses of printed layers reinforced with jute: (a) XY Plane, (b) YZ Plane, (c) XZ Plane, and (d) 3D Model.

By employing image analysis, the volumetric content of voids within the bioprinted material can be quantified. The total porosity of the sample, accounting for all types of voids, was measured at 11.7% (as depicted in Figure 4.6a and 4.7b). In comparison to Saidane et al. [35], who explored the utilization of continuous glass fiber reinforcement in FFF with extrusion-based impregnation methods, an upper limit of 8.0% porosity was reported. Furthermore, Chabaud et al. [36], in their investigation of the hygromechanical properties of 3D printed composites comprising continuous carbon and glass fiber reinforcement within a polyamide matrix, identified porosities reaching as high as 15.1%. Hence, it can be deduced that, despite the inherent organic nature of the fiber yarn, it exhibits porosity levels comparable to those achieved when employing synthetic fibers in the context of 3D printing.

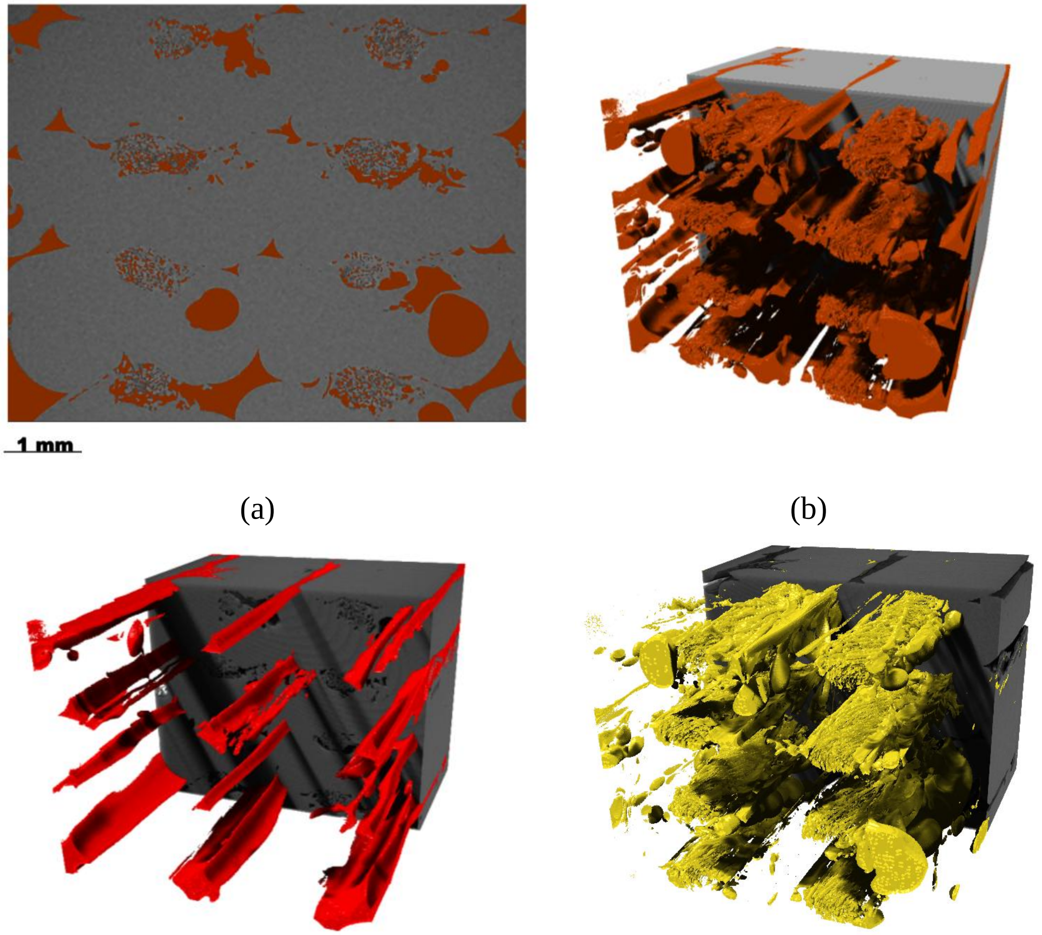

(a) (b)

(c) (d)

Figure 4.6 - Image processing of printed voids (in red) within the polymer matrix (in gray): (a) Cross section segmentation, (b) 3D model of all voids, (c) 3D model of inter-filament voids (in red), and (d) 3D model of fiber-matrix and bubbles voids (in yellow).

Of the total 11.7% porosity observed in the sample, 7.1% can be attributed to voids between the fiber-matrix interface and entrapped air bubbles, while the remaining 4.6% is associated with voids located between the filaments, i.e inter-filament voids. Figure 4.6c shows a 3D model highlighting the inter-filament voids and Figure 4.6d shows the fiber-matrix and bubbles voids, these cannot be analyzed separately since some of their element's overlap.

Figure 4.7 presents the volume and aspect ratio distribution of the segmented voids. The volume (Figure 4.7a and 4.8c) and aspect ratio (Figure 4.7b and 4.8d) are visually represented using a 32-color lookup table. Analyzing inter-filament voids in a segmented image reveals critical insights into potential rupture failure, which could compromise material integrity. The continuous nature of the inter-filament voids along the deposition layer can lead to delamination, resulting in a brittle failure in this region. Fiber-matrix and bubble voids are analyzed together, as they are mostly connected. The highest volumes (Figure 4.7c) are observed in fiber-matrix voids due to their interconnection within the yarn, highlighting impregnation challenges by the thermoplastic's limited time in the print nozzle to impregnate larger-diameter yarns. The aspect ratio (Figure 4.7d) is greater in bubbles due to their geometry. The aspect ratio plays a key role because various types of voids—such as inter-filament voids, fiber-matrix voids, and bubbles—originate from different mechanisms, which result in distinct shapes. Examining the aspect ratio allows for a more precise identification of these void types based on their geometric features. This distinction is critical for comprehending how each void type affects the overall behavior and performance of the material.

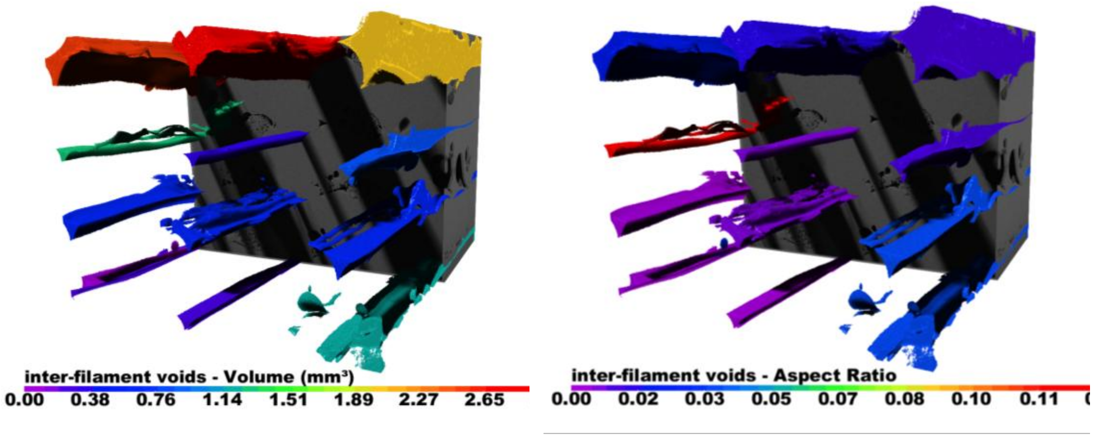

(a) (b)

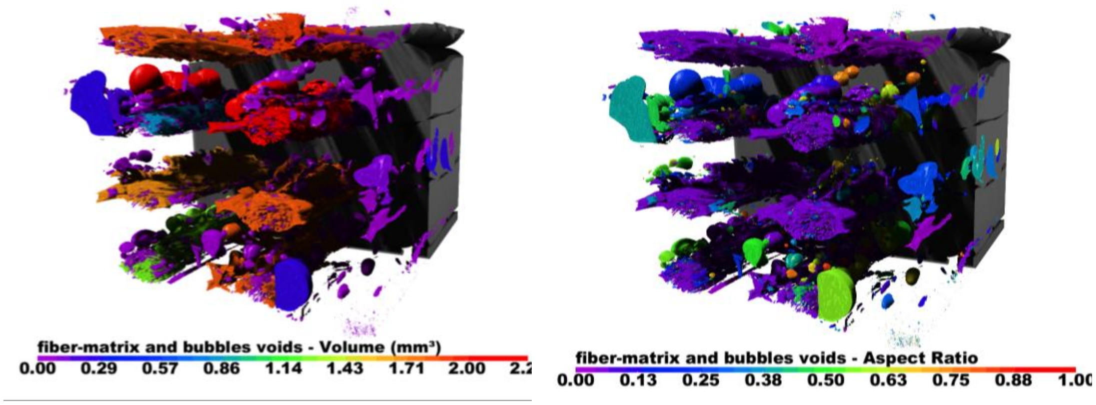

(c) (d)

Figure 4.7 - Segmentation: (a) 3D model of the volume of Inter-filament voids (b) 3D model of the aspect ratio of Inter-filament voids, (c) 3D model of the volume of fiber-matrix voids, and (d) 3D model of the aspect ratio of fiber-matrix voids.

Moreover, the cross-section of the jute yarn was subjected to a quantitative study, determining the volume of voids per yarn length (Figure 4.8). Consequently, by delineating the ratio between the void volume and the cross-sectional area of the yarn, it was possible to ascertain values reaching up to 57.0% of the total volume, thereby accentuating the insufficiency of material impregnation within the yarn structure. It is important to highlight that this percentage specifically corresponds to the region containing the yarn, where a detailed analysis was conducted by supposing the yarn as a perfect cylinder. To address this issue, a viable remedy involves the implementation of a pre-treatment method, exemplified by the flax fiber yarn optimization process as employed by Yang et al. [37], aimed at enhancing the impregnation level of prepreg filaments.

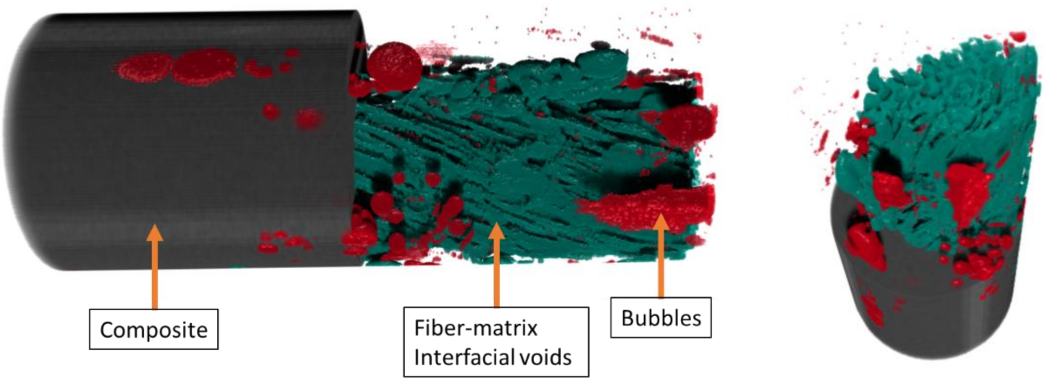

(a) (b)

Figure 4.8 - MicroCT image analysis of voids using Dragonfly^{TM}.

4.3.2 Thermal properties

The mechanical properties of biocomposites produced by FFF with continuous natural fiber reinforcement are significantly influenced by inherent process factors. These factors include the potential degradation of fibers as they pass through the hotend, which reaches temperatures up to 220°C [38], potentially compromising the structural integrity of the fibers.

4.3.2.1 Thermogravimetric analysis (TGA)

Figure 4.9 shows the mass variation (TGA) and the derivative of the mass variation (DTG) of the natural fibers used in the study. The process of pyrolysis involving the decomposition of the hemicelluloses, cellulose, and lignin occurred between 150 to 450 °C. The first stage is related to water loss and the decomposition of a small amount of hemicellulose and lignin in the natural fibers (temperatures up to 150 °C) [39]. The initial temperature of degradation was 305.9-329.2°C and the peak temperature was 339.7-361.0°C (onset and peak are shown in Table 4.6). The presence of water in the fiber is noticed in the first 100°C of the test (Figure 4.9a), where the mass variation indicates its evaporation.

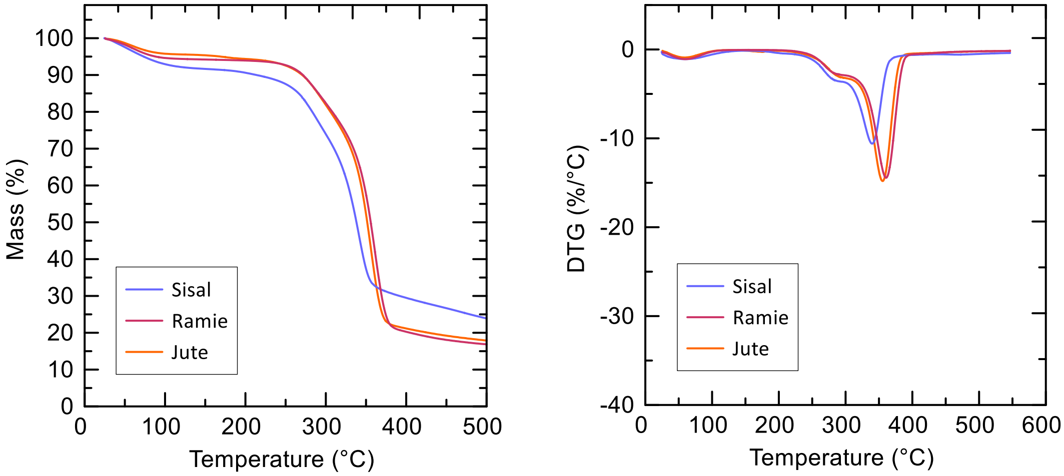

(a) (b)

Figure 4.9 - Thermogravimetric analysis of typical curves for the fibers: (a) TG and (b) DTG.

Table 4.6 - Properties of natural fibers degradation on thermogravimetric analysis.

Properties	**Sisal fiber**	**Ramie fiber**	**Jute fiber**
Sample mass	10.54 mg	12.78 mg	11.31 mg
$T_{\mathbf{Onset}}$	305.9 °C	329.2 °C	326.4 °C
$T_{\mathbf{Inflection}}$	343.4 °C	361.4 °C	356.1 °C
$T_{\mathbf{End}}$	354.8 °C	375.0 °C	369.2 °C
Mass Change	-53.65 %	-68.29 %	-66.06 %
Residual Mass (%)	21.83 %	16.01 %	17.02 %
	546.9 °C	547.0 °C	546.9 °C
Peak	339.7 °C	361.0 °C	355.7 °C

At 100°C, the sisal fiber showed a loss of 8% wt, while the jute and ramie fiber demonstrated lower mass loss, with values of 4.2% wt and 5.3% wt, respectively. Comparing to Benítez-Guerrero et al. [40] which reported that the sisal fiber presented a mass loss of 9.6% wt. In another study, Samouh et al. [41] found values of 9.6% wt in the first stage of thermal degradation, which is linked to the evaporation of the moisture within the fiber. In this way, a natural fiber yarn that has not gone through a pre-printing drying process can release water during printing, generating voids that can interfere with the quality of the interface and the mechanical properties of the printed layers [42].

Furthermore, it is noted that, while sharing a similar natural origin, the chemical differences of each natural fiber are expressed in their thermal stability. After the loss of water, jute and ramie presented similar thermal behavior, remaining stable until their degradation onset, and resulting in similar percentages of residual mass. The sisal fiber showed the lowest onset of degradation temperature (305.9°C) among all natural fibers. Moreover, an important factor is that fibers that do not undergo treatment (chemical or physical) and pre-drying may have high levels of hydroxyl groups that affect the fiber-matrix interaction and have constituents with low thermal values, such as hemicellulose. Finally, the ramie fiber presented a higher onset of degradation temperature value (329.2°C) compared to the sisal fiber (305.9°C) and the jute fiber (326.4°C). Moriana et al. [43] reported that a high cellulose content improves thermal stability. However, this improvement is also dependent on other fiber constituents [43,44].

Finally, it is worth noticing that the fiber degradation temperature is higher than the PLA working temperature of 160 to 220°C (this is also true for other types of commercial printing filaments) [38].

Through the DTG (Figure 4.9b), it is noted that natural fibers present two reactions: an initial mild curve and a second, more pronounced, which is the main cause of the material's degradation. Asim *et al.* [44] stated that natural fibers presented three distinct stages of degradation, namely: evaporation of moisture content at lower temperatures, decomposition of hemicellulose at medium temperatures, and the decomposition of lignin and cellulose at higher temperatures. The literature indicates that several factors affect the DTG curve, such as activation energy, chemical constituents of the fiber, pyrolysis kinetics, and atmosphere changing the characteristics for each type of natural fiber [43]. As shown in Table 4.6, the peak temperature found for jute showed similar patterns of 355.9°C. However, the peak temperature for sisal fiber was lower (339.7°C) when compared to the other studied cases. The data indicate that, despite being composed of the same chemical components—namely cellulose, lignin, hemicellulose, pectin, ash, and wax—the observed differences in TGA and DTG results suggest that the proportions of these components vary [43,45].

Figure 4.10 presents the TGA test results of the printed biocomposites of PLA reinforced with natural fibers. Once the composite is fabricated, water present in the fiber evaporates during the printing process of the specimens, not generating accumulated water as in the case of the TGA yarns. Therefore, at the melting temperature of PLA, all degradation occurs at once (Figure 4.10a). The literature shows that PLA has a temperature of degradation ranging approx. from 320 to 345°C. Furthermore, neat-PLA presents higher degradation temperature values when compared to composite materials reinforced by natural fibers found in similar studies [46,47]. This observation can be explained by Cavalcanti *et al.* [9], who found that the addition of fibers affects the material's thermal properties by reducing its crystallinity.

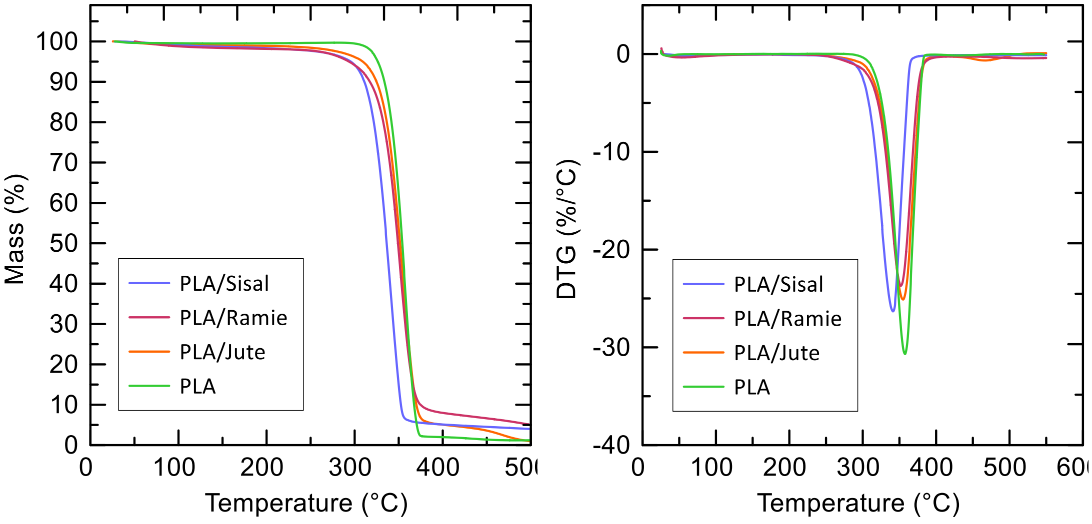

(a) (b)

Figure 4.10 - Thermogravimetric analysis of typical curves for the biocomposites: (a) TG and (b) DTG.

Table 4.7 indicates that the PLA-sisal composite has a slightly lower thermal stability (peak temperature) when compared to the other cases (PLA-sisal: 341.2 °C, PLA-ramie: 351.8 °C and PLA-jute: 355.2 °C). In biocomposite, the degradation phases were reduced to a single reaction step in a narrow temperature range, demonstrating behavior as a single homogeneous material (Figure 4.10b). Also, the peak of the biocomposite is between 341-355°C, with a residual mass of less than 3% in all cases (Table 4.7).

Table 4.7 - Properties of biocomposite degradation on thermogravimetric analysis.

Properties	**PLA**	**Sisal-PLA**	**Ramie-PLA**	**Jute-PLA**
Sample mass	10.06 mg	12.69 mg	11.20 mg	11.55 mg
$T_{\mathbf{Onset}}$	345.5 °C	318.4 °C	330.6 °C	340.2 °C
$T_{\mathbf{Inflection}}$	356.2 °C	335.3 °C	351.6 °C	354.7 °C
$T_{\mathbf{End}}$	363.8 °C	353.5 °C	365.6 °C	363.8 °C
Mass Change	-97.17 %	-90.22 %	-85.68 %	-90.54 %
Residual Mass (%)	1.11 %	2.88 %	1.20 %	1.48 %
	546.8°C	596.9 °C	596.9 °C	597.0 °C
Peak	357.5 °C	341.2 °C	351.8 °C	355.2 °C

4.3.2.2 Differential Scanning Calorimetry (DSC)

DSC and the main results investigated the thermal properties of the fibers and composites are shown in Table 4.8 and Table 4.9, respectively. Figure 4.11 shows the DSC curves of each fiber. Jute and ramie fibers have two endothermic peaks, where the first, in the range of 87-104°C, corresponds to the vaporization heat of the water absorbed by the fibers. Sinha *et al.* [48] suggest that this heat may be associated with the loss of water molecules on the surface of the fiber or liquid retained in the interstitial spaces of the fiber. The second endothermic peak occurs between 360-366°C due to fiber degradation, i.e. burning of cellulose forming active carbon. However, the sisal fiber presented two endothermic peaks (87.5 °C and 315 °C) and two exothermic peaks (294.6 °C and 353.1 °C). The first exothermic peak (294.6°C) is associated with the decomposition of polysaccharides and lignin [49] while the second endothermic peak (315°C) is associated with the degradation of α-cellulose. Finally, the second exothermic peak (353.1°C) is associated with cellulose degradation, as reported by Martin et al. [50] who found a peak value of 358°C. In another study, Belaadi et al. [49] observed analogous exothermic peak behavior for sisal fiber. Based on studies by Martin et al. [50], this result for sisal is due to the presence of hemicellulose, which also has exothermic peaks that dictate the behavior since sisal has the highest percentage of this component among the fibers studied. The other fibers presented behaviors governed by cellulose, which has an accentuated endothermic peak.

Table 4.8 - Properties of natural fibers degradation on differential scanning calorimetry.

Properties	**Sisal fiber**	**Ramie fiber**	**Jute fiber**
Weigh	6.87g	7.58g	7.98g
First peak	87.5 °C	88.8 °C	103.9 °C
Second peak	294.6 °C	366.1 °C	360.5 °C
Third peak	353.1 °C	-	-

Table 4.9 - Properties of biocomposite degradation on differential scanning calorimetry.

Properties	**PLA**	**PLA-sisal**	**PLA-ramie**	**PLA-jute**
First peak	65.2 °C	69.4 °C	66.8 °C	70.5 °C
Second peak	104.5 °C	105.4 °C	106.3 °C	102.6 °C
Third peak	179.5 °C	180.7 °C	179.7 °C	108.4 °C

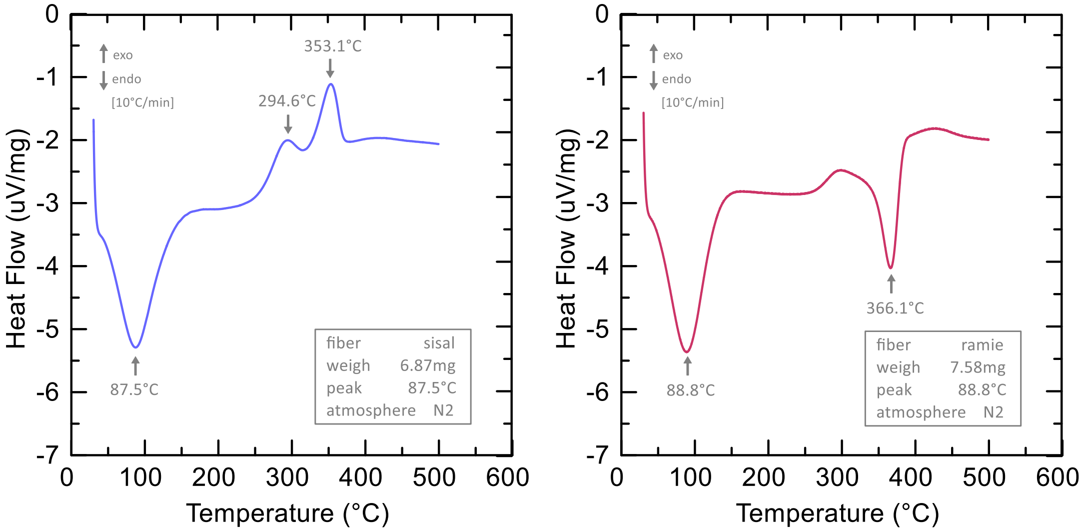

(a)

(b)

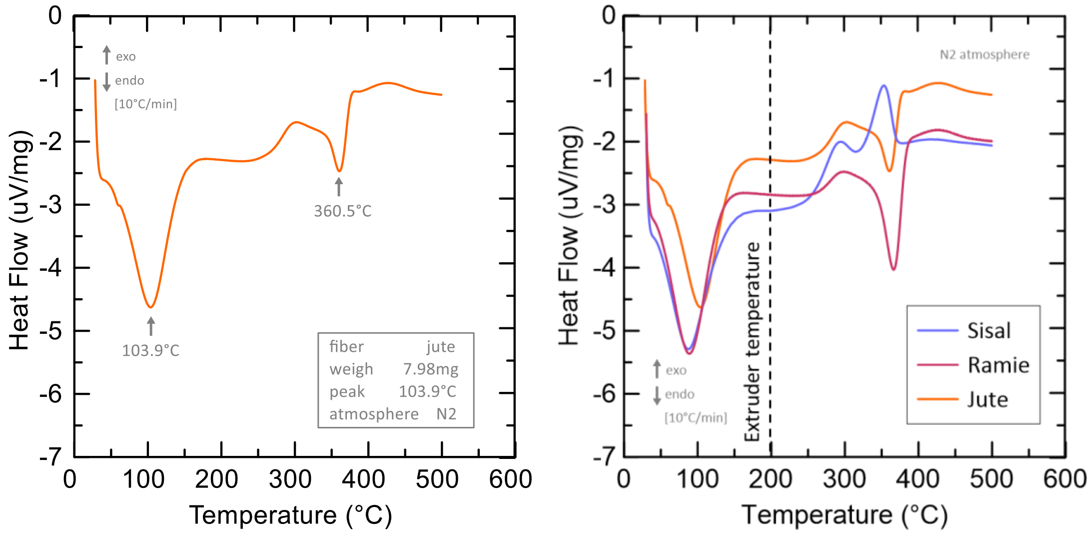

(c) (d)

Figure 4.11 - DSC of the fibers: (a) sisal, (b) ramie, (c) jute, and (d) Comparative.

Figure 4.12 shows the DSC tests of composites reinforced with natural fibers. The glass transition (T_g) occurs in samples at a temperature of 66.8-70.5°C. When compared with the glass transition of pure PLA at 65.2°C (Figure 4.12d), it can be seen that the presence of fibers generated changes in thermal properties, slightly raising the T_g. Mofokeng *et al.* [51] and Cavalcanti *et al.* [9] reported that natural fibers used as reinforcement can restrict the formation of polymeric chains, limiting the crystallization of the material and consequently altering its glass transition point. However, this variation should be interpreted with caution. The volumetric fraction of PLA interacting with the fibers is negligible, making it unlikely that fiber-induced restrictions on chain mobility would significantly affect the Tg at the molecular scale. Instead, this small increase can be attributed to experimental uncertainty and the inherent inaccuracy of identifying Tg at the peak of the inflection point in the thermogram.

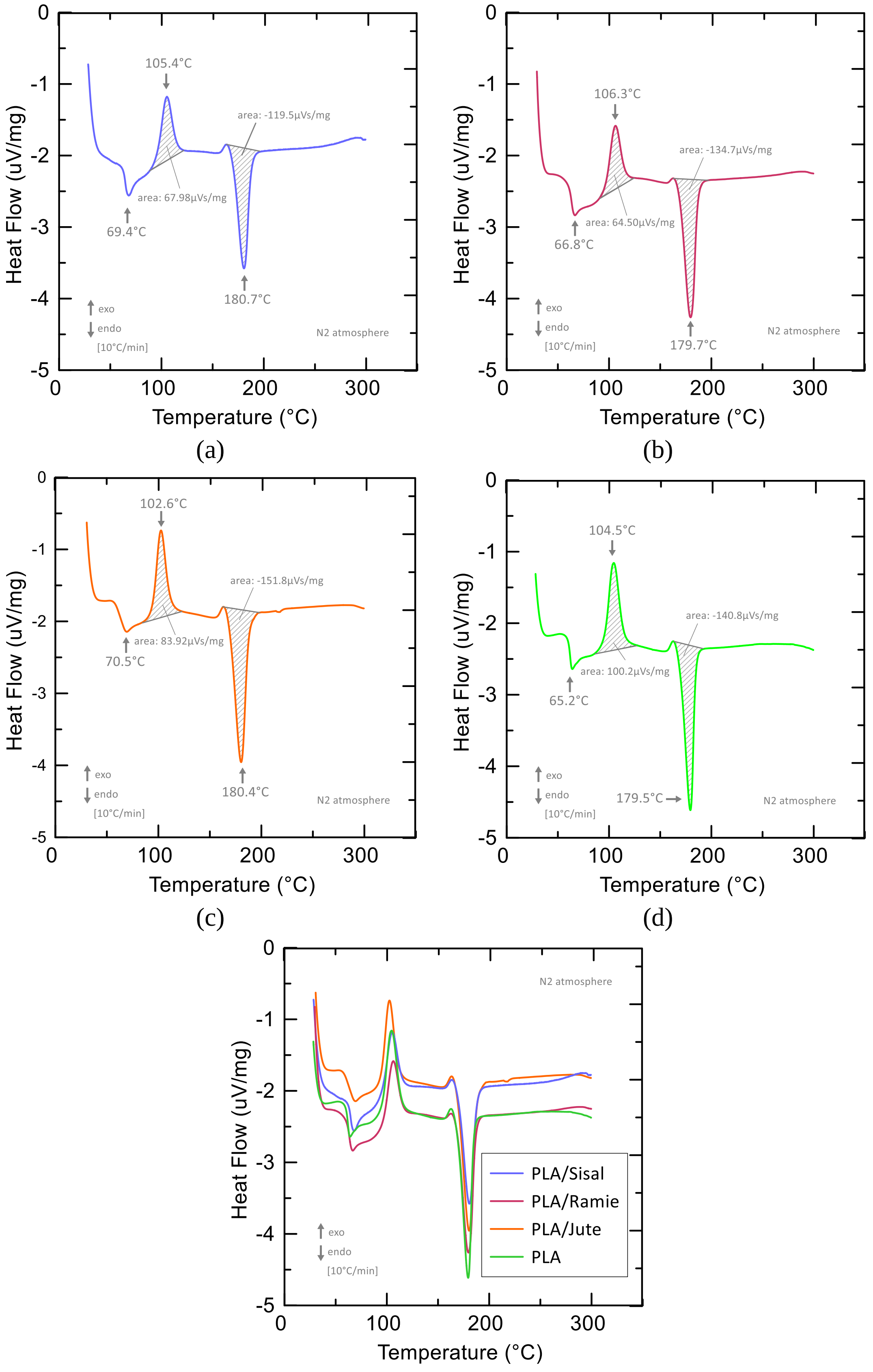
0
-1
-2
-3
-4
-5
Heat Flow (uV/mg)
Temperature (°C)
100
200
300
105.4°C
69.4°C
180.7°C
area: 67.98μVs/mg
area: -119.5μVs/mg
exo
endo
[10°C/min]
N2 atmosphere
106.3°C
66.8°C
179.7°C
area: 64.50μVs/mg
area: -134.7μVs/mg
102.6°C
70.5°C
180.4°C
area: 83.92μVs/mg
area: -151.8μVs/mg
104.5°C
65.2°C
179.5°C
area: 100.2μVs/mg
area: -140.8μVs/mg
PLA/Sisal
PLA/Ramie
PLA/Jute
PLA

(a)

(b)

(c)

(d)

(e)

Figure 4.12 - DSC of the biocomposites: (a) PLA-sisal, (b) PLA-ramie, (c) PLA-jute (d) neat PLA, and (e) Comparative.

Regarding the crystalline temperature (Tc), the composites showed values ranging from 102.6 °C to106.3 °C. Compared to the Tc of neat-PLA, all biocomposites, except for PLA-ramie, showed a slight reduction in Tc.

The melting temperature of composites reinforced with natural fibers ranged from 179.7-180.7°C. The incorporation of fibers resulted in a modest increase in temperature when compared to the neat PLA. Figure 4.12e compares DSC test results between all the studied composites.

The enthalpy can be evaluated to verify the fiber's influence on the composite's crystallinity. The enthalpy value is determined by calculating the area under the endothermic peak in the DSC curve, which corresponds to the heat absorbed during the melting process (ΔHfusion) of each sample. This involves measuring the energy required to change the material from a solid to a liquid state. While neat-PLA, a semi-crystalline and isotactic polymer, had a value of 140 μVs/mg, fiber-reinforced composites had values of 119.5-151.8 μVs/mg. Given this, it appears that sisal and ramie presented lower enthalpies (119.5 μVs/mg and 134.7 μVs/mg) generating reductions in the crystallinity of the material.

4.3.3 Effects of the fiber-matrix interface in the mechanical properties of printed composite

Figure 4.13a, 4.13b and 4.13c presents load-displacement representative curves during a yarn pull-out process of each fiber. Initially, the load-displacement curve exhibits a non-linear region, which may represent fiber realignment, pre-tensioning, gap closure, and load redistribution within the system. The yarn is loaded up to its maximum load, at which point complete debonding occurs. Subsequently, the load drops and the fiber yarn undergoes pull-out. This pull-out phenomenon, as also reported by Bheemreddy et al. [52] and Le Duigou et al.[53], is crucial in understanding the interfacial adhesion between the natural yarn and the matrix. The load-displacement curve provides insights into the forces required for debonding and subsequent pull-out, offering valuable data for evaluating the overall mechanical performance and reinforcing efficiency of the composite material. It is important to note that when using large yarns, the post-peak behavior due to dynamic friction is less significant compared to that observed in single-fiber pull-out tests. As shown in Figure 4.13d and observed by Bheemreddy *et al.* [52], in the case of isolated fiber pull-out, the fiber-yarn pull-out endures part of the load due to this dynamic friction, resulting in a progressive pull-out with displacement.

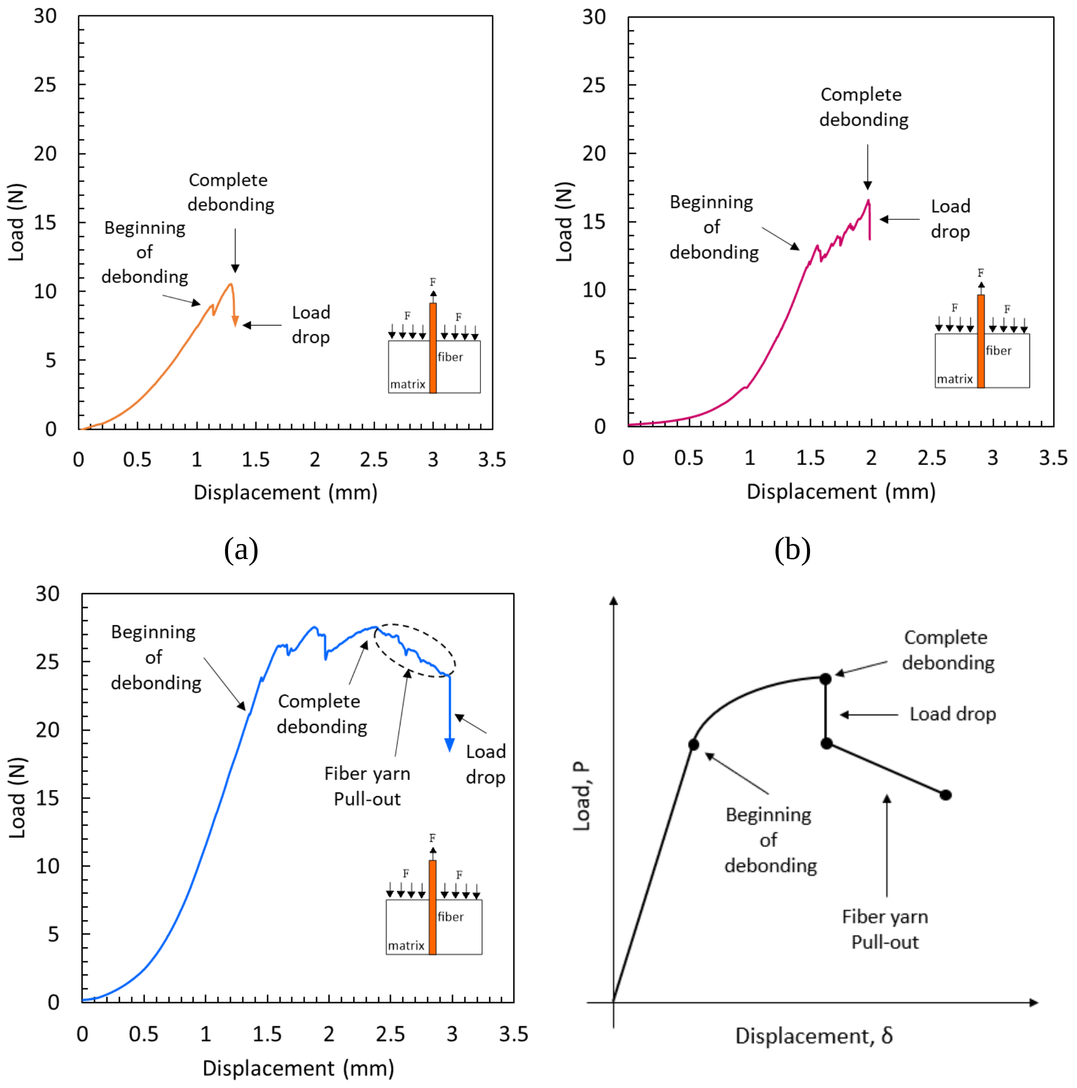

(a)

(b)

(c)

(d)

Figure 4.13 - Representative load-displacement curves: (a) jute, (b) ramie, (c) sisal yarn, and (d) typical load-displacement behavior of the fiber pull-out process (Adapted from [52]).

Table 4.10 presents the pull-out results for each yarn and their corresponding comparison with the apparent rigidity, respectively. Using the Anderson-Darling test hypothesis on the distribution of yarn diameters (Figure 4.14a, 4.14b, and 4.14c) and the interfacial strength results of each composite, the data from each group were analyzed to determine conformity to a normal distribution. Assessing whether the yarn diameters follow a normal distribution is a crucial preliminary step to ensure that mechanical tests involving these yarns capture the full range of their variability and reflect the natural inconsistencies in fiber properties. This ensures that the mechanical behavior observed in the tests represents the true diversity of the material, enhancing the reliability of the results. The dataset exhibits normal behavior, as evidenced by the p-values of each group. The sisal yarn samples exhibited a maximum interfacial tension of 0.44 MPa, 9.1% greater than the ramie samples, the second-best performing fiber. The increased viscosity of the polymer and the restricted impregnation time exacerbate these issues [54], leading to the formation of fiber-matrix voids due to insufficient yarn impregnation as discussed previously, which compromises the final strength of the composite. This behavior underscores the importance of studying both yarn diameter and matrix viscosity when optimizing the printing process to achieve optimal adhesion and mechanical performance in the resulting composites. An apparent rigidity analysis from the linear region of the load-displacement curves confirms the superior performance of sisal fibers. This can be attributed to the natural characteristics of sisal fibers within the yarn, as their longer length compared to other fibers allows for more effective load transmission. The commercial yarns used in this study have different fiber lengths. The sisal fibers had an average length of 83.2±9.3mm, while the ramie and jute fibers had an average length of 13.2±1.3mm and 15.0±3.2mm, respectively. This variation is directly related to their respective manufacturing processes, where ramie and jute fibers are cut into shorter lengths to facilitate yarn production. However, sisal is primarily used in coarser applications where fiber strength is the priority, and thus its length is typically preserved.

Table 4.10 - Pull-out results of average interfacial strength for each fiber.

Composite	**Yarn diameter (mm)**	**Yarn's p-value**	**τ_{ISS} (MPa)**	**τ_{ISS}'s p-value**
Jute-PLA	0.86±0.22	0.750	0.38±0.05	0.274
Ramie-PLA	0.96±0.16	0.495	0.40±0.05	0.452
Sisal-PLA	1.72±0.17	0.886	0.44±0.10	0.444

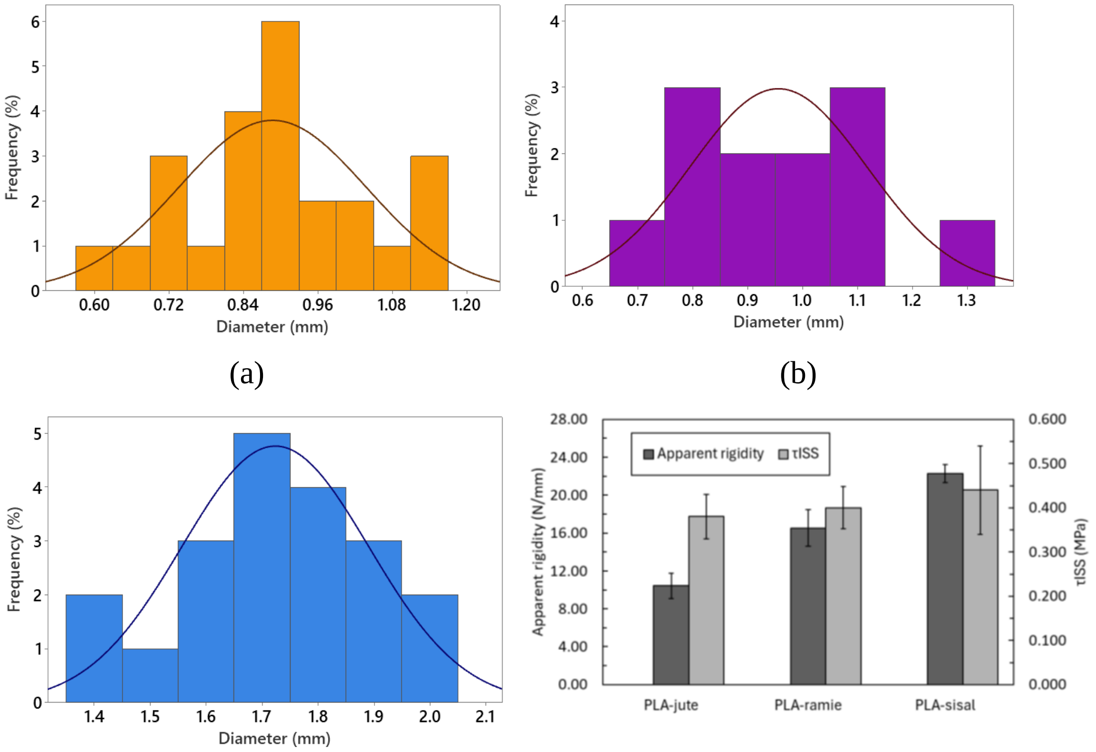

(a) (b)

(c) (d)

Figure 4.14 - Statistical distribution of diameter of (a) jute fibers, (b) ramie fibers, (c) sisal fibers.

Figure 4.15a illustrates the pull-out specimen both before and after the testing, showing that a portion of the fibers remains embedded in the matrix after the yarn pullout. For larger diameter yarns, the loss of adhesion is not unique, with detachment and/or breakage of the fibers occurring separately before total sliding. Figure 4.15b to Figure 4.15d illustrates the representative failure modes, where the schematic drawings indicate the cross-section of the composite, and the hexagons represent the set of fibers.

These failures can be identified by evaluating the mode in which the peripheral fibers remained attached to the PLA matrix. Figure 4.15b represents the PLA-ramie specimen after the pullout test demonstrating a side view of the tested specimen, where remaining fibers were still attached to the PLA matrix, with signs of fibrillation and fiber breakage. The whole peripheral section of the fiber was still attached to the PLA matrix. From Figure 4.15c, it can be observed that a portion of the peripheral jute fiber layers remained adhered to the polymeric matrix. For both cases (Figure 4.15c and 4.15d), the peripheral layers had undergone impregnation within the matrix, while the inner fibers were detached and pulled out separately. This indicates that the PLA-fiber interface is more resistant than the cohesive forces within the yarn.

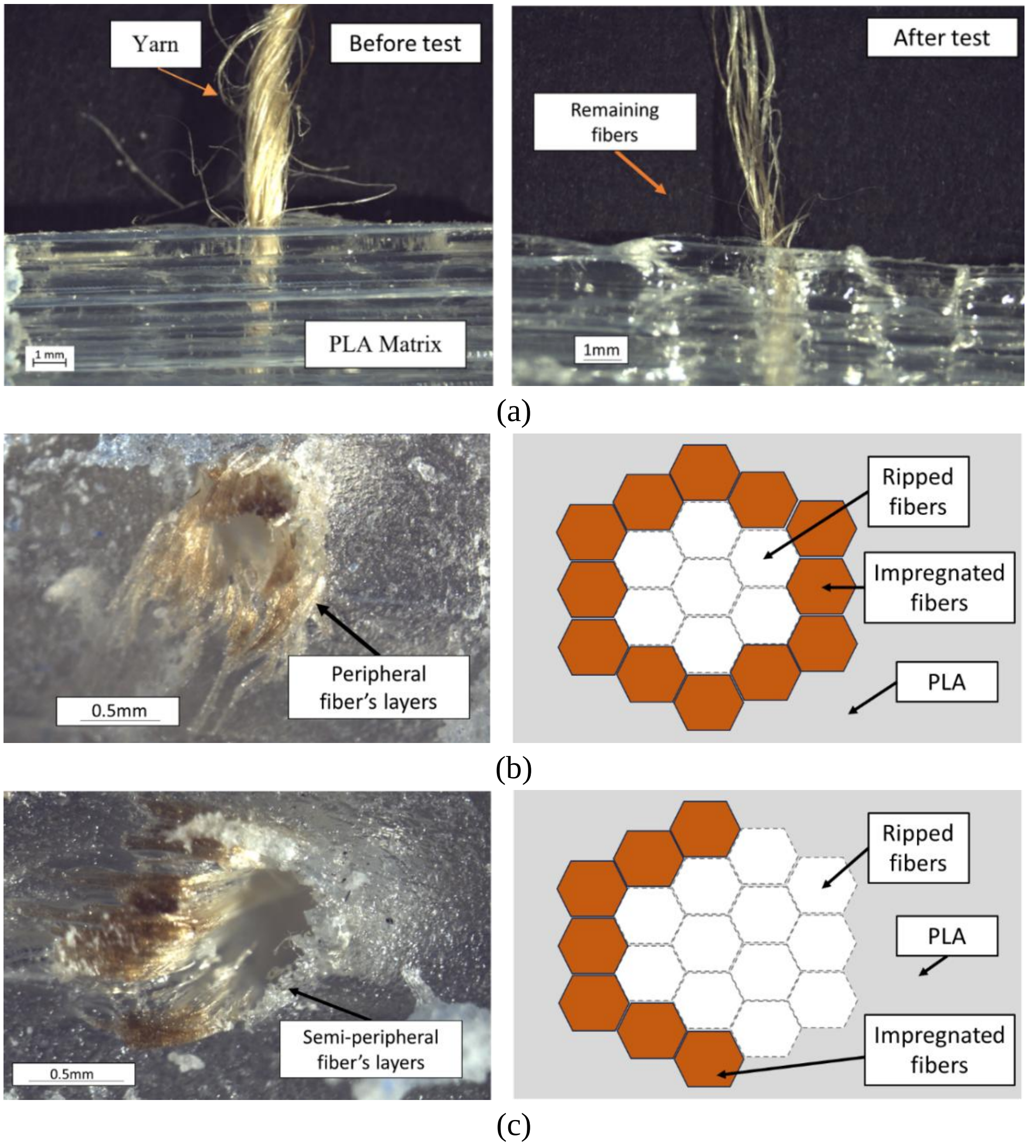

(a)

(b)

(c)

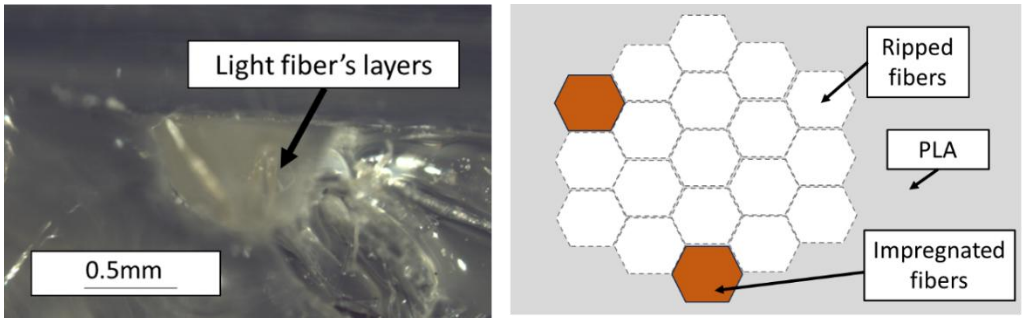

(d)

Figure 4.15 - Representative images of (a) Pull-out specimen before and after testing, (b) PLA matrix with complete peripheral layers still bonded, (c) PLA matrix with half peripheral layers still bonded, and (d) PLA matrix with few fibers' layers attached.

The fiber failure process in the polymer during the pull-out test allows for an analysis of the yarn failure behavior in 3D-printed composites reinforced with natural fiber yarns. Santos *et al.* [19] demonstrated the presence of yarn bridges formed after brittle matrix failure, indicating that the yarns bear part of the load applied to the composite. By analyzing the failure process, it is possible to enumerate the stages of its progression under composite loading. Initially, the brittle matrix undergoes an abrupt rupture (Figure 4.16a), where the composite does not fail due to the fibers acting as bridges between the two parts, preventing total separation. The individual fibers then begin to either break or undergo pull-out due to debonding at the fiber-matrix interface (Figure 4.16b). The remaining fibers experience increased tensile stress as they bear part of the remaining load (Figure 4.16c), leading to further breakages and pull-outs until complete composite failure occurs (Figure 4.16d). The failure mode described was observed in all tested samples.

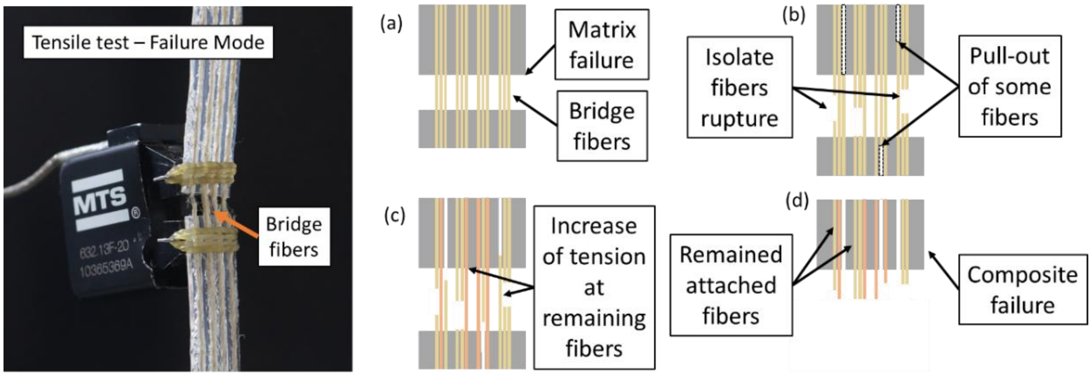

Figure 4.16 - Failure progression during the tensile test of printed biocomposite: (a) matrix failure and bridge fibers formation, (b) isolate fibers rupture and pull-out, (c) increase of tension at remaining fibers (d) Composite failure. Adapted from [19].

4.3.4 Effects of natural fiber composition on fiber-matrix interaction

The chemical characterization of jute, sisal, and ramie fiber reinforcements, as well as the PLA matrix, was performed using Fourier-transform infrared spectroscopy (FTIR) to analyze the fiber-matrix interactions in printing. The spectra are shown in Figure 4.17, while Table 4.11 shows the functional groups observed in each fiber's spectrum. These types of lignocellulosic fibers are natural composites of cellular structure, composed of different proportions of cellulose, hemicellulose, and lignin as shown in Table 4.2.

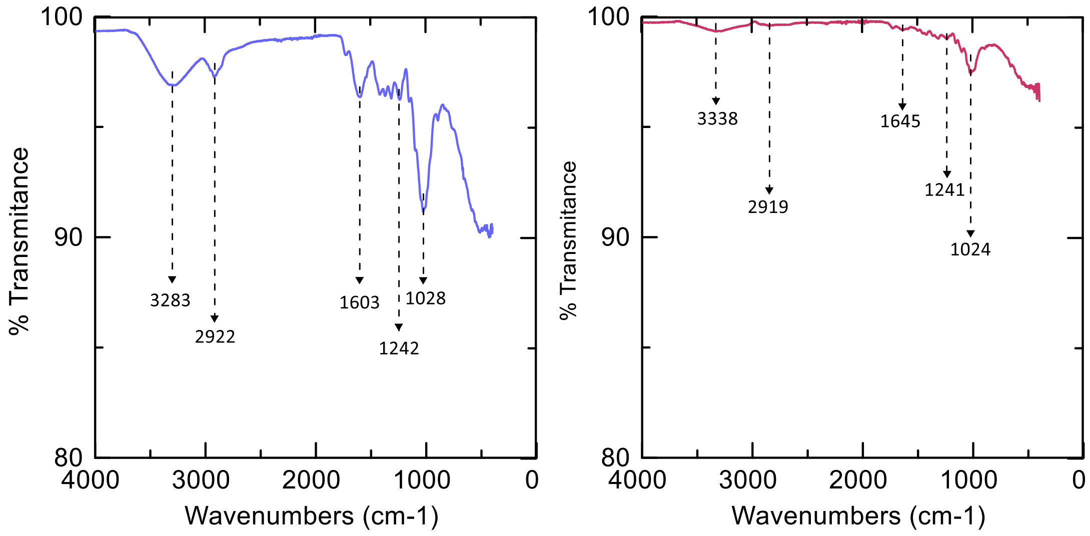

(a) (b)

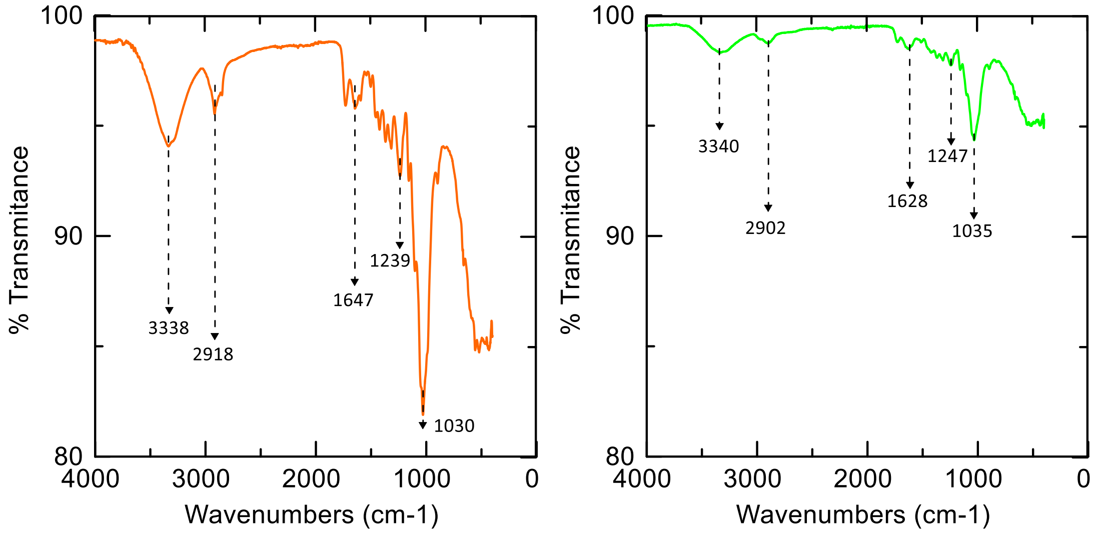

(c) (d)

Figure 4.17 - Results of FTIR tests: (a) sisal, (b) ramie, (c) jute, (d) neat PLA.

The FTIR presents an absorption bands spectrum for each component of these lignocellulosic fibers, the highest intensity peak occurs between 1024-1035 cm-1 indicating the asymmetric stretching of arabinose chains present in residual hemicellulose [55] caused by pyranose ring stretching (C-O-C) [56,57]. The peaks observed between 3283-3340 cm-1 refer to the hydroxyl groups (OH) (methanol acid) of intermolecular and intramolecular bonds of cellulose chains [58–60]. Additionally, the peaks between 2902-2922 cm-1 indicate the stretching of the bonds (CH) in the cellulose [56,57,59]. Finally, peaks between 1239-1247 cm-1 were observed, which are associated with the vibrations of the aromatic rings of lignin (CH) [55,58]. The OH bending of the adsorbed water can be seen between 1603-1647 cm-1 [59].

Table 4.11 - Functional groups and compounds identification.

Functional Group	**Compounds**	**Wavenumbers (cm^{-1})**				**Reference**
		PLA	Sisal	Ramie	Jute	
O-H	Acid, methanol	3340	3283	3338	3338	[54–56]
C-H	Stretching	2902	2922	2919	2918	[52,53,55]
O-H	Adsorbed water	1628	1603	1645	1647	[55]
C-H	Aromatic rings	1247	1242	1241	1239	[51,54]

C-O-C	Pyranose ring stretching	1035	1028	1024	1030	[52,53]

In other words, the results corroborate the argument that the accentuated band in jute fiber (Figure 4.17d) exhibits a purer constitution [59], as indicated by the intensity level and the unique peak in the DTG curve (Figure 4.17b). This is manifested through a singular decomposition and a low residual mass level (Figure 4.17a).

4.4 Conclusions

The primary objective of the present investigation was to analyze the thermal properties, and fiber-to-matrix adhesion within biocomposites fabricated using the FFF technique. Continuous natural fibers such as jute, ramie, and sisal, along with a PLA matrix, were employed to fabricate the specimens. The In-situ impregnation method during the 3D printing process was utilized. This experimental approach allowed for the evaluation of the impact of thermal characteristics and interfacial adhesion on the overall reinforcing efficiency of the natural fibers within the 3D printing paradigm. The following conclusions can be drawn:

- The use of the thermoplastic PLA matrix resulted in superficial impregnation of the outermost fibers of the yarn, compromising the mechanical properties of the composite, as evidenced by the pull-out of the external fibers of the reinforcement.
- The natural fibers remain intact when the matrix polymer reaches its melting point used in FFF as shown in the TGA analysis. DSC test results indicate that the addition of natural fibers increases the glass transition of the fiber-reinforced PLA composites.
- The primary challenge associated with the 3D printing of continuous natural fibers is attributed to the effective infiltrating of the thermoplastic matrix within the yarn. Nevertheless, the porosity level remains comparable to that observed in printed composites reinforced with synthetic fibers, thereby demonstrating its practical feasibility.

For future work, the authors recommend investigating potential pre-treatments of both the fiber and matrix to enhance yarn impregnation.

References

[1] Dubey D, Singh SP, Behera BK. Mechanical, thermal, and microstructural analysis of 3D printed short carbon fiber-reinforced nylon composites across diverse infill patterns. Progress in Additive Manufacturing 2024. https://doi.org/10.1007/s40964-024-00731-9.

[2] Mohammadizadeh M, Imeri A, Fidan I, Elkelany M. 3D printed fiber reinforced polymer composites - Structural analysis. Compos B Eng 2019;175:107112. https://doi.org/10.1016/j.compositesb.2019.107112.

[3] Dikshit V, Goh GD, Nagalingam AP, Goh GL, Yeong WY. Recent progress in 3D printing of fiber-reinforced composite and nanocomposites. INC; 2020. https://doi.org/10.1016/b978-0-12-819904-6.00017-7.

[4] Pervaiz S, Qureshi TA, Kashwani G, Kannan S. 3D Printing of Fiber-Reinforced Plastic Composites Using Fused Deposition Modeling: A Status Review. Materials 2021;14:4520. https://doi.org/10.3390/ma14164520.

[5] Gelhausen MG, Lenz D, Krull F, Korkmaz V, Agar DW. 3D Printing for Chemical Process Laboratories II: Measuring Liquid-Solid Mass Transfer Coefficients. Chem Eng Technol 2018;41:798–805. https://doi.org/10.1002/ceat.201700295.

[6] Hsueh MH, Lai CJ, Wang SH, Zeng YS, Hsieh CH, Pan CY, et al. Effect of printing parameters on the thermal and mechanical properties of 3d-printed pla and petg, using fused deposition modeling. Polymers (Basel) 2021;13. https://doi.org/10.3390/polym13111758.

[7] Papa I, Silvestri AT, Ricciardi MR, Lopresto V, Squillace A. Effect of fibre orientation on novel continuous 3d-printed fibre-reinforced composites. Polymers (Basel) 2021;13. https://doi.org/10.3390/polym13152524.

[8] Chicos LA, Pop MA, Zaharia SM, Lancea C, Buican GR, Pascariu IS, et al. Fused Filament Fabrication of Short Glass Fiber-Reinforced Polylactic Acid Composites: Infill Density Influence on Mechanical and Thermal Properties. Polymers (Basel) 2022;14. https://doi.org/10.3390/polym14224988.

[9] Cavalcanti DKK, Neto JSS, Queiroz HFM de, Wu Y, Neto VFS, Banea MD. Development and Mechanical Characterization of Short Curauá Fiber-Reinforced PLA Composites Made via Fused Deposition Modeling. Polymers (Basel) 2022;14. https://doi.org/10.3390/polym14225047.

[10] Nunna S, Chandra PR, Shrivastava S, Jalan AK. A review on mechanical behavior of natural fiber based hybrid composites. Journal of Reinforced Plastics and Composites 2012;31:759–69. https://doi.org/10.1177/0731684412444325.

[11] Monteiro SN, D'Almeida JRM. Pullout Test in Lignocellulosic Fibers – A Methodology of Analysis. Matéria (Rio de Janeiro) 2006;11:189–96. https://doi.org/10.1590/s1517-70762006000300004.

[12] Mangat AS, Singh S, Gupta M, Sharma R. Experimental investigations on natural fiber embedded additive manufacturing-based biodegradable structures for biomedical applications 2018.

[13] Shubhra QTH, Alam AKMM, Gafur MA, Shamsuddin SM, Khan MA, Saha M, et al. Characterization of plant and animal based natural fibers reinforced polypropylene composites and their comparative study. Fibers and Polymers 2010;11:725–31. https://doi.org/10.1007/s12221-010-0725-1.

[14] Wambua P, Ivens J, Verpoest I. Natural fibres: Can they replace glass in fibre reinforced plastics? Compos Sci Technol 2003;63:1259–64. https://doi.org/10.1016/S0266-3538(03)00096-4.

[15] Chand N, Hashmi SAR. Mechanical properties of sisal fibre at elevated temperatures. J Mater Sci 1993;28:6676–82. https://doi.org/10.1007/BF00356422.

[16] Georgopoulos ST, Tarantili PA, Avgerinos E, Andreopoulos AG, Koukios EG. Thermoplastic polymers reinforced with fibrous agricultural residues. Polym Degrad Stab 2005;90:303–12. https://doi.org/10.1016/j.polymdegradstab.2005.02.020.

[17] Thwe MM, Liao K. Durability of bamboo-glass fiber reinforced polymer matrix hybrid composites. Compos Sci Technol 2003;63:375–87. https://doi.org/10.1016/S0266-3538(02)00225-7.

[18] Gassan J, Bledzki AK. Effect of moisture content on the properties of silanized jute-epoxy composites. Polym Compos 1997;18:179–84. https://doi.org/10.1002/pc.10272.

[19] Santos N V., Cardoso DCT. 3D printing of vegetable yarn-reinforced polymer components. J Clean Prod 2023;415. https://doi.org/10.1016/j.jclepro.2023.137870.

[20] Le Duigou A, Barbé A, Guillou E, Castro M. 3D printing of continuous flax fibre reinforced biocomposites for structural applications. Mater Des 2019;180:107884. https://doi.org/10.1016/j.matdes.2019.107884.

[21] Fruleux T, Castro M, Correa D, Wang K, Matsuzaki R, Duigou A Le. Geometric limitations of 3D printed continuous flax-fiber reinforced biocomposites cellular lattice structures. Composites Part C: Open Access 2022;9. https://doi.org/10.1016/j.jcomc.2022.100313.

[22] Cheng P, Wang K, Chen X, Le Duigou A, Peng Y, Wen W. Compressive property and shape memory effect of 3D printed continuous ramie fiber reinforced biocomposite corrugated structures. Smart Mater Struct 2022;31:124003. https://doi.org/10.1088/1361-665x/ac95e4.

[23] Schindelin J, Arganda-Carreras I, Frise E, Kaynig V, Longair M, Pietzsch T, et al. Fiji: an open-source platform for biological-image analysis. 2012. https://doi.org/10.1038/nmeth.2019.

[24] Neto JSS, Lima RAA, Cavalcanti DKK, Souza JPB, Aguiar RAA, Banea MD. Effect of chemical treatment on the thermal properties of hybrid natural fiber-reinforced composites. J Appl Polym Sci 2019;136:1–13. https://doi.org/10.1002/app.47154.

[25] Mohanty AK, Misra M, Drzal LT. Natural fibers, biopolymers, and biocomposites. Taylor & Francis; 2005.

[26] Dragonfly 2022.2 [Computer software]. Comet Technologies Canada Inc. 2022.

[27] Pereira AL, Banea MD, Neto JSS, Cavalcanti DKK. Mechanical and Thermal Characterization of Natural Intralaminar Hybrid Composites Based on Sisal. Polymers (Basel) 2020;12:866. https://doi.org/10.3390/polym12040866.

[28] ASTM. ASTM E 1131 - Standard Test Method for Compositional Analysis by Thermogravimetry 2020.

[29] ASTM. ASTM D3418 - Standard Test Method for Transition Temperatures of Polymers by Differential Scanning Calorimetry 2021.

[30] ASTM. ASTM E1252 - Standard Practice for General Techniques for Obtaining Infrared Spectra for Qualitative Analysis 2021.

[31] Lima R de AA, Rocca D, Da Costa HRM, de Sousa JPB, Bettini P, Sala G, et al. Interfacial adhesion between embedded fibre optic sensors and epoxy matrix in composites. J Adhes Sci Technol 2019;33:253–72. https://doi.org/10.1080/01694243.2018.1537053.

[32] Kelly A, Tyson WR. Tensile properties of fibre-reinforced metals: Copper/tungsten and copper/molybdenum. Journal of the Mechanics and Physics of Solids 1965;13:329–38.

[33] Wang L, Sanders JE, Gardner DJ, Han Y. Effect of fused deposition modeling process parameters on the mechanical properties of a filled polypropylene. Progress in Additive Manufacturing 2018;3:205–14. https://doi.org/10.1007/s40964-018-0053-3.

[34] Cavalcanti DKK, Banea MD, de Queiroz HFM. Effect of material on the mechanical properties of additive manufactured thermoplastic parts. Annals of “Dunarea de Jos” University of Galati, Fascicle XII, Welding Equipment and Technology 2020;31:5–12. https://doi.org/10.35219/awet.2020.01.

[35] Saidane EH, Arnold G, Louis P, Pac MJ. 3D printed continuous glass fibre-reinforced polyamide composites: Fabrication and mechanical characterisation. Journal of Reinforced Plastics and Composites 2022;41:284–95. https://doi.org/10.1177/07316844211051746.

[36] Chabaud G, Castro M, Denoual C, Le Duigou A. Hygromechanical properties of 3D printed continuous carbon and glass fibre reinforced polyamide composite for outdoor structural applications. Addit Manuf 2019;26:94–105. https://doi.org/10.1016/j.addma.2019.01.005.

[37] Yang Z, Zhang Z, Long Y, Fu K, Li Y. Process optimization of continuous flax fiber/polylactic acid prepreg filaments toward high performance 3D-printed composites. Polym Compos 2023;44:6242–53. https://doi.org/10.1002/pc.27559.

[38] Mohanty AK, Misra M, Hinrichsen G. Biofibres, biodegradable polymers and biocomposites: An overview. Macromol Mater Eng 2000;276–277:1–24. https://doi.org/10.1002/(SICI)1439-2054(20000301)276:1<1::AID-MAME1>3.0.CO;2-W.

[39] Yuan J-M, Feng Y-R, He L-P. Effect of thermal treatment on properties of ramie fibers. Polym Degrad Stab 2016;133:303–11. https://doi.org/10.1016/j.polymdegradstab.2016.09.012.

[40] Benítez-Guerrero, Pérez-Maqueda, Artiaga LAB, C , Sánchez-Jiménez R, B , Pascual-Cosp PE. Structural and Chemical Characteristics of Sisal Fiber and Its Components: Effect of Washing and Grinding. Journal of Natural Fibers 2016:26–39. https://doi.org/https://doi.org/10.1080/15440478.2015.1137529.

[41] Samouh Z, Molnar K, Boussu F, Cherkaoui O, El Moznine R. Mechanical and thermal characterization of sisal fiber reinforced polylactic acid composites. Polym Adv Technol 2019;30:529–37. https://doi.org/10.1002/pat.4488.

[42] de Mendonça AC, Cavalcanti DKK, de Queiroz HFM, Neto JSS, Chaves FJP, Banea MD. Mechanical Characterization of Filler Modified Abs 3D Printed Composites Made Via Fused Filament Fabrication. Annals of "Dunarea de Jos" University of Galati, Fascicle XII, Welding Equipment and Technology 2022;33:27–34. https://doi.org/10.35219/awet.2022.02.

[43] Moriana R, Vilaplana F, Karlsson S, Ribes A. Correlation of chemical, structural and thermal properties of natural fibres for their sustainable exploitation. Carbohydr Polym 2014;112:422–31. https://doi.org/10.1016/j.carbpol.2014.06.009.

[44] Asim M, Paridah MT, Chandrasekar M, Shahroze RM, Jawaid M, Nasir M, et al. Thermal stability of natural fibers and their polymer composites. Iranian Polymer Journal 2020;29:625–48. https://doi.org/10.1007/s13726-020-00824-6.

[45] Monteiro SN, Calado V, Rodriguez RJS, Margem FM. Thermogravimetric Stability of Polymer Composites Reinforced with Less Common Lignocellulosic Fibers – an Overview. Journal of Materials Research and Technology 2012;1:117–26. https://doi.org/10.1016/S2238-7854(12)70021-2.

[46] Fang C cui, Zhang Y, Qi S yuan, Liao Y chang, Li Y yuan, Wang P. Influence of structural design on mechanical and thermal properties of jute reinforced polylactic acid (PLA) laminated composites. Cellulose 2020;8. https://doi.org/10.1007/s10570-020-03436-8.

[47] Gunti R, Ratna Prasad AV, Gupta AVSSKS. Mechanical and degradation properties of natural fiber-reinforced PLA composites: Jute, sisal, and elephant grass. Polym Compos 2018;39:1125–36. https://doi.org/10.1002/pc.24041.

[48] Sinha E, Rout SK. Influence of fibre-surface treatment on structural, thermal and mechanical properties of jute fibre and its composite. Bulletin of Materials Science 2009;32:65–76. https://doi.org/10.1007/s12034-009-0010-3.

[49] Belaadi A, Bezazi A, Bourchak M, Scarpa F, Zhu C. Thermochemical and statistical mechanical properties of natural sisal fibres. Compos B Eng 2014;67:481–9. https://doi.org/10.1016/j.compositesb.2014.07.029.

[50] Martin AR, Martins MA, Da Silva ORRF, Mattoso LHC. Studies on the thermal properties of sisal fiber and its constituents. Thermochim Acta 2010;506:14–9. https://doi.org/10.1016/j.tca.2010.04.008.

[51] Mofokeng JP, Luyt AS, Tábi T, Kovács J. Comparison of injection moulded, natural fibre-reinforced composites with PP and PLA as matrices. Journal of Thermoplastic Composite Materials 2012;25:927–48. https://doi.org/10.1177/0892705711423291.

[52] Bheemreddy V, Chandrashekhara K, Dharani LR, Hilmas GE. Modeling of fiber pull-out in continuous fiber reinforced ceramic composites using finite element method and artificial neural networks. Comput Mater Sci 2013;79:663–73. https://doi.org/10.1016/j.commatsci.2013.07.026.

[53] Le Duigou A, Davies P, Baley C. Exploring durability of interfaces in flax fibre/epoxy micro-composites. Compos Part A Appl Sci Manuf 2013;48:121–8. https://doi.org/10.1016/j.compositesa.2013.01.010.

[54] Zhang J, Shen H, Yang L, Ge D. Two-Step Preparation of CCF/PEEK Wrapped Yarn for 3D Printing Composites with Enhanced Mechanical Properties. Materials 2023;16. https://doi.org/10.3390/ma16031168.

[55] de Freitas RRM, do Carmo KP, de Souza Rodrigues J, de Lima VH, Osmari da Silva J, Botaro VR. Influence of alkaline treatment on sisal fibre applied as reinforcement agent in composites of corn starch and cellulose acetate matrices. Plastics, Rubber and Composites 2021;50:9–17. https://doi.org/10.1080/14658011.2020.1816119.

[56] Melikoğlu AY, Bilek SE, Cesur S. Optimum alkaline treatment parameters for the extraction of cellulose and production of cellulose nanocrystals from apple pomace. Carbohydr Polym 2019;215:330–7. https://doi.org/10.1016/j.carbpol.2019.03.103.

[57] Lingegowda DC, Kumar JK, Prasad AGD, Zarei M, Gopal S. Ftir Spectroscopic Studies on Cleome Gynandra – Comparative. Rom J Biophys 2013;22:137–43.

[58] Morán JI, Alvarez VA, Cyras VP, Vázquez A. Extraction of cellulose and preparation of nanocellulose from sisal fibers. Cellulose 2008;15:149–59. https://doi.org/10.1007/s10570-007-9145-9.

[59] César NR, Pereira-da-Silva MA, Botaro VR, de Menezes AJ. Cellulose nanocrystals from natural fiber of the macrophyte Typha domingensis: extraction and characterization. Cellulose 2015;22:449–60. https://doi.org/10.1007/s10570-014-0533-7.

[60] Sun XF, Sun RC, Su Y, Sun JX. Comparative Study of Crude and Purified Cellulose from Wheat Straw. J Agric Food Chem 2004;52:839–47. https://doi.org/10.1021/jf0349230.

Chapter 5 - EXPLORING PRINTING METHODS FOR CONTINUOUS NATURAL FIBER-REINFORCED THERMOPLASTIC BIOCOMPOSITES: A COMPARATIVE STUDY

This chapter was published under the reference:
Natália V. Santos, Alberto Giubilini, Daniel C.T Cardoso, Paolo Minetola, Exploring Printing Methods for Continuous Natural Fiber-Reinforced Thermoplastic Biocomposites: A Comparative Study, Sustainable Materials and Technologies 43 (2025). https://doi.org/10.1016/j.susmat.2025.e01253

Abstract

Continuous Fiber-Reinforced Thermoplastic Composites (CFRTPCs) are revolutionizing various industry sectors by enabling a combination of design, optimization, and high performance. The use of continuous natural fiber reinforcement integrates these factors with the potential for developing a sustainable product with a lower ecological footprint compared to traditional composites. However, challenges such as optimizing fiber-matrix impregnation and the identification of the most suitable manufacturing process for structural components remain significant. The objective of this study is to address these challenges by comparing the two main continuous printing methodologies - in-situ impregnation and semi-finished filament fabrication -in their application to natural fiber-reinforced composites. To achieve this, a method for manufacturing semi-finished filaments was developed and compared with the in-nozzle impregnation process by modifying a commercially available 3D printer. Image analysis, surface roughness measurements, deposition rates, and mechanical tests revealed that the semi-finished filament method resulted in better fiber-matrix impregnation, significantly improving tensile strength and elastic modulus by up to 18.4% compared to the in-nozzle method. Additionally, the semi-finished filament process demonstrated a higher deposition rate, reaching 400 mm/s, compared to 300 mm/s for the in-nozzle process.

5.1 Introduction

Fused Filament Fabrication (FFF) stands as a cornerstone in additive manufacturing (AM), revolutionizing the production landscape with its capacity to construct intricately detailed and optimized components. By extruding thermoplastic filaments layer by layer, FFF enables the creation of complex geometries with precision and efficiency. However, FFF components face challenges with porosity and surface roughness. Porosity can arise from incomplete layer fusion, voids formed during extrusion, or the use of improperly dried filaments, all of which may compromise mechanical properties such as strength and durability [1,2] . Similarly, surface roughness, inherent to the layer-by layer process, can influence both the aesthetic quality and functional performance of FFF parts [3,4]. Despite these limitations, one interesting aspect of this technique is its versatility, allowing the incorporation of multiple materials within a single print. This capability not only broadens design possibilities but also enhances the structural performance and functionality of the final components. Furthermore, FFF promotes sustainability by significantly reducing waste generation compared to traditional fabrication methods [5].

Aligned with the pursuit of sustainability, incorporating natural fibers as filler and reinforcement agents in the 3D printing process has been gaining attention. Due to their lightweight nature, biodegradability, and mechanical resilience, these fibers have become increasingly popular in many sectors. Utilizing natural fibers not only aligns with eco-conscious practices, but also enhances the overall performance and environmental footprint of the 3D-printed objects. As a result, this approach holds promise for fostering a more sustainable trajectory in AM processes. Table 5.1 shows the mechanical properties of the natural fibers most investigated in previous literature.

Table 5.1 - Mechanical properties of natural fibers.

Type of fiber	**Density (g/cm^3)**	**Tensile strength (MPa)**	**Elastic Modulus (GPa)**	**Reference**
Bamboo	1.2	73-505	10-40	[6]
Coir	1.2-1.3	95-220	3-6	[6,7]
Curauá	1.4	500-1150	11.8	[8]
Flax	1.4-1.5	345-1500	28-80	[7,9,10]
Hemp	1.4-1.5	550-900	34-70	[6,7]

Jute	1.3-1.5	400-800	10-30	[7,8,11]
Kenaf	1.4	930	53	[9]
Ramie	1.5-1.6	400-968	44-128	[7,8,11,12]
Sisal	1.3-1.5	347-1150	9-38	[6-8,11]

Natural fiber reinforcement can be incorporated in either discontinuous or continuous forms. Discontinuous fibers are generally used for manufacturing composite filaments, wherein a weight percentage of fibers is blended with the pellet matrix and extruded into filaments with dimensions compatible with market-available 3D printers [13]. The potential applications of Discontinuous Fiber-Reinforced Thermoplastic Composites (DFRTPCs) include various sectors [14], including biomedical [15–17], design [18–21], and non-structural construction [22], due to their capacity for material recycling and ability to reuse waste materials [23]. Nevertheless, from a mechanical behavior perspective, the inclusion of discontinuous natural fibers often results in a reduction in the mechanical characteristics of the composite (Table 5.2).

Table 5.2 - Mechanical properties of DFRTPCs using natural fibers. Adapted from [13].

Material	**Fiber percentage (wt%)**	**Tensile strength (MPa)**	**Reference**
PLA-Agave	0-10	51.0 (0 wt%) to 28.0 (10 wt%)	Figueroa-Velarde *et al.* [24]
PLA-Kenaf	0-7	56.3 (0 wt%) to 11.8 (7 wt%)	Shahar *et al.* [15]
PLA-Kenaf	0-2.5	49.9 (0 wt%) to 39.8 (2.5wt%)	Haryati *et al.* [25]
PLA-Sugarcane	0-15	64.2 (0 wt%) to 45.3 (15wt%)	Liu *et al.* [26]
PLA-Rubber	0-20	56.4 (0 wt%) to 34.3 (20 wt%)	Fekete *et al.* [27]
PLA-Soybean	0-10	36.4 (0 wt%) to 21.5 (10 wt%)	Dey *et al.* [28]

The 3D printing methods using Continuous Fiber Reinforced Thermoplastic Composites (CFRTPCs) offer an effective option to improve the mechanical properties of components produced by FFF. Pervaiz et al. [29] pointed out three main types: semi-finished filament (SF), in-situ impregnation (IN), and out-of-nozzle printing (ON). In the SF approach, a composite filament is pre-manufactured by embedding the fiber in the matrix, to be used with conventional 3D printers [29]. However, this method limits flexibility in terms of material composition, as it imposes a fixed fiber volumetric fraction that cannot be modified during the printing process. The fiber content is entirely determined by the specifications of the pre-manufactured composite filament, making real-time adjustments impossible. Moreover, continuous fiber addition increases filament stiffness, leading to storage issues, especially in the case of stiffer fibers [30]. The IN method integrates the fiber into the polymer matrix during the 3D printing process. This integration within the printhead mechanism is achieved by feeding the fiber through an inlet or an auxiliary entrance in the coldend of the printhead, allowing to merge with the matrix before reaching the nozzle [29,30]. This method facilitates the variation of fiber volume ratio and allows the printing of pure filament and mixed fiber plastic and fiber parts. However, it requires special printhead modifications and is more likely to clog [11,29]. Lastly, the ON method uses two nozzles, one for the main polymer and another for the fiber reinforcement, which can be incorporated using either the SF [31,32] or IN [33] method. It is a versatile method that uses different fibers and matrices [29]. Table 5.3 summarizes the main studies of CFRTCs, divided by insertion method.

Table 5.3 - CFRTCs insertion methods using natural fibers. Adapted from [16].

Method		**Reference**	**Matrix**	**Fiber**
Semi-finished filament (SF)	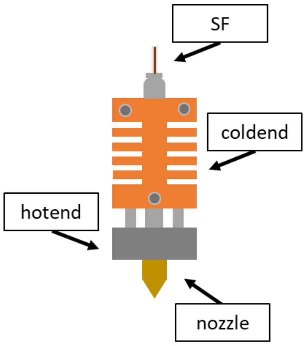	Le Duigou *et al.* [34,35]	PLA	Flax
		Fruleux *et al.* [36,37]	PLA	Flax

***In-situ* impregnation (IN)**	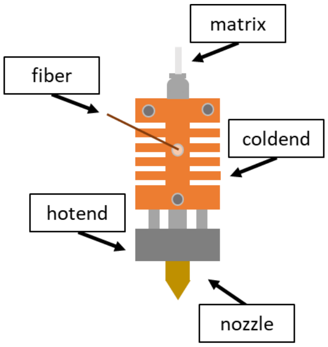	Cheng et al. [38-40]	PLA	Ramie
		Suteja et al. [41]	PLA	Pineapple leaf
		Matsuzaki *et al.* [42]	PLA	Jute
		Long *et al.* [43]	PLA	Flax
		Santos *et al.* [11]	PLA	Sisal, ramie and jute
		Cai *et al.* [44]	PLA	Ramie
		Terekhina *et al.* [45]	PA 6	Flax
		Rivero-Romero *et al.* [46]	PLA	Banana

Out-of-nozzle printing (ON)	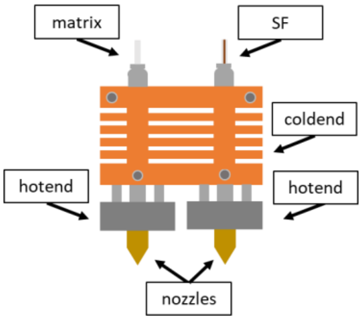	Zhang *et al.* [31,32]	PLA	Flax
	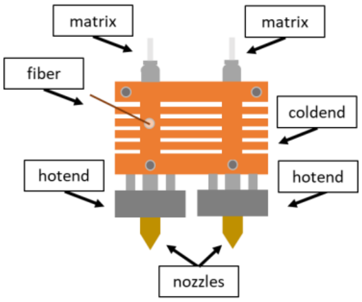	Ginoux *et al.* [33]	PLA	Hemp
		Wu *et al.* [47]	PLA	Hemp

Applying CFRTPCs with natural fibers poses a primary challenge concerning the utilization of yarn-form fibers, given that their natural length is discontinuous and inherently restricted by the size of the originating plant. The textile yarn is the final product of a long spinning process, where the final identification parameter is the yarn's title, which represents its diameter or thickness. In a simplified manner, fibers undergo cleaning following harvesting, alignment by carding and combing machines, regulated by draw frames, refinement through roving frames, twisting into yarns at the ring spinning mill, and packaging onto bobbins [44,45]. A major limitation in CFRTPC processing is the difficulty in impregnating the fiber yarns effectively [7]. This phenomenon challenges the efficiency of the process, requiring innovative approaches to ensure the complete penetration of the thermoplastic polymer within the yarn.

Although the in-nozzle method can be used with raw natural fibers [7,38], the fiber-matrix contact in the printing nozzle for a few seconds does not allow complete penetration [12], especially in the case of larger-diameter yarns for large-scale printing [7]. This uncompleted impregnation increases voids [7,38] and reduces mechanical properties [46]. To address this issue, various solutions have been reported, such as preheating the yarn before insertion in the printing nozzle [38] and the fiber's surface and sizing treatment [39,47]. Moreover, in semi-finished filaments, the composite is subjected to two heating processes: one during filament manufacturing and the second during deposition through the printing nozzle. However, this method also allows the presence of voids and irregularities in the composite [48], especially in larger yarns [49]. Treatments like coextrusion [28] and resin impregnation [49] are used to mitigate these issues. Coextrusion prepreg involves drawing continuous fibers into a single-screw pellet-extruder, while resin impregnation immerses continuous fibers in a resin impregnation tank.

A previous investigation developed a technique for continuous reinforcement using large-diameter yarns with a modified FFF hotend, customized for in-situ impregnation of natural fibers within a biopolymer matrix for large-scale layers. This study assessed tensile properties and the applicability of the method to various natural fibers, emphasizing the importance of understanding fiber-matrix interfacial mechanical properties in CFRTPCs [7]. Nevertheless, a knowledge gap exists regarding the most effective continuous fiber printing method for continuous natural fibers in larger-scale diameters, both in mechanical terms and interface properties, to achieve enhanced characteristics of the novel biocomposite.

This study compares the main printing methodologies, namely in-nozzle and semi-finished filament, for producing composites reinforced with continuous natural fibers. Mechanical tests were conducted using flax yarns within a PLA matrix, accompanied by image analyses to understand deeper the effects of the 3D printing processes on the final biocomposite.

5.2 Materials and Methods

5.2.1 Materials

The reinforcing materials used in this work consisted of flax yarn supplied by Bricolino (Vicenza, Italy) (Figure 5.1). A polylactic acid filament (PLA 3D850) with a diameter of 1.75 mm and PLA pellets (SMARTFIL PLA) provided by Smar Materials

3D (Jaén, Spain) were used for the matrix. Table 5.4 presents the main properties of the natural yarn from literature and PLA from producer data sheet, respectively.

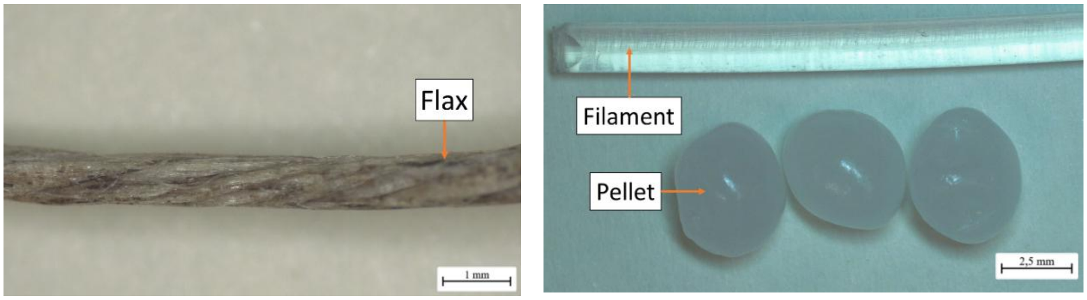

(a) (b)

Figure 5.1 - Matrix and reinforcement materials: (a) Natural fibers and (b) PLA matrix (Leica MSV266 optical microscope).

Table 5.4 - Properties of the natural yarns and polymer matrix [7,8,10,11,54].

Property	**Flax yarn**	**PLA 3D850**	**Smartfil PLA**
Type	yarn	filament	pellet
Diameter (mm)	0.77±0.03	1.75	-
Density (g/cm^3)	1.4-1.5	1.24	1.24
Linear density (g/m)	0.50±0.01	-	-
Tensile strength (MPa)	345-1500	57.7	110
Young modulus (GPa)	28-80	2.64	3.31
Ultimate strain (%)	-	3.10	-
Cellulose (%)	65-80	-	-
Hemicellulose (%)	12-16	-	-
Lignin content (%)	2-5	-	-
Moisture absorption (%)	7	-	-
Melting temperature (°C)	-	205-220	200-240

5.2.2 Printing Fabrication

5.2.2.1 Semi-finished filament (SF)

To produce the semi-finished filaments reinforced with continuous natural fibers, modifications were made to the nozzle of the single-screw extruder, model NEXT 1.0 from 3Devo (Utrecht, Netherlands), to enable simultaneous extrusion of both the matrix and the reinforcement. This process involved extending the nozzle and integrating a specialized fiber inlet. An external heating system was employed to sustain the nozzle at the optimal manufacturing temperature. The outcome of these modifications, along with the key components of the single-screw extruder, is depicted in Figure 5.2a and Figure 5.2b.

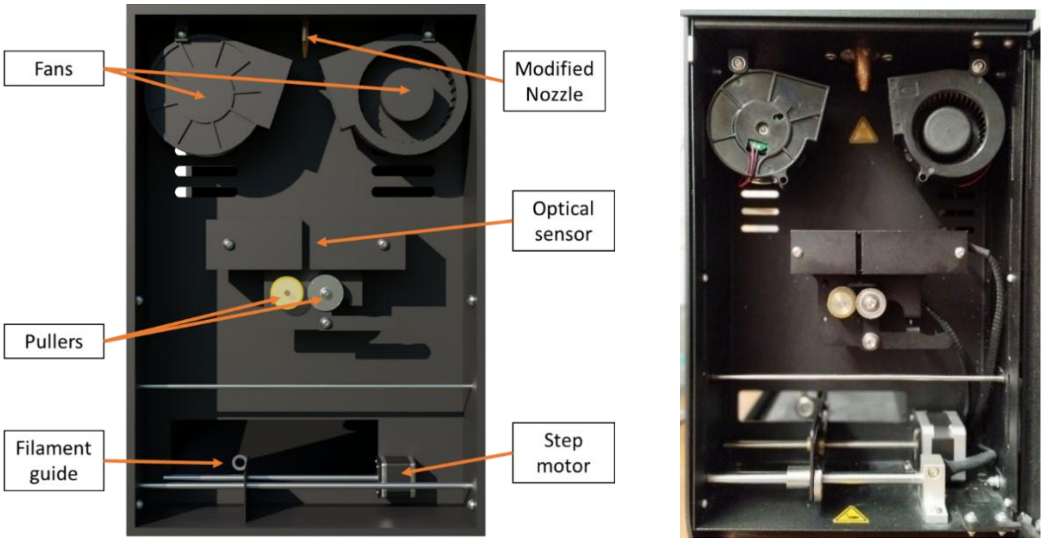

(a) (b)

Figure 5.2 - Single-screw extruder modification: (a) Single-screw extruder components and (b) final single-screw extruder setup.

The fabrication of filaments depends on key parameters such as temperature, extruder speed, and puller speed. Figure 5.3 illustrates a schematic representation of the single-screw extrusion process. Temperature control within the single-screw extruder is divided into three distinct zones: feeding, transitioning, and metering. Each of these zones plays a pivotal role in ensuring consistent filament circularity and diameter during production [56].

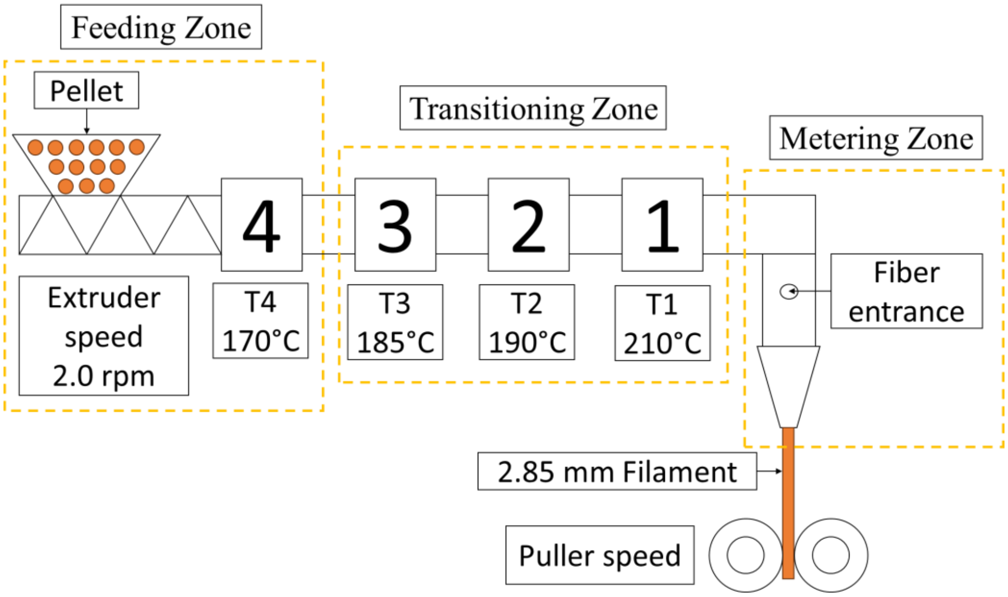

Figure 5.3 - Schematic diagram of the single-screw extruder, adapted from the manufacturer's design [55].

In the feeding zone, the extruder speed determines the flow of material produced, and the temperature (T4) is linked to the viscosity of the material, requiring a minimum viscosity to avoid clogging the equipment. Along the transitioning zone, the temperatures T3 to T1 and flow pressure create a homogeneous material, avoiding bubbles and voids. Low temperatures within the nozzle can result in bubble formation and blockages, whereas excessively high temperatures may compromise the workability of the filament. Finally, the metering zone regulates the puller speed by the filament diameter, measured by the optical sensor. The main modification occurred in the nozzle, where it was replaced with a longer one with a specific hole to allow the entrance of the natural yarn, as shown in Figure 5.4a. Figure 5.4b, on the other hand, depicts a moment during the extrusion of the biocomposite filament. The extrusion parameters of the semi-finished filament are presented in Table 5.5.

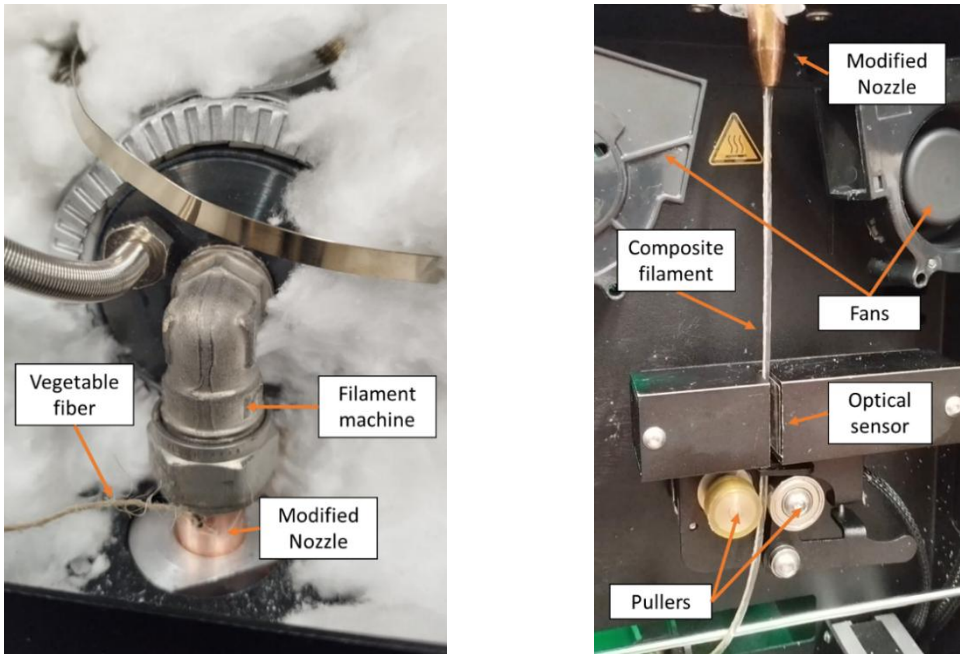

(a) (b)

Figure 5.4 - Fabrication of Semi-finished Filament: (a) Fiber insertion into the modified nozzle, (b) semi-finished filament extrusion process.

Table 5.5 - Single-screw extruder settings.

Property	**Value**
T1 (°C)	210
T2 (°C)	190
T3 (°C)	185
T4 (°C)	170
Extruder speed (rpm)	2.0
Filament fan (%)	25
Filament diameter (mm)	2.85±0.15
Spooling speed	automatic

5.2.2.2 In-situ impregnation (IN)

Modifications for *in-situ* impregnation were implemented in the Ender 3 V2 printer (Figure 5.5), drawing inspiration from the work of Santos and Cardoso [11]. A 2 mm diameter hole was drilled into the coldend section of the extruder to facilitate impregnation. Additionally, alterations were made to the fan-fixing case to enable the insertion of yarn without requiring the removal of the extruder.

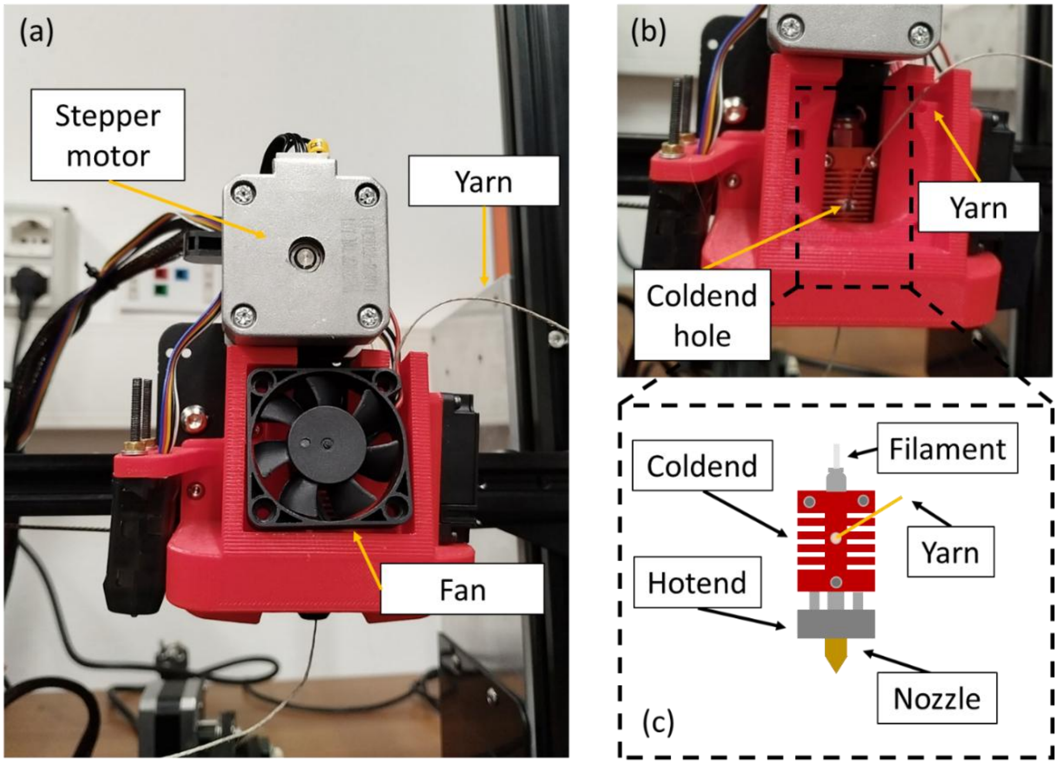

Figure 5.5 - Printer modification to *in-situ* printing: (a) Extruder, (b) fiber-entrance detail, and (c) schematic drawing.

5.2.2.3 Printing nomenclature

The test nomenclature was defined to capture the effects of fiber addition, printing method, and matrix format utilized. The two printing methods were *in-situ* and semi-finishing, while the matrix formats used were filament and pellet. Table 5.6 presents the terminology used for each combination, clarifying the specific conditions studied.

Table 5.6 - CFRTPCs' terminology.

Nomenclature	**Presence of flax yarn**	**Type of PLA**	**Method**
PLA-F	No	Filament	*In-situ*
IN-F	Yes	Filament	*In-situ*
PLA-P	No	Pellet	*In-situ*
IN-P	Yes	Pellet	*In-situ*
SF	Yes	Pellet	Semi-finished

5.3 Samples Characterization

5.3.1 Roughness test

The roughness tests were performed using an ATOS Compact Scan (Zeiss, Oberkochen, Germany) in the Reverse Laboratory (Polito, Piemonte, Italy). The testing protocol followed the recommendations of ISO 4288 [57]. The specimens display 20 mm×15 mm×3.0 mm of geometry, prepared with a double layer containing continuous filaments with fibers oriented in the loading direction, with the same printed geometry characteristics of the tensile test samples. For each of the five conditions studied, measurements were taken at three distinct sections on each sample, and the average roughness was calculated. The roughness values were obtained from the upper profiles of the cross-sections of the samples. Figure 5.6 illustrates the method used to acquire these measurements. This testing was conducted to analyze the surface of the printed material, highlighting the effects on layer interconnection and understanding the implications for interface bonding.

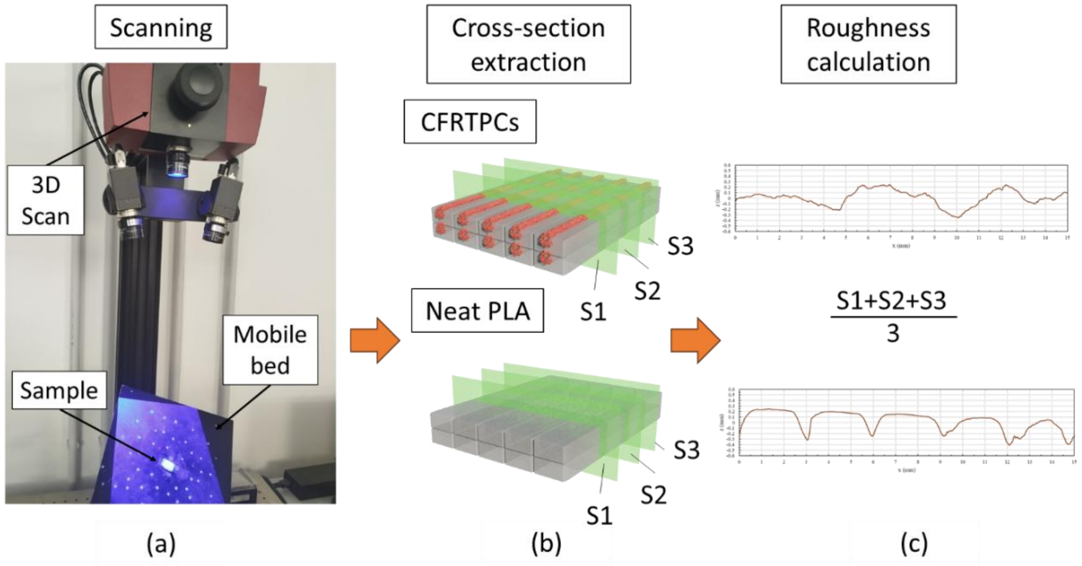

Figure 5.6 - Schematic representation of the surface roughness characterization method: (a) Scanning, (b) cross-section extraction, and (c) roughness calculation.

5.3.2 Deposition rate test

The deposition rate tests were analyzed using an Ender 3V2 printer available in the Rapid Manufacturing Laboratory (RMLab) in the Integrated Additive Manufacturing Center (IAM@PoliTO, Turin, Italy). The printed samples were produced at varying speeds, ranging from 100 mm/min (S100) to 500 mm/min (S500), or until detachment of the composite from the print bed occurred. A constant temperature was maintained in all cases to ensure consistent yarn impregnation by the matrix. Figure 5.7 provides a detailed illustration of the schematic path and schematic configuration for evaluating deposition rate and speed. Figure 5.7a depicts the printing path on the print bed (x and y axes with dimensions of 230 mm), where successive serpentine lines are deposited at incrementally increasing speeds. The process begins at 100 mm/min (denoted as S100) and increases by 100 mm/min with each subsequent line, culminating at 500 mm/min. Figure 5.7b complements this by showing an image of the actual 3D printing process, offering a visual representation of the test setup. Four tests were conducted for each practical condition (i.e., IN-F and SF), and the printing properties are summarized in Table 5.7.

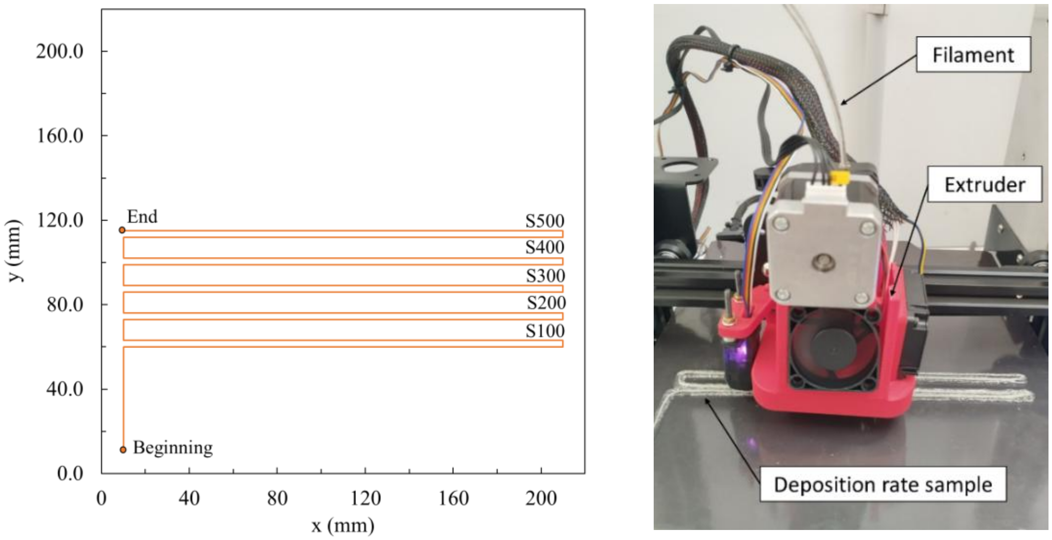

(a) (b)

Figure 5.7 - Deposition rate test: (a) Schematic of path and speed configuration and (b) printing process.

Table 5.7 - Deposition rate test's printing parameters.

Property	**Value**
Nozzle diameter (mm)	2.0
Speed range (mm/min)	100 - 500
Extruder temperature (°C)	200
Bed temperature (°C)	60
Layer height (mm)	1.5
Layer width (mm)	3.0

5.3.3 Tensile test

The tensile tests were conducted using an Aura 10T universal testing machine from Easydur (Arcisate, Italy). An independent strain measurement was conducted with an external X-Sight 2000 series optical extensometer (X-Sight s.r.o, Brno, Czech Republic), available in the Department of Management and Production Engineering (Polito, Turin, Italy). Figure 5.8 illustrates the experimental setup for tensile characterization, including a specific representation of the tensile-tested samples. The testing protocol followed the recommendations of ASTM D3039 [58]. The tests were performed under displacement control at a rate of 5 mm/min until failure. The specimens, with dimensions of 220 mm×28 mm×3.0 mm, were prepared with a double layer of continuous filaments containing flax yarns aligned in the loading direction. Five samples were tested for each condition, with the printing parameters kept the same for both examined approaches and consistent with those used in the detachment test, detailed in Table 5.7. Based on the results of the deposition test, a printing speed of 200 mm/min was selected. To ensure a fair comparison between the 3D printing methods, the same printing parameters were applied to both approaches. While the optimal parameters for each method may differ, the chosen parameters were standardized across both methods to provide a comparison of approaches, with consistent 3D printing parameters.

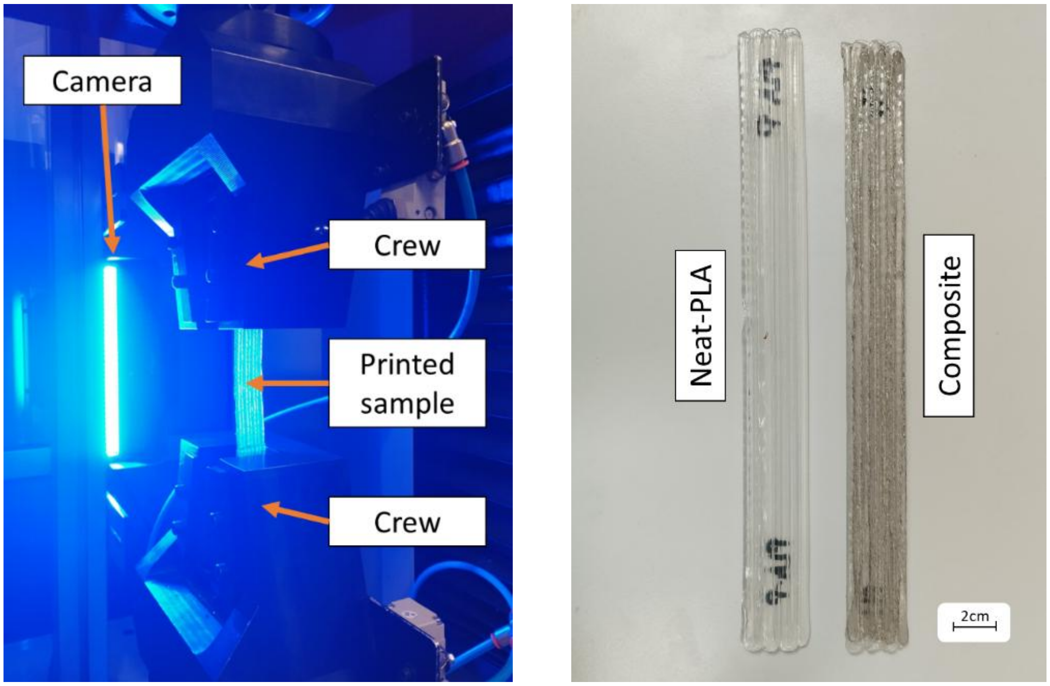

(a) (b)

Figure 5.8 - Tensile specimen test: (a) Setup and (b) printed samples.

5.3.4 Differential Scanning Calorimetry (DSC)

The DSC test was carried out using a NETZSCH DSC 200F3 Maia equipment, available in the LADES (CEFET/RJ, Rio de Janeiro, Brazil). The experiment was conducted with a heating rate of 20 K/min over a temperature range of 40-220 °C, under a nitrogen (N2) flow of 50 mL/min. Approximately 20 mg of each sample were analyzed, following ASTM D3418 procedures [59]. The test aimed to determine the glass transition temperature (Tg), crystalline melting temperature (Tm), and factors such as the degree of crystallinity. In the context of this research, DSC was employed to evaluate the thermal effects of each printing method on the final crystallinity and enthalpy of the material. The enthalpy, which indicates the process's influence on the composite's crystallinity, is determined by the area under the exothermic peak in the DSC curve. Additionally, the degree of crystallization can be calculated using Equation (1) as reported by Kong et al. [60].

$$X_c = \frac{\Delta H_m - \Delta H_{cc}}{\Delta H_m^o} \times 100 \tag{1}$$

where,

X_c- The weight fraction extent of crystallinity.

ΔH_m - The enthalpy of melting.

ΔH_{cc} - The enthalpy of cold crystallization.

ΔH_m^o - The enthalpy is the theoretical melting enthalpy of a purely crystalline PLA which was assumed to be equal to 93 J/g [61].

5.3.5 Scanning Electron Microscopy (SEM) Analysis

The cross-sections of the specimens were analyzed using a TESCAN CLARA Scanning Electron Microscope (SEM), available at the Rheology Group (Greo) (PUC-Rio, Rio de Janeiro, Brazil). The equipment operated at 2 keV. Prior to analysis, the samples were dried in an oven at 60 °C for 24 hours and stored in a desiccator to minimize moisture content. To enhance conductivity, the samples underwent a metallization process, in which they were coated with a thin layer of gold.

5.4 Results and Discussion

5.4.1 Effects of temperature and speed parameters on filament and printing quality and efficiency

The cross-sections of the specimens were analyzed using a TESCAN CLARA Scanning Electron Microscope (SEM), available at the Rheology Group (Greo) (PUC-Rio, Rio de Janeiro, Brazil). The equipment operated at 2 keV. Prior to analysis, the samples were dried in an oven at 60 °C for 24 hours and stored in a desiccator to minimize moisture content. To enhance conductivity, the samples underwent a metallization process, in which they were coated with a thin layer of gold (Figure 5.9a). Conversely, higher temperatures can excessively reduce viscosity, preventing the polymer from achieving the necessary consistency to form a filament with the required diameter (Figure 5.9b). For PLA, the optimal working temperature range is between 180 °C and 220 °C. When incorporating thicker yarns, a higher temperature, within the material's workable limits, is selected to achieve superior impregnation. In this study, a temperature of 210 °C was employed to ensure optimal yarn impregnation within the filament matrix.

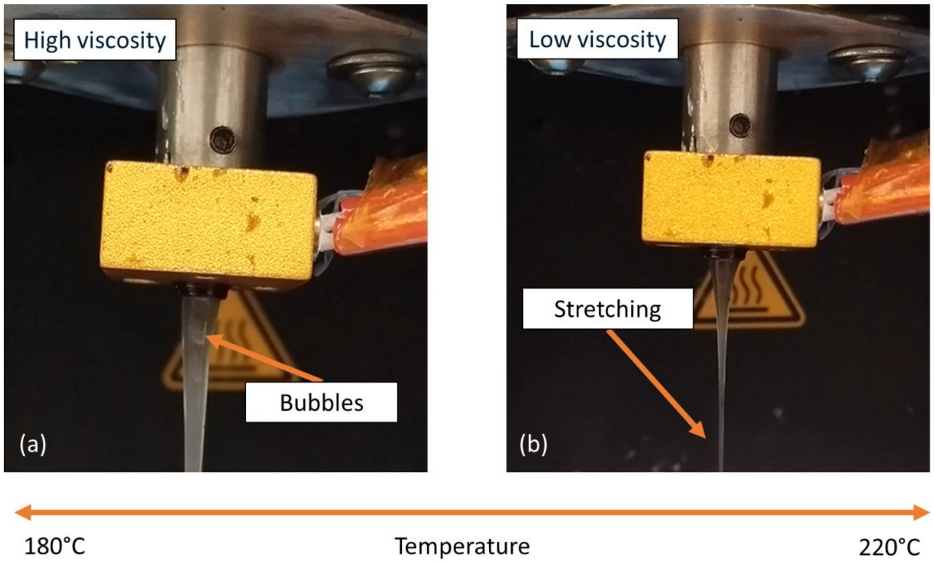

Figure 5.9 - Filament fabrication temperature with two distinct issues: (a) low viscosity and (b) high viscosity.

Figure 5.10a shows a representation of the obtained semi-finished filament produced with a diameter of 2.85±0.15 mm and a fiber volumetric fraction of 13.5%. The variation in filament diameter, approximately 0.15 mm or around 5%, observed in the extrusion of pellets reinforced by natural fibers, is attributed to internal flow variations within the filament extruder, as reported in other works in the literature [13]. Figure 5.10b presents an optical micrograph of a cross-section of the obtained biocomposite filament, where it is possible to note the non-uniform distribution of fibers, as an inherent consequence of the CFRTPCs process. As a matter of fact, during extrusion, the flow of the molten composite material exerts a drag force on the fibers, which partially displaces them from the deposited line, leading to misalignment. This behavior, which results in fiber distribution irregularities, has been previously observed by Rivero-Romero et al. [46] and Cheng et al. [38]. Further process optimization may help mitigate this issue, but it remains a challenge associated with the current filament fabrication technique.

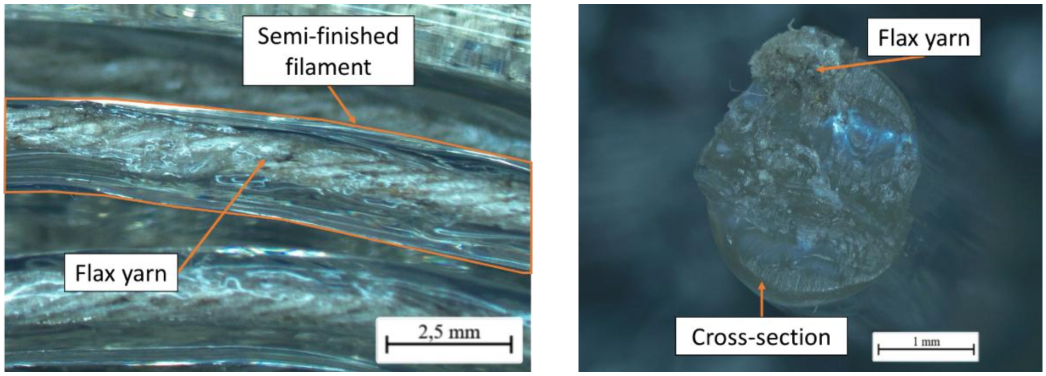

(a) (b)

Figure 5.10 - Semi-finished filaments: (a) Photograph of a semi-finished flax filament, (b) Micrograph of biocomposite filament cross-section.

In the filament manufacturing process, the addition of continuous yarn introduces several effects. These include yarn eccentricity within the filament (Figure 5.11a), the presence of inherent material impurities and bubbles (Figure 5.11b), variations in the cross-section dimensions, and regions lacking sufficient impregnation (Figure 5.11c). Yarn eccentricity (Figure 5.11d) is also observed in SF printing, as it occurs in the IN-F process. In these cases, it is due to the stresses generated during 3D printing, where the yarn is tensioned between the fixed part on the print bed and the impregnated part inside the extruder.

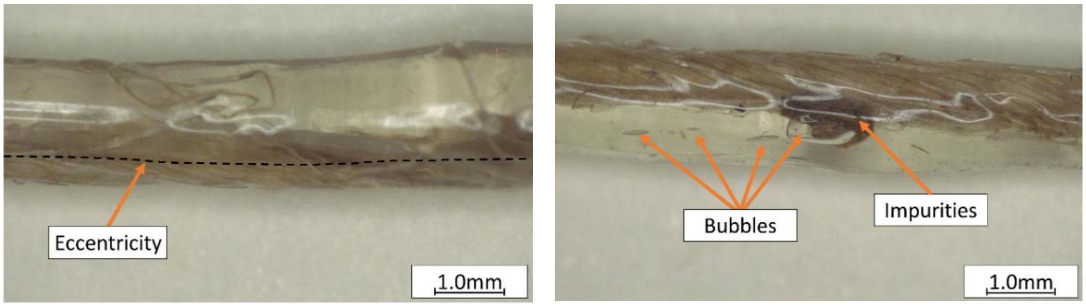

(a) (b)

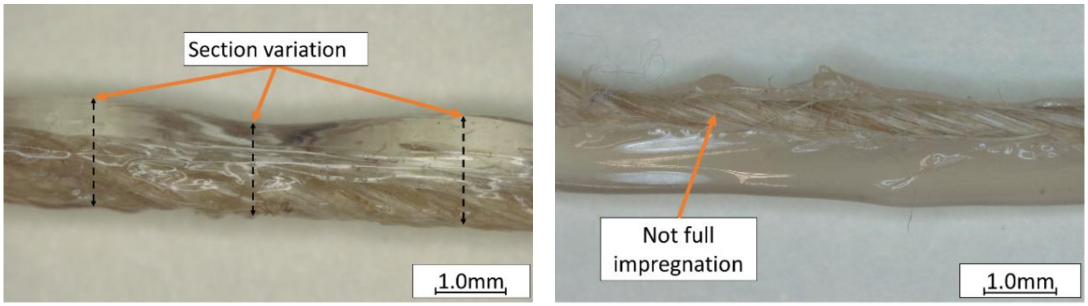

(c) (d)

Figure 5.11 - Composite filament manufacturing problems: (a) Eccentricity of the fiber, (b) impurities and bubbles, (c) section variation, and (d) not complete impregnation.

Similarly, high extruder speeds result in inconsistent flow and increased bubble formation, which consequently reduces the quality of the printing filament. This necessitates balancing the optimal polymer extrusion speed with the energy consumption required for its production. In this research, a speed of 2.0 rpm was selected for composite fabrication, as the introduction of fibers increases the bubble formation rate, requiring more precise control of the flow.

The printing speeds of the two methods (SF and IN) may be constrained by the specific process employed. In the IN method, the yarn is pulled through friction between the matrix and the reinforcement, allowing for some variation in matrix flow during printing, as the fiber moves more freely. In contrast, in the SF method, both the matrix and reinforcement are uniformly pushed by a stepper motor, limiting flow variation due to the fixed filament volume. Consequently, the SF method requires specific flow conditions (Figure 5.12). Reduced flow rates can lead to persistent fiber fractures, negatively impacting overall continuity, while excessive flow rates may result in material curling due to over-extrusion. The optimal flow condition involves depositing the yarn in a single, consistent, and linear manner.

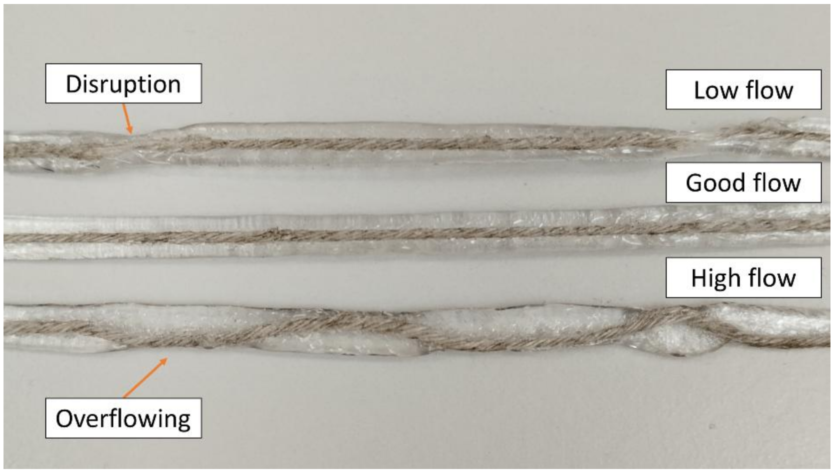

Figure 5.12 - Flow variation in the deposition rate test of flax composite filaments.

Finally, in the deposition rate test, where printing speeds ranging from 100 to 500 mm/min were tested under consistent bed and nozzle temperatures, the outcome of continuous yarn printing using SF impregnation revealed a clear dependence on optimal flow. The maximum speeds of SF (Figure 5.13) and IN-F (Figure 5.14) were 400 mm/min and 300 mm/min, respectively, showing a 33.3% increase in maximum printing speed when the yarn was pre-impregnated into a single composite filament. This improvement can be attributed to the SF method, which may reduce pre-tension in the yarn during deposition, as the stepper motor extrudes both the matrix and fiber reinforcement uniformly.

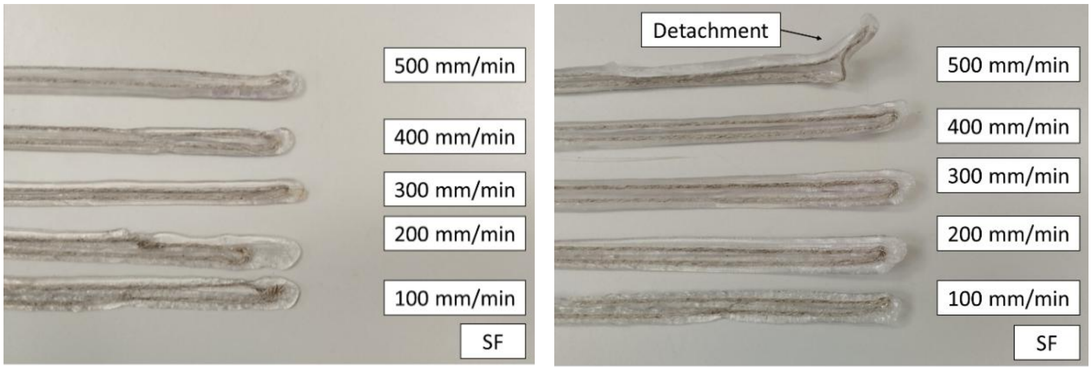

(a) (b)

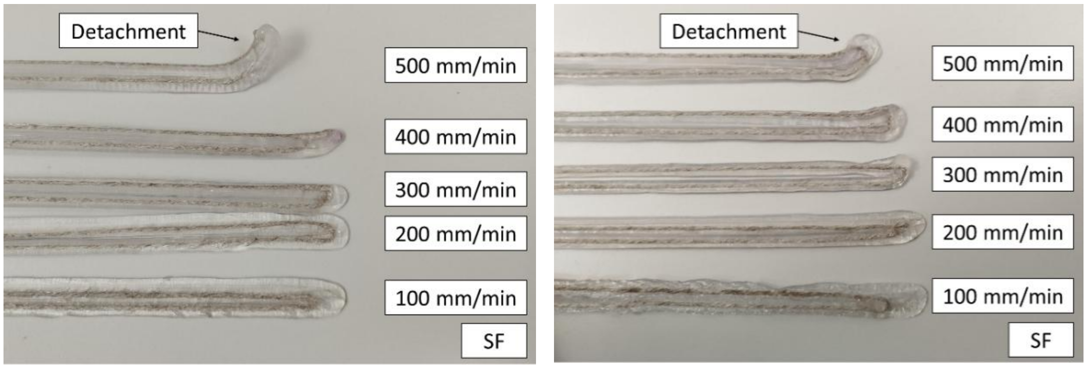

(c) (d)

Figure 5.13 - Assessment of flax filament impregnation as a function of printing speed, based on four independent tests, demonstrating the reproducibility of the results using semi-finished filament process.

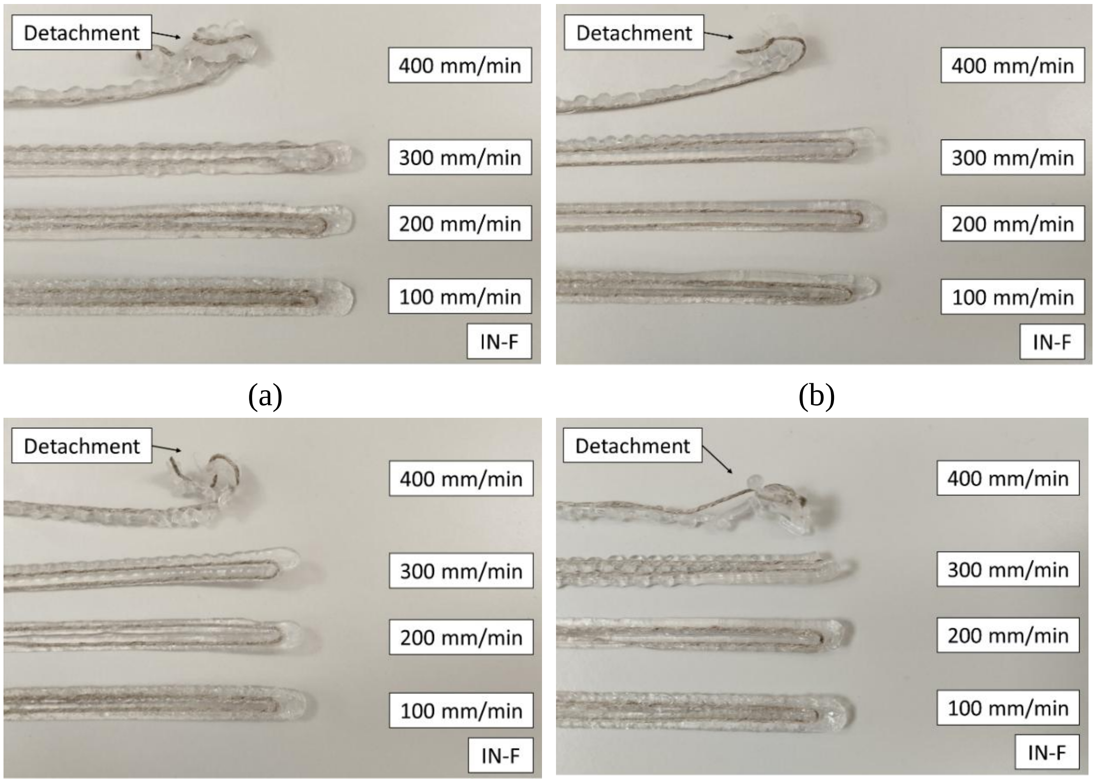

(a) (b)

(c) (d)

Figure 5.14 - Assessment of flax filament impregnation as a function of printing speed, based on four independent tests, demonstrating the reproducibility of the results using *in-situ* impregnation process.

5.4.2 Evaluation of fiber impregnation and composite roughness

The roughness of fiber insertion was analyzed using different methods to determine the main effects of each process. Figure 5.15 and Table 5.8 show the roughness curves and measured parameters for each process. Comparing PLA-F and PLA-P, the matrix produced from pellets (PLA-P) exhibited greater uniformity between layers (Figure 5.13b). However, this uniformity resulted in lower inter-layer adhesion, as evidenced by a higher surface roughness for PLA-P (Ra^{PLA-P}=0.170±0.008 mm) compared to PLA-F (Ra^{PLA-F}=0.071±0.000 mm). This trend is further supported by the amplitude parameters: Rq (Rq^{PLA-F}=0.085±0.000 mm and Rq^{PLA-P}=0.217±0.005 mm) and Rz (Rz^{PLA-F}=0.336±0.026 mm and Rz^{PLA-P}=0.960±0.120 mm).

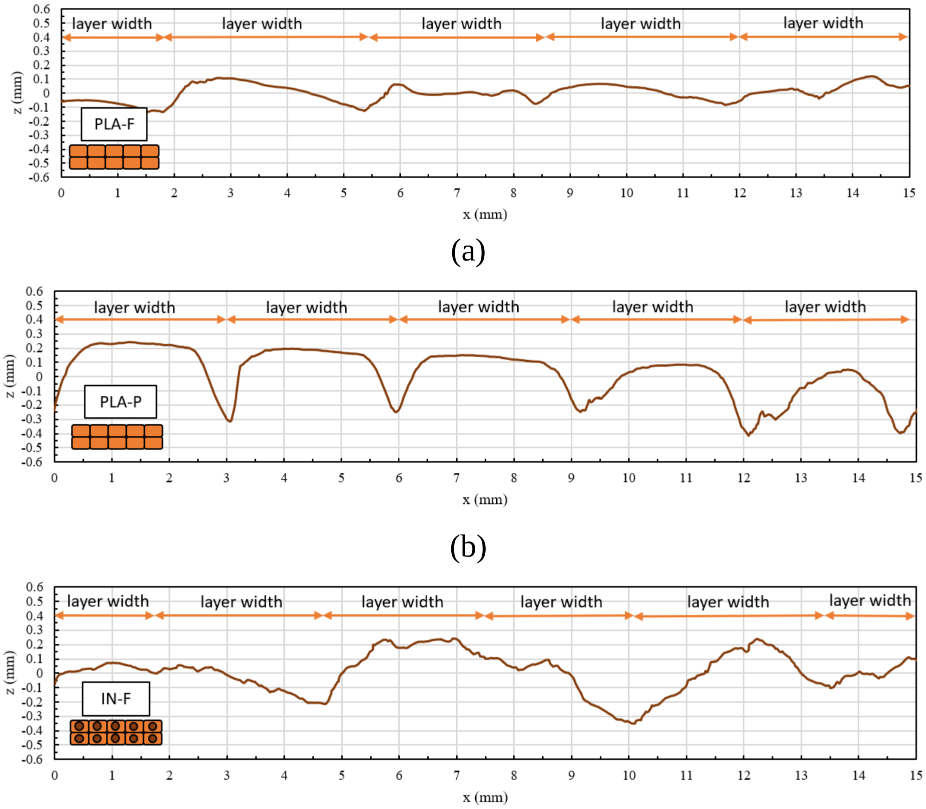

(a)

(b)

(c)

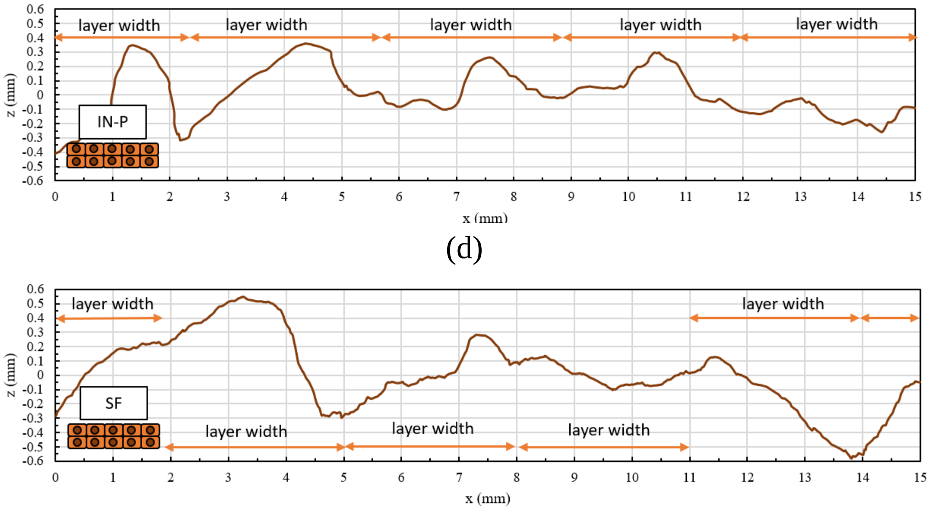

(d)

(e)

Figure 5.15 - Surface roughness of printed materials: (a) PLA-F, (b) PLA-P, (c) IN-F, (d) IN-P, and (e) SF.

Table 5.8 - Surface roughness parameters.

Roughness Property	**PLA-F**	**PLA-P**	**IN-F**	**IN-P**	**SF**
Ra (mm)	0.071 ±0.000	0.170 ±0.008	0.142 ±0.019	0.159 ±0.013	0.223 ±0.011
Rq (mm)	0.085 ±0.000	0.217 ±0.005	0.177 ±0.019	0.199 ±0.017	0.289 ±0.017
Rz (mm)	0.336 ±0.026	0.960 ±0.120	0.725 ±0.026	0.827 ±0.061	1.251 ±0.125

Some phenomena were observed when inserting the fiber reinforcement. Using commercial filament and the in-nozzle method (IN-F), there was a 100% increase in roughness (Ra^{PLA-F}=0.071±0.000 mm and Ra^{IN-F}=0.142±0.019 mm), approximately a 116% increase in amplitude (Rz^{PLA-F}=0.336±0.026 mm and Rz^{IN-F}=0.725±0.026 mm), and an increase in Root Mean Square (RMS) roughness inherent in the combination of these materials.

In the case of pellet-based matrix, the reinforcement reduced roughness by 5.8% for the in-nozzle method (Ra^{PLA-P}=0.170±0.008 mm and Ra^{IN-P}=0.159±0.013 mm) but increased by 31.2% for the semi-finished method (Ra^{SF}=0.223±0.011 mm). Despite this difference, both methods led to a loss of layer uniformity (Figure 5.13b, 5.13d, and 5.13e). Comparing the two printing methods, although the SF shows higher roughness (Ra^{SF}=0.223±0.011 mm) compared to IN (Ra^{IN-F}=0.142±0.019 mm and Ra^{IN-P}=0.159±0.013 mm), optical microscope analysis revealed noticeable differences in fiber insertion.

To support these results, Figure 5.16 presents the SEM images of the fibers and the fiber-matrix interface for each method, offering insight into their respective efficiency. In the SF method, PLA impregnation into the fiber is clearly observable (Figure 5.16b), whereas, in the IN-F method, such impregnation is lacking (Figure 5.16a). This difference significantly affects the fiber-matrix interface: the IN-F method resulted in a poor interface characterized by a clear and detrimental separation between the fiber and matrix, potentially compromising the composite's mechanical performance (Figure 5.16c). Conversely, the SF method yields a more integrated interface, with partial fiber impregnation enhancing the bond between the fiber and matrix (Figure 5.16d). However, the presence of unimpregnated fibers in the SF method indicates an incomplete process, particularly for larger diameter yarns, underscoring the necessity for pre-treatment strategies to optimize fiber impregnation and, consequently, the overall composite integrity.

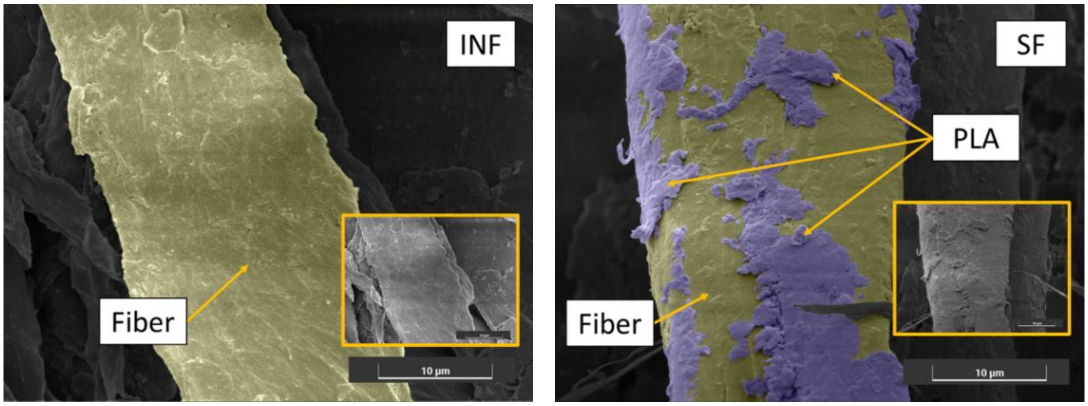

(a) (b)

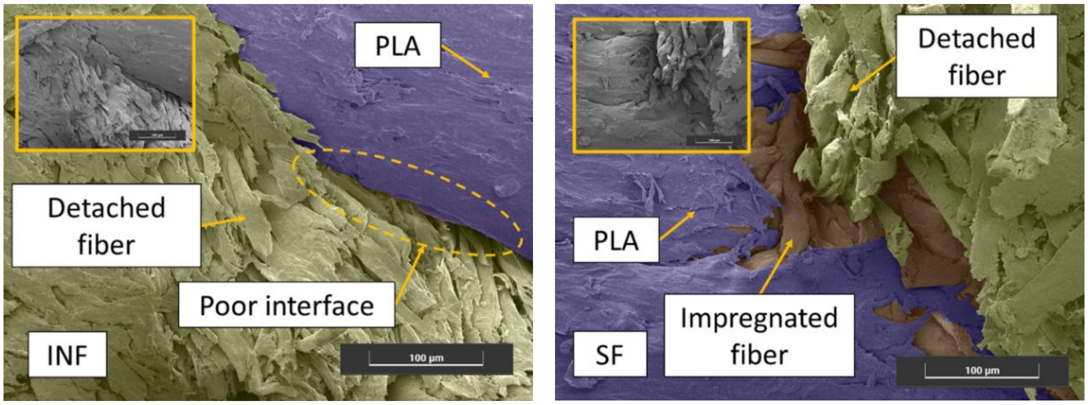

(c) (d)

Figure 5.16 - SEM images of (a) IN-F fiber, (b) SF fiber), (c) IN-F interface, and (d) SF interface. Note: Images have been artificially colored for better visualization.

5.4.3 Analysis of thermal and mechanical performance for in-nozzle and semi-finished approaches

To compare the two investigated approaches in terms of their key mechanical performance, tensile tests were conducted, with the main results summarized in Table 5.9 and Figure 5.17. Both the in-nozzle and semi-finished methods demonstrated improvements in mechanical properties when flax fiber was added, compared to neat PLA. In the case of in-situ impregnation using the industrial PLA filament as matrix (IN-F), tensile strength and elastic modulus increased by 34.8% and 14.1%, respectively, compared to the neat matrix (PLA-F). For the in-nozzle method using a matrix manufactured from PLA pellets (IN-P), tensile strength and Young's modulus increased by 12.7% and 2.4%, respectively, relative to neat PLA (PLA-P). The semi-finished method showed improvements of 29% in tensile strength and 21.3% in elastic modulus compared to PLA-P. It is noteworthy the comparison between the two fiber-reinforced methods using the same matrix (PLA-P), the SF method outperformed the IN-P method, with tensile strength and elastic modulus gains of 14.5% and 18.4%, respectively.

Table 5.9 - Tensile test results.

Sample	Tensile strength (MPa)	Elastic modulus (GPa)	Tensile strain (%)
PLA-F	35.01±2.39	2.43±0.12	1.64±0.20
PLA-P	40.96±1.70	2.49±0.18	1.87±0.21
IN-F	57.96±5.12	2.68±0.13	2.43±0.29

IN-P	46.15±4.54	2.55±0.16	2.30±0.14
SF	52.84±5.89	3.02±0.28	1.85±0.12

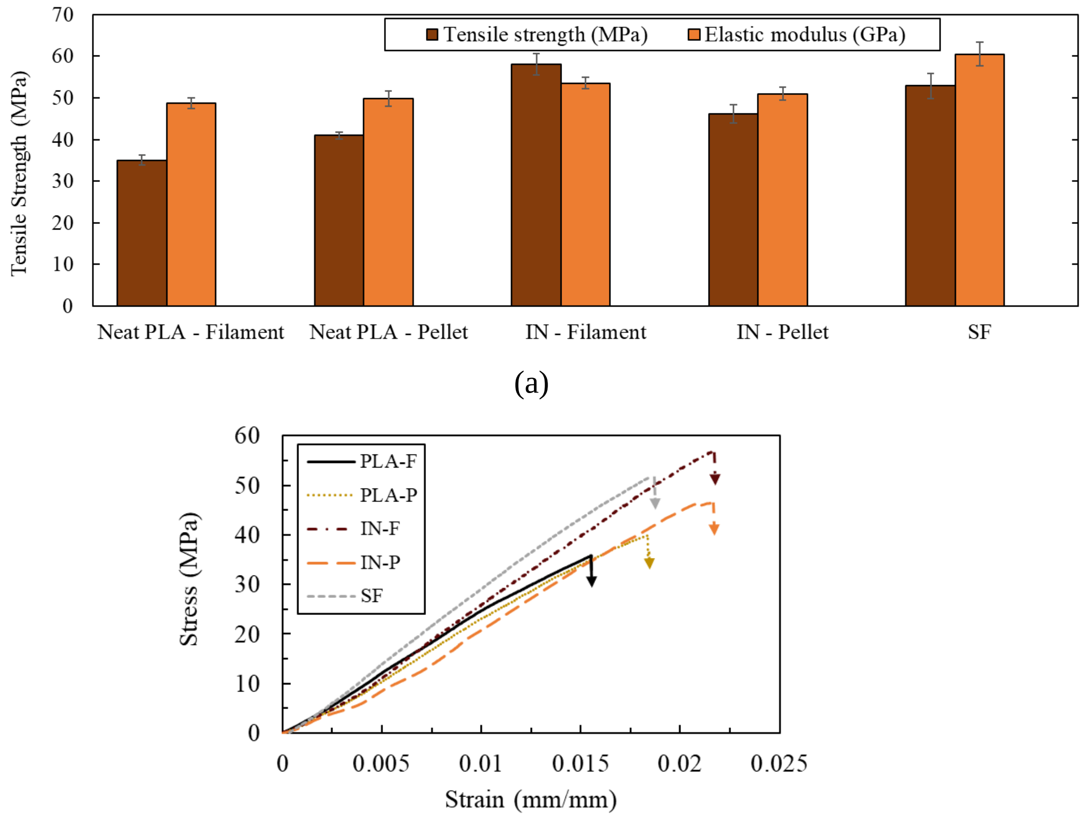

(a)

(b)

Figure 5.17 - Overview of the tensile test results: (a) Comparison of tensile strength and elastic modulus (b) stress-strain curves.

The tensile strength data for each sample were analyzed using the Anderson-Darling test hypothesis to assess normality (Table 5.10). The data exhibited a normal distribution, as confirmed by p-values higher than the 5% significance level. A comparison of the normal distribution curves, with a 95% confidence interval, revealed that none of the results completely overlapped (Figure 5.18a, 16b, and 16c).

Table 5.10 - Anderson-Darling test for tensile strength.

Sample	**Mean (MPa)**	**Standard Deviation (MPa)**	**Number of samples**	**Anderson Darling parameter**	**p-value**
PLA – F	35.01	2.39	5	0.178	0.834
PLA – P	40.96	1.70	5	0.154	0.899

IN – F	57.96	5.12	5	0.248	0.563
IN – P	46.15	4.54	5	0.473	0.126
SF	52.84	5.89	5	0.303	0.414

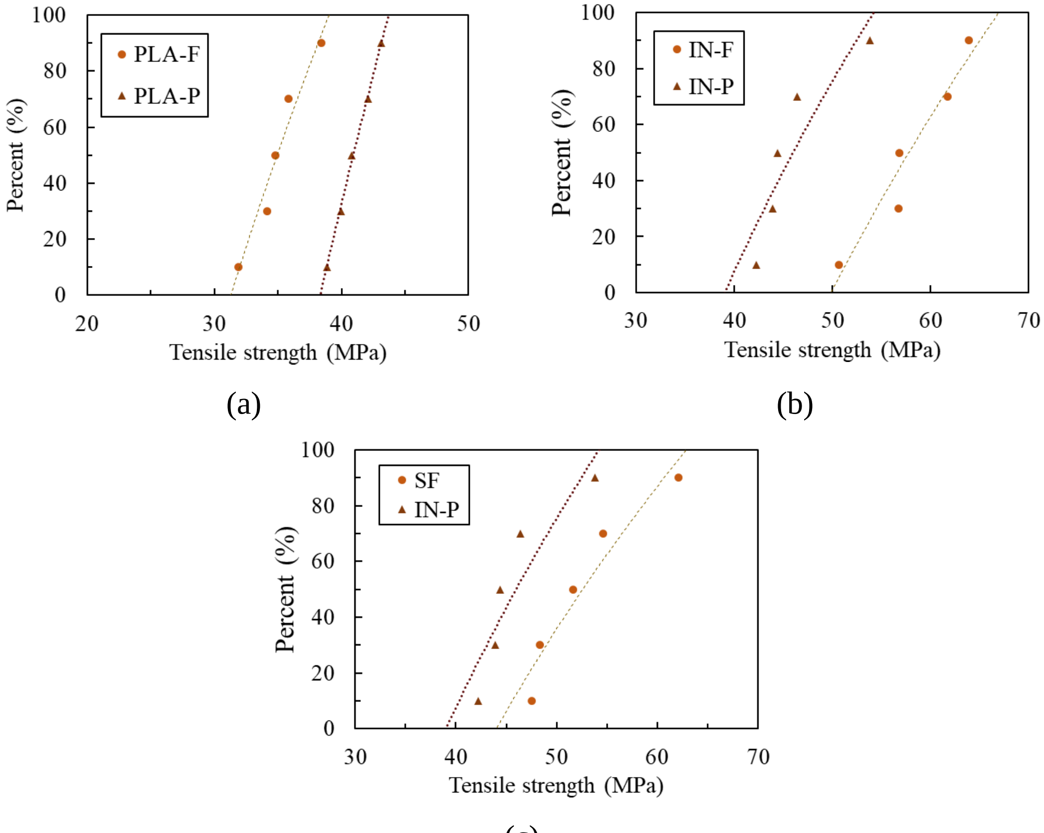

(a) (b)

(c)

Figure 5.18 - Normal probability graphic analysis: (a) neat PLA-F and PLA-P, (b) the in-nozzle method IN-F and IN-P, and (c) different methods with the same matrix (IN-P and SF).

Figure 5.19 illustrates the failure modes observed in the tensile samples tested. All samples exhibited brittle rupture in the matrix, initiating with crack propagation across the transverse section. Similar behavior was reported by Santos et al. [11] and Le Duigou [34], who attributed it to imperfect impregnation caused by the twisted yarn structure. The matrix’s brittleness, which dominates the composite’s overall behavior, leads to reduced reinforcement efficiency in the post-cracking regime of the composite. Additionally, in the post-cracking regime, the flax fiber yarns experienced pullout from the matrix, which further demonstrates the fragility of the fiber-matrix interface.

Figure 5.19 - Example of failure modes of the tensile samples.

The effects on the thermal properties of the 3D printed composites were evaluated through DSC testing, with the main results summarized in Table 4.9 and the corresponding DSC curves illustrated in Figure 5.20. The first thermal event observed was the glass transition temperature (T_g), followed by the cold crystallization temperature (T_{cc}), and finally the melting temperature (T_m). The T_g values were recorded between 66.9 °C and 67.5 °C, while the T_{cc} values ranged from 100.1 °C to 101.5 °C, characterized by an exothermic peak. This is likely due to the polymer's limited time to properly crystallize during the rapid cooling rates of FFF, which can reach several tens of degrees per minute [62,63]. The T_m values were observed within the range of 179.2 °C and 181.9 °C.

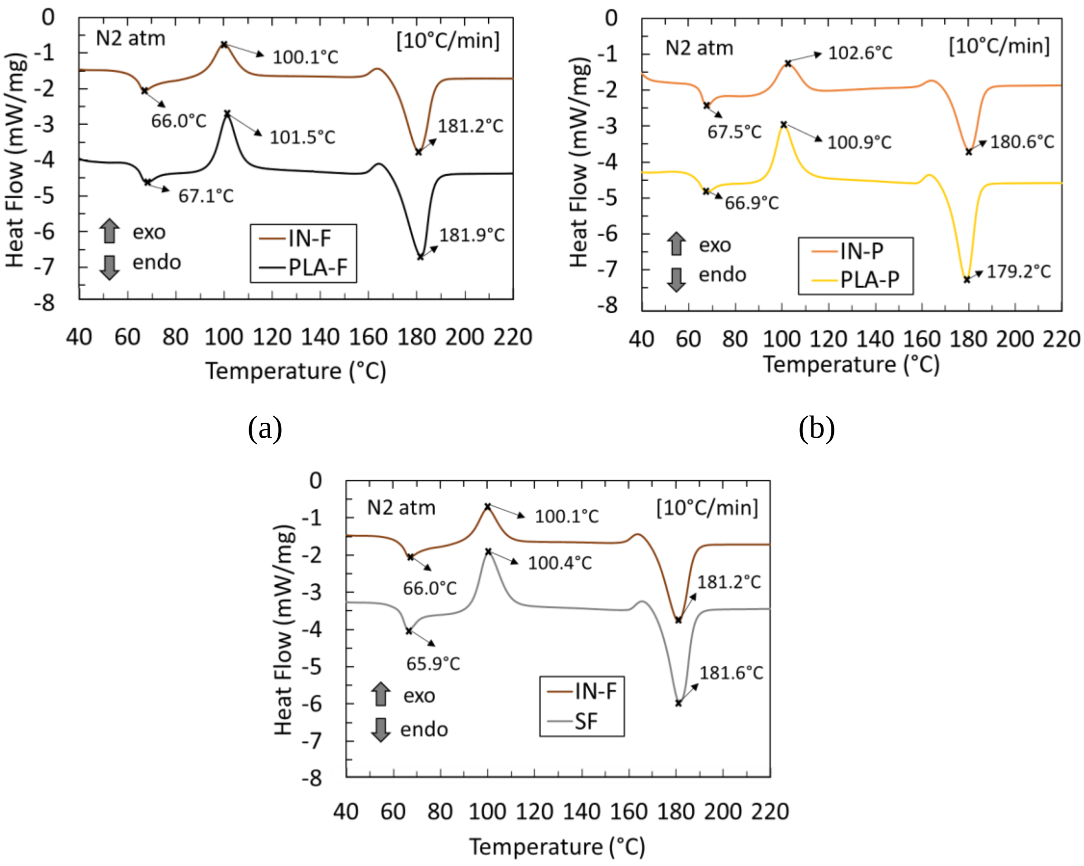

(a) (b)

(c)

Figure 5.20 - Comparative DSC scans of the 3D printing methods: (a) IN-F and PLA-F, (b) IN-P and PLA-P, (c) IN-F and SF.

Table 5.11 - Thermal properties of different composites evaluated with DSC.

Properties	**PLA-F**	**IN-F**	**PLA-P**	**IN-P**	**SF**
T_g - Glass transition temperature (°C)	67.1	66.0	66.9	67.5	65.9
T_{cc} - Cold crystallization temperature (°C)	101.5	100.1	100.9	102.6	100.4
ΔH_{cc} - Cold crystallization enthalpy (J/g)	86.3	66.7	94.3	56.6	102.8
T_m - Melting temperature (°C)	181.9	181.2	179.2	180.6	181.6
ΔH_m – Melting enthalpy (J/g)	130.0	121.8	134.3	100.4	137.2
X_c – Degree of crystallinity (%)	47.0	59.2	43.0	47.1	37.0

The degree of crystallinity (X_c) of the samples was calculated by determining the experimental enthalpies of fusion (ΔH_m) and cold crystallization (ΔH_{cc}), as outlined in Eq. 1. This evaluation was particularly important to assess the actual influence of processing methodologies on the crystallinity of the 3D printed specimens. A comparison of the X_c values revealed an increase in crystallinity when fibers were added: PLA without yarn (PLA-F) had a degree of crystallinity of 47.0%, while PLA with yarn (IN-F) showed a value of 59.2%. Similarly, for samples produced through the pellet fusion process, the degree of crystallinity increased from 43% (PLA-P) to 47.1% (IN-P) when fibers were incorporated. In both cases, the addition of fibers led to an increase in crystallinity, indicating that higher crystallinity is achieved through natural yarn-reinforcement FFF fiber. Andrzejewski and Nowakowski noted that sufficient fiber reinforcement content fosters crystalline growth on fiber surfaces, promoting a more favorable spherulite structure, which enhances the material's reinforcing properties [64].

However, the SF process exhibited lower crystallinity (37.0%) compared to the IN-F process (59.2%), suggesting that lower crystallinity is associated with 3D printing with the SF method. These differences highlight the distinct heating cycles involved in each method. For the *in-situ* process, the heating processing of the composite is limited to the 3D printing stage, whereas an additional thermal cycle is involved for the semi-finished filament fabrication. This extra thermal cycle can reduce crystallinity, as repeated heating and cooling may disturb the ordered molecular regions, preventing polymer chains from realigning into a crystalline structure during cooling. Supporting this observation, Yi *et al.* demonstrated that biocomposites reinforced with cellulose-based fibers exhibited a progressive reduction in the degree of crystallinity with each thermal cycle [65].

It is important to note that Eq. 1 does not initially account for the presence of fibers in the sample composition, which means that a fraction of the material does not contribute to the melting enthalpy of the PLA matrix. Therefore, the calculation of melting enthalpy has been corrected to consider the fiber fraction, ensuring a more accurate assessment of crystallinity. Although fibers can act as nucleating agents by promoting the formation of crystalline nuclei, the macroscopic size of the fibers and their limited degree of impregnation suggest that their nucleating effect may be negligible in this study. Additionally, the presence of non-impregnated fibers can introduce defects that interfere with crystallization, rather than enhancing it.

5.5 Conclusions

The research aimed to investigate the differences in physical and mechanical properties resulting from the use of large-diameter natural fiber yarns in FFF 3D-printed PLA, comparing two insertion methods: in-nozzle impregnation during 3D printing (IN) and semi-finished filament (SF). The study found that the SF method resulted in better fiber-matrix bonding, as evidenced by image analysis, and demonstrated superior tensile strength and elastic modulus, with improvements of up to 18.4% over the IN method. Additionally, the SF method allowed for faster printing speeds of up to 400 mm/min, compared to the 300 mm/min limit of the IN method. The presence of fibers also increased the degree of crystallinity, though this was reduced after repeated thermal cycles, which disrupted the crystalline regions.

The study's limitations include the lack of exploration of yarn pre-treatments and multi-filament strategies for large-scale applications. Future developments should address these gaps by improving impregnation quality, investigating the effect of exposure time to the heated nozzle on impregnation, and optimizing inter-ply strength through detailed mechanical analyses. These efforts will be crucial for enhancing composite performance and fully understanding the impact of processing parameters. Despite these limitations, the results highlight the potential of the SF method for advancing natural fiber-reinforced composites in FFF 3D printing. The demonstrated improvements in mechanical properties and process efficiency pave the way for innovative and sustainable application scenarios.

References

[1] Kechagias J, Zaoutsos S. Effects of 3D-printing processing parameters on FFF parts' porosity: outlook and trends. Materials and Manufacturing Processes 2024;39:804–14. https://doi.org/10.1080/10426914.2024.2304843.

[2] Buj-Corral I, Bagheri A, Sivatte-Adroer M. Effect of Printing Parameters on Dimensional Error, Surface Roughness and Porosity of FFF Printed Parts with Grid Structure. Polymers (Basel) 2021;13:1213. https://doi.org/10.3390/polym13081213.

[3] Buj-Corral I, Sánchez-Casas X, Luis-Pérez CJ. Analysis of am parameters on surface roughness obtained in pla parts printed with fff technology. Polymers (Basel) 2021;13. https://doi.org/10.3390/polym13142384.

[4] Kechagias JD. Surface roughness assessment of ABS and PLA filament 3D printing parts: structural parameters experimentation and semi-empirical modelling. International Journal of Advanced Manufacturing Technology 2024;134:1935–46. https://doi.org/10.1007/s00170-024-14232-0.

[5] Plymill A, Minneci R, Alexander Greeley D, Gritton J, Greeley D, Minneci R, et al. Graphene and Carbon Nanotube PLA Composite Feedstock Development for Fused Deposition Modeling 2016.

[6] Arsène, M-A Savastano Jr, H. Allameh, S. M. Ghavami K, Soboyejo WO. Cementitious composites reinforced with vegetable fibers. Proceedings of the 1st Interamerican Conference on Non-Conventional Materials and Technologies in the Eco-Construction and Infrastructure (IAC-NOCMAT) 2003:13–6.

[7] Wambua P, Ivens J, Verpoest I. Natural fibres: Can they replace glass in fibre reinforced plastics? Compos Sci Technol 2003;63:1259–64. https://doi.org/10.1016/S0266-3538(03)00096-4.

[8] Neto JSS, Lima RAA, Cavalcanti DKK, Souza JPB, Aguiar RAA, Banea MD. Effect of chemical treatment on the thermal properties of hybrid natural fiber-reinforced composites. J Appl Polym Sci 2019;136:1–13. https://doi.org/10.1002/app.47154.

[9] Mohanty AK, Misra M, Drzal LT. Natural fibers, biopolymers, and biocomposites. Taylor & Francis; 2005.

[10] Morrison WH, Archibald DD, Sharma HSS, Akin DE. Chemical and physical characterization of water- and dew-retted flax fibers. Ind Crops Prod 2000;12:39–46. https://doi.org/10.1016/S0926-6690(99)00044-8.

[11] Santos N V., Cardoso DCT. 3D printing of vegetable yarn-reinforced polymer components. J Clean Prod 2023;415. https://doi.org/10.1016/j.jclepro.2023.137870.

[12] Eichhorn SJ, Baillie CA, Zafeiropoulos N, Mwaikambo LY, Ansell MP, Dufresne A, et al. Current international research into cellulosic fibres and composites. J Mater Sci 2001;36:2107–31. https://doi.org/10.1023/A:1017512029696.

[13] Ahmad MN, Ishak MR, Mohammad Taha M, Mustapha F, Leman Z. A Review of Natural Fiber-Based Filaments for 3D Printing: Filament Fabrication and Characterization. Materials 2023;16. https://doi.org/10.3390/ma16114052.

[14] Romani A, Suriano R, Levi M. Biomass waste materials through extrusion-based additive manufacturing: A systematic literature review. J Clean Prod 2023;386. https://doi.org/10.1016/j.jclepro.2022.135779.

[15] Shahar FS, Hameed Sultan MT, Safri SNA, Jawaid M, Abu Talib AR, Basri AA, et al. Physical, thermal and tensile behaviour of 3D printed kenaf/PLA to suggest its usability for ankle–foot orthosis – a preliminary study. Rapid Prototyp J 2022;28:1573–88. https://doi.org/10.1108/RPJ-08-2021-0207.

[16] Tao Y, Li P, Zhang J, Wang S, Shi SQ, Kong F. A review of fused filament fabrication of continuous natural fiber reinforced thermoplastic composites: Techniques and materials. Polym Compos 2023;44:8200–22. https://doi.org/10.1002/pc.27477.

[17] Durfee WK, Iaizzo PA. Medical applications of 3D printing. Engineering in Medicine: Advances and Challenges, Elsevier; 2018, p. 527–43. https://doi.org/10.1016/B978-0-12-813068-1.00021-X.

[18] Pringle AM, Rudnicki M, Pearce JM. Wood furniture waste-based recycled 3-D printing filament. For Prod J 2018;68:86–95. https://doi.org/10.13073/FPJ-D-17-00042.

[19] Yang F, Zeng J, Long H, Xiao J, Luo Y, Gu J, et al. Micrometer copper-zinc alloy particles-reinforced wood plastic composites with high gloss and antibacterial properties for 3d printing. Polymers (Basel) 2020;12. https://doi.org/10.3390/polym12030621.

[20] Sanandiya ND, Ottenheim C, Phua JW, Caligiani A, Dritsas S, Fernandez JG. Circular manufacturing of chitinous bio-composites via bioconversion of urban refuse. Sci Rep 2020;10. https://doi.org/10.1038/s41598-020-61664-1.

[21] Sauerwein M, Zlopasa J, Doubrovski Z, Bakker C, Balkenende R. Reprintable paste-based materials for additive manufacturing in a circular economy. Sustainability (Switzerland) 2020;12:1–15. https://doi.org/10.3390/su12198032.

[22] Cislaghi A, Sala P, Borgonovo G, Gandolfi C, Bischetti GB. Towards more sustainable materials for geo-environmental engineering: The case of geogrids. Sustainability (Switzerland) 2021;13:1–21. https://doi.org/10.3390/su13052585.

[23] Romani A, Rognoli V, Levi M. Design, materials, and extrusion-based additive manufacturing in circular economy contexts: From waste to new products. Sustainability (Switzerland) 2021;13. https://doi.org/10.3390/su13137269.

[24] Figueroa-Velarde V, Diaz-Vidal T, Cisneros-López EO, Robledo-Ortiz JR, López-Naranjo EJ, Ortega-Gudiño P, et al. Mechanical and physicochemical properties of 3d-printed agave fibers/poly(Lactic) acid biocomposites. Materials 2021;14. https://doi.org/10.3390/ma14113111.

[25] Haryati A, Razali N, Petrů M, Taha M, Muhammad N, Ilyas RA. Effect of chemically treated kenaf fibre on mechanical and thermal properties of PLA composites prepared through fused deposition modeling (FDM). Polymers (Basel) 2021;13. https://doi.org/10.3390/polym13193299.

[26] Liu H, He H, Peng X, Huang B, Li J. Three-dimensional printing of poly(lactic acid) bio-based composites with sugarcane bagasse fiber: Effect of printing orientation on tensile performance. Polym Adv Technol 2019;30:910–22. https://doi.org/10.1002/pat.4524.

[27] Fekete I, Ronkay F, Lendvai L. Highly toughened blends of poly(lactic acid) (PLA) and natural rubber (NR) for FDM-based 3D printing applications: The effect of composition and infill pattern. Polym Test 2021;99. https://doi.org/10.1016/j.polymertesting.2021.107205.

[28] Dey A, Rahman MM, Yodo N, Grewell D. Development of biocomposite filament for fused filament fabrication from soy hulls and soy protein isolate. Mater Today Commun 2023;34. https://doi.org/10.1016/j.mtcomm.2023.105316.

[29] Pervaiz S, Qureshi TA, Kashwani G, Kannan S. 3D Printing of Fiber-Reinforced Plastic Composites Using Fused Deposition Modeling: A Status Review. Materials 2021;14:4520. https://doi.org/10.3390/ma14164520.

[30] Wang T, Li N, Link G, Jelonnek J, Fleischer J, Dittus J, et al. Load-dependent path planning method for 3D printing of continuous fiber reinforced plastics. Compos Part A Appl Sci Manuf 2021;140. https://doi.org/10.1016/j.compositesa.2020.106181.

[31] Zhang H, Lei X, Hu Q, Wu S, Aburaia M, Gonzalez-Gutierrez J, et al. Hybrid Printing Method of Polymer and Continuous Fiber-Reinforced Thermoplastic Composites (CFRTPCs) for Pipes through Double-Nozzle Five-Axis Printer. Polymers (Basel) 2022;14. https://doi.org/10.3390/polym14040819.

[32] Zhang H, Liu D, Huang T, Hu Q, Lammer H. Three-dimensional printing of continuous flax fiber-reinforced thermoplastic composites by five-axis machine. Materials 2020;13. https://doi.org/10.3390/ma13071678.

[33] Ginoux G, Wu X, Laqraa C, Soulat D, Paux J, Ferreira M, et al. Continuous additive manufacturing of hemp yarn-reinforced biocomposites with improved impregnation method. Compos Sci Technol 2024;251:110561. https://doi.org/10.1016/j.compscitech.2024.110561.

[34] Le Duigou A, Barbé A, Guillou E, Castro M. 3D printing of continuous flax fibre reinforced biocomposites for structural applications. Mater Des 2019;180:107884. https://doi.org/10.1016/j.matdes.2019.107884.

[35] Le Duigou A, Davies P, Baley C. Exploring durability of interfaces in flax fibre/epoxy micro-composites. Compos Part A Appl Sci Manuf 2013;48:121–8. https://doi.org/10.1016/j.compositesa.2013.01.010.

[36] Fruleux T, Castro M, Sauleau P, Matsuzaki R, Le Duigou A. Matrix stiffness: A key parameter to control hydro-elasticity and morphing of 3D printed biocomposite. Compos Part A Appl Sci Manuf 2022;156. https://doi.org/10.1016/j.compositesa.2022.106882.

[37] Fruleux T, Castro M, Correa D, Wang K, Matsuzaki R, Duigou A Le. Geometric limitations of 3D printed continuous flax-fiber reinforced biocomposites cellular lattice structures. Composites Part C: Open Access 2022;9. https://doi.org/10.1016/j.jcomc.2022.100313.

[38] Cheng P, Wang K, Chen X, Wang J, Peng Y, Ahzi S, et al. Interfacial and mechanical properties of continuous ramie fiber reinforced biocomposites fabricated by in-situ impregnated 3D printing. Ind Crops Prod 2021;170:113760. https://doi.org/10.1016/j.indcrop.2021.113760.

[39] Cheng P, Wang K, Chen X, Le Duigou A, Peng Y, Wen W. Compressive property and shape memory effect of 3D printed continuous ramie fiber reinforced biocomposite corrugated structures. Smart Mater Struct 2022;31:124003. https://doi.org/10.1088/1361-665x/ac95e4.

[40] Cheng P, Peng Y, Wang K, Le Duigou A, Yao S, Chen C. Quasi-static penetration property of 3D printed woven-like ramie fiber reinforced biocomposites. Compos Struct 2023;303:116313. https://doi.org/10.1016/j.compstruct.2022.116313.

[41] Suteja J, Firmanto H, Soesanti A, Christian C. Properties investigation of 3D printed continuous pineapple leaf fiber-reinforced PLA composite. Journal of Thermoplastic Composite Materials 2022;35:2052–61. https://doi.org/10.1177/0892705720945371.

[42] Ryosuke Matsuzaki, Masahito Ueda, Masaki Namiki, Tae-Kun Jeong H, Keisuke Horiguchi, Taishi Nakamura A& YH. Three-dimensional printing of continuous-fiber composites by in-nozzle impregnation 2016.

[43] Long Y, Zhang Z, Fu K, Li Y. Efficient plant fibre yarn pre-treatment for 3D printed continuous flax fibre/poly(lactic) acid composites. Compos B Eng 2021;227. https://doi.org/10.1016/j.compositesb.2021.109389.

[44] Cai R, Lin H, Cheng P, Zhang Z, Wang K, Peng Y, et al. Investigation on dynamic strength of 3D-printed continuous ramie fiber reinforced biocomposites at various strain rates using machine learning methods. Polym Compos 2022;43:5235–49. https://doi.org/10.1002/pc.26816.

[45] Terekhina S, Egorov S, Tarasova T, Skornyakov I, Guillaumat L, Hattali ML. In-nozzle impregnation of continuous textile flax fiber/polyamide 6 composite during FFF process. Compos Part A Appl Sci Manuf 2022;153. https://doi.org/10.1016/j.compositesa.2021.106725.

[46] Rivero-Romero O, Barrera-Fajardo I, Unfried-Silgado J. Effects of printing parameters on fiber eccentricity and porosity level in a thermoplastic matrix composite reinforced with continuous banana fiber fabricated by FFF with in situ impregnation. International Journal of Advanced Manufacturing Technology 2023;125:1893–901. https://doi.org/10.1007/s00170-022-10799-8.

[47] Wu X, Ginoux G, Paux J, Allaoui S. Damage and fracture studies of continuous flax fiber-reinforced composites 3D printed by in-nozzle impregnation additive manufacturing. International Journal of Damage Mechanics 2024. https://doi.org/10.1177/10567895241279845.

[48] Pereira de Moraes J, Nunes Martins de Lima L, Miranda Barbosa R. Yarns and weaves: the know-how and the orality of spinners and weavers in Xixá. História Oral 2023;26:30–50. https://doi.org/10.51880/ho.v26i2.1373.

[49] Camargo VCB, Almada-Lobo B, Toledo FMB. Integrated lotsizing, scheduling and blending decisions in the spinning industry. Pesquisa Operacional 2021;41. https://doi.org/10.1590/0101-7438.2021.041s1.00233486.

[50] Zhuo P, Li S, Ashcroft IA, Jones AI. Material extrusion additive manufacturing of continuous fibre reinforced polymer matrix composites: A review and outlook. Compos B Eng 2021;224. https://doi.org/10.1016/j.compositesb.2021.109143.

[51] Li N, Li Y, Liu S. Rapid prototyping of continuous carbon fiber reinforced polylactic acid composites by 3D printing. J Mater Process Technol 2016;238:218–25. https://doi.org/10.1016/j.jmatprotec.2016.07.025.

[52] Chabaud G, Castro M, Denoual C, Le Duigou A. Hygromechanical properties of 3D printed continuous carbon and glass fibre reinforced polyamide composite for outdoor structural applications. Addit Manuf 2019;26:94–105. https://doi.org/10.1016/j.addma.2019.01.005.

[53] Matsuzaki R, Nakamura T, Sugiyama K, Ueda M, Todoroki A, Hirano Y, et al. Effects of Set Curvature and Fiber Bundle Size on the Printed Radius of Curvature by a Continuous Carbon Fiber Composite 3D Printer. Addit Manuf 2018;24:93–102. https://doi.org/10.1016/j.addma.2018.09.019.

[54] Mohanty AK, Misra M, Drzal LT. Natural fibers, biopolymers, and biocomposites. Taylor & Francis; 2005.

[55] 3D DEVO. Netherlands 2024.

[56] Johnson D. Filament extrusion using recycled materials. Halmstad University, 2020.

[57] British Standards Institution., British Standards Institution. BS EN ISO 4288:1998 : Geometric product specifications (GPS) - surface texture : profile method : rules and procedures for the assessment of surface texture. British Standards Institution; 1998.

[58] ASTM. ASTM D3039 / D3039M - Standard Test Method for Tensile Properties of Polymer Matrix Composite Materials. Annual Book of ASTM Standards n.d.;15.03. https://doi.org/10.1520/D3039_D3039M-17.

[59] ASTM. ASTM D3418 - Standard Test Method for Transition Temperatures of Polymers by Differential Scanning Calorimetry 2021.

[60] Kong Y, Hay JN. The measurement of the crystallinity of polymers by DSC. n.d

[61] Zhang C, Lan Q, Zhai T, Nie S, Luo J, Yan W. Melt crystallization behavior and crystalline morphology of Polylactide/Poly(ε-caprolactone) blends compatibilized by lactide-caprolactone copolymer. Polymers (Basel) 2018;10. https://doi.org/10.3390/polym10111181.

[62] Lannunziata E, Colucci G, Minetola P, Giubilini A. Effect of annealing treatment and infill percentage on 3D-printed PEEK samples by Fused Filament Fabrication. International Journal of Advanced Manufacturing Technology 2024;131:5209–22. https://doi.org/10.1007/s00170-024-13347-8.

[63] Zhang J, Vasiliauskaite E, De Kuyper A, De Schryver C, Vogeler F, Desplentere F, et al. Temperature Analyses in Fused Filament Fabrication: From Filament Entering the Hot-End to the Printed Parts. 3D Print Addit Manuf 2022;9:132–42. https://doi.org/10.1089/3dp.2020.0339.

[64] Andrzejewski J, Nowakowski M. Development of toughened flax fiber reinforced composites. Modification of poly(lactic acid)/poly(butylene adipate-co-terephthalate) blends by reactive extrusion process. Materials 2021;14. https://doi.org/10.3390/ma14061523.

[65] Yi C, Tian L, Tang F, Wang L, Zou H, Xu W. Crystalline transition behavior of sisal in cycle process. Polym Compos 2010;31:933–8. https://doi.org/10.1002/pc.20885.

Chapter 6 - MONO AND BI-MATERIAL ADHESIVE JOINTS WITH ADDITIVELY MANUFACTURED CONTINUOUS NATURAL FIBER REINFORCED BIOCOMPOSITE ADHERENDS

This chapter was published under the reference:

Natália V. Santos, Daniel K. K. Cavalcanti, Henrique F. M. de Queiroz, Jorge S. S. Neto, Mariana D. Banea, Daniel C.T Cardoso, Mono and bi-material adhesive joints with additively manufactured continuous natural fiber reinforced biocomposite adherends, Polymer Composites (2025). http://doi.org/10.1002/pc.29674

The scope of 3D printing is limited by its maximum printing area, necessitating joints for assembling larger structural elements. Natural fibers have been employed to reinforce printed materials, enhance their mechanical properties, and reduce polymer usage. However, the effects of these fibers on bonded joints, particularly in the context of continuous natural yarns, remain underexplored in the literature. This study examines 3D-printed single-lap joints (SLJ) with biocomposite adherends made via Fused Filament Fabrication (FFF), using continuous jute fiber-yarn reinforced polymer (JFRP) and Polylactic Acid (PLA). Mechanical characterization, surface roughness analysis, and single-lap shear tests were conducted for combinations of PLA-PLA, JFRP-JFRP, JFRP-steel, and JFRP-wood joints. JFRP joints showed higher failure loads than neat PLA joints due to increased roughness and strength from the jute yarn. JFRP-wood joints demonstrated the best performance, exceeding neat PLA SLJ strength by approximately 57%. Analytical models were used to understand better the effects of materials and reinforcement on load distribution along the adhesive.

6.1. Introduction

The advent of Additive Manufacturing (AM), also known as 3D printing, has been instrumental in transforming various sectors of the industry [1], especially civil construction, primarily attributable to its capacity for fabricating complex components and minimizing waste generation and labor requirements [2,3]. However, the extent of AM printing is constrained by the equipment's printing area, necessitating the establishment of efficient connections between the fabricated components. In this context, bonded joints emerge as an excellent option to ensure load-transfer ability and structural integrity, efficiently connect distinct printed parts and overcome the limitations imposed by the printing area size.

Among the possibilities of connections, bonded joints are a crucial component in materials engineering and structural mechanics, representing a sophisticated integration of materials through adhesive interactions. These joints involve the strategic connection of different materials, such as polymers or composites, and offer enhanced design flexibility for structural projects, enabling more innovative and efficient designs [4]. This approach leverages the synergistic properties of adhesives to distribute loads, enhance durability, and mitigate stress concentrations introduced by mechanical fasteners, thereby optimizing the overall performance of joined components [4,5].

The behavior of adhesively bonded joints with 3D-printed adherends was investigated by several researchers [1,3,4,6,7]. One of the aspects investigated was the effect of adhesive type on the joint’s performance. For example, Bürenhaus et al. [8] studied the influence of adhesive type (acrylate resin, polyurethane adhesive, and epoxy resins), surface treatment (mechanical roughening and plasma activation), surface structure, and joint design on the bond strength of Fused Filament Fabrication (FFF) manufactured parts made of ULTEM 9085 resin. Yap et al. [9] compared epoxy and cyanoacrylate adhesives on 3D-printed Acrylonitrile Styrene Acrylate (ASA) and Nylon 12 Carbon Fiber (NCF) materials. The authors showed that the choice of adhesive-adherend combination is essential in printed adherends and directly affects the failure mode of the bonded joint. The best combination was observed with ASA and cyanoacrylate, yielding higher adhesive strength and resulting in cohesive failure of the joint. This differs from all other cases where the failures were adhesive. Even with heat and surface treatments, the epoxy adhesive strength remained notably weaker than that of cyanoacrylate.

An additional critical factor in 3D printing and composite materials is the geometric tailoring of the adherends. Among the studies conducted on this topic, Cavalcanti et al. [10], investigated the effect of 3D-printed PLA (polylactic acid) bonded joints in two types of orientation (flatwise and edgewise direction) with flat and wave geometry joints. They state that modifying the adherend geometry to enlarge the contact surface proportionally can enhance the ultimate strength of the bonded joint.

Kovan et al. [11] investigated the impact of layer thickness and print orientation on the bond strength between 3D-printed materials through single-lap shear joints. The results indicate that the edgewise orientation exhibits superior bonding strength for thinner layers, whereas the flatwise orientation demonstrates the highest bonding strength for thicker layers. According to the authors, the variation in adhesive bonding strength across different print orientations can be attributed to a combination of the notch effect, area effect, and surface roughness.

Regarding mechanical properties, Garcia et al. [12] used 3D printing to modify the surface of laminated composites. By applying printed layers superimposed on the bonded joint to impart texture to bond regions, the authors observed that these joints manifested higher average peak loads, showing a maximum increase of up to 832% concerning pure adhesive joints.

Khosravani et al. [13] studied the influence of 3D printing parameters and adhesive thickness on the performance of 3D-printed PLA adhesively bonded joints. They determined an optimal adhesive thickness of 0.2 mm for printed joints, resulting in higher mechanical properties than those for other thicknesses studied. Atahan et al. [14] investigated the effect of loading rate on the tensile and bending strength of 3D-printed PLA adhesively bonded joints, showing the dependence of the mechanical behavior of the printed joint on the path in which it was printed.

The applications of bi-material joints partially composed of printed materials have been increasing, as the combination of materials allows the integration of 3D printing with various materials, facilitating the creation of intelligent and optimized structures. Golewski et al. [7] analyzed the response mechanisms of hybrid joints composed of ABS and 6061-grade aluminum in various geometries, as the polymer-aluminum combination has significant applications in the aerospace sector. This new joining technique increased the maximum force from an initial value of 400.4 N to 832.5 N due to the increased stiffness generated by adding a more rigid material.

Dugbenoo et al. [15] discussed using additive manufacturing to enhance bonding in 3D-printed continuous-fiber composites by creating a porous bonding surface, significantly improving strength and toughness. Similarly, Pizzorni et al. [3] analyzed the effect of joint-design factors (overlap length, adhesive type, and substrate geometry) on the adhesively bonded joints with adherends consisting of 3D-printed short and continuous carbon-fiber composites. They suggest that the limitations of the printed composite joint are mainly attributable to the substrate's low transverse strength, which is compromised by the substantial peel stresses at the overlap terminations.

Concerning the use of natural fibers, Cavalcanti et al. [16] explored the integration of natural fibers (jute and curauá) and synthetic fibers (glass) in the additively manufactured PLA and ABS adherends. The authors demonstrate that the mechanical properties of adhesively single-lap joints (SLJs) were enhanced by incorporating natural fiber fabric laminate over the 3D-printed adherends. The most significant improvement in joint failure load, approximately 150%, was observed when employing curauá fabric compared to neat PLA. However, this incorporation only occurred after the printing process, through the lamination of the fabric onto the joint. The behavior of bonded joints produced with 3D-printed biocomposites remains unexplored.

The focus on the utilization of AM parts has been concentrated in the aerospace and transport industries. However, AM has gained attention due to its unique advantages for the Architecture, Engineering, and Construction (AEC) sectors [17–21].

Therefore, owing to the likely reduction in structural weight, cost, and waste, this application may prove valuable to enhancing projects in the construction sector. Specifically for the civil engineering sector, any technique that will aid in reducing structural total carbon footprint is invaluable given the current unsustainable emission levels, especially replacing of traditional materials with low energy consumption natural fiber composites [22].

In a previous study [23], a method to produce 3D-printed components using continuous yarn reinforcement was developed, utilizing a modified FFF's hotend adapted for in-nozzle impregnation of natural fibers within a biopolymer matrix. The process combines natural yarns with polylactic acid (PLA) to produce bio-based printed filaments with diameters up to 3 mm. It enhances material properties compared to plain biopolymer, increasing productivity and enabling its use in large-scale elements. However, print size limitations generated the need to analyze the possible connections of printed biocomposites to enable their large-scale use. Furthermore, combining 3D printing with primary construction materials has led to innovative applications that excel in creating robust and functional mixed architectural elements. This represents a significant advancement in the field of civil construction.

The main objective of this study is to investigate the mechanical performance of SLJs made of AM adherends made of jute fiber-reinforced polymer biocomposites, analyzing the effects of fiber incorporation on roughness and its impact on adhesion. Additionally, an analysis of mixed joints of this printed biocomposite with traditional construction materials (wood and steel) was carried out to verify the applicability of this technique to the civil construction sector. The innovation of this research lies in the novel application of natural yarn-reinforced composites in similar and dissimilar joints for the construction sectors. The utilization of biodegradable 3D-printed composites presents an intriguing alternative to conventional joints. This approach enhances the environmental sustainability of both industries and reduces waste. Consequently, the present study is a crucial foundation for further research on these types of joints.

6.2. Materials and Methods

6.2.1 Materials and Material Characterization

The first phase of this work was a comprehensive material characterization to understand the properties and behavior of additively manufactured biocomposites. The material was produced with continuous jute fiber reinforcement embedded in a PLA matrix. The choice of PLA was made due to its biodegradable nature and natural origin. As a reinforcement material, jute was selected for its abundance, natural properties, and cost-effectiveness. Additionally, continuous printing with jute yarn allows for greater control over the fiber percentage throughout the printing process. The jute yarn was provided by Sisal Sul (São Paulo, Brazil), while the 1.75mm diameter polylactic acid filament (PLA) was supplied by 3DLAB (Minas Gerais, Brazil). This work adopted two additional adherend materials (wood and steel) chosen for their widespread use in civil construction, thereby allowing the evaluation of the potential application of the printed biomaterial in mixed structures within the sector. The wood samples were made of Erisma uncinatum provided by Madeira Batista (Orleans, Brazil). The steel samples were made using high-strength steel (DIN C65 heat treated). Table 6.1 shows the main properties of the substrate materials.

Table 6.1 - Properties of the substrate materials [23–31].

Property	**Jute yarn**	**PLA**	**Wood**	**Steel**
Classification	Corchorus	Polylactic Acid	Erisma uncinatum	DIN C65 heat-treated
Diameter	0.52-1.17	-	-	-
Density (g/cm^3)	1.3-1.5	1.21-1.25	0.625	-
Linear density (g/m)	0.31±0.05	-	-	-
Tensile strength (MPa)	393-800	21-60	31-67	861-930
Young modulus (GPa)	10-30	0.35-3.5	9.7-17.0	210
Melting temperature (°C)	-	160-220	-	-
Cellulose (%)	58-71	-	-	-
Hemicellulose (%)	12	-	-	-
Lignin content (%)	12-14	-	-	-
Moisture absorption (%)	12	-	-	-

A structural epoxy-based adhesive, AR345, provided by E-composite (Rio de Janeiro, Brazil), was selected as the adhesive material. The manufacturer specified the adhesive’s mechanical properties [32]: Young's modulus of 3.1 GPa, the tensile strength of 53.1 MPa, and the ultimate tensile strain of 4.3%.

To produce the printed adherends, the jute-PLA composite, and the neat PLA, an Ender 3 V2 printer was adapted for printing polymer and continuous natural fiber yarns simultaneously through the in-nozzle impregnation method [11,27]. Figure 6.1a shows a schematic drawing of the extruder configuration, while Figure 6.1b shows the in-nozzle printing process using the extruder. Based on previous studies [23], Table 6.2 shows the main printing parameters used for biocomposite fabrication. The selection of a 1.5 mm nozzle was made to increase the printing flow and make the application of this method feasible for large-scale construction elements.

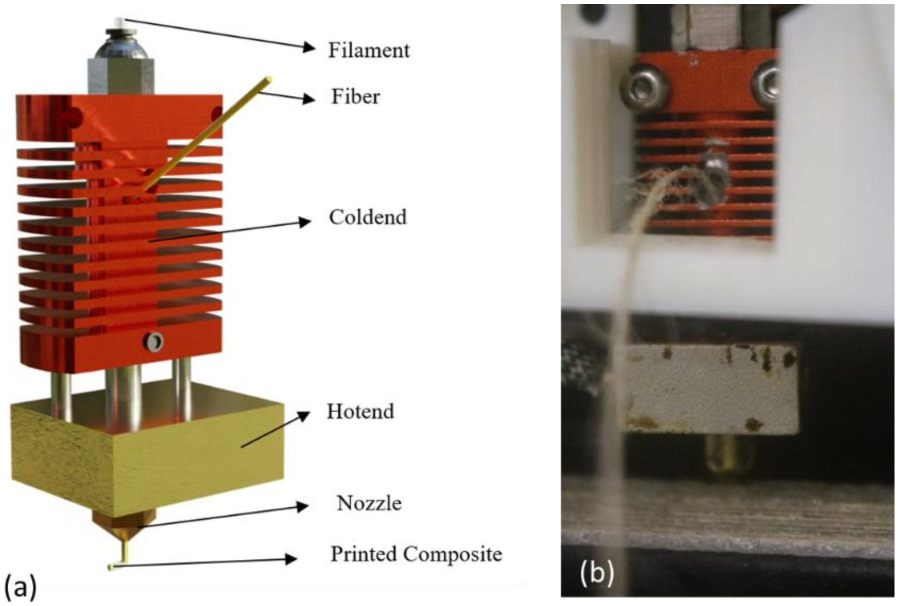

Figure 6.1 - Extruder printer of the composite (a) schematic drawing and (b) photo of the extruder while printing.

Table 6.2 - Printing parameters.

Property	**Value**
Nozzle	1.5mm
Speed	130mm/min

Extruder temperature	200°C
Bed temperature	60°C
Layer height	1.5mm
Layer width	1.5mm
Number of layers	2
Fiber volume fraction (%)	12.5-21.8

Roughness and tensile tests were carried out to characterize the adherends. The roughness tests were performed using an ATOS Compact Scan (Zeiss, Oberkochen, Germany) available at the Reverse Laboratory (Polito, Piemonte, Italy). The testing protocol followed the recommendations of ISO 4288 [33]. The specimens had dimensions of 20×10×3.0 mm. Figure 6.2 shows the test setup and the samples.

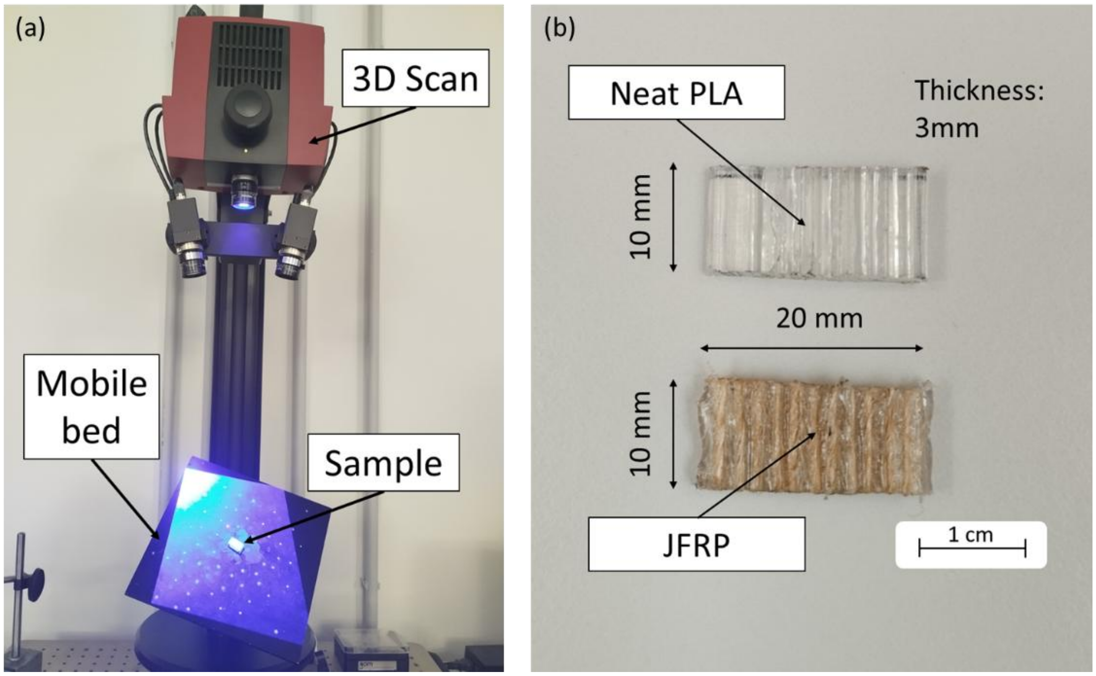

Figure 6.2 - Roughness test: (a) setup and (b) samples.

The tensile tests were performed using an Instron®5966 universal testing machine equipped with a 10kN external load cell available at the Laboratory of Adhesives and Composites Materials (LADES) (CEFET/RJ, Rio de Janeiro, Brazil). The testing protocol followed the recommendations of ASTM D3039 [34]. The tests were conducted at room temperature of 23°C and 50% relative humidity at a displacement control rate of 1mm/min up to failure. The specimens had a prismatic geometry of 200×25×3.0 mm (length x width x thickness).

6.2.2 Single-Lap Shear Tests

The manufacturing process of bonded joints involves several sequential steps. First, the surfaces of the wood and steel substrates were sanded to remove impurities and achieve a flat surface with a uniform finish. All the substrates used to fabricate the joints were cleaned with acetone before applying the adhesive. A metallic mold with a bonded joint holder was prepared. Subsequently, the bottom substrate was placed, and the alignment tab and bottom metallic spacer were positioned. Following this, the top metallic spacer was carefully positioned. The next step involved applying adhesive to both substrates, ensuring thorough and uniform coverage with 0.2mm of thickness ensured by the presence of alignment tabs. Finally, the top printed substrate was placed, completing the assembly of the bonded joint. The metallic mold was then placed in the hot press at 60°C for the curing process for 24 hours. Figure 6.3 shows the manufacturing process of the bonded joints.

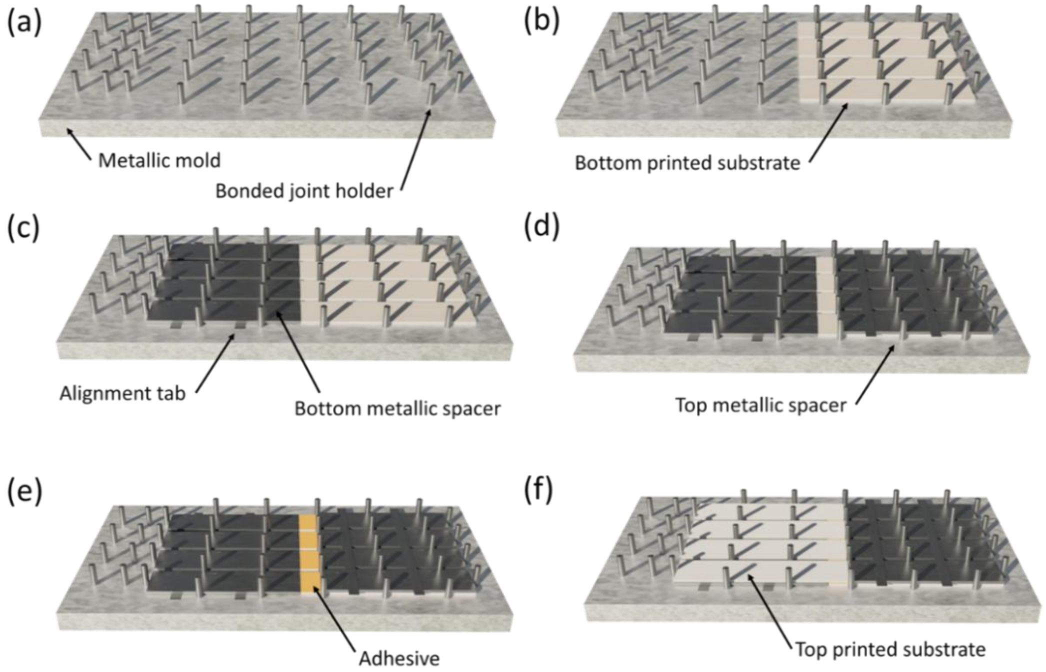

Figure 6.3 - Bonded joints manufacture process: (a) Metallic mold with bonded joint holder, (b) placing bottom substrate, (c) fitting of alignment tab and bottom metallic spacer, (d) positioning of the top metallic spacer, (e) application of the adhesive in both substrates and (f) placing of the top printed substrate.

The dimensions and the types of the SLJ can be observed in Figure 6.4. Mono-material SLJs were fabricated using printed adherends and the following combinations of materials: neat PLA-PLA (Polylactic Acid adherends without fiber) and JFRP-JFRP (Jute Fiber-Reinforced Polymer adherends). The bi-material bonded joints considered in this work were JFRP-wood and JFRP-steel. Four samples of each combination were fabricated.

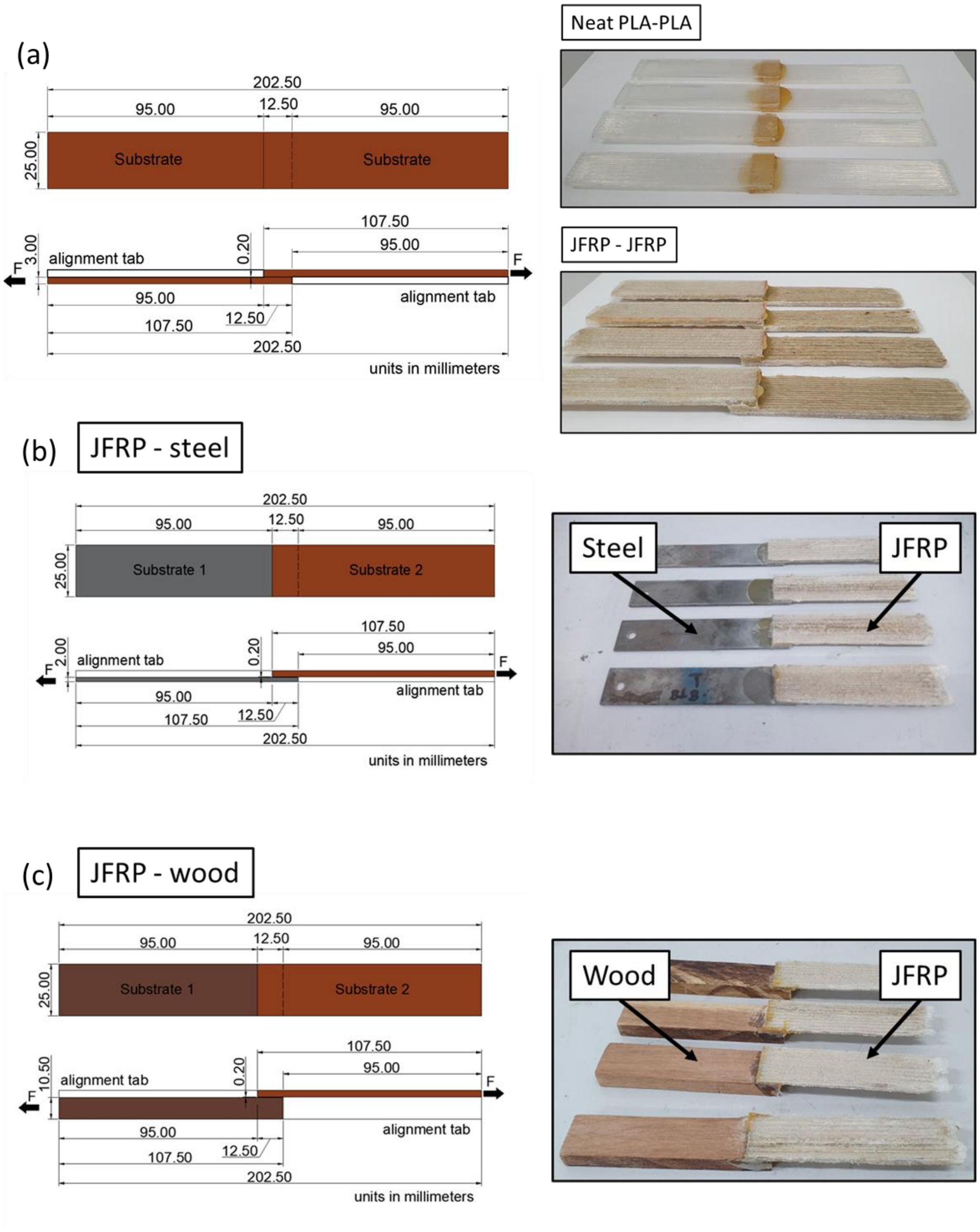

Figure 6.4 - SLJ specimen geometry: (a) Mono-materials, (b) JFRP-steel, and (c) JFRP-wood.

SLJ tests were performed using an Instron® 5966 universal testing machine (Norwood, MA, USA) equipped with a 10 kN external load cell available at the Laboratory of Adhesives and Composites Materials (LADES) (CEFET/RJ, Rio de Janeiro, Brazil). The testing protocol followed the recommendations of ASTM D1002 [35]. The tests were conducted at room temperature of 23°C and 50% relative humidity at a displacement control of 1mm/min rate up to failure.

6.2.3 Analytical Models

For the mono-material joints, the analytical model of Goland-Reissner's peel stress and shear stress distribution [36] were obtained according to Equations (1) and (8), respectively. This load distribution allows a better understanding of the joint’s failure behavior.

$$\sigma = \frac{P\prime t}{c^2\Delta}\left[\begin{array}{c}\left(R_2\lambda^2\frac{k}{2}+\lambda k'\cosh(\lambda)\cos(\lambda)\right)\cosh\left(\lambda\frac{x}{c}\right)\cos\left(\lambda\frac{x}{c}\right)+\\ \left(R_1\lambda^2\frac{k}{2}+\lambda k'\sinh(\lambda)\sin(\lambda)\right)\sinh\left(\lambda\frac{x}{c}\right)\sin\left(\lambda\frac{x}{c}\right)\end{array}\right] \tag{1}$$

Where,

$$\gamma = \sqrt[4]{6\frac{E_a}{E}\frac{t}{t_a}} \tag{2}$$

$$\lambda_{GR} = \gamma\frac{c}{t} \tag{3}$$

$$R_1 = cosh\lambda sin\lambda + sinh\lambda cos\lambda \tag{4}$$

$$R_2 = sinh\lambda cos\lambda + cosh\lambda sin\lambda \tag{5}$$

$$\Delta = \frac{1}{2}(sinh2\lambda + sin2\lambda) \tag{6}$$

$$k' = \frac{kc}{t}\sqrt{3(1-\nu^2)\frac{P\prime}{tE}} \tag{7}$$

$$\tau = -\frac{P\prime}{8c}\left[\frac{\beta c}{t}(1+3k)\frac{\cosh\left(\frac{\beta c}{t}\frac{x}{c}\right)}{\sinh\frac{\beta c}{t}} + 3(1-k)\right] \tag{8}$$

Where,

$$\beta = \sqrt{\frac{8G_a t}{E t_a}} \tag{9}$$

$$u_1 = \sqrt{\frac{P'}{D_1}} \; and \; u_2 = \sqrt{\frac{P'}{D_2}} \tag{10}$$

$$D_1 = \frac{D_2}{8} = \frac{Et^3}{12\,(1-\nu^2)} \tag{11}$$

$$k = \frac{\cosh(u_2 c)}{\cosh(u_2 c) + 2\sqrt{2}\, sinh(u_2 c)} \tag{12}$$

For the bi-material joints, the analytical model of Volkersen's shear stress distribution [37] for bi-material joints with different thicknesses was obtained according to Equation (13). The necessity to use the Volkersen model [37] for bi-materials instead of the Goland-Reissner model [36] arises because, although it is simpler and does not allow for the identification of peel stress, the Volkersen model [37] enables the analysis of adherents with different thicknesses and mechanical properties.

$$\tau = \bar{\tau} \frac{\lambda l}{\phi \sin(\lambda l)} [(\phi - 1)\cos(\lambda(l - x)) + \cosh(\lambda x)] \tag{13}$$

Where,

$$\phi = \frac{E_1 t_1}{E_2 t_2} \tag{14}$$

$$\lambda_V = \sqrt{\frac{G_a}{t_a}\left(\frac{1}{E_1 t_1} + \frac{1}{E_2 t_2}\right)} \tag{15}$$

6.3. Results and Discussion

6.3.1 Material Characterization

Regarding the mechanical characterization of the printed materials, Table 6.3 presents the results for tensile strength, Elastic modulus, and ultimate tensile strain for neat PLA and JFRP. At the same time, Figure 6.5a illustrates the representative stress-strain curves of the materials. Incorporating of continuous jute yarn reinforcement led to a 0.42% increase in tensile strength compared to neat PLA. However, using the two-sample t-test, it was found that with a confidence level corresponding to a p-value of

0.767, there is no statistically significant difference in the tensile strength between the tested samples. Despite the non-effective change in tensile strength, jute yarns imparted the composites with superior final rupture characteristics, which is crucial in developing structural elements. The low volumetric fraction of the jute reinforcements within the composite (12.5-21.8%) in conjunction with the fiber's large diameter, resulting in a limited matrix penetration within the fiber structure, can be considered the primary responsibility of the JFRP composite lower mechanical properties. The fiber's hydrophilic characteristics also hamper proper matrix/fiber interfaces, reducing overall load transfer.

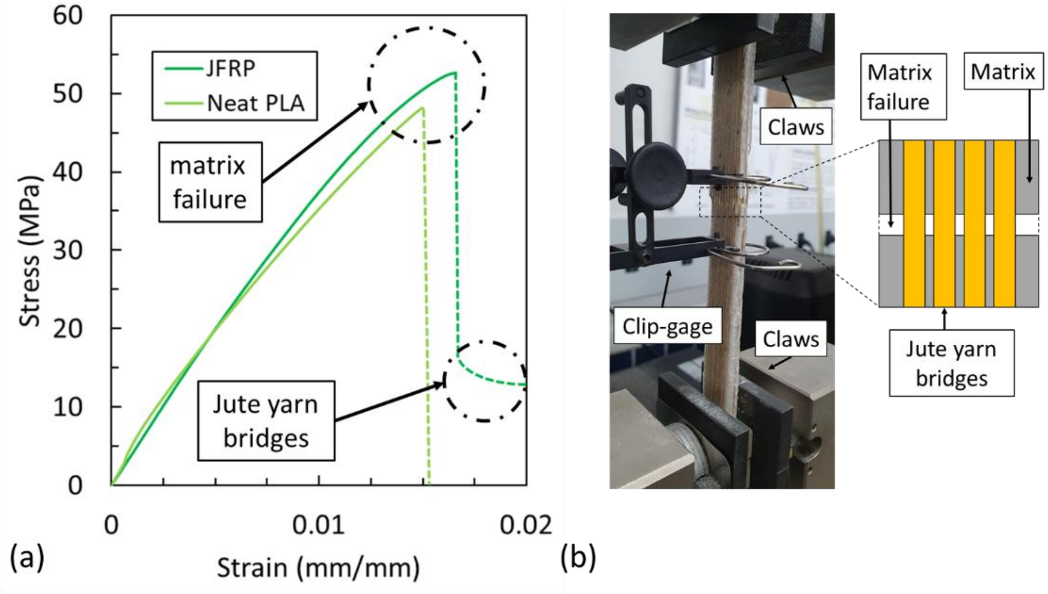

Figure 6.5 - Representative tensile test results: (a) stress x strain curve and (b) failure mode.

Table 6.3 - Mechanical properties of the printed material.

Type	Tensile strength (MPa)	p-value	Elastic modulus (GPa)	p-value	Tensile strain (%)	p-value
Neat PLA	52.97±4.20	0.076	3.40±0.10	0.078	1.56±0.11	0.487
JFRP	53.91±2.85	0.118	3.27±0.39	0.497	1.66±0.12	0.601

The JFRP exhibited a brittle failure, similar to the PLA’s pre-peak behavior [23]. However, the JFRP differs in its post-peak behavior, with the fibers mitigating catastrophic failure in the form of fiber bridges (Figure 6.5a) throughout the sample. A mix of fiber pull-out and fiber breakage prevents an abrupt loss of the composite's structural integrity. The detail of the failure surface presented in Figure 6.5b shows the fiber's bridges after cracking.

In terms of roughness of the cross-section, the presence of jute fibers on the surface results in an increase in contact area and notch effect, ultimately leading to a higher load-carrying capacity of the joint [11], mainly generated by the eccentricity of the natural fiber from the in-nozzle printing process [23]. Figure 6.6 shows the roughness curve of PLA and JFRP samples, respectively, demonstrating the difference in the roughness of each sample by the measured parameters of Ra (Arithmetic Mean Roughness), Rq (Root Mean Square Roughness), and Rz (Maximum Height of the Profile) (Table 6.4).

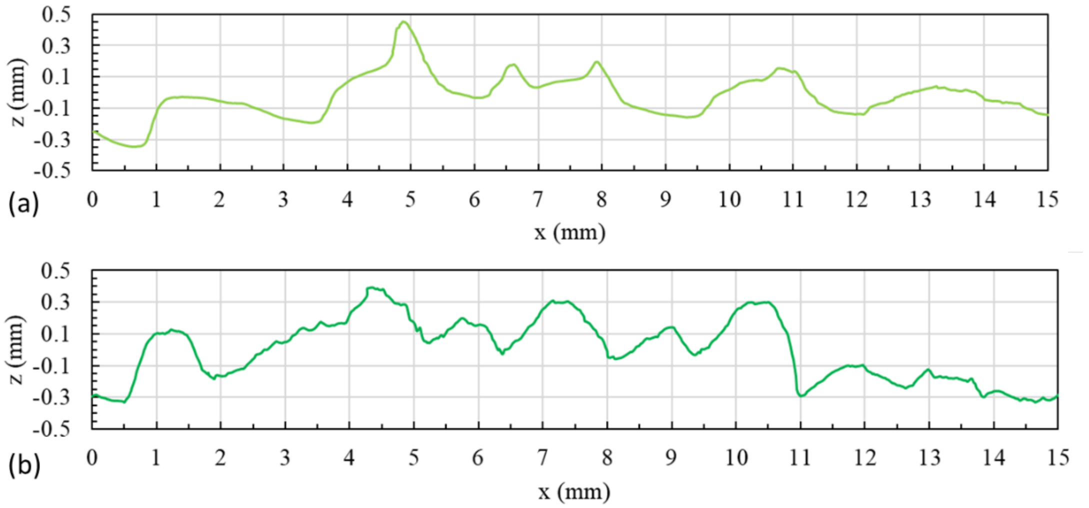

Figure 6.6 - Surface roughness of printed materials: (a) Neat PLA and (b) JFRP.

Table 6.4 - Surface roughness properties of neat PLA and JFRP.

Roughness Property	**Neat PLA**	**JFRP**
Ra (mm)	0.125±0.011	0.184±0.008
Rq (mm)	0.163±0.019	0.222±0.011
Rz (mm)	0.820±0.137	0.926±0.011

The JFRP exhibited significantly elevated surface roughness (Ra_{JFRP} = 0.125±0.011mm) compared to the neat PLA counterpart (Ra_{PLA} = 0.184±0.008mm), i.e. an increase of 47.20%. The greater roughness in the

JFRP specimens indicates a more intricate surface morphology, likely attributable to the incorporation of jute fibers. Conversely, the surface of neat PLA specimens showcased a relatively smoother texture characterized by a regular and periodic striped pattern. The amplitude parameters Rq ($Rq_{PLA} = 0.163\pm0.019mm$ and $Rq_{JFRP} = 0.222\pm0.011mm$) and Rz ($Rz_{PLA} = 0.820\pm0.137mm$ and $Rz_{PLA} = 0.926\pm0.011mm$) also indicate the tendency to change the surface texture of the sample with the addition of natural fiber, revealing increases of 36.20% and 12.93%, respectively.

Additionally, a Scanning Electron Microscopy (SEM) analysis was conducted on the surfaces of the samples (Figure 6.7). This analysis revealed a distinct difference in surface texture between the neat PLA and the JFRP. The surface of the neat PLA was smooth, with its roughness attributed to the formation of surface crystals. However, the addition of non-centralized jute yarn in the layers, resulting from the in-nozzle printing process [23], became exposed on the material's surface, producing a significant increase in roughness. This increased roughness was less detectable in the scanner than the resolution due to the resolution limits of the equipment.

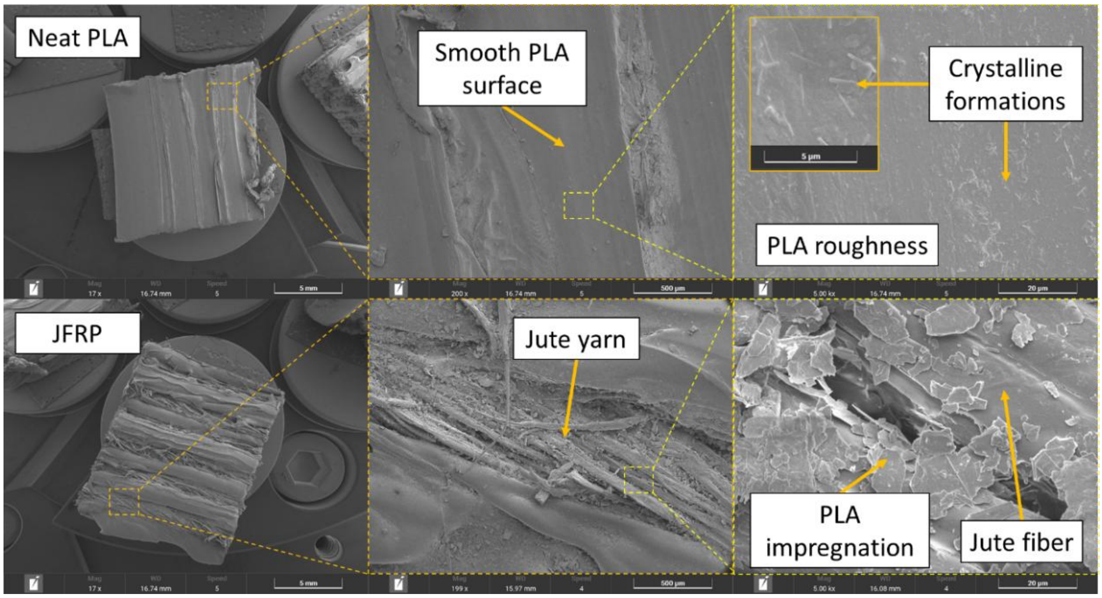

Figure 6.7 - SEM image of the surface of printed materials.

6.3.2 Single-Lap Shear Results for Mono-Material Joints

Table 6.5 summarizes the average failure loads, displacements, and lap shear strength of neat PLA-PLA and JFRP-JFRP. Initially, it is possible to identify an increase of 66.53% in the lap shear strength of JFRP when compared to neat PLA. Employing the Anderson-Darling test hypothesis, the failure load data from each group underwent analysis to ascertain conformity to a normal distribution (Figure 6.8a). The dataset demonstrates normal behavior, corroborated by p-values of 0.178 for neat PLA-PLA and 0.362 for JFRP-JFRP. A comparison of the normal distribution curves within a 95% confidence interval indicates a complete non-overlap of the results. The difference in the bonding strength between FFF samples with and without fiber can be explained through the roughness of the adherends [38], as shown in the roughness test. Representative load-displacement curves for neat PLA-PLA and JFRP-JFRP SLJs can be seen in Figure 6.8b.

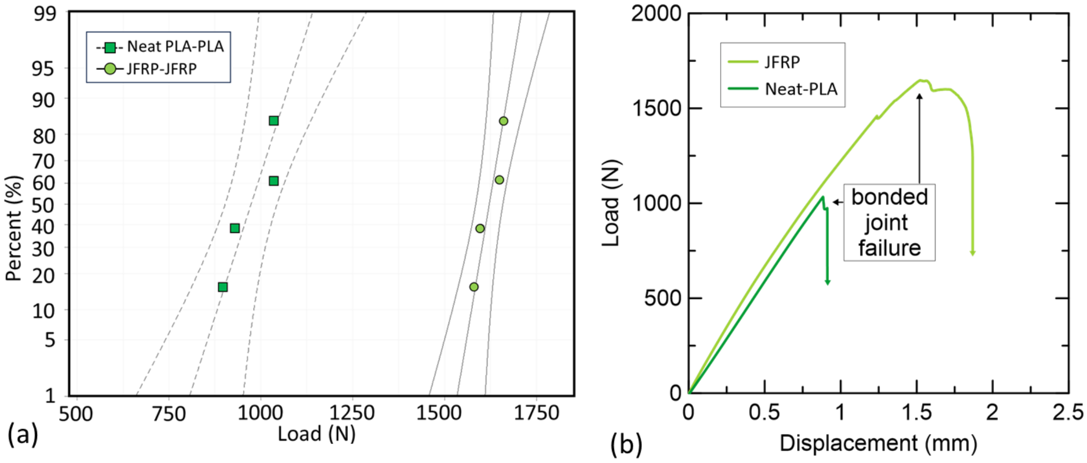

Figure 6.8 - Results from mono-material joints: (a) statistical analysis of the fiber's influence in the printed bonded joint; (b) representative load-displacement curves of neat PLA-PLA and JFRP-JFRP's SLJ.

Table 6.5 - Summary of results for mono-material joints.

Joint Type	**Peak Load (N)**	**Displacement at the peak (mm)**	**Lap Shear Strength (MPa)**
Neat PLA-PLA	973.85±72.06	0.90±0.08	3.12±0.23
JFRP-JFRP	1621.79±37.71	1.58±0.11	5.19±0.12

The SLJ’s failure surfaces were visually analyzed following ASTM D5573 [40]. Failures can be divided into: adhesive failure (ADH) (i.e., a rupture in the adherend-adhesive interface), cohesive failure (CF) (i.e., failure inside the adhesive layer), fiber-tear failure (FTF) (i.e., failure inside the composite adherend) and stock break (SB) (i.e., failure caused by adherend fracture).

Figure 6.9 shows representative failure modes of neat PLA-PLA and JFRP-JFRP specimens, respectively. In Figure 6.9a, it is possible to verify that the rupture of the bonded joint was characterized as ADH for neat PLA-PLA. In some situations, the substrate exhibited partial failure (Figure 6.9b), but the adhesive interfacial strength still governed the final failure. The failure of the JFRP-JFRP differed from that found for the neat PLA-PLA specimens. In the case of JFRP-JFRP, the failure mode occurred through interlayer shear rupture, with SB of the composite (Figure 6.9c and 9d), with part of the natural fibers being pulled out of the matrix. According to Mattey et al. [41], these interfaces result from differential cooling during the deposition process and are expected to have lower strength than the bulk-printed composite.

Consequently, propagation is expected on these surfaces when the adhesive interface exhibits greater resistance than the printed layer-to-layer interface. From a structural perspective, it is important to highlight the differences in ductility upon material failure. The adhesive failure of the PLA-PLA joint was significantly more brittle than to the JFRP-JFRP biocomposite, which exhibited interlaminar crack formation, promoting gradual energy dissipation.

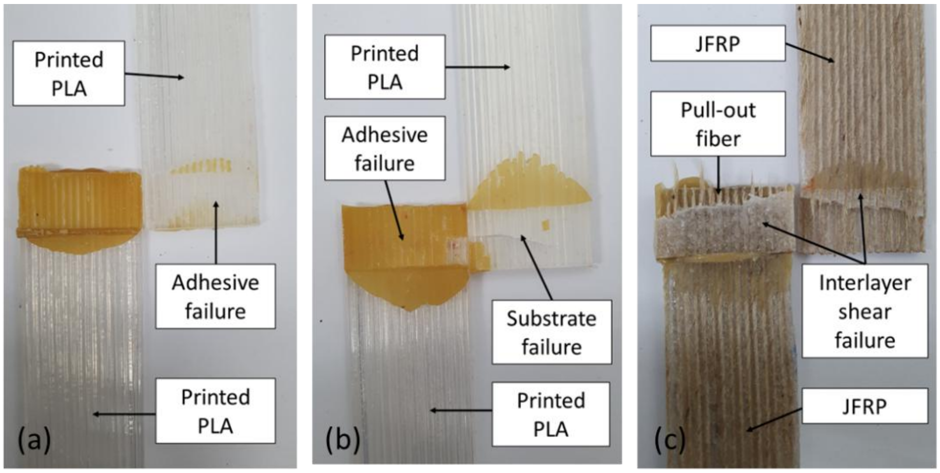

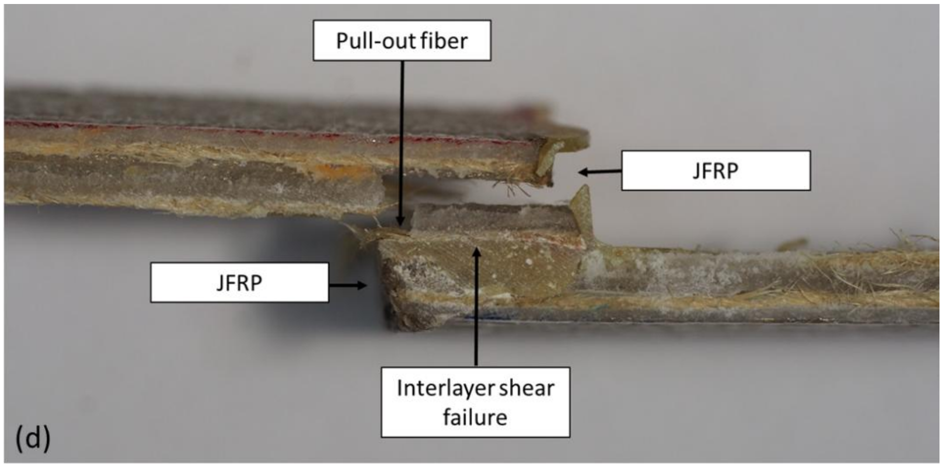

Figure 6.9 - Mono-material representative failure modes: (a,b) Neat PLA-PLA and (c,d) JFRP-JFRP.

Analyzing the JFRP-JFRP joint failure, the interlaminar cracks form due to the through-thickness stresses introduced resulting from the peel stresses developed at the joint (Figure 6.10a and 10b). The SLJ has its load transmission supported only by the remaining adhered layer, thus suffering a brittle rupture in this layer (Figure 6.10c). These results are consistent with those reported by Khosravani et al. [13], who verified the failure modes of bonded PLA joints and reported that the greatest loads were observed when the rupture of the adjacent printed structure governed failure.

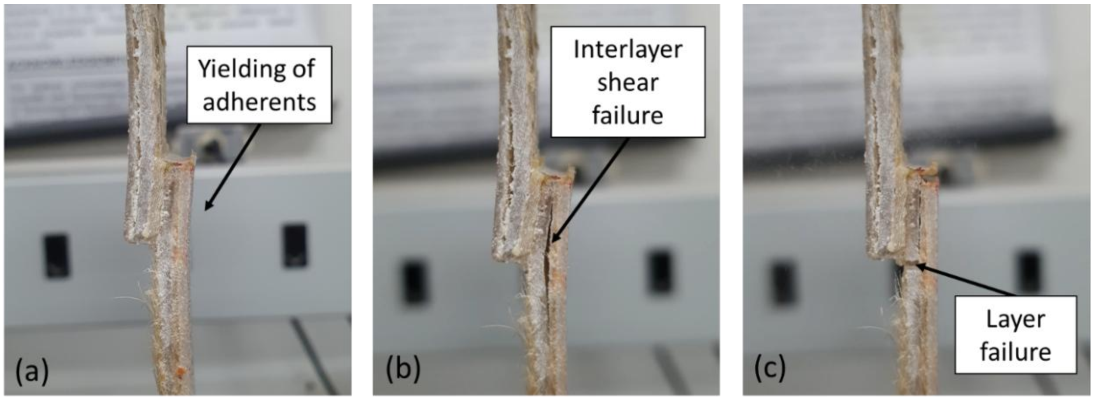

Figure 6.10 - Examples of failure progression during loading of JFRP: (a) yielding of adherends, (b) interlayer shear failure, and (c) layer failure.

Given the existence of two non-collinear forces generating the rotation of the joints that causes the interlayer shear failure observed in Figure 6.10b, the Goland-

Reissner's model [36] for stress analysis along the adhesive was used to understand this behavior. This model considers the existence of a moment resulting from the lack of geometric linearity caused by this rotation of the joints (Figure 6.10a), causing the displacements to lose proportionality to the applied force [42]. Figure 6.11b, 11c, and 11d show that the highest stresses caused by the peak stress are located near the ends of the joint, accentuating failure at these points. These points resist the forces until the stress limit between printing layers is reached, resulting in interlaminar delamination and subsequent material failure.

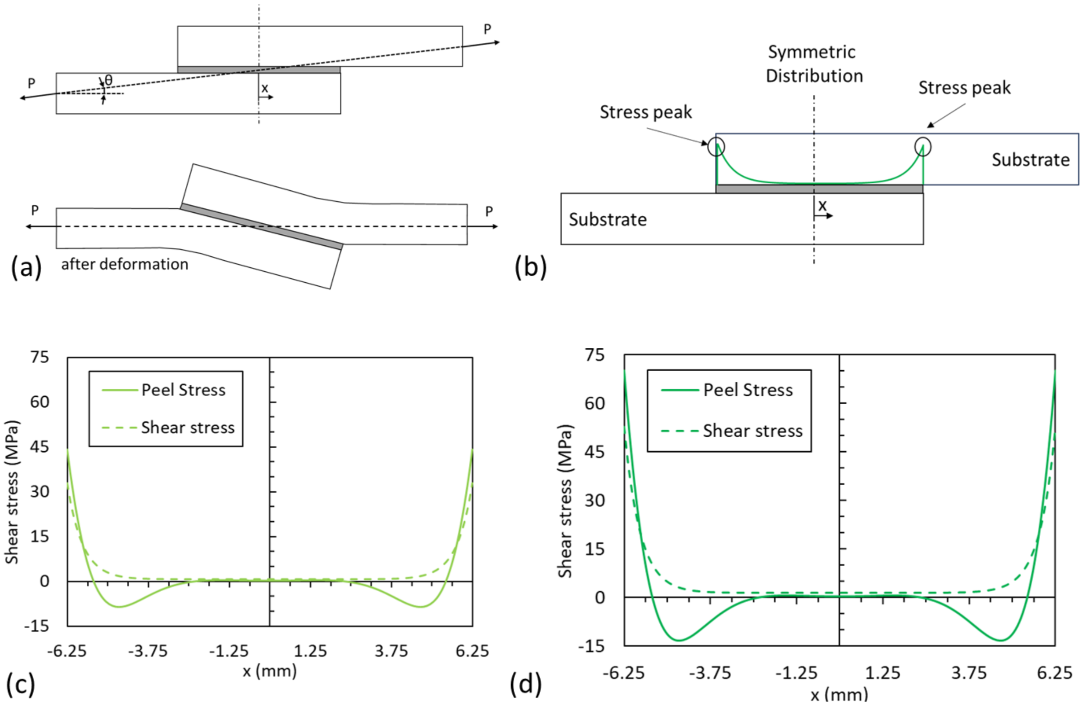

Figure 6.11 - Behavior and distribution of stresses in the SLJ: (a) Deformation of SLJ under tension, (b) shear stress schematic distribution, (c) Neat PLA-PLA, and (d) JFRP-JFRP shear and peel stress distribution.

6.3.3 Single-Lap Shear Results for Bi-Material Joints

Table 6.6 and Figure 6.12 summarize the data obtained from bi-material joints and compare them with mono-material joints. The joints' performance of the joints significantly varied as a function of the adherend material.

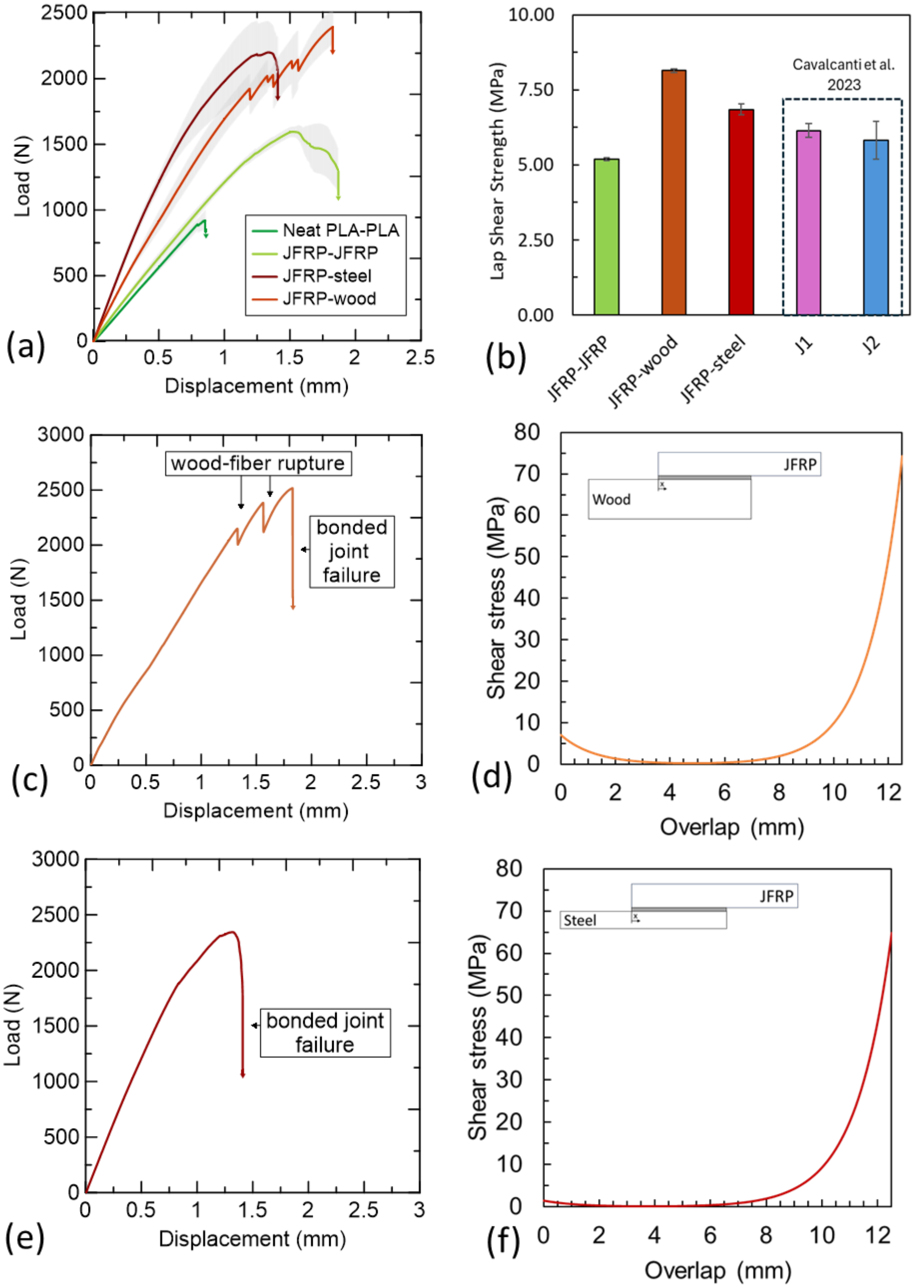

Figure 6.12 - Results as a function of material: (a) Load-displacement representative curves, (b) Lap shear strength [16], (c) Load-displacement representative curve of JFRP-wood, (d) Shear stress distribution in the JFRP-wood's SLJ based on Volkersen's analytical model [37], (e) Load-displacement representative curve of JFRP-steel SLJs, (f) Shear stress distribution in the JFRP-wood's SLJ based on Volkersen's analytical model [37].

Table 6.6 - Comparative of mono-material and bi-materials SLJ average failure loads and displacements.

Joint Type	**Failure Load (N)**	**Displacement (mm)**	**Lap shear strength (MPa)**
Neat PLA-PLA	973.85 ± 72.06	0.90 ± 0.08	3.12 ± 0.23
JFRP-JFRP	1621.79 ± 37.71	1.58 ± 0.11	5.19 ± 0.12
JFRP-wood	2543.76 ± 43.52	2.17 ± 0.36	8.14 ± 0.14
JFRP-steel	2140.89 ± 119.90	1.14 ± 0.27	6.85 ± 0.38

An observed trend of joint rigidity increased progressively from the joint with the lowest stiffness (mono-materials) to the highest (bi-materials). However, despite the highest strength and rigidity of the steel adherends, the highest failure load was found for the JFRP-wood's SLJ specimens. This may be linked to the reduction of joint rotation based on wood joint geometry. Reis et al. [43] highlight that using one adherend with higher stiffness contributes to reducing joint rotation, promoting a more uniform distribution of stresses in the adhesive and a consequent increase in the strength of the bonded joint. Golewski et al. [7] also indicated that bi-material joints composed partially of printed material and partially of higher stiffness material enhance the overall stiffness of the joint.

Figure 6.12b compares the data found in the present work with those in the relevant literature. The natural jute yarn-reinforced composites used in an SLJ configuration presented in Cavalcanti et al. [16] show a reduction in strength of up to 18.4% compared to direct lamination of one jute fabric (J1). However, when considering two layers of overlapping fiber fabric (J2), this value decreases to 12.2%. The superior mechanical properties presented by Cavalcanti et al. [16] can likely be attributed to the improved fiber-matrix interface quality in the lamination process, which involves a thermoset resin that, after compression molding, presented better fiber wettability than the in-nozzle process. This process makes the interface between fiber layers weaker and prone to breaking under the moment generated by the lower stiffness of the in-nozzle samples. However, when considering bi-material joints, the stiffness of the assembly and, consequently, a reduced joint rotation, the Lap Shear Strength was 32.4% higher when comparing the JFRP-wood joint to the J1.

Compared to the JFRP-JFRP, the JFRP-wood presented an average increase of 56.85% in average failure load. As seen in the representative load-displacement curve in Figure 6.12c, the load remains constant until isolated ruptures of the wood fibers occur. The material redistributes the load to its limit, leading to catastrophic failure of the wood material.

Otherwise, analyzing the shear stress (Figure 6.12d) calculated using Volkersen's model [37], it is possible to note that the difference in stiffness and dimensions of the joints which leads to a consequent imbalance due to geometry resulted in a difference in shear tension. The stresses will be higher on the less stiff adherend [44], leading to joint failure in this region.

Figure 6.13a and 13b show the failure mode of the JFRP-wood joint. An interlaminar rupture in the wood fibers was observed in the region with a higher stress peak (Figure 6.13e). The failure of the bonded joint occurs through wood inter-fiber fracture due to shear in the longitudinal direction of the fibers, where the tendency to separate occurs due to the slippage of the fibers, resulting in wood delamination [45,46]. This failure is expected once wood behaves essentially linearly elastic, and failure is marked by a brittle fracture with crack formation [47].

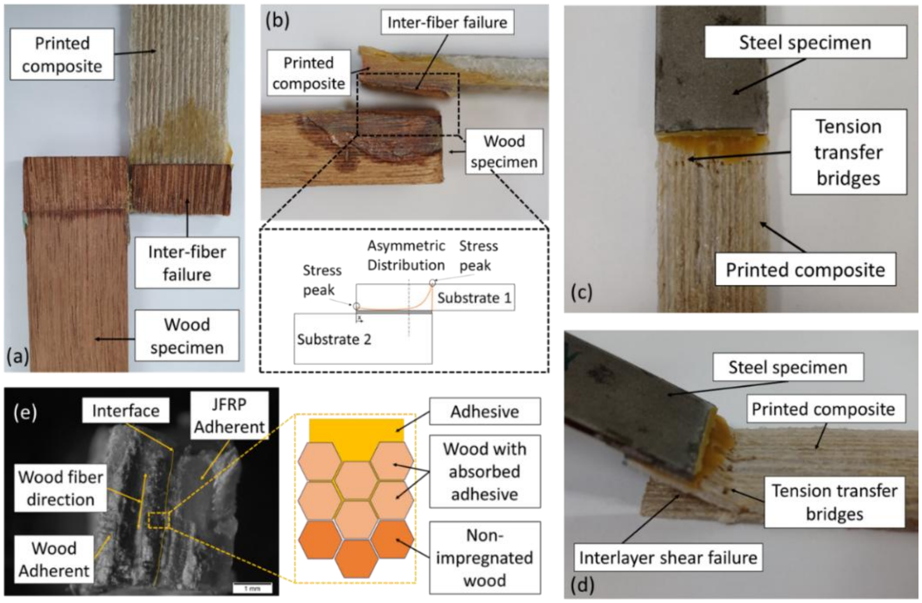

Figure 6.13 - Bi-material's representative failure modes: (a,b) JFRP-wood, (c,d) JFRP-steel, (d) JFRP-wood interface representation of adhesive impregnation.

It has been observed that the shear strength of the wood fibers is comparatively lesser than the ultimate strength exhibited by the adhesive and the longitudinal shear strength of the composite material, as also noted by Budhe et al. [48]. As Jalali et al. [46] mentioned, upon applying of a resin adhesive, a portion of this permeates between the wood fibers, ensuring good adhesion between this adherend and the adhesive. Consequently, failure mode occurs within this region and the non-impregnated area, where the interface between longitudinally arranged wood fibers is weaker.

In the case of JFRP-steel's bonded joints, compared to the JFRP-JFRP, the JFRP-steel combination shows an average load gain of 32.01%. The increase in failure load can explained by the reduction in joint rotation due to the higher resistance of the metallic adherend ($E_{steel}t_{steel} \gg E_{JFRP}t_{JFRP}$). Figure 6.12e and 12f show the representative load-displacement curve and shear stress based on Volkersen's model of JFRP-steel joint. Comparing the analytical model with the joint failure modes (Figure 6.13c), the shear stress reached the joint's peak stress, leading to the printed composite's interlaminar detachment. Unlike wood, which has lower resistance when subjected to tension perpendicular to the fibers, steel, an isotropic material with greater resistance, does not suffer damage at this loading level.

Representative failure modes of the JFRP-steel joint are illustrated in Figure 6.13c and 13d. In this case, the rupture occurred in the printed adherend. The crack initiated near the overlap edge, on the steel side of the printed adherend, due to the peak peel stresses observed in the shear stress x overlap graphic (Figure 6.12f). Given the brittle nature of the PLA, the crack propagates along the overlap edge, following the rotation tendency (Figure 6.13a). The adhesive/PLA interface demonstrated higher resistance than the composite interface, resulting in crack nucleation at the overlap edge and propagation through the interlaminar space within the composite, leading to a generalized delamination failure. Figure 6.13b shows that the PLA failed in a brittle manner, and the printed layers delaminated, indicating lower interfacial quality and strength.

6.4. Conclusions

This study evaluated the use of natural fibers as reinforcement in printed adherends for single-lap adhesively bonded joints and their application in bi-material combinations. This experimental approach enabled the assessment of their mechanical properties and joint behavior. The relationship between surface roughness and the performance of bonded joints with traditional AEC materials, such as wood and steel, provided interesting insights. The key findings from this study are:

- The addition of natural continuous yarn reinforcement affected both the composite and the mechanical behavior of the printed bonded joint. Despite this effect, no gain in tensile strength of JFRP compared to neat PLA was observed, and the brittle failure was mitigated by the presence of jute yarn bridges.
- In mono-material joints, the addition of continuous natural jute fibers increased the SLJ's failure load by 66.53% compared to the neat PLA-PLA joint due to an increase in JFRP's surface roughness of 47.20% compared to the neat PLA material, generating an expansion of contact area and notch effect.
- Bi-material joints showed greater results due to the presence of one of the adherends with a higher rigidity than mono-material joints. The JFRP-wood bonded joints present the best results with a failure load up to 2543.76N (56.85% higher than JFRP-JFRP), indicating a promising combination for mixed, sustainable structures. The JFRP-steel combination shows an average load gain of 32.01%, with a failure mode in the printed material.

Applying natural continuous yarn-reinforced printed joints has proven effective in improving the adhesive-adherend interface and its compatibility with other materials, particularly JFRP-wood and JFRP-steel. This demonstrates promising results for mixed structural applications in the AEC sector, offering a potentially innovative approach to enhance mechanical properties with sustainable solutions and lowering carbon footprint. For future studies, the authors recommend exploring methods to enhance interlayer adhesion quality, optimizing printing parameters for fiber-reinforced bonded components, and conducting large-scale testing to advance this technology.

References

[1] Khosravani MR, Božić Ž, Zolfagharian A, Reinicke T. Failure analysis of 3D-printed PLA components: Impact of manufacturing defects and thermal ageing. Eng Fail Anal 2022;136. https://doi.org/10.1016/j.engfailanal.2022.106214.

[2] El Moumen A, Tarfaoui M, Lafdi K. Additive manufacturing of polymer composites: Processing and modeling approaches. Compos B Eng 2019;171:166–82. https://doi.org/10.1016/j.compositesb.2019.04.029.

[3] Pizzorni M, Lertora E, Parmiggiani A. Adhesive bonding of 3D-printed short- and continuous-carbon-fiber composites: An experimental analysis of design methods to improve joint strength. Compos B Eng 2022;230. https://doi.org/10.1016/j.compositesb.2021.109539.

[4] Cavalcanti DKK, Medina M, De Queiroz HFM, Neto JSS, Chaves FJP. Recent advances in adhesive bonding of 3d-printed parts and methods to increase their mechanical performance. Annals of "Dunarea de Jos" University of Galati, Fascicle XII, Welding Equipment and Technology 2023;Volume 34:17–24.

[5] Khosravani MR, Soltani P, Reinicke T. Failure and fracture in adhesively bonded 3D-printed joints: An overview on the current trends. Eng Fail Anal 2023;153. https://doi.org/10.1016/j.engfailanal.2023.107574.

[6] Bagnato T, Ravindran AR, Mirabedini A, Ladani RB, Kandare E, Orifici AC, et al. Superior interfacial toughening of hybrid metal-composite structural joints using 3D printed pins. Compos Part A Appl Sci Manuf 2023;168:107479. https://doi.org/10.1016/j.compositesa.2023.107479.

[7] Golewski P, Sadowski T, Nowicki M. Mechanical response of adhesive and hybrid joints containing novel additive manufacturing adherends. Constr Build Mater 2023;379. https://doi.org/10.1016/j.conbuildmat.2023.131230.

[8] Bürenhaus F, Moritzer E, Hirsch A. Adhesive bonding of FDM-manufactured parts made of ULTEM 9085 considering surface treatment, surface structure, and joint design. Welding in the World 2019;63:1819–32. https://doi.org/10.1007/s40194-019-00810-4.

[9] Yap YL, Toh W, Koneru R, Lin R, Chan KI, Guang H, et al. Evaluation of structural epoxy and cyanoacrylate adhesives on jointed 3D printed polymeric materials. Int J Adhes Adhes 2020;100. https://doi.org/10.1016/j.ijadhadh.2020.102602.

[10] Cavalcanti DKK;, Banea MD;, de Queiroz HFM. Mechanical Characterization of Bonded Joints Made of Additive Manufactured Adherends. Annals of "Dunarea de Jos" University of Galati, Fascicle XII, Welding Equipment and Technology 2019;Vol. 30:27–33.

[11] Kovan V, Altan G, Topal ES. Effect of layer thickness and print orientation on strength of 3D printed and adhesively bonded single-lap joints. Journal of Mechanical Science and Technology 2017;31:2197–201. https://doi.org/10.1007/s12206-017-0415-7.

[12] Garcia R, Prabhakar P. Bond interface design for single lap joints using polymeric additive manufacturing. Compos Struct 2017;176:547–55. https://doi.org/10.1016/j.compstruct.2017.05.060.

[13] Khosravani MR, Soltani P, Weinberg K, Reinicke T. Structural integrity of adhesively bonded 3D-printed joints. Polym Test 2021;100. https://doi.org/10.1016/j.polymertesting.2021.107262.

[14] Atahan MG, Apalak MK. Loading-rate effect on tensile and bending strength of 3D-printed polylactic acid adhesively bonded joints. J Adhes Sci Technol 2022;36:317–44. https://doi.org/10.1080/01694243.2021.1922022.

[15] Dugbenoo E, Arif MF, Wardle BL, Kumar S. Enhanced Bonding via Additive Manufacturing-Enabled Surface Tailoring of 3D-Printed Continuous-Fiber Composites. Adv Eng Mater 2018;20. https://doi.org/10.1002/adem.201800691.

[16] Cavalcanti DKK, de Queiroz HFM, Banea MD. Performance enhancement of adhesive joints of additive manufactured parts by using different types of fibre reinforcements. Int J Adhes Adhes 2023;124. https://doi.org/10.1016/j.ijadhadh.2023.103371.

[17] Heshmati M, Haghani R, Al-Emrani M. Environmental durability of adhesively bonded FRP/steel joints in civil engineering applications: State of the art. Compos B Eng 2015;81:259–75. https://doi.org/10.1016/j.compositesb.2015.07.014.

[18] Marchione F, Chiappini G, Munafò P. Shear performance of timber-GFRP double-lap adhesive joints for civil engineering applications. J Adhes Sci Technol 2022;36:1978–92. https://doi.org/10.1080/01694243.2021.1998295.

[19] Yang Y, Zhao J, Zhang S, Marques EAS, Carbas RJC, Machado JJM, et al. Determination of fracture toughness of an adhesive in civil engineering and interfacial damage analysis of carbon fiber reinforced polymer–steel structure bonded joints. Proceedings of the Institution of Mechanical Engineers, Part L: Journal of Materials: Design and Applications 2021;235:2423–40. https://doi.org/10.1177/14644207211021385.

[20] Beserra JHN, de Melo JVA de MC, Cardoso DCT. Development of a novel 3D-printed moment connection for pultruded profiles joints. Structures 2024;60. https://doi.org/10.1016/j.istruc.2024.105850.

[21] Zarna C, Chinga-Carrasco G, Echtermeyer AT. Bending properties and numerical modelling of cellular panels manufactured from wood fibre/PLA biocomposite by 3D printing. Compos Part A Appl Sci Manuf 2023;165. https://doi.org/10.1016/j.compositesa.2022.107368.

[22] Jauhari N, Mishra R, Thakur H. Natural Fibre Reinforced Composite Laminates - A Review. Mater Today Proc 2015;2:2868–77. https://doi.org/10.1016/j.matpr.2015.07.304.

[23] Santos N V., Cardoso DCT. 3D printing of vegetable yarn-reinforced polymer components. J Clean Prod 2023;415. https://doi.org/10.1016/j.jclepro.2023.137870.

[24] Neto JSS, Lima RAA, Cavalcanti DKK, Souza JPB, Aguiar RAA, Banea MD. Effect of chemical treatment on the thermal properties of hybrid natural fiber-reinforced composites. J Appl Polym Sci 2019;136:1–13. https://doi.org/10.1002/app.47154.

[25] Arsène, M-A Savastano Jr, H. Allameh, S. M. Ghavami K, Soboyejo WO. Cementitious composites reinforced with vegetable fibers. Proceedings of the 1st Interamerican Conference on Non-Conventional Materials and Technologies in the Eco-Construction and Infrastructure (IAC-NOCMAT) 2003:13–6.

[26] Wambua P, Ivens J, Verpoest I. Natural fibres: Can they replace glass in fibre reinforced plastics? Compos Sci Technol 2003;63:1259–64. https://doi.org/10.1016/S0266-3538(03)00096-4.

[27] Mohanty AK, Misra M, Drzal LT. Natural fibers, biopolymers, and biocomposites. Taylor & Francis; 2005.

[28] Morrison WH, Archibald DD, Sharma HSS, Akin DE. Chemical and physical characterization of water- and dew-retted flax fibers. Ind Crops Prod 2000;12:39–46. https://doi.org/10.1016/S0926-6690(99)00044-8.

[29] Velde K Van De, Kiekens P. Biopolymers: overview of several properties and consequences on their applications. Eb - Elektrische Bahnen 2001;99:483.

[30] Hsueh MH, Lai CJ, Wang SH, Zeng YS, Hsieh CH, Pan CY, et al. Effect of printing parameters on the thermal and mechanical properties of 3d-printed pla and petg, using fused deposition modeling. Polymers (Basel) 2021;13. https://doi.org/10.3390/polym13111758.

[31] Antonio Rocco Lahr F, Nascimento Arroyo F, Hendrigo de Almeida T, Menezes de Almeida Filho F, Santos Mendes I, Luis Christoforo A. Full Characterization of Erisma uncinatum Warm Wood Specie. International Journal of Materials Engineering 2016;6:147–50. https://doi.org/10.5923/j.ijme.20160605.01.

[32] E-composite. Datasheet Epoxy AR345. n.d.

[33] British Standards Institution., British Standards Institution. BS EN ISO 4288:1998 : Geometric product specifications (GPS) - surface texture : profile method : rules and procedures for the assessment of surface texture. British Standards Institution; 1998.

[34] ASTM. ASTM D3039 / D3039M - Standard Test Method for Tensile Properties of Polymer Matrix Composite Materials. Annual Book of ASTM Standards n.d.;15.03. https://doi.org/10.1520/D3039_D3039M-17.

[35] ASTM. D1002: 2019 : Standard Test Method for Apparent Shear Strength of Single-Lap-Joint Adhesively Bonded Metal Specimens by Tension Loading (Metal-to-Metal) 1 2019. https://doi.org/10.1520/D1002-10R19.

[36] Goland M and Reissner E. J. . J Appl Mech; 1944.

[37] Volkersen O. Luftfahrtforschung. . 1938.

[38] Naat N, Boutar Y, Mezlini S, da Silva LFM, Alrasheedi NH, Hajlaoui K. Study of the effect of bio-inspired surface texture on the shear strength of bonded 3D-printed materials: Comparison between stainless steel and polycarbonate joints. Int J Adhes Adhes 2024:103658. https://doi.org/10.1016/j.ijadhadh.2024.103658.

[39] Cavalcanti DKK, Banea MD, de Queiroz HFM. Mechanical characterization of bonded joints made of additive manufactured adherends. Annals of "Dunarea de Jos" University of Galati, Fascicle XII, Welding Equipment and Technology 2019;Vol. 30:27–33. https://doi.org/10.35219/awet.2019.04.

[40] ASTM. ASTM D5573 - Classifying Failure Modes in Fiber-Reinforced-Plastic (FRP) Joints. 2019.

[41] Mattey R, Jewell B, Ghosh S, Sain T. Phase-field fracture coupled elasto-plastic constitutive model for 3D printed thermoplastics and composites. Eng Fract Mech 2023;291. https://doi.org/10.1016/j.engfracmech.2023.109535.

[42] Yang C, Pang SS. Stress-strain analysis of single-lap composite joints under tension. Journal of Engineering Materials and Technology, Transactions of the ASME 1996;118:247–55. https://doi.org/10.1115/1.2804896.

[43] Reis PNB, Ferreira JAM, Antunes F. Effect of adherends rigidity on the shear strength of single lap adhesive joints. Int J Adhes Adhes 2011;31:193–201. https://doi.org/10.1016/j.ijadhadh.2010.12.003.

[44] Banea MD, Rosioara M, Carbas RJC, da Silva LFM. Multi-material adhesive joints for automotive industry. Compos B Eng 2018;151:71–7. https://doi.org/10.1016/j.compositesb.2018.06.009.

[45] Li Y, Howes K, Dillard DA, Frazier CE, Case SW. Using auxiliary adherends to eliminate need for grain control in fracture testing of adhesively bonded wood. Int J Adhes Adhes 2021;110. https://doi.org/10.1016/j.ijadhadh.2021.102917.

[46] Jalali S, Borges C da SP, Carbas RJC, Marques EA de S, Akhavan-Safar A, Barbosa ASOF, et al. A Novel Technique for Substrate Toughening in Wood Single Lap Joints Using a Zero-Thickness Bio-Adhesive. Materials 2024;17. https://doi.org/10.3390/ma17020448.

[47] Vallée T, Tannert T, Fecht S. Adhesively bonded connections in the context of timber engineering–A Review. Journal of Adhesion 2017;93:257–87. https://doi.org/10.1080/00218464.2015.1071255.

[48] Budhe S, Ghumatkar A, Birajdar N, Banea MD. Effect of surface roughness using different adherend materials on the adhesive bond strength. Applied Adhesion Science 2015;3. https://doi.org/10.1186/s40563-015-0050-4.

Chapter 7 - ENHANCING STRUCTURAL PRINTED COMPONENT JOINT PERFORMANCE WITH OPTIMIZATION PATHS AND CONTINUOUS NATURAL YARN REINFORCEMENT IN ADDITIVE MANUFACTURING

Natália V. Santos, K. S. de Oliveira, T. Doca, Alberto Giubilini, Paolo Minetola,
Mariana D. Banea, Daniel C.T Cardoso

Optimization of printing paths is essential in enhancing the performance of high-strength structures, but the inherent complexity of such geometry often challenges traditional manufacturing methods. Additive manufacturing (AM) addresses these limitations by enabling the creation of intricate designs reinforced with continuous fibers, and when combined with natural yarns, it also offers a sustainable alternative to synthetic materials. This study investigates the impact of different printing paths and the integration of Continuous Natural Yarn Reinforcement (CNYR) on the mechanical performance of Continuous Fiber-Reinforced Thermoplastic Composites (CFRTPCs) for structural applications. Results reveal that optimizing layer orientation and introducing strategically placed intermediate layers significantly enhance stiffness and strength, with improvements of up to 35.2% and 80.0%, respectively, albeit with increased brittleness. Meanwhile, incorporating continuous natural yarns improved stiffness and strength by 34.9% and 43.2%, respectively, while reducing the likelihood of brittle failure. These findings advance the understanding of how CNYR interacts with AM technologies to improve mechanical performance, offering a promising route for sustainable reinforcement in complex structural components. This research underscores AM's potential for tailoring composite structures capable of withstanding complex loading conditions, thereby opening avenues for broader applications of natural yarn composites in eco-friendly and high-performance engineering solutions.

Keywords: CFRTPCs, CNYR, AM, Natural fibers, Optimization path.

7.1 Introduction

Continuous Fiber-Reinforced Thermoplastic Composites (CFRTPCs) represent a cutting-edge material category that combines the superior mechanical properties of continuous fibers with the versatility and lightweight nature of thermoplastic matrices. These composites have gained significant attention for their potential in additive manufacturing (AM), offering a unique pathway to produce high-performance, tailored components. However, the integration of continuous fibers — typically in yarn form — into AM processes poses specific challenges. Uninterrupted fiber deposition is critical to maintaining reinforcement continuity, as stress concentrations at starting points often lead to structural weaknesses under tensile loads, as noted by Melena et al. [1]. Additionally, the complexities of AM, including fiber alignment optimization, connectivity issues, support structure requirements, surface roughness, and material property variations, as highlighted by Zhu et al. [2], further emphasize the need for meticulous process calibration. Despite these challenges, the strategic alignment of fibers along the printing path can unlock the full potential of CFRTPCs, enabling their application in advanced manufacturing scenarios [3].

Various path-planning strategies have been explored to optimize the orientation and deposition of continuous fibers in CFRTPCs, aiming to maximize mechanical performance and structural efficiency. Bittrich et al. [4] highlight the frequent use of the principal stress criterion, as opposed to optimization-based approaches, for designing curvilinear fiber paths in CFRTPCs. This method aligns fiber trajectories with the principal stress directions to enhance structural load-bearing efficiency [5]. Several path-planning methods have been proposed in the literature, including the Offset, Equally-Spaced (EQS), and Streamline methods [6].

The Offset method generates fiber paths through lines parallel to the boundary of the element geometry. These parallel lines are spaced at a fixed distance corresponding to the print layer width and terminate when they intersect previously created lines. An interpolation process is then applied to align the fiber angles within each cell to the orientation vector. The EQS method creates continuous fiber paths parallel to the geometric boundary of the optimized structure, distributed along its largest dimension. In this approach, a constant number of points is equally spaced across each cross-section of a solid area and connected along the span direction. In contrast, the Streamline method generates paths where the lines are tangent to the vector field that defines the fiber orientations, resulting in smooth trajectories similar to those of the EQS method [6,7]. Additionally, Wang et al. [6] developed a load-dependent path planning (LPP) method for 3D printing. This method generates a single print path that achieves a proportional distribution across the cross-section, providing an effective solution for CFRTPCs. However, a limitation of this method is the occurrence of fiber crossings within the same layer, which can lead to height variations across the printed surface.

Consequently, the definition of printing paths directly influences the mechanical properties of the components. Li et al. [8] integrated continuous carbon fibers into a topologically optimized suspension component to reduce strain energy but found that non-optimized components with continuous reinforcement were impractical to print, complicating fiber inclusion analysis. Chen & Ye [9] demonstrated significant improvements by fabricating a topologically optimized carbon fiber-reinforced beam, achieving an 1163% increase in load capacity compared to unreinforced components. Similarly, Huang et al. [10] showed that aligning Kevlar fibers parallel to the loading direction enhanced load capacity by 64.4%, though they stressed the need for further comparisons between reinforced and unreinforced components.

Current research has predominantly focused on the use of uniform printing paths across all layers, which limits the potential of structural components that need to withstand varying types of loads. This approach overlooks the benefits of optimizing fiber orientations layer by layer to address specific mechanical demands. Additionally, another significant limitation lies in the scale of production, as the use of continuous yarn reinforcements with small diameters becomes impractical for manufacturing larger structural elements. Furthermore, nearly all studies in this area concentrate on synthetic fibers, neglecting the potential of natural fibers, which offer significant sustainability benefits. These constraints highlight the need for further studies to explore sustainable, scalable, and more adaptable path-planning strategies.

This research investigates how to effectively combine different printing paths with the addition of continuous natural yarn reinforcements to create the most efficient structural component. The primary research question focuses on identifying the optimal combination of printing strategies and reinforcement techniques to enhance the mechanical performance of printed components. The study aims to analyze layers with varying printing paths, both with and without continuous natural fiber reinforcement. By examining the influence of different fiber orientations and reinforcement strategies in a Printed Component Joint (CJ), the objective is to improve the overall structural performance of 3D-printed elements. This includes enhancing their ability to withstand combined loads and addressing the challenges posed by the CFRTPCs process, particularly the low interlayer adhesion, which can undermine the mechanical strength of the final printed component. The research seeks to provide insights into how these factors can be optimized for better performance, while also considering the sustainability benefits of incorporating natural fibers in reinforced 3D-printed structures.

7.2 Methodology

7.2.1 Materials

The materials utilized in this study comprised flax yarn supplied by Bricolino (Vicenza, Italy) as the reinforcing phase and polylactic acid (PLA) filament with a 1.75 mm diameter provided by 3DLAB (Minas Gerais, Brazil) as the polymer matrix. Table 5.4 presents the main properties of the natural yarn from the literature and PLA from the producer data sheet, respectively.

Table 7.1 - Properties of the natural yarns and polymer matrix [11-15].

Property	**Flax yarn**	**PLA**
Type	Yarn	Filament
Diameter (mm)	0.77±0.03	1.75
Density (g/cm^3)	1.4-1.5	1.24
Linear density (g/m)	0.50±0.01	-
Tensile strength (MPa)	345-1500	46.0

Elastic modulus (GPa)	28-80	1.90
Ultimate strain (%)	-	3.69
Cellulose (%)	65-80	-
Hemicellulose (%)	12-16	-
Lignin content (%)	2-5	-
Moisture absorption (%)	7	-
Melting temperature (°C)	-	165-180

7.2.2 Printing process

Printing composites were manufactured using Fused Filament Fabrication (FFF) with an Ender 3 V2 printer that was modified to allow the simultaneous printing of polymer and continuous natural fiber yarns through an in-nozzle impregnation method [16]. This adaptation allows for the integration of the natural yarns within the polymer matrix, thereby enhancing the overall mechanical properties of the composites. To allow the printing flow for large-scale production and enable the incorporation of larger diameters of natural reinforcement yarns, specific parameters were carefully studied until an optimal configuration has been established, this configuration is detailed in Table 7.2. These parameters were rigorously applied to all component joints (CJ) and samples produced during this study. This careful calibration of printing conditions is essential for achieving desirable outcomes in terms of both structural integrity and performance of the final composite.

Table 7.2 - Printing parameters.

Parameter	**Value**
Nozzle diameter	2.1 mm
Printing speed	3.75 mm/s
Extruder temperature	200 °C
Bed temperature	60 °C
Layer height	1.5 mm
Layer width	3.0 mm

7.2.3 Component joints' fabrication

7.2.3.1 Printing path and groups

To analyze the mechanical behavior of the printed CJs, large-scale printing was conducted to achieve optimal results, focusing on the effects of different printing paths on the outcome. Table 7.3 presents the printing paths used. CLP refers to the continuous longitudinal printing path aligned with the geometry of the CJ, while P45 and P315 represent paths designed to counteract shear forces within the structure.

The printing paths are strategically arranged within seven-layer CJs to enhance the mechanical performance and structural integrity of the printed components. Each layer is deposited following the specific sequence outlined in Table 7.4, ensuring optimal alignment and interaction between adjacent layers. This arrangement aims to improve load distribution, minimize internal stresses, and enhance resistance to shear forces. Proper sequencing of the paths is critical to achieving strong interfacial bonding, reducing void formation, and ensuring consistent mechanical behavior throughout the structure.

Table 7.3 - Basic description of the printing paths.

Type	Path nomenclature	Description
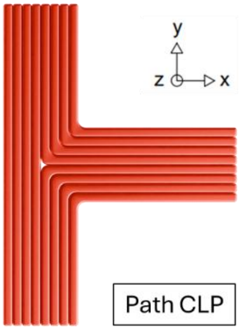	CLP	Printing path whose geometry corresponds to that used as a continuous longitudinal path.

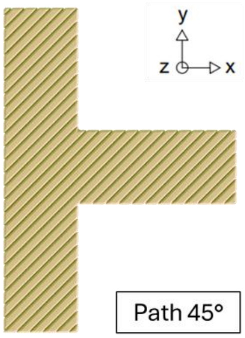	P45	Printing path with a geometry aligned at a 45-degree angle to the right of the Y-axis.
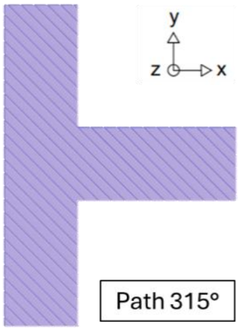	P315	Printing path with a geometry aligned at a 45-degree angle to the left of the Y-axis.

Table 7.4 - Printing group types.

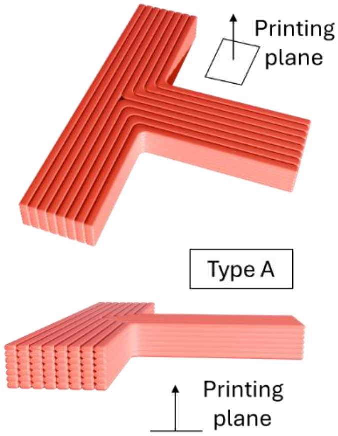	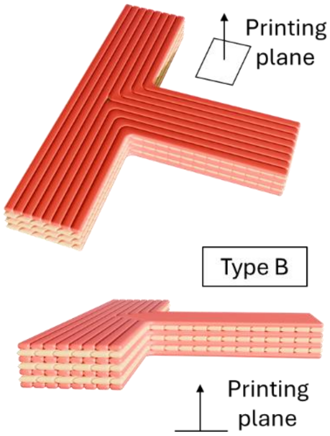
Nomenclature	**Nomenclature**
Type A	Type B
Printing Layers Order	**Printing Layers Order**
CLP-CLP-CLP-CLP-CLP-CLP-CLP	CLP-P45-CLP-P45-CLP-P45-CLP

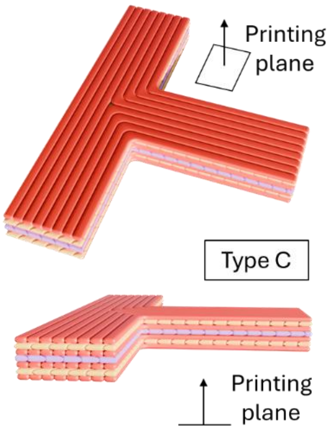	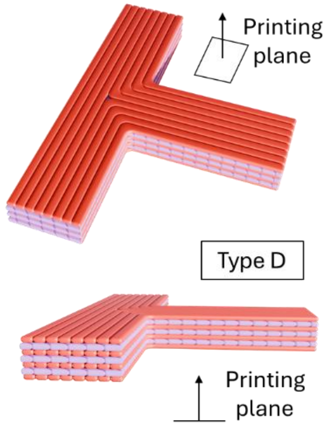
Nomenclature	**Nomenclature**
Type C	Type D
Printing Layers Order	**Printing Layers Order**
CLP-P45-CLP-P315-CLP-P45-CLP	CLP-P315-CLP-P315-CLP-P315-CLP

7.2.3.2 In-situ impregnation

To enable *In-situ* impregnation for CFRTPCs with flax yarns, the Ender 3 V2 printer was modified according to the methodology outlined by Santos and Cardoso [16]. A 2 mm diameter hole was precisely drilled into the cold-end section of the extruder, allowing for the controlled insertion of flax yarns during printing and ensuring their uniform dispersion within the polymer matrix. The addition of yarns was focused on the component joint group, where the path configuration allows the fibers to counteract shear forces in the joint by being subjected to tension, i.e. Type D. This strategy improved the structural integrity of critical regions by enhancing the composite’s tensile strength through the addition of flax yarns while preserving its lightweight and sustainable characteristics. The objective was to develop components with superior mechanical performance (Table 7.5), suitable for demanding structural applications, without compromising environmental sustainability. Figure 7.1 shows the printing process reinforced with flax fiber by *In-situ* impregnation.

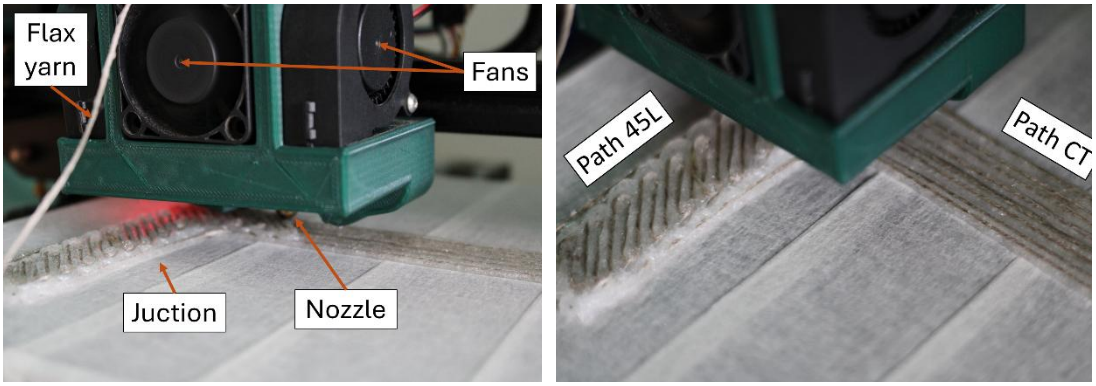

(a) (b)

Figure 7.1 - Printing process reinforced with flax fiber by In-situ impregnation.

Table 7.5 - Mechanical properties of CFF and Neat PLA aligned with the loading direction.

Nomenclature	Elastic Modulus [GPa]	Tensile strength [MPa]	Tensile strain [%]
Neat PLA	2.43±0.12	35.01±2.39	1.64±0.20
CFF	2.68±0.13	57.96±5.12	2.43±0.29

7.2.4 Component joint test

The CJ tests were performed using an EMiC Series 23 universal testing machine with a 5 kN load cell available in the Laboratory of Structures and Materials (PUC-Rio, Rio de Janeiro, Brazil). To evaluate the mechanical behavior of the CJ and validate the processes involved in its development, a series of Moment x Rotation tests were conducted on samples printed with variations in curvature and path. The samples were divided into groups with and without fiber insertion during the printing process through In-nozzle impregnation. The tests were performed under displacement control at a loading rate of 1.00 mm/min until either failure or a 20 mm displacement limit was reached, using a model 23–30 EMiC Series 23 universal testing machine equipped with a 5 kN external load cell. Digital Image Correlation (DIC) software VIC-3D© from Correlated Solutions, paired with two digital cameras, was employed to analyze internal stresses and crack propagation. Figure 7.2 shows the CJ test setup.

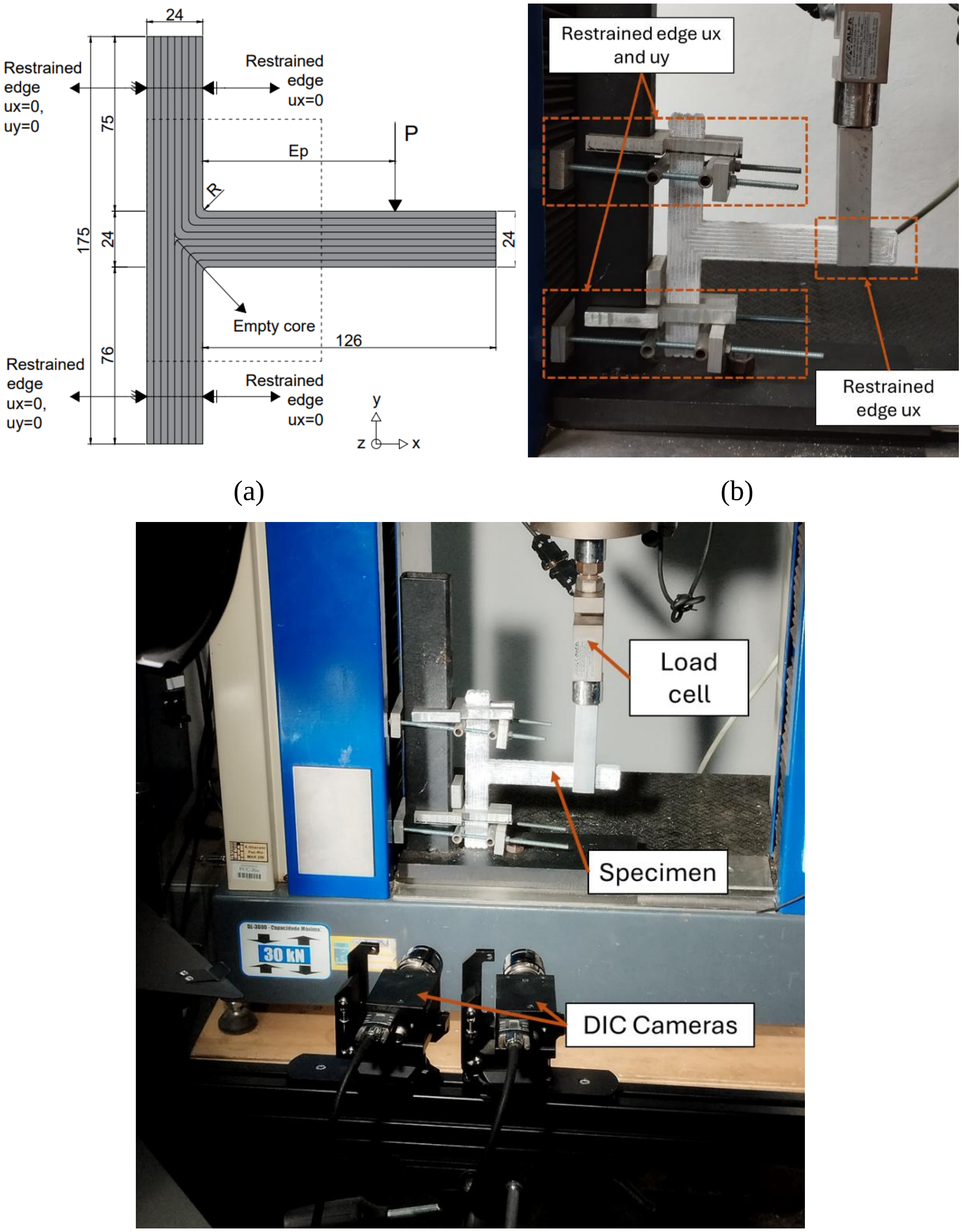

(a) (b)

(c)

Figure 7.2 - (a) Typical test assembly, (b) Restrained edges setup, and (c) Experimental setup used for Moment-Rotation.

7.3 Results and Discussion

7.3.1 Printing path disposition

7.3.1.1 Moment-rotation test

Upon completing all tests, the bending moment (M) versus rotation (φ) curves for the specimens were plotted, as defined by Eq. (1) and Eq. (2). In these equations, P represents the applied force, Ep is the lever arm, and φ denotes the system's rotation. Additionally, U corresponds to the energy absorption up to the peak load (Eq. (3)), expressed in mJ. Mi represents the bending moment at point “i,” while φi is the corresponding rotation of the joint at point “i”. Figure 7.3 shows the Moment-rotation behavior for each group.

$$M = P \times Ep \quad (1)$$

$$\varphi = tan^{-1}(\delta/Ep) \quad (2)$$

$$U = \sum_{i=1}^{n-1} \left(\frac{M_i+M_{i+1}}{2}\right) \times (\varphi_{i+1} - \varphi_i) \quad (3)$$

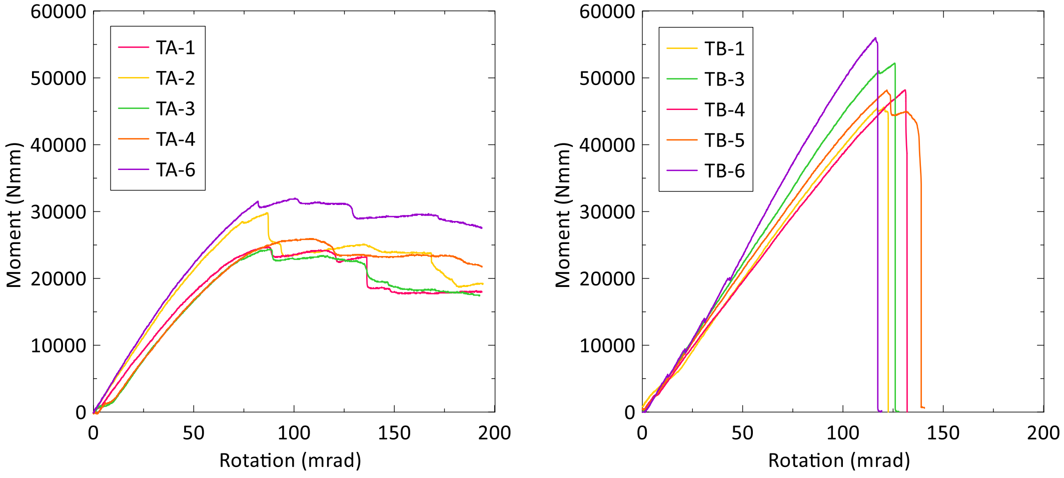

(a) (b)

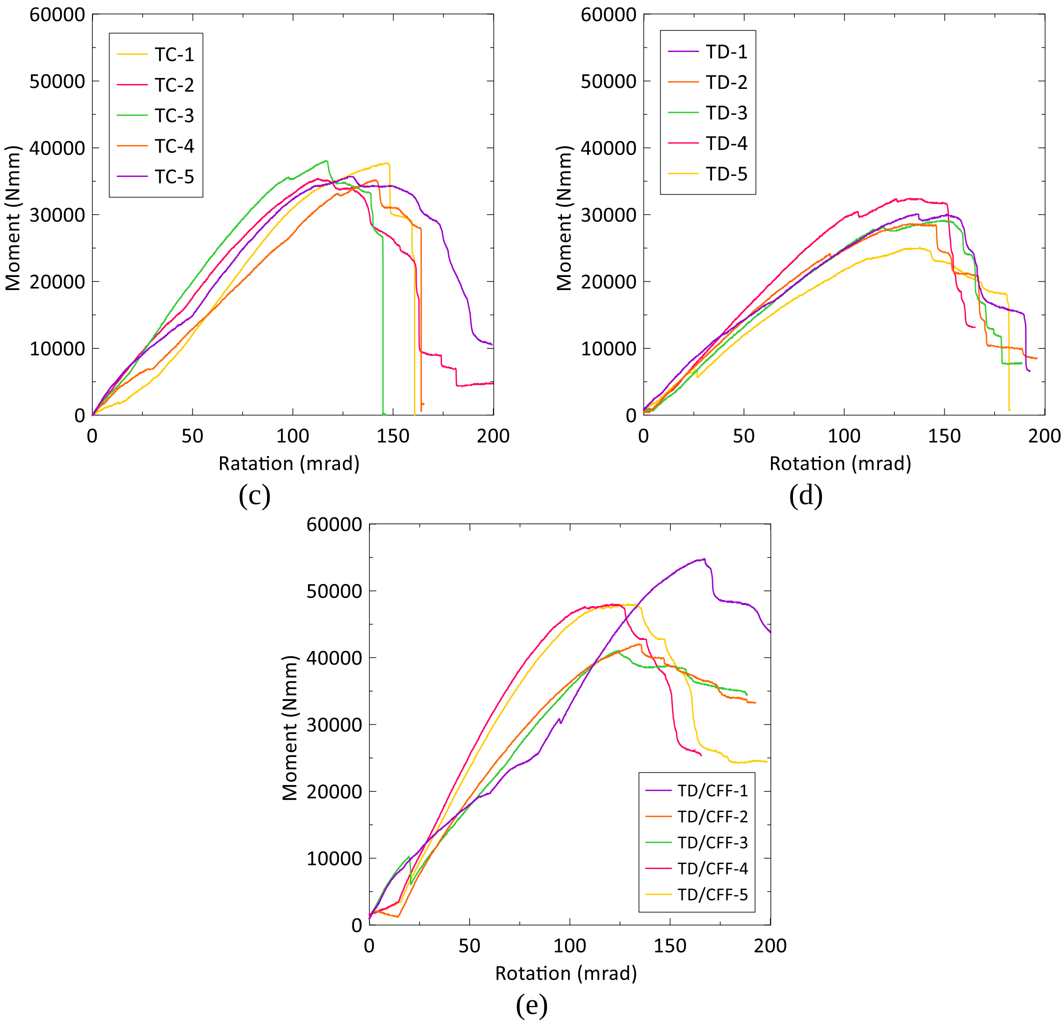

(c) (d)

(e)

Figure 7.3 - Moment-rotation for groups: (a) Type A, (b) Type B, (c) Type C, (d) Type D, (e) Type D/CFF.

7.3.1.2 Type A

Figure 7.3a illustrates the M × φ behavior for Type A and Figure 7.4 shows the main phases of the process. During the elastic phase of Type A loading, stresses concentrate at the CJ's center and corners, with tensile stresses developing at the upper corner and compressive stresses at the lower one (Figure 7.5a and b). As the loading progresses, these stresses increase until layer detachment occurs between the printed layers, which is expected due to the lower resistance at the interlayers [17], significantly influencing the strength [18], and limiting the potential of the proposed CJs. This detachment initiates crack propagation along the interlayer regions, increasing the CJ’s rotation and shear stress at the corners - eventually, a 45° shear crack forms at the tensile corner. The propagation of these cracks continues, progressively reducing the load-carrying capacity until ultimate failure occurs.

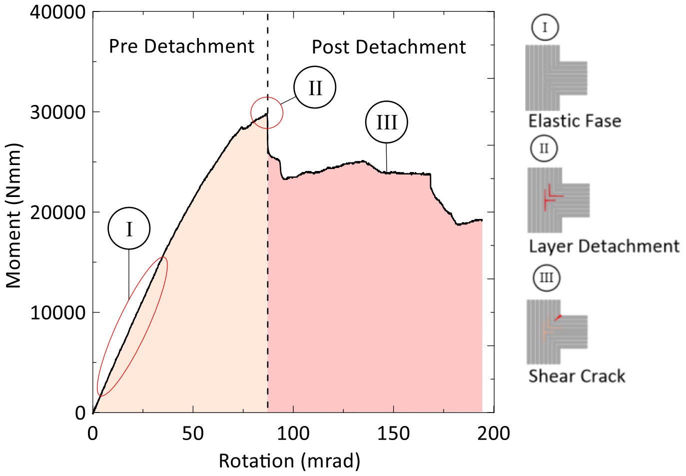

Figure 7.4 - Representative curve of Moment-rotation behavior for Type A.

Figure 7.5c and d show the failure mode for Type A, while Figure 7.5e demonstrates the consistency of this failure mode across all samples. As detailed in Table 7.6, which presents the key variables analyzed — Mmax (Moment at peak load), Φmax (Rotation at peak load), K (Stiffness), and U (Energy absorption until peak load) — the specimens exhibit similar behavior, significantly varying stiffness and strength values. These variations in strength and stiffness may be attributed to factors such as slight inconsistencies in the material properties, such as layer-layer adhesion [19], or small path variations from coding to real printing [20]This highlights the complex nature of the material behavior and its sensitivity to minor changes in the printing path. It also highlights the need to include intermediate printing paths to mitigate the weak resistance between layers. Such adjustments can enhance interlayer bonding, improve structural integrity, and reduce the risk of premature failure due to layer detachment or crack propagation.

Table 7.6 - Summary of results for Type A.

Sample	**M_{max} (Nmm)**	**Φ_{max} (mrad)**	**K (Nmm/mrad)**	**U(mJ)**
TA-1	24452.8	88.2	277.3	1269.9
TA-2	29473.9	87.1	338.5	1533.0
TA-3	24392.1	88.3	276.2	1214.3

TA-4	25945.2	109.4	237.2	1769.2
TA-5	31720.1	101.6	312.2	2050.1
Mean	27196.8	94.9	288.3	1567.3
S.D	3263.7	10.0	38.6	349.3
C.O.V	12.0%	10.6%	13.4%	22.3%
M_{max} - Moment at peak load; Φ_{max} - Rotation at peak load; K - stiffness; U - Energy absorption until peak load.				

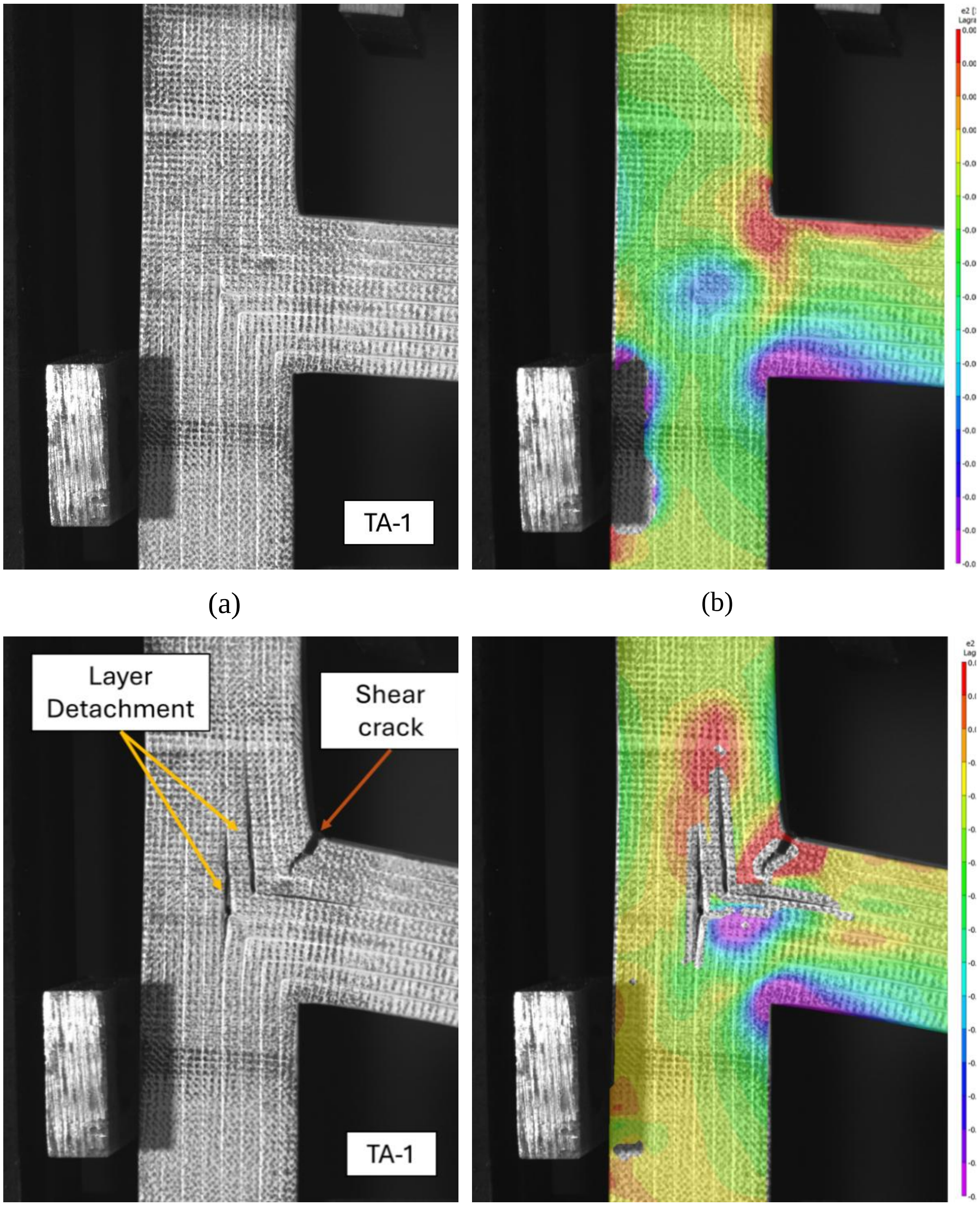

(a) (b)

(c) (d)

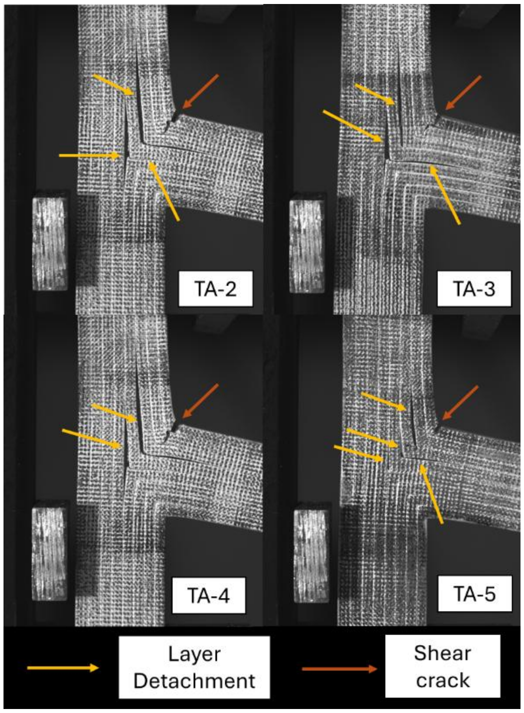

(e)

Figure 7.5 - Failure mode progression observed for Type A: (a) Elastic phase, (b) Typical strain distribution for Type A for elastic phase, (c) Representative failure, (d) Typical strain distribution for Type A after failure, and (e) Replicability of the failure.

7.3.1.3 Type B

The moment-rotation (M × φ) for each Type B sample is shown in Figure 6b. In this configuration, as identified in Figure 7.6, the curve has an initial elastic phase (Figure 7.7a and b) with stress concentration in the corners, followed by a sudden drop (Figure 7.7c), corresponding to the complete failure of the CJ. Figure 7.7d presents the replicability of the failure of Type B which can also be demonstrated by Table 7.7 where stiffness and strength values show minimal variability.

Despite a significant increase in load capacity attributed to the P45 layer arrangement, which effectively mitigates delamination and enhances moment resistance, the component ultimately exhibits extremely brittle behavior, failing without any warning. This lack of ductility is a critical limitation, as it prevents the material from providing visible or measurable signs of impending failure, such as gradual deformation or crack propagation. The sudden and catastrophic nature of the failure underscores the need for further optimization of the design and material composition to improve energy absorption and post-yield behavior. Addressing this limitation is essential for ensuring the reliability and safety of the printed component in structural applications.

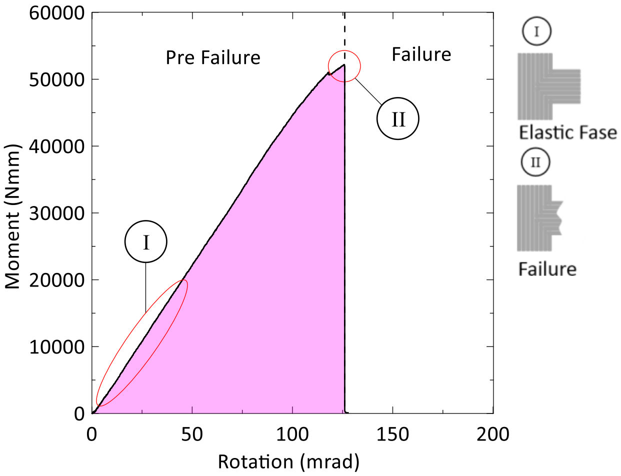

Figure 7.6 - Effect of increasing stiffness by modifying the arrangement of intermediate layers at 45°.

Table 7.7 - Summary of results for Type B.

Sample	**Mmax (Nmm)**	**Φmax (mrad)**	**K (Nmm/mrad)**	**U(mJ)**
TB-1	45604.9	120.9	377.3	2905.8
TB-2	52196.8	125.9	414.6	3513.0
TB-3	48716.1	129.7	375.5	3334.3
TB-4	48091.5	121.8	394.8	3101.6
TB-5	50183.2	129.7	386.9	3293.5
Mean	48958.5	125.6	389.8	3229.6
S.D	2451.7	4.2	15.9	232.7
C.O.V	5.0%	3.3%	4.1%	7.2%
M_{max} - Moment at peak load; Φ_{max} - Rotation at peak load; K - stiffness; U - Energy absorption until peak load.				

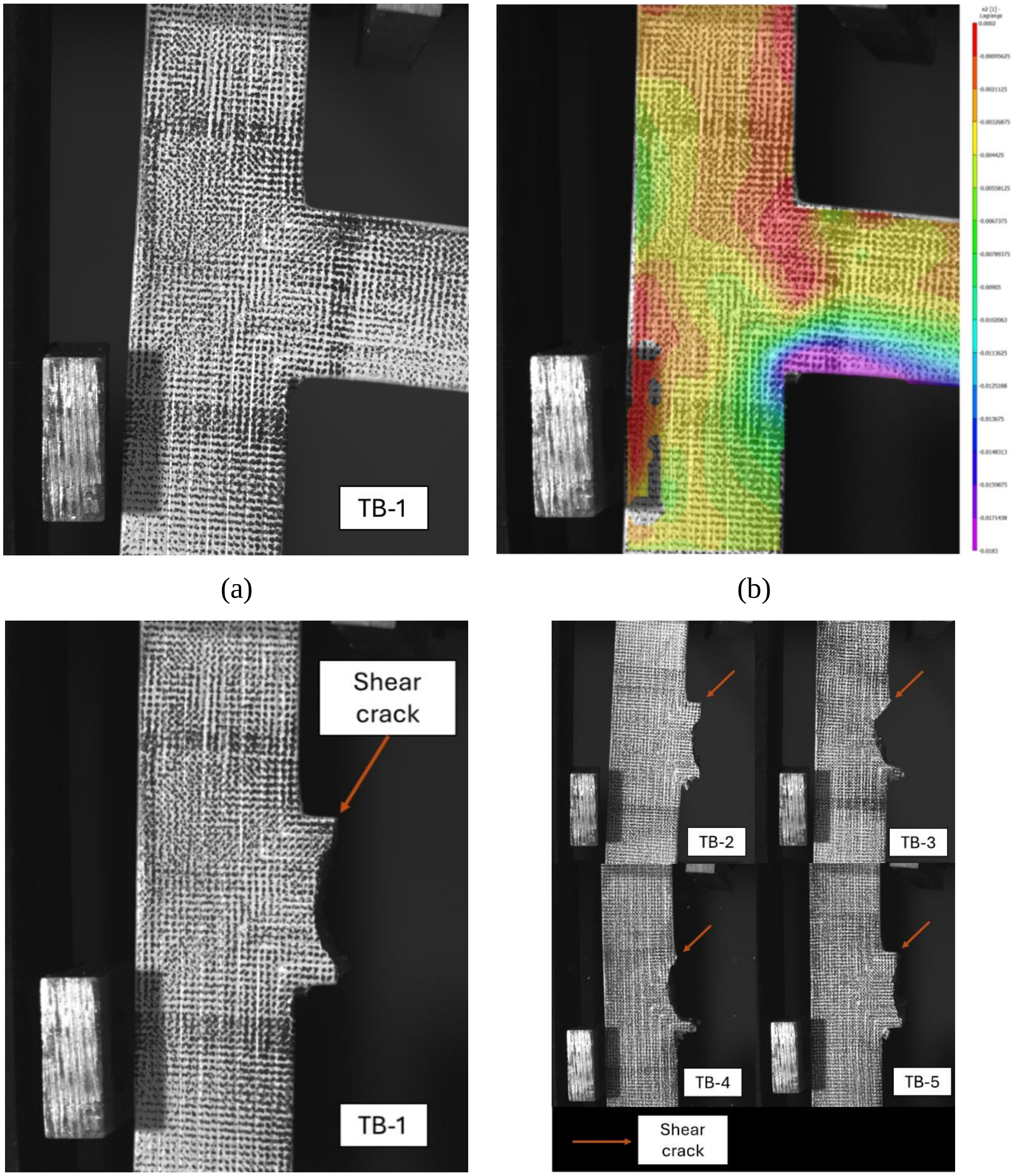

(a) (b)

(c) (d)

Figure 7.7 - Failure mode progression observed for Type B: (a) Elastic phase, (b) Typical strain distribution for Type B pre-failure, (c) Representative failure, and (d) Replicability of the failure.

7.3.1.4 Type C

In Figure 7.3c, the M × φ relationship for Type C is shown. In the elastic phase, similar to Type B, stress concentrations are located at the corners of the CJ (Figure 7.9a and b). As the load increases during the test, these stresses intensify, initiating the formation of a 45° shear crack at the corner under tension (Figure 7.9c and d). The propagation of this single shear crack progresses steadily, compromising the structure's integrity until complete failure occurs (Figure 7.9e). Figure 7.9f shows the replicability of the failure; however, some specimens did not experience complete rupture before reaching the displacement limit set by the test. Table 7.8 reveals a noticeable consistency in strength values across the tested specimens, indicating uniform load-carrying capacity.

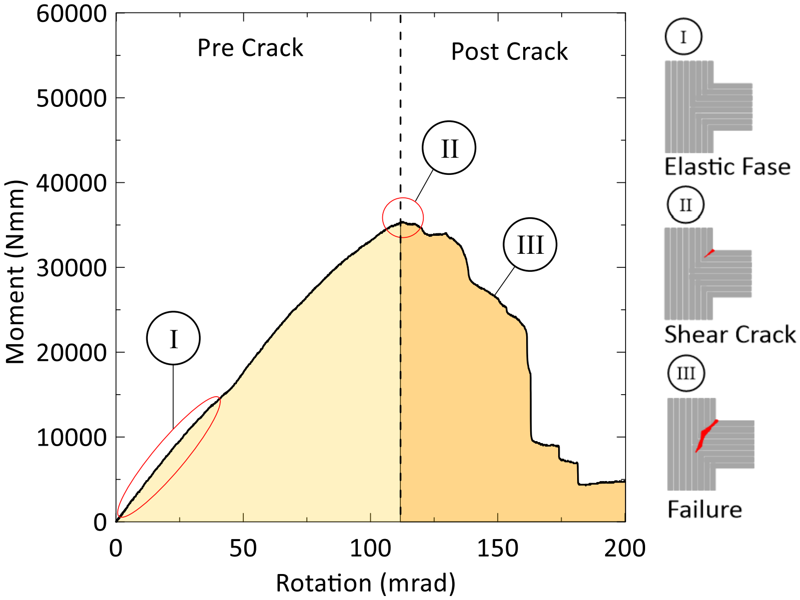

Figure 7.8 - Effect of increasing stiffness by modifying the arrangement of intermediate layers at 45°R and 45°L.

Table 7.8 - Summary of results for Type C.

Sample	Mmax (Nmm)	Φmax (mrad)	K (Nmm/mrad)	U(mJ)
TC-1	37699.1	147.4	255.7	2978.1
TC-2	35364.7	113.0	312.9	2232.6
TC-3	38062.6	124.4	306.0	2561.8
TC-4	35178.5	141.5	248.5	2687.7
TC-5	34793.2	133.5	260.7	2710.1

Mean	36219.6	132.0	280.7	2634.1
S.D	1535.8	13.7	30.3	270.8
C.O.V	4.2%	10.4%	10.9%	10.3%
M_{max} - Moment at peak load; Φ_{max} - Rotation at peak load; K - stiffness; U - Energy absorption until peak load.				

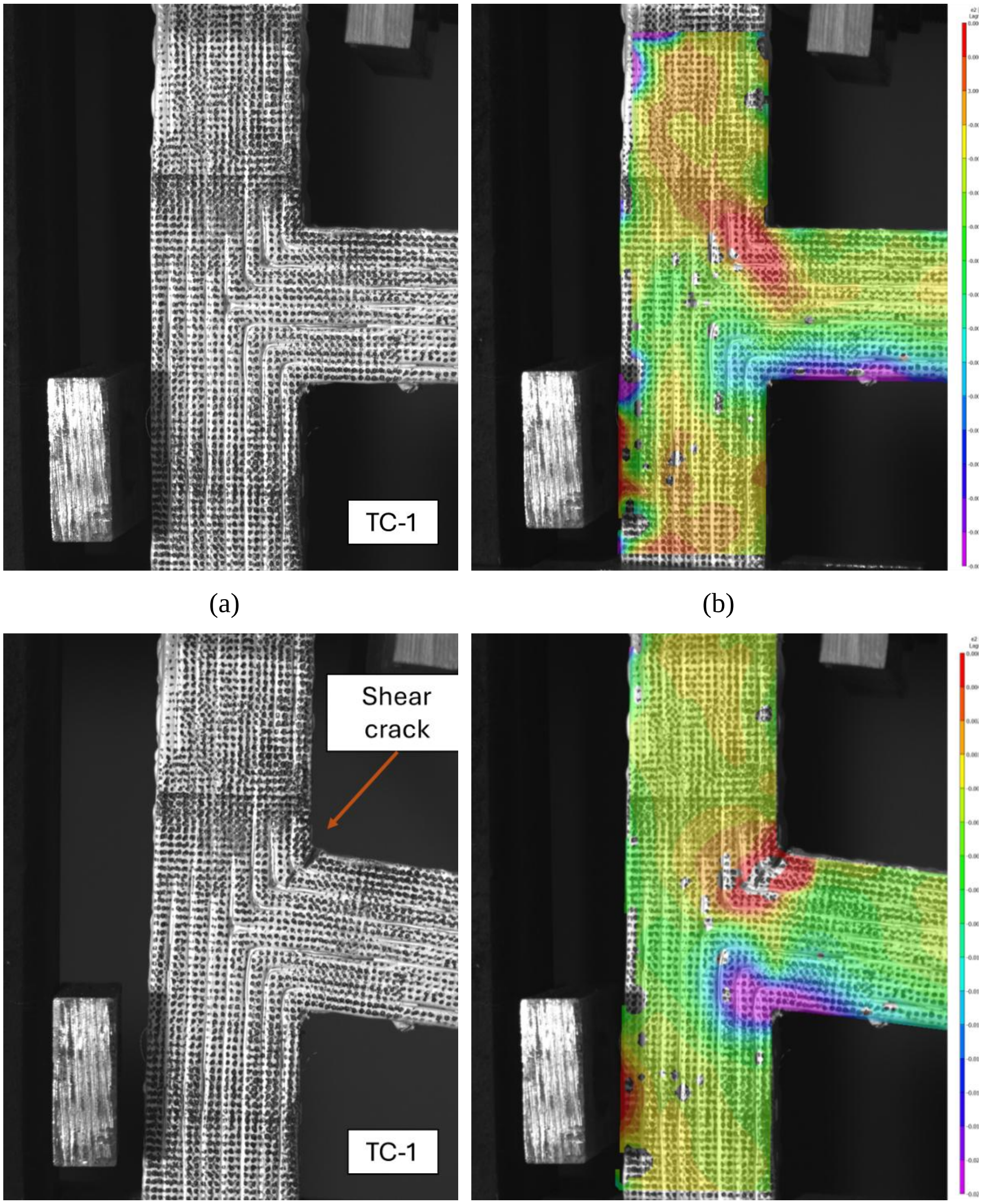

(a) (b)

(c) (d)

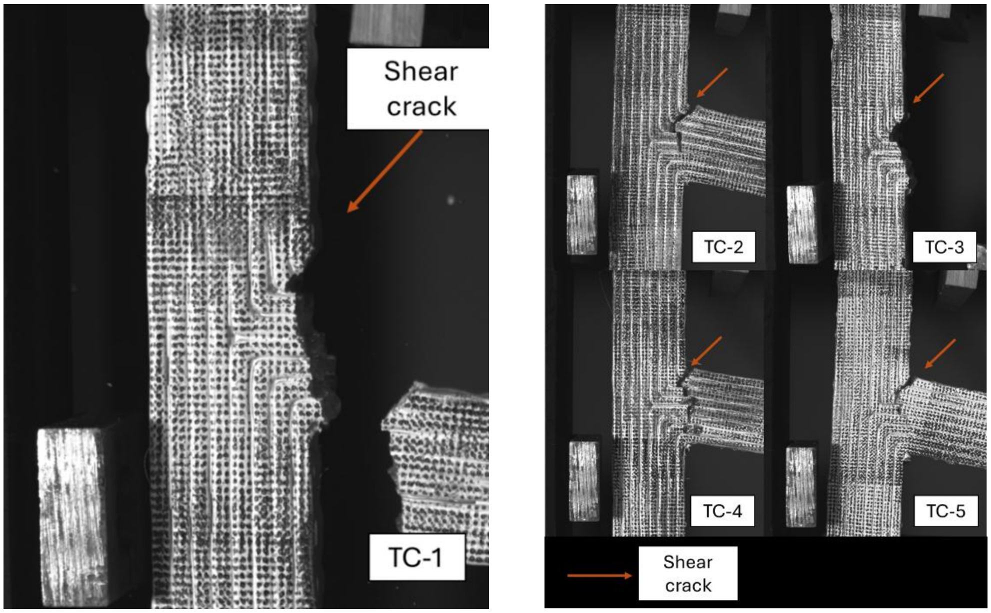

(e) (f)

Figure 7.9 - Failure mode observed for Type C: (a) Elastic phase, (b) Typical strain distribution for Type C for elastic phase, (c) Shear crack initiation, (d) Typical strain distribution for Type C after shear crack, (e) Failure mode, and (f) Replicability of the failure.

7.3.1.5 Type D

Figure 7.3d shows the M × φ behavior for each Type D sample, while Table 7.9 highlights that the specimens behave similarly. The behavior of Type D, as shown in Figure 7.10, begins with an elastic phase (Figure 7.11a and b) until the formation of the first shear crack. The crack then propagates to the interface between two printed layers of the CLP, where it continues to spread along the layer boundaries (Figure 7.11c and d). This propagation persists until it transitions to subsequent layers through shear cracks, ultimately leading to the complete failure of the structure. This behavior, consistently observed as indicated in Table 7.9 and Figure 7.11e, highlights the inadequacy of the P315 configuration, as its transverse alignment fails to effectively counteract shear cracks and is not favorable for moment resistance due to its misalignment with the principal stress directions during bending. Furthermore, the results underline the insufficient performance of neat PLA in resisting shear stress. The material lacks the necessary mechanical properties to counteract the shear forces, resulting in premature failure in regions of high-stress concentration. To address this limitation, the addition of tensile reinforcement is critical. Incorporating fibers or other reinforcements capable of efficiently withstanding tensile loads would improve the material's ability to distribute stresses without creating brittle material, mitigate crack propagation, and enhance both shear and flexural resistance, paving the way for more reliable structural applications.

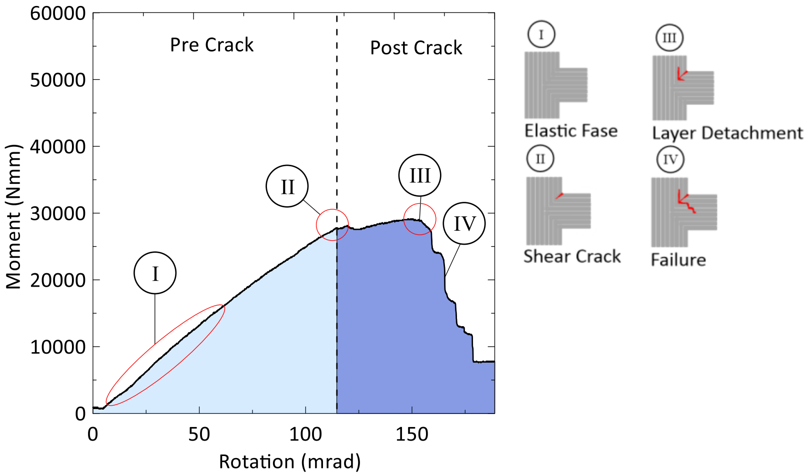

Figure 7.10 - Effect of increasing stiffness by modifying the arrangement of intermediate layers at P315.

Table 7.9 - Summary of results for Type D.

Sample	**Mmax (Nmm)**	**Φmax (mrad)**	**K (Nmm/mrad)**	**U(mJ)**
TD-1	27548.1	147.9	186.2	2382.5
TD-2	26367.8	144.3	182.7	2294.9
TD-3	26489.4	162.5	163.0	2638.6
TD-4	26945.5	148.4	181.6	2314.7
TD-5	30730.9	149.6	205.5	2732.6
Mean	27616.3	150.6	183.8	2472.6
S.D	1801.7	7.0	15.1	199.9
C.O.V	6.5%	4.6%	8.2%	8.1%
M_{max} - Moment at peak load; Φ_{max} - Rotation at peak load; K - stiffness; U - Energy absorption until peak load.				

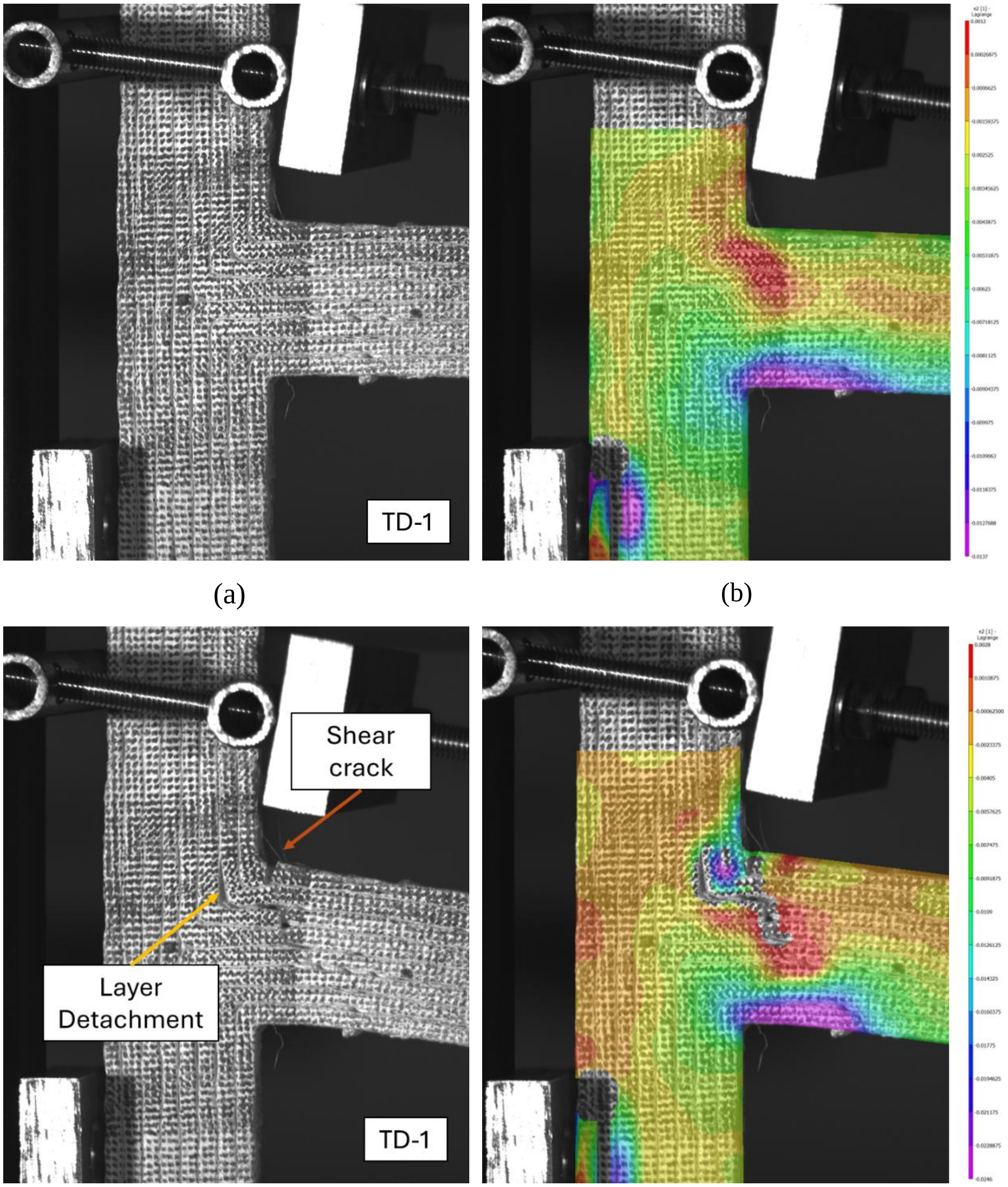
TD-1
e2 [1] - Lagrange
0.0012
0.00026875
-0.0006625
-0.00159375
-0.002525
-0.00345625
-0.0043875
-0.00531875
-0.00625
-0.00718125
-0.0081125
-0.00904375
-0.009975
-0.0109063
-0.0118375
-0.0127688
-0.0137
Shear crack
Layer Detachment
TD-1
e2 [1] - Lagrange
0.0028
0.0010875
-0.00062500
-0.0023375
-0.00405
-0.0057625
-0.007475
-0.0091875
-0.0109
-0.0126125
-0.014325
-0.0160375
-0.01775
-0.0194625
-0.021175
-0.0228875
-0.0246

(a) (b)

(c) (d)

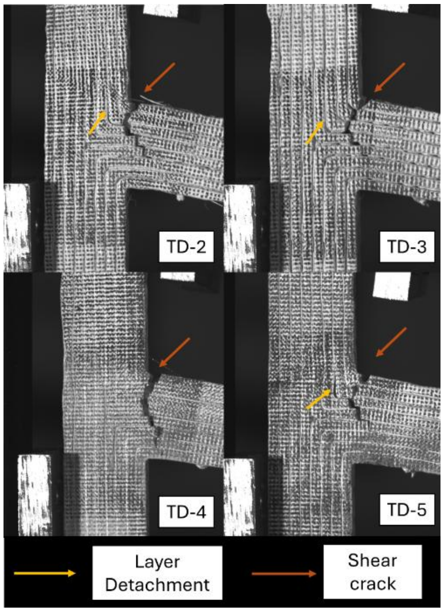

(e)

Figure 7.11 - Failure mode observed for Type D: (a) Elastic phase, (b) Typical strain distribution for Type D for elastic phase, (c) Failure mode, (d) Typical strain distribution for Type D after Failure mode, and (e) Replicability of the failure.

7.3.1.6 Comparison

Table 7.10 summarizes the results for the groups. Figure 7.12a and Figure 7.12b compares the maximum strength-stiffness and moment-rotation curves for all the groups studied, highlighting a representative curve for each group. Type B exhibits a 35.2% increase in stiffness (K) (389.8 ± 15.9 vs. 288.3 ± 38.9) and an 80.0% increase in strength (Mmax) (48958.5 ± 2451.7 vs. 27196.8 ± 3263.7) compared to Type A, representing a remarkable improvement. These results demonstrate the consistency, stiffness, and strength enhancements achieved by Type B. The substitution of longitudinal layers with 45° layers (P45) effectively countered the shear forces at the tensile corner, preventing layer detachment and enhancing structural performance. The moment-rotation behavior further confirms the structural advantages of this design modification, with Type B displaying superior mechanical performance across all tested parameters. However, despite these advantages, Type B exhibits a fast brittle failure mode, limiting its suitability for structural applications. The abrupt nature of its failure, without warning signs, poses a critical safety concern, emphasizing the need for designs that offer greater ductility and energy absorption under load.

In contrast, Type A, with a stiffness of 288.3 ± 38.9 and a strength of 27196.8 ± 3263.7, is limited by its uniform layer orientation, where failure is dominated by weak interlayer adhesion. This weakness, common in additively manufactured materials [21], defines its ultimate strength and highlights the need for treatments to enhance interlayer bonding. However, even with such improvements, this issue will likely remain a fundamental challenge in additive manufacturing, making Type A less suitable for applications requiring high strength and reliability. Type C occupies an intermediate position between Types B and D, offering a 33.2% increase in strength compared to Type A (36219.6 ± 1535.8 vs. 27196.8 ± 3263.7) but showing a slight reduction in stiffness by 2.6% (280.7 ± 35.8 vs. 288.3 ± 38.9). Additionally, its layer arrangement introduces variability in performance, leading to less consistent mechanical responses. This lack of control diminishes its reliability for demanding applications. Finally, Type D demonstrates the limitations of altering the printing direction without material reinforcement. Despite a strength of 27616.3 ± 1801.7, no significant gains in strength were achieved compared to Type A (27196.8 ± 3263.7). Additionally, a 32.9% reduction in stiffness was observed (216.9 ± 12.2 vs. 288.3 ± 38.9), highlighting its structural limitations. As evidenced by the Probability Plot (Figure 7.12c)), these results indicate that the neat PLA configuration is ineffective for this loading condition, underscoring the necessity of alternative designs or material modifications to enhance performance under such stresses.

Table 7.10 - Comparative of results.

Sample	**Mmax (Nmm)**	**Φmax (mrad)**	**K (Nmm/mrad)**	**U(mJ)**
Type A	27196.8±3263.7	94.9±10.1	288.3±38.9	1567.3±349.3
Type B	48958.5±2451.7	125.6±4.2	389.8±15.9	3229.6±232.7
Type C	36219.6±1535.8	130.5±15.1	280.7±35.8	2634.1±270.8
Type D	27616.3±1801.7	138.6±6.3	216.9±12.2	2472.6±199.9
M_{max} - Moment at peak load; Φ_{max} - Rotation at peak load; K - stiffness; U - Energy absorption until peak load.				

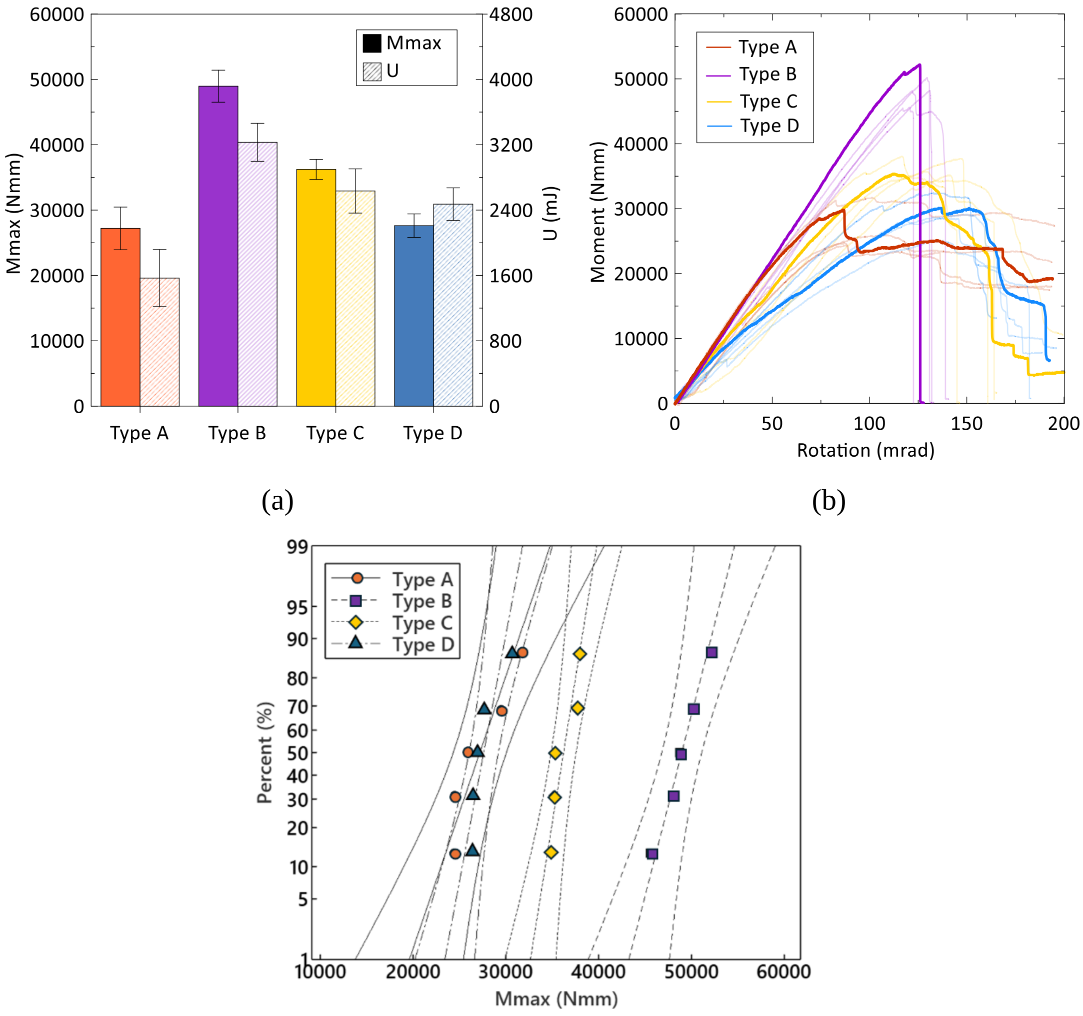

(a) (b)

(c)

Figure 7.12 - Comparative behavior for the four groups: (a) Bar charts of Mmax and U, (b) Moment x Rotation curves, and (c) Probability Plot of Mmax.

7.3.2 Incorporation of CNYR

CNYR was added at the CJ in the Type D configuration because the P315 orientation allows the yarn to act in tension in the region where the shear crack opening occurs. This arrangement was strategically chosen to optimize the mechanical performance of the composite by aligning the fibers with the principal stress paths. The fiber orientation at P315 enhances the material's capacity to resist shear forces, as it effectively engages the tensile strength of the yarn to counteract crack propagation.

Although the P45 configuration demonstrated better overall results compared to P315, the addition of fibers in the P45 orientation would place them under compression, which is not effective for mitigating abrupt failure. This highlights the importance of selecting configurations where fibers can work in tension, particularly in complex stress-stressed areas, to improve structural integrity and load redistribution.

The initial analysis of the printing process with CNYR, as shown in Figure 7.13, highlights that the use of larger continuous fiber yarns in the printing process exhibits a greater tendency for misalignment. This misalignment can occur due to the difficulty in maintaining precise control over the placement of yarns during deposition, which may lead to deviations from the intended path. This is consistent with the findings of Rivero-Romero et al. [22], Fruleux et al. [20], and Cheng et al. [23], who observed that the flow of molten composite material exerts a drag force on the fibers, partially displacing them from the deposited line and causing misalignment and fiber-matrix’s lack of adherence. This issue is further exacerbated by the increased stiffness of larger yarns, which reduces their ability to conform to the intended trajectory during deposition, reducing the printing quality, diminishing the overall printing quality, and consequently compromising the material's full potential.

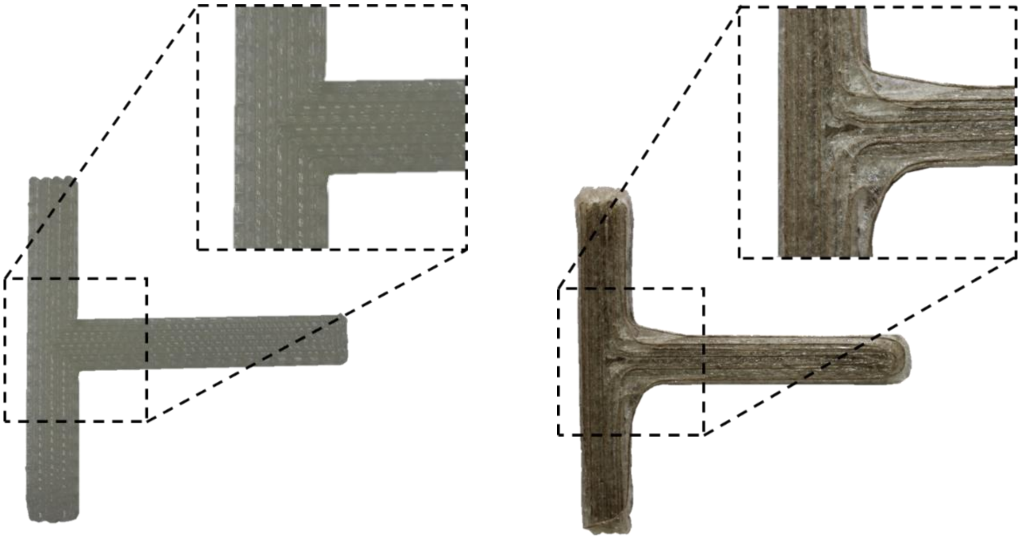

(a) (b)

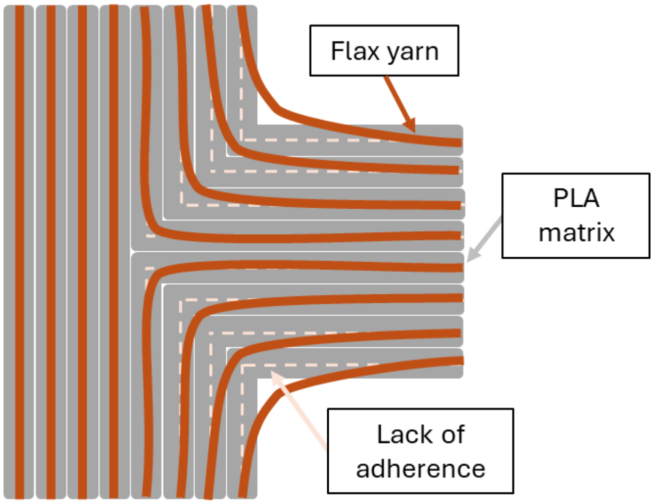

(c)

Figure 7.13 - Fiber addition on the CJ print path: (a) Neat PLA (Type B), (b) CFF (Type D/CFF), and (c) Lack of adherence in CFRTPCs.

Figure 7.3d presents the M × φ behavior for Type D/CFF, and Table 7.11 shows the main data after the incorporation of CNYR. The behavior, shown in Figure 7.14a, begins with an elastic phase (Figure 7.15a and b), followed by the initiation of a shear crack that propagates until material failure where the fibers bridges mitigate the abrupt failure (Figure 7.15c and d). The results highlight a significant enhancement in mechanical performance when compared to the original Type D configuration. The strength capacity increased from 27616.3 ± 1801.7 to 42979.6, representing an improvement of 43.2%. Compared to the baseline group (Type A: 27196.8 ± 3263.7), the strength shows an even more remarkable gain of 58.0%. In terms of stiffness, Type A exhibited a value of 288.3 ± 38.9, while Type D showed a reduction to 216.9 ± 12.2. With the incorporation of CNYR into Type D/CFF, the stiffness increased significantly by 34.9%, underscoring the contribution of the fibers in enhancing structural rigidity. These performance gains can be attributed primarily to the effectiveness provided by the CNYR. Their incorporation effectively mitigated the influence of shear forces, particularly in the tensile corner—a region recognized for its susceptibility to stress concentration and potential failure—by controlling the crack opening. The yarns' ability to distribute and absorb stress contributed significantly to enhancing the composite's load-bearing capacity and stiffness, as the yarns force failure to occur due to the separation between layers.

In addition to the improvements in strength and stiffness, the energy absorption capacity also showed significant gains Figure 7.14b). For Type A, the energy absorption was 1567.3 ± 349.3mJ. With the change to the Type D configuration, this value increased to 2472.6 ± 199.9mJ, representing an improvement of 57.7%. Following the incorporation of CNYR fibers into Type D/CFF, the energy absorption reached an impressive 3566.5 ± 798.7mJ, reflecting a further increase of 44.2% compared to Type D and an overall enhancement of 127.5% relative to Type A. Notably, the larger variation in standard deviation observed for the Type D/CFF configuration can be attributed to issues associated with the printing of continuous fibers. Variations in fiber alignment, bonding quality between layers, and potential imperfections during the extrusion process contribute to this inconsistency. Nevertheless, these substantial gains underscore the role of fibers in enhancing energy dissipation, effectively improving the composite's resistance to catastrophic failure.

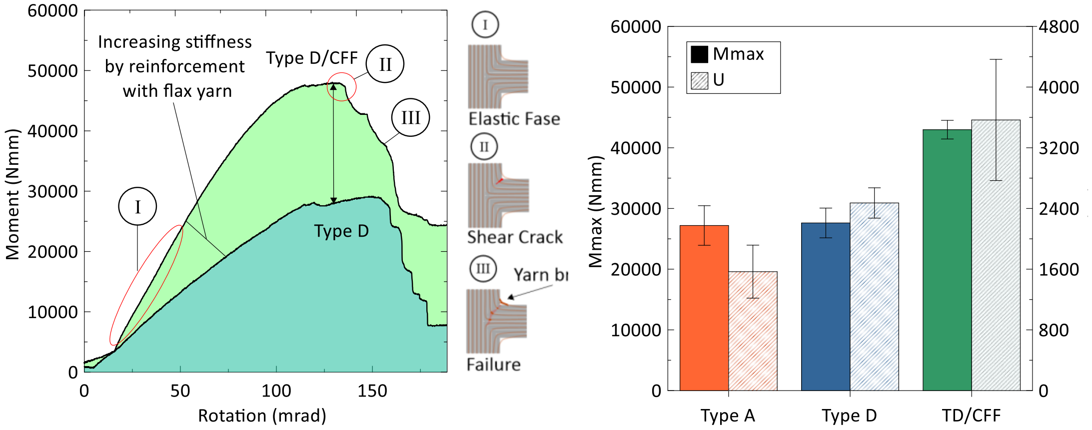

(a) (b)

Figure 7.14 - Comparative graphics of effects of addition of CNYR: (a) Moment x Rotation curves, and (b) Bar charts of Mmax and U.

Table 7.11 - Summary of results for Type B/CFF.

Sample	Mmax (Nmm)	Φmax (mrad)	K (Nmm/mrad)	U(mJ)
TD/CFF-1	50080.6	181.2	276.4	4883.9
TD/CFF-2	38605.5	146.2	264.0	3229.9

TD/CFF-3	36996.7	137.6	268.9	2803.9
TD/CFF-4	43383.4	138.0	314.4	3236.4
TD/CFF-5	45832.0	135.2	338.9	3678.1
Mean	42979.6	147.6	292.5	3566.5
S.D	5330.4	19.2	32.6	798.7
C.O.V	12.4%	13.0%	11.2%	22.4%

Figure 7.15 illustrates the failure modes observed in the Type D/CFF configuration, emphasizing the transformative effect of fiber addition on the material’s mechanical behavior. The incorporation of continuous fibers significantly reduced the occurrence of brittle failure, a common limitation in unreinforced printed composites. This improvement is attributed to the formation of load bridges at the CJ, where the yarn effectively distributes and absorbs stress. Additionally, the fibers notably enhanced the material's delamination resistance by controlling crack propagation along the interlayer regions. By countering stress concentrations and delaying the onset of crack growth, the fibers contribute to a more controlled and predictable failure mechanism. This ability to modulate the material’s failure mode underscores its suitability for structural applications, where reliability and performance under stress conditions are critical. The results demonstrate that the addition of fibers not only enhances the load-bearing capacity but also improves overall durability, particularly under complex or variable loading scenarios, by mitigating delamination and ensuring structural integrity.

Furthermore, the optimized interaction between the fibers and the matrix plays a pivotal role in achieving these enhancements. This synergy ensures effective stress transfer and minimizes issues such as delamination or interfacial weakness. The combination of improved structural integrity, controlled failure behavior, and increased durability positions this approach as a highly promising solution for the development of advanced 3D-printed structural elements with superior performance and long-term reliability.

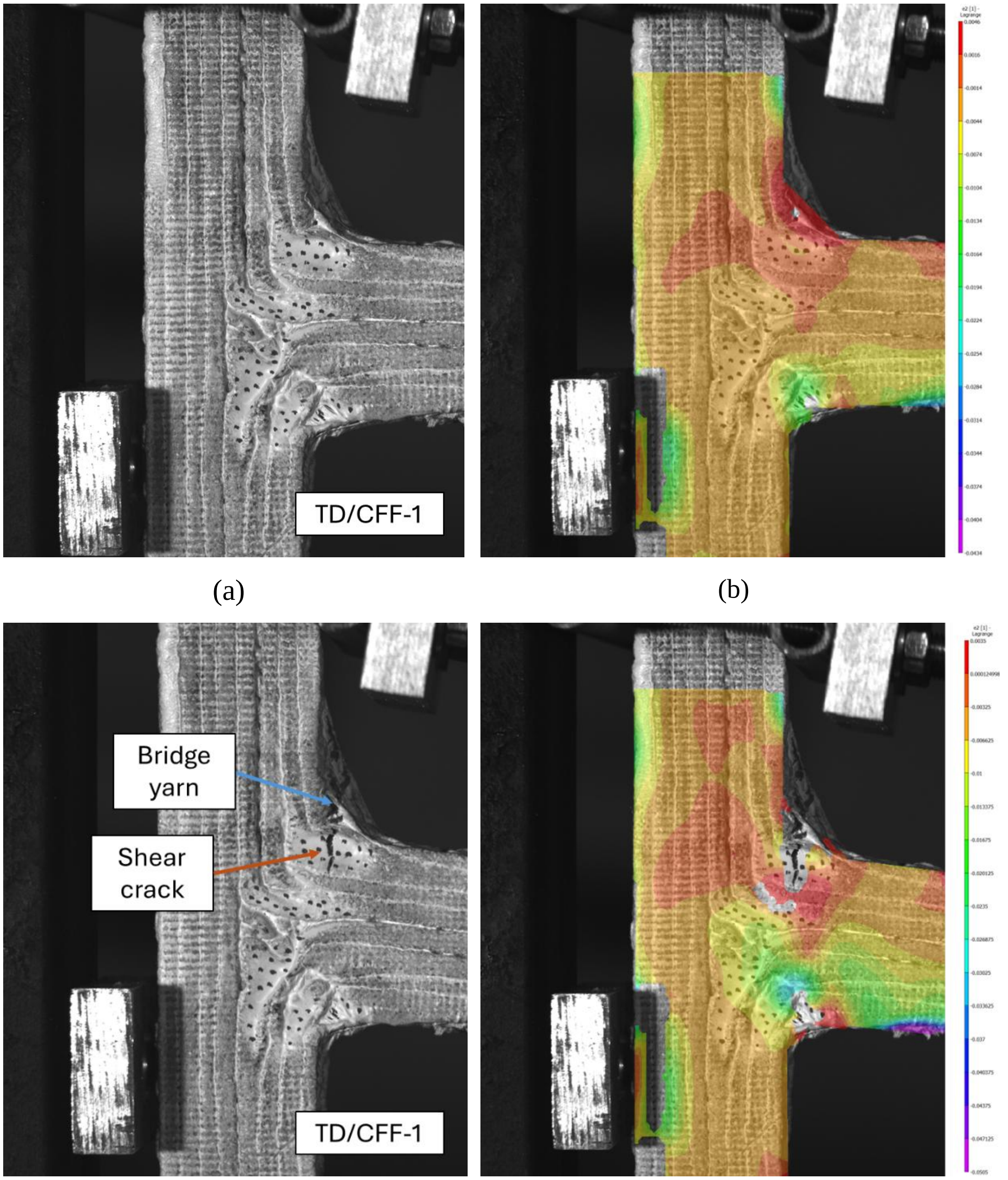
TD/CFF-1
e2 [1] - Lagrange
0.0046
0.0016
-0.0014
-0.0044
-0.0074
-0.0104
-0.0134
-0.0164
-0.0194
-0.0224
-0.0254
-0.0284
-0.0314
-0.0344
-0.0374
-0.0404
-0.0434
Bridge yarn
Shear crack
TD/CFF-1
e2 [1] - Lagrange
0.0035
0.000124998
-0.00325
-0.006625
-0.01
-0.013375
-0.01675
-0.020125
-0.0235
-0.026875
-0.03025
-0.033625
-0.037
-0.040375
-0.04375
-0.047125
-0.0505

(a) (b)

(c) (d)

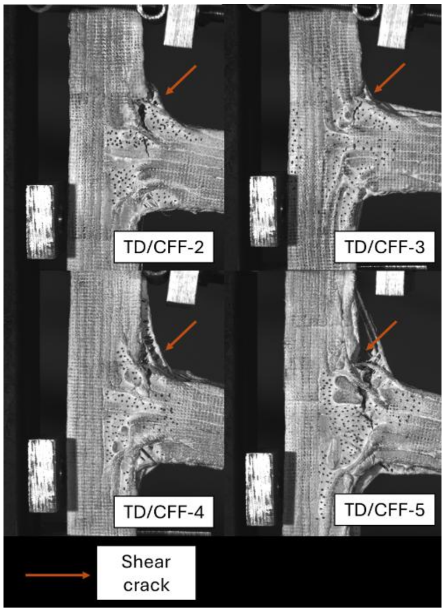

(e)

Figure 7.15 - Failure mode observed for Type D/CFF: (a) Representative failure, (b) Typical strain distribution for Type D/CFF after failure, (c) Representative failure, and (d) Replicability of the failure.

7.4 Conclusions

This study evaluated optimization paths for high-performance biostructures using AM, which allows precise control over layer orientation to counteract combined stresses, enhancing mechanical performance and enabling tailored design optimization. The key findings are:

- The sensitivity of the material to the printing path was evident, with Type B showing improved stiffness (35.2%) and strength (80.0%) compared to Type A, demonstrating that layer orientation has a significant impact on the mechanical properties. The optimized path for Type B maximized the alignment of the fibers, leading to more efficient load transfer and increased structural integrity.Replacing longitudinal layers with P45 layers enhanced the performance of printed composites by increasing stiffness due to a reduction in the lever arm but exacerbated the brittle failure effect indicating that while structural optimization can improve one property, it may introduce new challenges such as fracture propagation, which must be mitigated through further material modifications.

- The addition of CNYR to Type D/CFF increased strength (43.2%) and stiffness (34.9%) compared to Neat PLA Type D, while reducing brittle failure through stress distribution at CJs. This result highlights the beneficial role of natural fiber reinforcement in improving the mechanical performance and toughness of the biocomposite. However, the degree of misalignment of the fibers remained a limiting factor in optimal stress transfer, and addressing this issue could further enhance the material's properties.

Future work should explore the scalability of this approach, its applicability to various composite configurations, and enhanced impregnation treatments to improve fiber-matrix interaction and overall material performance.

References

[1] Garrett W. Melenkaa, Benjamin K.O. Cheunga, Jonathon S. Schofielda, Michael R. Dawsonb JPC. Evaluation and Prediction of the Tensile Properties of Continuous Fiber-Reinforced 3D Printed Structures Authors: Garrett W. Melenka 2016.

[2] ZHU J, ZHOU H, WANG C, ZHOU L, YUAN S, ZHANG W. A review of topology optimization for additive manufacturing: Status and challenges. Chinese Journal of Aeronautics 2021;34:91–110. https://doi.org/10.1016/j.cja.2020.09.020.

[3] Tekinalp HL, Kunc V, Velez-Garcia GM, Duty CE, Love LJ, Naskar AK, et al. Highly oriented carbon fiber-polymer composites via additive manufacturing. Compos Sci Technol 2014;105:144–50. https://doi.org/10.1016/j.compscitech.2014.10.009.

[4] Bittrich L, Spickenheuer A, Almeida JHS, Müller S, Kroll L, Heinrich G. Optimizing Variable-Axial Fiber-Reinforced Composite Laminates: The Direct Fiber Path Optimization Concept. Math Probl Eng 2019;2019. https://doi.org/10.1155/2019/8260563.

[5] Kelly DW, Hsu P, Asudullah M. Load paths and load flow in finite element analysis. Eng Comput (Swansea) 2001;18:304–13. https://doi.org/10.1108/02644400110365923.

[6] Wang T, Li N, Link G, Jelonnek J, Fleischer J, Dittus J, et al. Load-dependent path planning method for 3D printing of continuous fiber reinforced plastics. Compos Part A Appl Sci Manuf 2021;140. https://doi.org/10.1016/j.compositesa.2020.106181.

[7] Papapetrou VS, Patel C, Tamijani AY. Stiffness-based optimization framework for the topology and fiber paths of continuous fiber composites. Compos B Eng 2020;183:107681. https://doi.org/10.1016/j.compositesb.2019.107681.

[8] Li N, Link G, Wang T, Ramopoulos V, Neumaier D, Hofele J, et al. Path-designed 3D printing for topological optimized continuous carbon fibre reinforced composite structures. Compos B Eng 2020;182:107612. https://doi.org/10.1016/j.compositesb.2019.107612.

[9] Chen Y, Ye L. Topological design for 3D-printing of carbon fibre reinforced composite structural parts. Compos Sci Technol 2021;204:108644. https://doi.org/10.1016/j.compscitech.2020.108644.

[10] Huang Y, Tian X, Zheng Z, Li D, Malakhov A V., Polilov AN. Multiscale concurrent design and 3D printing of continuous fiber reinforced thermoplastic composites with optimized fiber trajectory and topological structure. Compos Struct 2022;285:115241. https://doi.org/10.1016/j.compstruct.2022.115241.

[11] Mohanty AK, Misra M, Drzal LT. Natural fibers, biopolymers, and biocomposites. Taylor & Francis; 2005.

[12] Wambua P, Ivens J, Verpoest I. Natural fibres: Can they replace glass in fibre reinforced plastics? Compos Sci Technol 2003;63:1259–64. https://doi.org/10.1016/S0266-3538(03)00096-4.

[13] Santos N V., Cardoso DCT. 3D printing of vegetable yarn-reinforced polymer components. J Clean Prod 2023;415. https://doi.org/10.1016/j.jclepro.2023.137870.

[14] Neto JSS, Lima RAA, Cavalcanti DKK, Souza JPB, Aguiar RAA, Banea MD. Effect of chemical treatment on the thermal properties of hybrid natural fiber-

reinforced composites. J Appl Polym Sci 2019;136:1–13. https://doi.org/10.1002/app.47154.

[15] Morrison WH, Archibald DD, Sharma HSS, Akin DE. Chemical and physical characterization of water- and dew-retted flax fibers. Ind Crops Prod 2000;12:39–46. https://doi.org/10.1016/S0926-6690(99)00044-8.

[16] Santos N V., Cardoso DCT. 3D printing of vegetable yarn-reinforced polymer components. J Clean Prod 2023;415. https://doi.org/10.1016/j.jclepro.2023.137870.

[17] Cavalcanti DKK, Banea MD, de Queiroz HFM. Effect of material on the mechanical properties of additive manufactured thermoplastic parts. Annals of "Dunarea de Jos" University of Galati, Fascicle XII, Welding Equipment and Technology 2020;31:5–12. https://doi.org/10.35219/awet.2020.01.

[18] Beserra JHN, de Melo JVA de MC, Cardoso DCT. Development of a novel 3D-printed moment connection for pultruded profiles joints. Structures 2024;60. https://doi.org/10.1016/j.istruc.2024.105850.

[19] Zhang H, Lei X, Hu Q, Wu S, Aburaia M, Gonzalez-Gutierrez J, et al. Hybrid Printing Method of Polymer and Continuous Fiber-Reinforced Thermoplastic Composites (CFRTPCs) for Pipes through Double-Nozzle Five-Axis Printer. Polymers (Basel) 2022;14. https://doi.org/10.3390/polym14040819.

[20] Fruleux T, Castro M, Correa D, Wang K, Matsuzaki R, Duigou A Le. Geometric limitations of 3D printed continuous flax-fiber reinforced biocomposites cellular lattice structures. Composites Part C: Open Access 2022;9. https://doi.org/10.1016/j.jcomc.2022.100313.

[21] Yang C, Tian X, Liu T, Cao Y, Li D. 3D printing for continuous fiber reinforced thermoplastic composites: Mechanism and performance. Rapid Prototyp J 2017;23:209–15. https://doi.org/10.1108/RPJ-08-2015-0098.

[22] Rivero-Romero O, Barrera-Fajardo I, Unfried-Silgado J. Effects of printing parameters on fiber eccentricity and porosity level in a thermoplastic matrix composite reinforced with continuous banana fiber fabricated by FFF with in situ impregnation. International Journal of Advanced Manufacturing

Technology 2023;125:1893–901. https://doi.org/10.1007/s00170-022-10799-8.

[23] Cheng P, Wang K, Chen X, Wang J, Peng Y, Ahzi S, et al. Interfacial and mechanical properties of continuous ramie fiber reinforced biocomposites fabricated by in-situ impregnated 3D printing. Ind Crops Prod 2021;170:113760. https://doi.org/10.1016/j.indcrop.2021.113760.

Chapter 8 - CONCLUSIONS AND FUTURE WORK

8.1. Conclusions

This study explored the potential of continuous natural fiber-reinforced biocomposites fabricated via 3D printing, offering valuable insights into both material performance and technological advancements. It has highlighted both the opportunities and challenges associated with using vegetable yarns as reinforcements in thermoplastic matrices for structural components. Although mechanical improvements were achieved, further optimization is required to fully harness the benefits of continuous natural fibers within additive manufacturing processes.

The research demonstrated that the incorporation of continuous fiber yarns—such as flax, jute, ramie, and sisal—contributed to improved mechanical properties, increased crystallinity, and reduced polymer consumption, which supports sustainable manufacturing goals. However, achieving consistent fiber-matrix adhesion remains a key challenge. Different insertion methods were evaluated, with the semi-finished filament (SF) approach offering better fiber impregnation, superior mechanical performance, and faster printing speeds compared to in-nozzle (IN) impregnation. Additionally, the mechanical performance of printed components was found to be highly dependent on fiber impregnation, fiber diameter, and printing parameters.

Adhesively bonded joints with continuous natural fiber-reinforced adherends also presented promising results for mono- and bi-material combinations. JFRP-wood joints exhibited the highest failure load, highlighting the potential of combining natural fibers with stiffer materials for sustainable hybrid structures. Despite the brittle nature of PLA-based joints, the inclusion of continuous fibers mitigated catastrophic failure, enhancing joint performance and structural integrity.

Furthermore, this investigation demonstrated that natural fibers remain intact at the melting temperature of PLA, as confirmed by TGA and DSC analyses, ensuring their compatibility with FFF. However, void formation and fiber slippage during angled-layer deposition emphasized the need for optimized printing parameters specific to multi-layered components. Future research should focus on pre-treatments for both the fiber and matrix to enhance fiber impregnation and interlayer bonding, improving the load-bearing capacity of biocomposites.

Finally, this study also highlights the importance of optimizing printing paths in additive manufacturing to enhance the performance of high-strength structures. Strategically placed intermediate layers and optimized layer orientations were shown to significantly improve stiffness and strength. The integration of continuous natural yarn reinforcement (CNYR) demonstrated additional benefits, including increased mechanical performance and a reduced likelihood of brittle failure. These advancements emphasize the potential of combining innovative reinforcement strategies with sustainable materials to address complex structural demands.

8.2. Suggestions for future works

While this study has provided valuable insights into the use of natural fiber yarns in 3D-printed biocomposites, it also highlights new areas for further investigation. Although improvements in mechanical performance were achieved, challenges remain regarding interlayer adhesion and the optimization of printing parameters for fiber-reinforced components.

Further testing could be carried out on components such as beams and pipes, as well as the influence of environmental effects (temperature and humidity) and loading conditions (including torsion and cyclical loading) to better understand and improve the performance of these biocomposites.

Future research should focus on methods to enhance interlayer adhesion quality and investigate pre-treatments (like alkali or enzymatic) of both the fiber and matrix to improve yarn impregnation, ensuring better fiber-matrix bonding and enhanced mechanical performance in load-bearing applications. Additionally, researchers are encouraged to conduct large-scale testing to advance the technology’s applicability. The potential of combining multiple filaments for large-scale flow applications also presents a promising avenue for future exploration.